The Melting Greenland Ice Sheet and the Implications for the Ocean

Jennifer B Ross

A Thesis Submitted for the Degree of Doctor of Philosophy

The Department of Geography
University of Sheffield

May 2022

Acknowledgements

First and foremost I would like to thank my primary supervisor, Prof. Grant Bigg. He was the most supportive person I could have possibly asked for, and getting to this point would have been impossible without him. Also, my co-supervisor at Cranfield University, Dr Yifan Zhao, was really helpful with all things concerning the WERR model and the machine learning approach. In Southampton, my co-supervisor Prof. Bob Marsh provided a useful insight on the NEMO chapter, while Dr Bablu Sinha was also extremely helpful whenever I had questions about the NEMO model.

I would like to thank the Ocean Risk team at AXA XL for funding my project, especially Lindsay Getschel and Chip Cunliffe. My supervisor at AXA XL, Dr John Wardman, was exceptionally supportive throughout the project, but notably during the 6-week secondment in London, where he made the time productive and enjoyable.

Special thanks go to Dr David Wilton, who was invaluable in getting the FRUGAL model to run, and to Prof. Edward Hanna for sending us his SMB data each year, for the iceberg forecast.

I would like to thank my housemate, Yiwei Zhang, for being with me every step of this process. Last but not least, my mum and my sister have been the absolute best, supporting my northern quest. My a'th kar!

I would also like to note here that the PhD was completed during the Covid 19 pandemic, and as such has some associated limitations to do with data availability, analysis and interpretation. This is especially true where the NEMO ocean model is concerned, as I only had access to the two runs discussed in the thesis.

Abstract

The Greenland Ice Sheet (GrIS) loses mass through two main processes: ice sheet melt (and subsequent runoff) and iceberg calving. This thesis focuses on how these two processes affect the ocean at present, and how they are likely to change in the future, in the context of global climate change. To achieve this aim, three models of increasing complexity have been considered: the WERR control systems model, the FRUGAL ocean-iceberg model, and the NEMO ocean-iceberg model. The WERR model is combined with a new machine learning approach to forecast iceberg flux past the 48th parallel (I48N). This forecast is released to the International Ice Patrol each year. FRUGAL has been run five times, starting with the control run. Runs 2-5 include an additional meltwater component, varying over time. The ocean-iceberg model NEMO, has not been directly run for this thesis, instead outputs from an existing run (ORCA12-N512) have been analysed. This run has been forced with a high emission scenario with an approximate surface warming of 8.5 Wm^{-2} by 2100. Outputs from the FRUGAL and NEMO models are compared. It was found that runoff from the GrIS is likely to increase by 2050, while iceberg calving decreases. Additionally, it was found that I48N is likely to decrease in the future, however this will not necessarily reduce iceberg risk, as Arctic shipping is likely to increase over time. It was also found that increased runoff from the GrIS would have an impact on the strength of ocean circulation, but this will not necessarily result in wide-scale sea level rise by 2050. Instead, the relative increase/decrease in the strength of major ocean currents will cause a variable reaction in sea level. Nevertheless, with the associated exacerbation of extreme climatic events, increased global flooding would still occur.

Contents

4. Assessing Meltwater Impacts and Iceberg Trends to 2050 Using a High Complexity Ocean Model

List of Tables

List of Figures

Declaration

I, the author, confirm that the Thesis is my own work. I am aware of the University's Guidance on the Use of Unfair Means (www.sheffield.ac.uk/ssid/unfair-means). This work has not previously been presented for an award at this, or any other, university.

1. Literature review and Research Aims

1.1 Introduction

The Greenland Ice Sheet (GrIS) loses mass through two dominant processes: surface melt and runoff, and iceberg calving. This loss has been accelerating over the last twenty years, but with an observed slowdown between 2003 and 2017 as a result of cooler atmospheric conditions (The IMBIE Team, 2020). However this overall increasing trend is expected to continue in a warming climate (IPCC, 2013). As the second largest ice sheet on Earth, the GrIS holds the equivalent of 7.36m of sea level rise (Bigg, 2015). While it would be unlikely to see this scale of change over the next hundred years, even a comparatively small input of meltwater into the ocean could have far-reaching effects on coastal flood defences, due to sea level rise, and regional climate warming as a result of changes in ocean circulation. Iceberg calving has also been gradually increasing over the last hundred years.

The International Ice Patrol (IIP) has been monitoring iceberg activity in the region off Newfoundland, Canada since 1914. Before 1945, an iceberg year with more than 844 icebergs crossing 48^{o}N was considered ‘extremely high’. In 2021 this number of icebergs would only register as ‘moderate’. While icebergs pose a direct threat to shipping and stationary oil platforms, they also locally cool and freshen the surface ocean as they melt, which can result in enhanced sea ice extent, duration and/or thickness (Jongma et al., 2009; Bügelmayer et al., 2015). As sea ice cover restricts wind driven mixing of the surface ocean, this can result in increased stratification, hindering deep convection (Jongma et al., 2009). Therefore, both meltwater input and iceberg calving have physical and societal implications on a localised and global scale. This range of direct and indirect effects of a shrinking GrIS will be explored in this chapter.

The structure of this chapter is as follows: a literature review portion (sections 1.2 - 1.5) followed by a discussion of the project research aims and objectives (S1.6), then an outlined thesis structure (S1.7). The literature review focuses on physical and societal risks associated with icebergs and increased meltwater input, and begins with a brief overview of the mass balance of the GrIS.

1.2 The Mass Balance of the Greenland Ice Sheet

Located in the Northern Hemisphere, Greenland is often geographically considered to be part of North America, however it is a politically autonomous territory of Denmark. The ice sheet covers most of the island, with two significant high regions: the North and South Domes. The presence of a smaller South Dome is due to a combination of the effect of high precipitation towards the southern tip of Greenland, owing to the North Atlantic storm belt, and the overall topography of the region (Bigg, 2015). This combination of topography and climate allows the ice to reach the surrounding ocean in a variety of different ways, ranging from ice shelves in the north to narrow fjords (Bigg, 2015).

In general, the GrIS gains mass from solid precipitation and loses mass through ice sheet melt, and subsequent runoff, and iceberg calving. As the GrIS reaches relatively far south for such a large ice mass, it is highly susceptible to global climate change (Wilton et al., 2017). Mass loss and gain had been fairly balanced before the end of the last century, however since then ice sheet melt has been accelerating, partially attributed to a reduced surface albedo which forms a positive feedback with reduced ice cover (Hofer et al., 2017). Warming ocean temperatures may also exacerbate subaerial ice sheet melt (Hanna et al., 2013). A coincidental reduction in summer cloud cover has also contributed (Shepherd et al., 2020). There is significant natural variation, for example in 2012 an annual mass loss of around 500 Gt was observed, yet in 2013 the GrIS was near balance (McMillan et al., 2016). However, while there is natural variation between years, this does not explain the trend of accelerated mass loss. Overall, from satellite measurements a mass loss from the GrIS of 51 ± 65 Gt/yr was recorded for the early part of the 1990's, compared to 263 ± 30 Gt/yr between the years 2005 and 2010 (Shepherd et al., 2020). Similarly, Mankoff et al. (2020) found that solid ice discharge from the GrIS was close to steady between 1986 and 2000, dramatically increased from 2000 to 2005, then steadied out again, with an average ice loss of 487±49 Gt/yr from 2010 to 2019.

There is also high regional variability across Greenland. From Figure 1.1, it can be seen that while the south-western section contributes the most to average ice sheet runoff, it is the north westerly sections that have seen the greatest relative increase over the last 30 years. Overall, the figure shows that while runoff is not occurring uniformly across the GrIS, even the historically low runoff contribution from the northern regions may become significant in the future if current trends persist. Noël et al. (2019) also found that the ablation zone in northern Greenland expanded by 46% compared to the south which saw a 25% increase from 1991 to 2017. In a globally warming climate, the GrIS is highly likely to continue this accelerated mass loss.

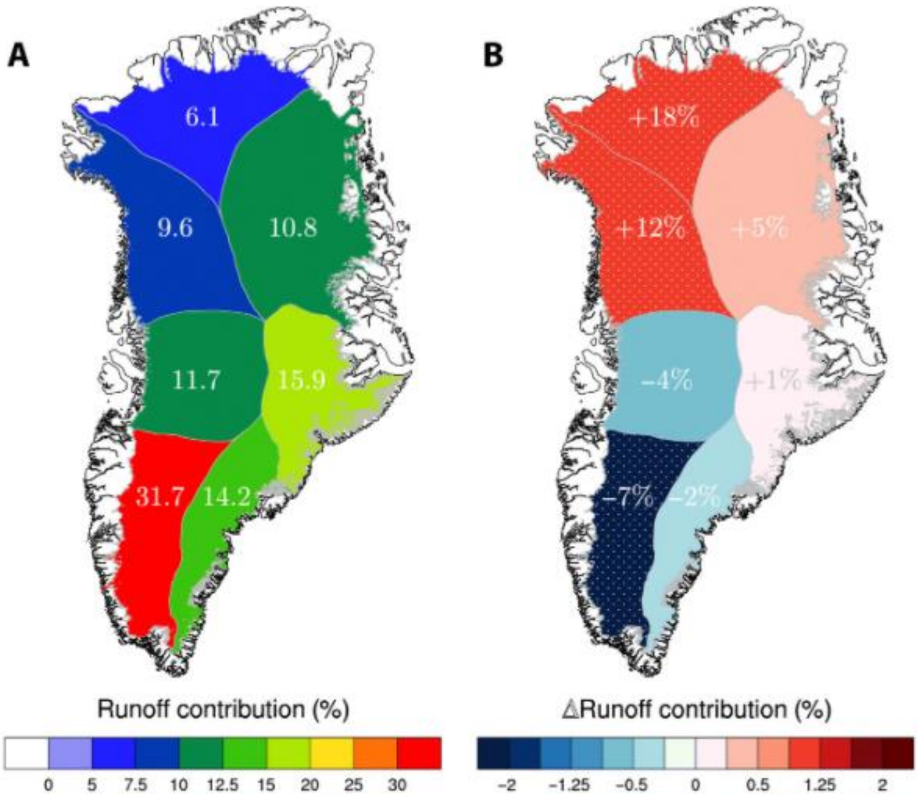

Figure 1.1. From Noël et al. (2019) showing the average runoff contribution between 1959-1990 (A) and the change in runoff contribution after 1990 (B) calculated from the average runoff per sector (1991–2017 minus 1958–1990), with relative change labelled.

1.3 Icebergs

1.3.1 The Physical Impact of Icebergs on the Surrounding Ocean

It is commonly held that Arctic icebergs travel in the direction of the surface ocean currents and at 2% of the wind speed, however other factors such as wave drag and sea ice cover also have an effect (Bigg et al., 1997). Therefore, it is important to understand the movement of the main ocean currents in the region likely to be transporting icebergs (Bigg et al., 1997; Wagner et al., 2017). The main ocean currents in the North Atlantic can be seen in

Figure 1.2. The surface ocean currents relevant for transporting icebergs are described below, but overall show an anticlockwise circulation. Cold, fresh meltwater is also carried along these paths.

The East Greenland Current brings cold, Arctic water south, down the east coast of Greenland. The West Greenland Current then moves the cold water round the southern tip of Greenland and north, up the west coast into Baffin Bay. The Labrador Current transports the cold water south, down the east Canadian coast. This cold boundary current allows icebergs to exist in more concentrated numbers than in the warmer interior of the Labrador Sea, however few icebergs exist further south than the outer Grand Banks, Newfoundland (Marsh et al., 2018). This general pattern of ocean currents is unlikely to carry any single iceberg the complete route (Wilton et al., 2015). Many will be transported for only part of the course and some will even take a short-cut across the Labrador Sea or the Davis Strait.

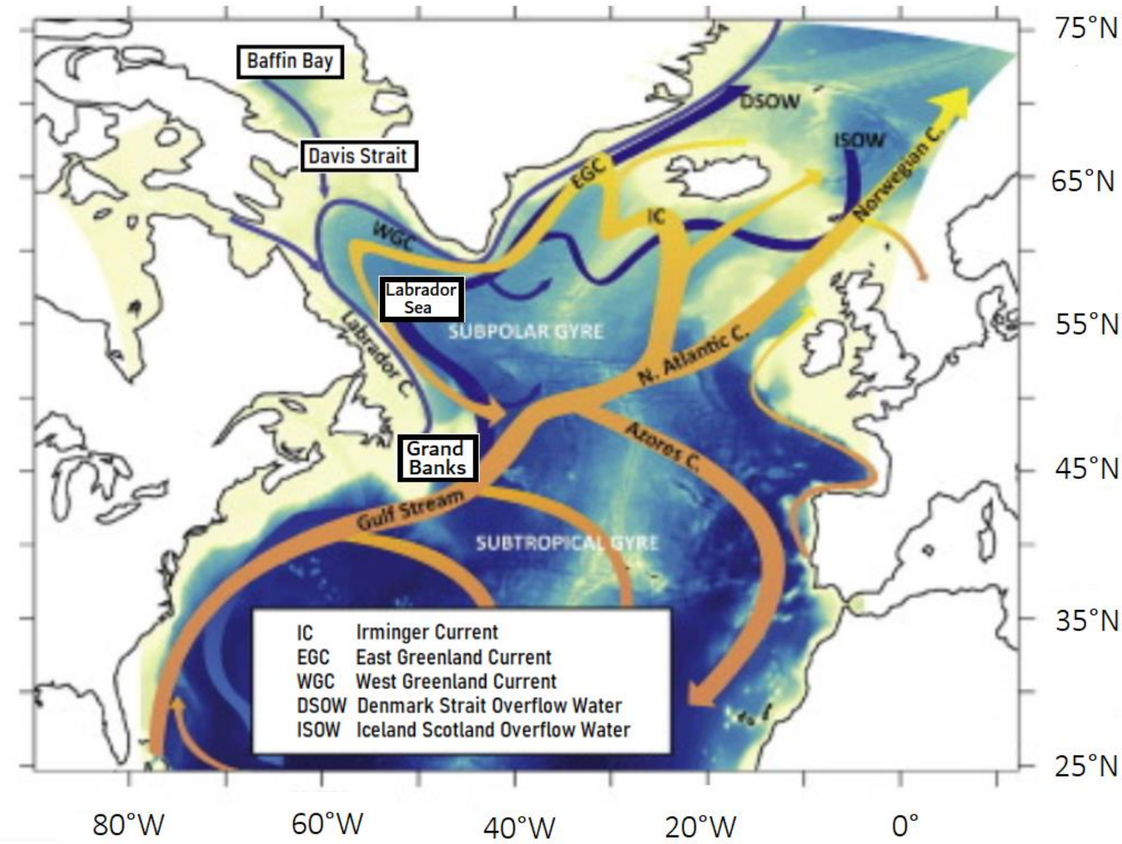

Figure 1.2 Edited from Marzocchi et al., 2015, showing the main ocean currents, and their direction, in the North Atlantic.

On this path, icebergs gradually melt, locally releasing cold and fresh water into the surface ocean, which can result in enhanced sea ice extent, duration and/or thickness (Jongma et al., 2009; Bügelmayer et al., 2015). However, this is a complex relationship as sea ice cover is negatively correlated to surface air temperatures, and helps to protect icebergs from wave erosion, both factors which promote longevity of the icebergs (Connolly et al., 2017). As sea ice cover restricts wind driven mixing of the surface ocean, this can result in increased stratification, hindering deep convection (Jongma et al., 2009). This is potentially exacerbated by the direct input of fresh meltwater from icebergs (Mackie et al., 2020), however this was found to be true in the Antarctic where icebergs tend to be much larger, therefore the effects on stratification directly in the Arctic are debatable but assumed to be much less significant. For further discussion on the impact of freshwater on the surface ocean, see section 1.4.

As icebergs melt, they also release any particulate matter that was present at their formation. Most notably in the case of Greenland is Saharan dust that is deposited on the ice sheet, then calved off as part of an iceberg. A similar quantity of iron also enters the North Atlantic Ocean from sub-glacial erosion, however this is much more localised with less transport to the open ocean (Hawkings et al., 2014). This sediment provides key nutrients to Arctic waters, most notably iron (Hopwood et al., 2019). This iron has the potential to increase marine productivity and carbon storage, and therefore forming a negative climate feedback. However, as iron availability limits production in the Southern Ocean, iceberg enrichment may be more significant there (Raiswell et al., 2008). Nevertheless, as icebergs tend to follow similar paths, even relatively small levels of enrichment may produce observable benefits in ocean productivity (Stephenson et al., 2011).

1.3.2 Iceberg Risk in the North Atlantic Ocean

Icebergs that have calved from the GrIS pose a direct risk to shipping and stationary platforms in the North West Atlantic. The first recorded iceberg incident with North Atlantic shipping occurred in 1686, with the *Happy Return* sinking in the Hudson Bay while on a trade operation for the North West Fur Company (Hill, 2000). Hundreds of lives were lost in collisions in the following three centuries, with notable years include 1856, where over 300 people were killed in the first two months alone, and 1884, where 12 vessels were damaged or sunk (Hill, 2000). While these sorts of tragedies were fairly common, the sinking of the *RMS Titanic* in 1912 with the loss of more than 1500 lives dramatically drew widespread public attention. With 1038 icebergs recorded south of 48°N (the latitude past which icebergs enter international shipping lanes - both of the time and at present) that year, this would have been a high ice year for the time, but not unusually so. There had been strong north to north-westerly winds that year, bringing very low temperatures, which facilitated icebergs surviving further south than the average, although not beyond the ice limit for the 20th century (Bigg & Billings, 2014). Therefore, while the iceberg risk for 1912 was high, it was not unprecedented.

The International Ice Patrol (IIP) was established in the following year to try and prevent any more such incidents occurring. Today, combining data compiled from air surveillance, ship reports, satellite analysis and iceberg trajectory models, the IIP release daily charts of iceberg locations and weekly outlooks that are distributed through the North American Ice Service (available at https://www.navcen.uscg.gov/?pageName=iipCharts&year=2020). In their hundred year history, the IIP have significantly reduced the risk to life, with no human or major commercial losses to vessels following IIP advice in the patrolled region (Murphy et al., 2012). However, as Arctic sea ice extent decreases there has been more interest in tourist vessels venturing north. Commercial shipping routes (see Figure 1.3) are also edging further north and staying open for longer each year (Melia et al., 2016). While shorter shipping times are economically desirable, the risk of collision increases. Changing routes to avoid areas of high iceberg risk is currently done on a short term basis, however longer term forecasts could provide ship's captains with enough warning to set an alternative course, rather than diverting. This aspect will be explored later in the thesis. However at present, the vast majority of ships travelling north of 48°N adhere to the Polar Code, implying that they have been strengthened with double hulls and have engines that are built to survive the freezing temperatures (Bai, 2015).

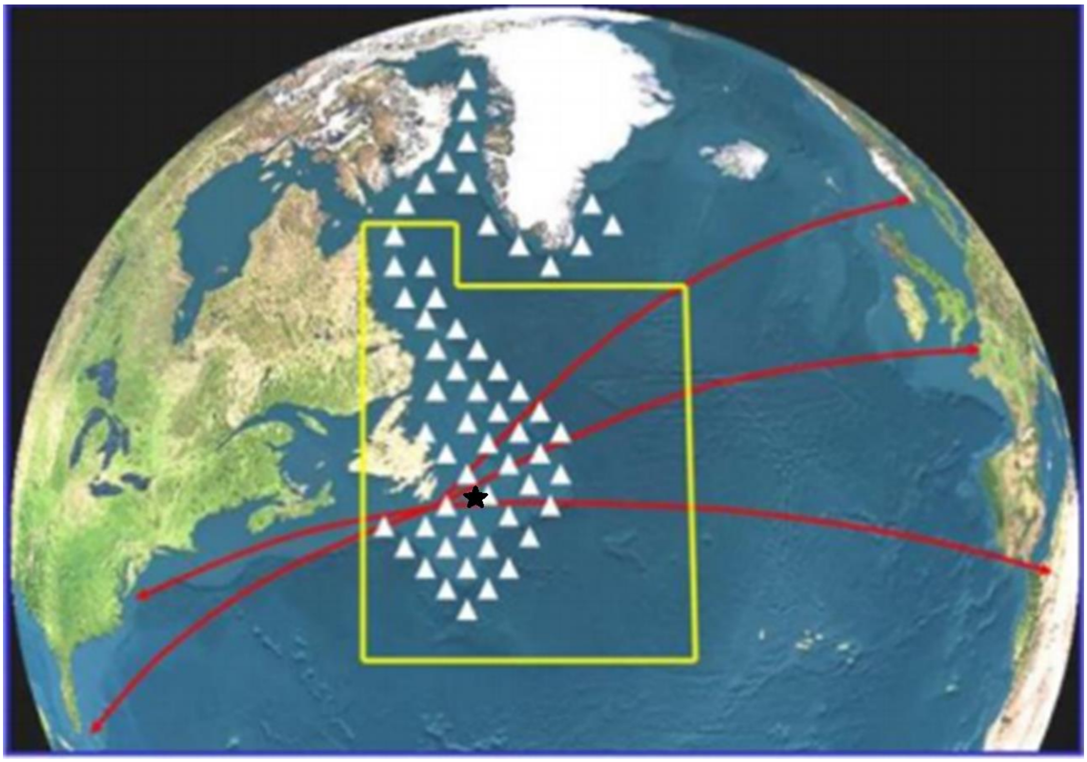

Figure 1.3. The white triangles show where icebergs are commonly found in the ice season, and the yellow box shows the area patrolled by the IIP during this time. The red arrows are popular shipping routes and the black star is the approximate location of the Hibernia platform. (Navcen.uscg.gov, 2019).

Icebergs also pose a threat to oil rigs and other stationary structures in the region. While this threat is costly to counter, the economic return on oil is high and therefore can, in some cases, be decided to be worth the risk. For example, the Hibernia platform was set up on the Grand Banks, Canada, which is an area where icebergs are commonly found. A number of schemes were implemented to reduce the risk of significant damage from collision, such as managing approaching icebergs with water cannons and towing, initiating a shutdown of the rig if the iceberg cannot be re-routed and strengthening of the rig as a last resort (Fuglem et al., 2015). These precautions were taken in an area of shallow water, where the rig is unlikely to be hit by very large icebergs due to grounding beforehand.

Icebergs also have the potential to trigger submarine landslides (as seen in Figure 1.4). This has implications for undersea cables and pipelines, which can be buried and/or damaged by such events, as well as by direct collision. This is a known problem in the Grand Banks region (south-east of Newfoundland) where pipelines are laid in trenches to reduce the likelihood of iceberg (or iceberg triggered) damages (Barrette et al., 2018; Normandeau et al., 2021).

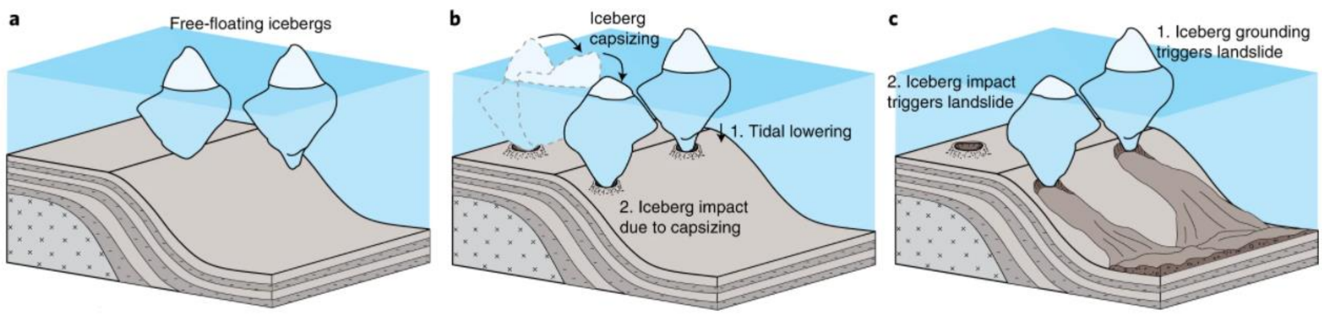

Figure 1.4. An overview of how grounding icebergs can trigger submarine landslides (from Normandeau et al., 2021). Panel a) shows floating icebergs colliding with the seafloor. b) shows two examples: 1. of the tide receding and 2. of the iceberg capsizing. Both scenarios have the potential to trigger panel c) submarine landslides.

1.4 The Impact of Increased Meltwater Input on a Localised and Global scale

Sea level rise is a direct risk associated with meltwater input. The IPCC suggests that it is ‘very likely’ that the contribution of the GrIS to global sea level has increased from 0.09 mm yr^{-1} between 1992–2001 to 0.59 mm yr^{-1} for the period 2002–2011 (Church et al., 2013). Meanwhile, the IMBIE Team (2020) estimated that between 1992 and 2018 the melting GrIS was responsible for 10.8 ± 0.9 mm of sea level rise, while the IPCC noted a 3.6 mm/yr increase over the period 2006–2015 (Oppenheimer et al., 2019). It has also been estimated that the reducing GrIS is responsible for 25% of current sea level rise (Straneo et al., 2019). Therefore, this is a highly significant region when considering future change, as any major sea level rise would have global implications.

As the global population is expected to continue to increase, and therefore also the number of people living in zones of potential coastal flooding, more money will have to be spent on coastal defences. However as population growth in coastal regions is predicted to increase most rapidly in emerging economies such as India, Bangladesh and Indonesia where much of the population is typically low-income, this could have serious social and economic impacts (Neumann et al., 2015). However, even in countries with a generally high disposable income, sea level rise could have widespread impacts, notably on house insurance, maintaining or upgrading current flood defences or dealing with large scale flood events (for example of the New York subway). Any coastal country would be financially strained by investing significant resources in protecting an entire coastline.

A less direct impact of meltwater input is changes in ocean circulation. This meltwater is cold and fresh and therefore decreases the density of the surface ocean locally, as salinity dominates temperature here, reducing the rate at which this cold water sinks (Hansen et al., 2016). This is important because the Labrador Sea is one of the main areas of North Atlantic Deep Water (NADW) formation (Balaguru et al., 2018; Yu et al., 2016), which is a significant component of the Atlantic Meridional Overturning Circulation (AMOC), responsible for distributing heat around the Atlantic Ocean, and through this the wider ocean system. It is worth noting recent suggestions that convection of water in the Irminger and Iceland basins may contribute more to the total overturning circulation than the Labrador Sea (Lozier et al., 2019). However, as the AMOC has a widespread effect on the climate, any changes to its strength could result in altered precipitation patterns, regional temperature and the location and strength of the North Atlantic storm track (Jackson et al., 2015). Increased stratification will also likely affect the distribution of fish species in the water column. Decreasing vertical mixing would result in less oxygen penetrating deep into the mid-layers and, as organisms in these regions continue to respire, this could result in oxygen minimum zones where only the smaller organisms, with a lower oxygen demand, can survive (IPCC, 2014). Larger fish will be forced higher in the water column, with implications on fishing and the wider ecosystem. Inputted meltwater would also have an impact on horizontal density gradients, leading to changes in the strength of ocean currents, and in shifting their position. Notably, the route that the Gulf Stream takes is dependent on the strength of the AMOC, with a strong AMOC associated with a northerly Gulf Stream path, and vice versa (Joyce & Zhang, 2010).

A fairly recent example of changes in ocean circulation is the Great Salinity Anomaly, a low salinity event that occurred in the 1960s and 1970s. This event was linked to increased sea ice export from the Arctic, through the Fram Strait, that stabilised the upper ocean and therefore reduced Labrador Sea deep water production (Dima & Lohmann, 2011). The extreme sea ice years in the late 1960s were aided by a negative phase of the NAO, and the associated milder winter temperatures (Kim et al., 2021). This increase in ocean stratification led to a total shutdown of deep convection between 1968 and 1971, although in 1972 this was reinstated after a bitterly cold winter (Gelderloos et al., 2012). The wider effects of this salinity event were felt around the globe, with increased sea surface temperatures in the

Southern Hemisphere, and a rapid decrease in Northern Hemisphere temperatures (Hodson et al., 2014).

Further back in history, to glacial times, there have been instances of large quantities of freshwater entering the ocean, and having wide-scale effects. A notable example of rapid climate change is the Younger Dryas, a cooling event that occurred around 12 thousand years ago and is often considered to have been initiated by a large input of meltwater from the glacial Lake Agassiz, Canada (Renssen et al., 2015). While it is an example of abrupt change, the large scale effect of meltwater input on climate can be clearly seen. This type of catastrophic change is very unlikely to be seen in the current climate, due in part to there currently being no ice marginal (or known subglacial) lakes of sufficient volume to rapidly add enough freshwater to the North Atlantic (Norris et al., 2021). This freshwater would then have likely been channelled into the North West Atlantic. This was a time of general warming after the Last Glacial Maximum, which occurred around 20 thousand years ago, but substantial parts of North America were still covered by the Laurentide Ice Sheet (Margold et al., 2015). It is theorised that this dramatic input of meltwater was sufficient to weaken the AMOC, as a result of restricted NADW formation. This is supported by δ13C records, which can be used as a proxy for carbon storage in the deep ocean, and therefore strength of circulation (Oppo et al., 2015; Peterson & Lisiecki, 2018). During this time, cooling of more than 5°C occurred over the North Atlantic, with significantly less cooling seen in the Southern Hemisphere. A 20% reduction in soil moisture in Northern Africa and a 15% increase in moisture in southeast North America can also be seen (Renssen et al., 2015). While this large-scale meltwater input is not comparable to modern times, it gives a plausible basis for the indirect possible effects of meltwater input in the Labrador Sea.

1.5 Conclusions

There are a variety of direct and indirect effects associated with a GrIS losing mass as icebergs and runoff. Icebergs pose an infamous risk to shipping, and as Arctic sea ice retreats and shipping routes drift north, this risk can only increase. Arctic tourism is also on the rise as accessibility increases. Even a relatively small collision, especially at speed, can result in a ship sinking. Meltwater input, from icebergs and direct runoff, may act to enhance sea ice extent. While greater sea ice cover would increase the albedo, and reflect more incoming solar radiation, ice sheet melt generally decreases ice sheet surface albedo with a positive feedback on climate. Large-scale changes in ocean circulation, due to meltwater input, could also have far reaching consequences, from changes to regional temperature and rainfall. This has a direct impact on human life on this planet. However, from an ecological standpoint, icebergs may also increase marine productivity, with the potential for a negative feedback loop, helping to cool the planet.

1.6 Research Aims and Objectives

The overall aim of this thesis is to assess how the accelerating mass loss from the GrIS will affect the ocean and to study the direct and indirect risks associated with this. This will be achieved through a combination of improving seasonal forecasting of the spatial density of iceberg occurrence (henceforth referred to as iceberg density) in the region off Newfoundland, Canada, and assessing the effects of inputting meltwater from the GrIS into the ocean.

This project uses three models (of increasing complexity) to look at the effect that a reducing GrIS is likely to have on the ocean, in terms of iceberg concentration and meltwater input. In order of ascending complexity, the models are the WERR (Windowed Error

Reduction Ratio) statistical iceberg prediction model, the Sheffield based FRUGAL (Fine Resolution Greenland and Labrador) ocean model and the Southampton based NEMO (the Nucleus for European Modelling of the Ocean) ocean model. These models were chosen as they are amongst the few climate/ocean models to contain an iceberg component. A machine learning element is also introduced, to add confidence to the WERR prediction. The project focuses on using these models to assess the direct and indirect risks of ice mass loss from the GrIS, where ocean risk is defined as a function of exposure and vulnerability to a hazard that is a result of a changing ocean (Niehorster & Murnane, 2018), and is a product of probability and impact. No risk scores have been calculated in this thesis, rather the focus is on discussing the risks (here defined as the potential for loss - either monetarily or in any other way negatively affecting human life) from the various hazards (defined as the object or event responsible for causing said loss) associated with climate change. There is a specific focus on how changing iceberg activity in the Labrador Sea may lead to a greater potential for ship collisions in the future, how meltwater input may alter large scale ocean circulation patterns (and the associated changing weather patterns) and sea level rise (and its effect on coastal living).

1.7 Thesis Structure

The rest of the thesis will be structured as follows:

Chapter 2 will focus on the WERR control systems model iceberg forecast, and has been combined with machine learning techniques for the 2020, 2021 and 2022 prediction. The yearly forecasts, beginning 2019, will be presented, and their success evaluated.

Chapter 3 looks at using the FRUGAL ocean model to address the impact of increased meltwater on the North Atlantic, and the wider ocean, by assessing the effect of five runs of variable freshwater input on global ocean currents.

Chapter 4 analyses the NEMO ocean model results in two runs: a past run (1983-2014) and a future (2015-2050) run, in a high-emission scenario. It will be determined if this data is useful for detecting iceberg flux past the 48th parallel, and whether satellite data could also be used for this purpose. There is also a focus on the impact of meltwater on global sea surface salinity and temperature patterns.

Chapter 5 compares NEMO and FRUGAL model results, with a focus on assessing the impact of meltwater impact on sea level.

Chapter 6 places the research in the context of ocean risk.

Chapter 7 concludes the project and discusses the limitations of the thesis and potential future work.

2. Predicting Iceberg Behaviour off the North-East Canadian Coast

2.1 Introduction

This chapter is based on the published paper:

Ross, J.B., Bigg, G.R., Zhao, Y. and Hanna, E., 2021. A Combined Control Systems and Machine Learning Approach to Forecasting Iceberg Flux off Newfoundland. Sustainability, 13(14), p.7705.

2.1.1 Introduction to Iceberg Forecasting

Icebergs have been a threat to shipping in the North Atlantic Ocean for hundreds of years (Hill, 2000). However, the sinking of the Titanic in 1912 drew widespread public attention and in response the International Ice Patrol (IIP) was set up to mitigate iceberg risk in the region off Newfoundland, Canada (see Chapter 1, Section 1.3.2 for more details). The IIP release daily charts of iceberg locations, and directly offer advice to ships' captains on avoiding ice-heavy areas (Navcen.uscg.gov. 2021).

While short term forecasts reduce the risk of serious collisions, longer term predictions could have a significant impact on marine planning, potentially altering iceberg monitoring and even shipping routes months in advance. This would be of great economic benefit, particularly as in recent decades the total number of icebergs each year entering the shipping lanes of the NW Atlantic have significantly increased compared to earlier in the twentieth century (Bigg et al., 2014). Between 1988 and 2006, Hill (2006) calculated the probability of a ship colliding with an iceberg to be 0.05% based on data from American and Canadian ports. Even at this relatively low rate, if the exposure to icebergs were to increase (see various projections of Arctic shipping increase: Stephenson et al., 2018; Dawson, 2019; Bergström et al., 2020 and more), the risk necessarily increases.

This chapter presents an existing control systems model and a new machine learning approach to forecasting the coming year's iceberg season. The outcomes from both modelling approaches are compared and used to create one prediction for the iceberg season that can be distributed to the relevant/interested parties. Beginning with an overview of the relevant data, the chapter discusses the Windowed Error Reduction Ratio (WERR) model developed in Bigg et al. (2014), and how well this model recreates iceberg variability. Next is an introduction to the machine learning models, other applications of these models, and how well they represent I48N. The following section presents a retrospective look at previous years' icebergs forecasts, and a discussion of common combinations of the machine learning models outputs. The 2022 forecasting method is discussed, with the overall prediction presented. Next, there is a discussion on including bergy bits (very small icebergs) in the forecast. The final section concludes the chapter.

2.1.2 Data

It will be seen in section 2.2.1 that the three monthly input variables for prediction of I48N for both the machine learning models and the WERR model are the surface mass balance of the Greenland Ice Sheet (SMB), which affects how many icebergs calve from Greenland, the NAO, which affects atmospheric temperatures and precipitation in the region, and the mean Labrador Sea surface temperature (LSST), which affects both the calving rate of icebergs and the survivability of icebergs once in the ocean. This data is taken from the previous year(s) for the machine learning models, and from the 9 months leading up to the prediction for the WERR model. The calculation method for SMB is given in (Hanna et al., 2011; Wilton et al., 2017), and is the difference between ice sheet mass gain from snow accumulation and mass loss from ice sheet meltwater runoff, based on positive degree day runoff retention modelling (Janssens & Huybrechts, 2000). Here SMB data extended to 2021, and based on newly-available European Centre for Medium-Range Weather Forecasts ERA-5 meteorological reanalysis data, are used. The LSST data can be found in the Physical Sciences Division of NOAA, under Kaplan v2 SST, and consists of monthly sea surface temperature anomalies in the Labrador Sea, over the area 55-67°N, 45-65°W (https://psl.noaa.gov/data/gridded/data.kaplan_sst.html). NAO data are available at https://www.cpc.ncep.noaa.gov/data/teledoc/nao.shtml. The monthly time series data for these three environmental variables can be seen in Figure 2.1.

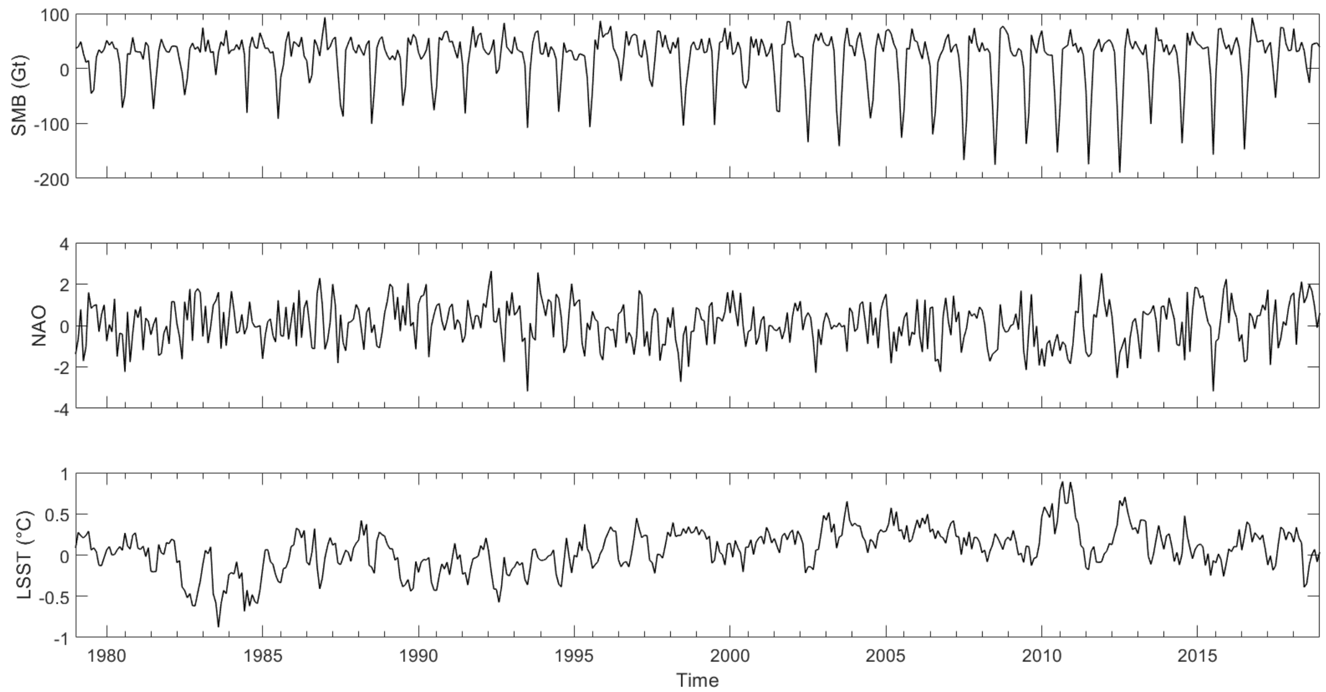

Figure 2.1 Plot of the monthly time series data of SMB, NAO and LSST.

I48N, the number of icebergs south of the 48th parallel in a given month as recorded by the IIP and available through their Annual Reports (see, for example International Ice Patrol, 2019), is generally accepted to reflect annual variability in iceberg activity in the Labrador Sea (Bigg et al., 2014). The latitude of 48°N is also the point beyond which icebergs begin to enter the trans-Atlantic shipping lanes (Figure 2.2). It is worth noting that iceberg identifying and tracking techniques have dramatically increased over the last century, for example the heightened numbers recorded in 1983 after the IIP included airborne radar technology (Report of the International Ice Patrol in the North Atlantic, 2019). Previously all observations had used the human eye only, therefore the addition of radar allowed for much greater coverage in adverse weather conditions (Anderson, 1993). Despite the restrictions early on in the dataset, the IIP record is the longest running and most complete record of iceberg sightings available.

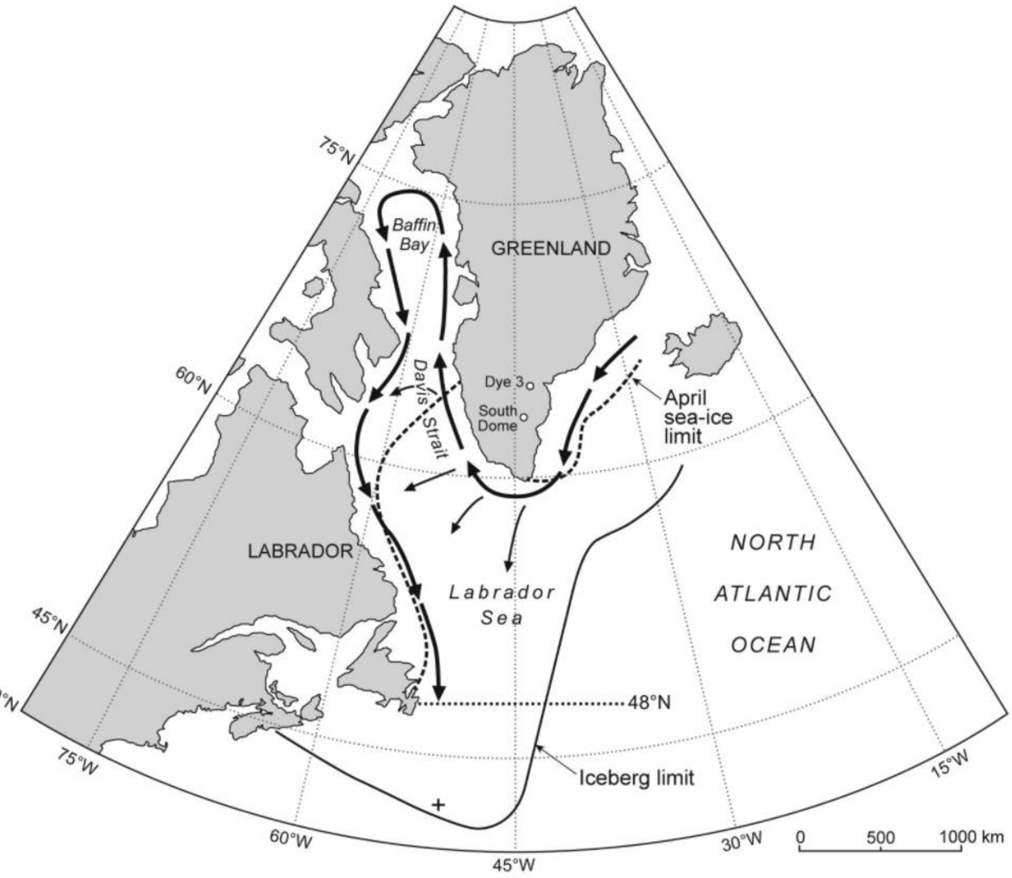

Figure 2.2. Map showing the major iceberg paths in the region, with mean April sea

ice extent represented by the dashed line. The dotted line estimates 48°N, while the '+' shows the location of the sinking of the Titanic. (Taken from Bigg et al., 2021).

Due to the complex interactions between the environmental variables and I48N, no clear linear relationship can be established. This is shown in the low maximum correlation (note a lag range of 0-10 months was considered) between the variables and I48N, when considering monthly data from 1950 to 2021: the NAO and SMB have no statistically significant correlation at the 5% level (-0.0076 and 0.0302 respectively), while LSST does have a statistically significant correlation of -0.1952 (at the 1% level). This is likely to represent the established link between sea ice extent and I48N (Marson et al., 2018), with low sea ice years generally aligning with high LSST and low I48N. This link is continually observed in the IIP annual reports (available at https://www.navcen.uscg.gov/?pageName=IIPAnnualReports), along with observations of the NAO impacting sea ice development (see the 2021 report for an example of a low year, and 2019 for a high year). As the majority of icebergs that drift south of 48°N calve from the GrIS, variations in SMB have a significant impact on I48N, after a minimum lag of 8 months - which is the shortest time it takes for an iceberg to reach 48°N from Greenland (Bigg et al., 2021). Bigg et al. (2014) found that variability in iceberg calving was predominantly responsible for yearly changes in I48N, especially on decadal timescales. Overall, the three environmental variables have strong, established, but non-linear, links to I48N, and are therefore the selected input variables for both modelling approaches.

2.2 The Models

2.2.1 A Windowed Error Reduction Ratio Approach

A model for I48N was developed in Bigg et al. (2014) using a Windowed Error Reduction Ratio (WERR) control systems method, where a sliding time-window, non-linear and time-lagged polynomial regression model, forced with the three environmental factors of SMB, NAO and LSST, is optimised for the observed number of icebergs passing 48°N. This method computes the linear and non-linear correlations between the input and output signals directly to select the model terms one by one. The full mathematical basis behind the WERR model can be seen in Zhao et al. (2017). The WERR method was shown in Zhao et al. (2016) to produce an output that had a correlation of 0.84 with the annual variation in the number of icebergs passing 48°N between 1900 and 2008.

The original WERR model was a non-autocorrelative interpretative tool for I48N, rather than a predictive one, and so polynomial terms with time lags between 0 and 48 months were allowed within the library of candidate terms available for the model optimisation (Zhao et al., 2017). However, the dominant terms in the original WERR model had a lag of 8 months or longer, reflecting a minimum timescale between calving and icebergs reaching 48^{o}N, so the model was adapted for predictive purposes by only allowing polynomial terms with a lag of this size to be available during the model optimisation (Bigg et al., 2021). This predictive model has a reduced, but still statistically significant (at the 1% level), correlation of 0.60 between the January-September I48N values and the WERR model predictions over a 20 year test period, with a confidence of 80% in assessing whether a year was a high or low iceberg year relative to the 1997-2016 annual mean of 592.

Seasonal forecasts produced from an ensemble of sliding-temporal windows of this revised WERR model (see Bigg et al., 2021 for details) have been released to the IIP for several years. The ensemble nature of the forecasts gives a measure of the error through its standard deviation. In addition, to take account of the largely bimodal nature of the I48N iceberg number, Bigg et al. (2021) also categorised the forecasts as “high” or “low”, relative to the mean 1997-2016 I48N mean value of 497. Thus, the 2017 iceberg season forecast was 766±297, with an observed total of 1008, so this was therefore a formal success, and both forecast and observed numbers fall in the “high” category. In 2018 the forecast was 685±207, with an observed number of 208. While the forecast was lower than the 2017 observed total it was still “high”, while the observed I48N was clearly a “low” year, thus the 2018 forecast was a failure. The 2019 forecast was for 516±150 icebergs. By the end of the season the total number had reached 1515. The 2019 forecast was therefore a formal failure, although it was predicting a “high” year, as was observed. The 2020 forecast (including the machine learning approach) was for a low/medium ice year with 584±303 icebergs by the end of July. The observed number by this point was 169 (personal communication, Michael Hicks, IIP), representing a “low” iceberg year. The observed 2020 iceberg number fell outside the error bars, but there was an exceptionally large uncertainty in the 2020 forecast, with 4 of the 11 members of the ensemble falling into the “low” category. This spread in the forecast probability amplified the need for alternative approaches; these are provided by the new machine learning models discussed below and it will be seen that their forecast for 2020 was definitely for a “low” iceberg year. The 2021 forecast was for 675±123 icebergs, with the machine learning models predicting a medium year. As only one iceberg was observed, early in the year in February, 2021 was an extremely low year and the forecast was a failure.

As it was previously found that using WERR model ensemble members generated from more recent years seemed to produce closer ensemble results to reality than those earlier in the trial period (as they better represent the dominant environmental factors at play at that time), here the twenty year WERR model training period has been moved forward two years to 2018 (see Appendices Table S1). Only the terms with a time lag time of at least eight months were selected, which allows production of a predictive model eight months ahead. The selected terms are also required to have an ERR (Error Reduction Ratio) of 0.02 or higher, where the ERR is a measure of how well the selected term explains fluctuations in system variance (Zhao et al., 2017). This contribution is shown in the following equation (1):

$$\mathrm{ERR}_{j,i}\,(t) = \frac{\hat{g}_i^{\,2}\ \sum_{k=1}^{H} x_i^{\,2}\,(k)}{\sum_{k=1}^{H} y_{j,w}^{\,2}\,(k)} \tag{1}$$

Note that y_j is the system output and x_i comes from $P = X \times V$, where P is the matrix of potential terms and V is an upper triangular unit matrix. Where g is estimated by equation (2):

$$\hat{g}_b = \frac{\sum_{k=1}^{H} x_b\,(k)\ y_{j,w}\,(k)}{\sum_{k=1}^{H} x_b^{\,2}\,(k)} \tag{2}$$

The ERR outcome is a percentage, and therefore has a maximum value of 100%. Greater values of ERR represent a higher contribution by the selected variable (Zhao et al., 2017).

The time series of the performance of the WERR model over the period 1989–2018 is shown in Figure 2.3. While the model often under-estimates the peak spring value of I48N, and over-estimates iceberg numbers in very low iceberg years, its representation of the annual cycle (upper panel) and the annual total (lower panel) is good, with the latter having a statistically significant (at the 1% level) correlation of 0.87.

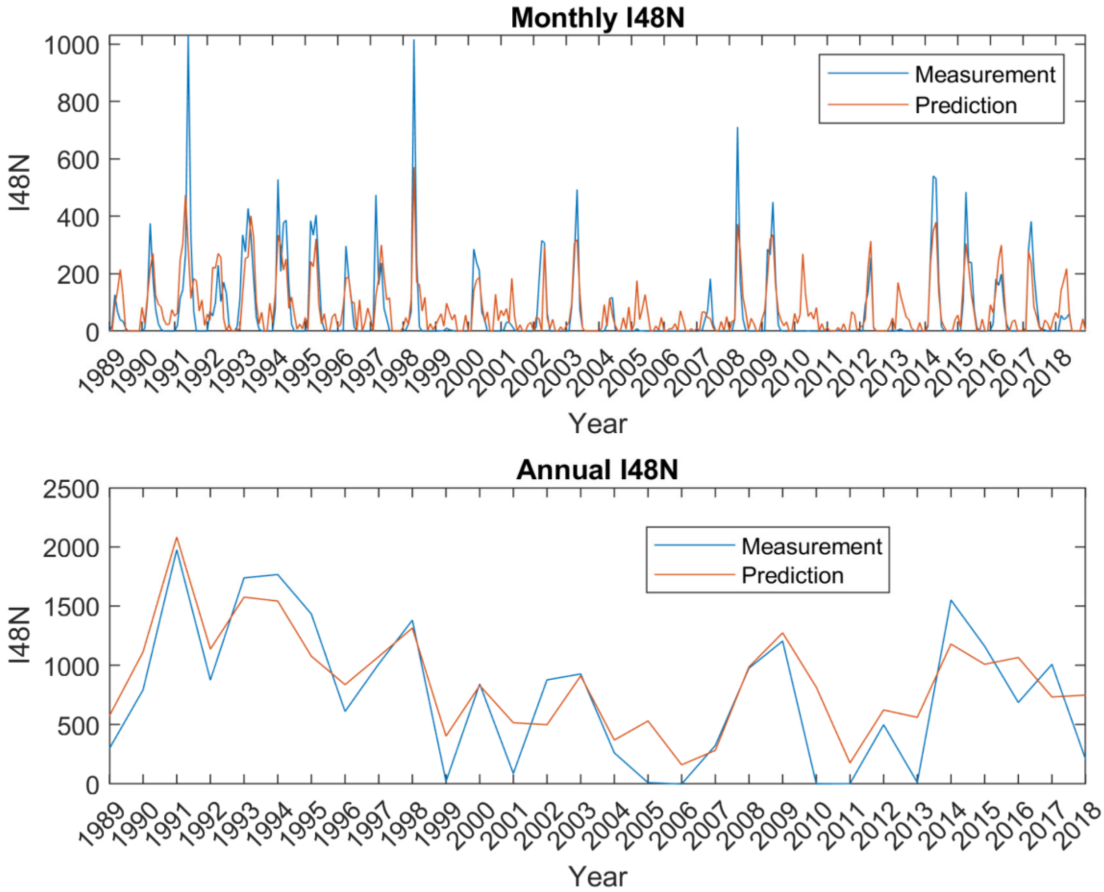

Figure 2.3 Plot of WERR model fit vs. observed data for the latest 30-year window model. Upper panel shows the monthly fit, while the lower panel shows the annual total produced by the model, compared to observations.

Overall, the WERR model can be used to model complex systems where the variables have a non-linear correlation, which is useful in this application as the lead up to iceberg calving is a non-linear process (Zhao et al., 2017). The ensemble of WERR models can be seen in the Appendices (Table S1), where the terms in bold were found to have a significant enough correlation to be included in the forecast. This is read into a Matlab file, where the environmental data is inputted, and run to produce a cumulative forecast of monthly iceberg numbers south of 48°N, up to 9 months ahead.

2.2.2 A Machine Learning Approach

2.2.2.1 The Additional Yearly Iceberg Properties

While a prediction of the total number of icebergs past 48°N in a year is a useful tool in understanding iceberg risk, other factors, including how early and late in each season icebergs will enter the shipping lanes, are also of use to shipping (personal communication with Michael Hicks, IIP). Therefore, three new measures have been included in the iceberg forecast, using a machine learning approach. These are a prediction of the peak month, the number of peaks and the rate of change. The machine learning tools have also been used to create a forecast of the maximum annual I48N number, to supplement the WERR model prediction.

In an average year, North Atlantic icebergs are most prevalent in the months between March and June (Figure 2.4). However, which month contains the greatest flux, and so has the greatest risk to shipping, is variable. Therefore a prediction for the month in which the ‘peak’ occurs has been made for the 2021 ice season, estimated based on monthly values. An outcome of ‘0’ reflects a prediction that the peak will occur between January and March. A result of ‘1’ reflects April, and ‘2’ denotes May. A value of ‘3’ suggests the peak month will be in June or later in the year.

Figure 2.3 also suggests that it is usual to have one dominant peak in monthly iceberg number, however, this is not necessarily the case. In some years, including 2019 (International Ice Patrol, 2019), more than one peak was observed. Therefore, machine learning tools have been used to predict the number of peaks in the 2021 iceberg forecast. A result of ‘1’ suggests a single peak, whereas ‘2’ denotes a year with multiple peaks. As daily data are only available for the last decade, monthly values have been used to estimate whether a year had one or more peaks.

The rate of change prediction is a measure of how rapidly icebergs are passing 48°N and entering the shipping lanes (calculated by the number of icebergs in each month passing 48°N compared to the yearly total - due to the historically small amount of available daily iceberg data). Iceberg numbers can vary significantly in a short period of time, and having some warning of this would be of use to ship’s captains. Therefore, the maximum rate of increase in each ice year from 1900 to 2020 was calculated, and, when ordered, the lower third were categorised as low, ‘0’, the centre third as medium, or ‘1’, and the highest third as ‘2’ or high.

In addition to the measures predicting iceberg behaviour, a machine learning approach has also been used to predict the annual I48N total. Here the categories are defined by the IIP, therefore a low year, ‘0’, has less than 231 icebergs past 48°N, a medium year, ‘1’, has between 231 and 1036, and a high year, ‘2’, has more than 1036. In order to improve model accuracy only three categories have been used for prediction, however the IIP also includes a definition for an extremely high ice year of more than 1399 icebergs.

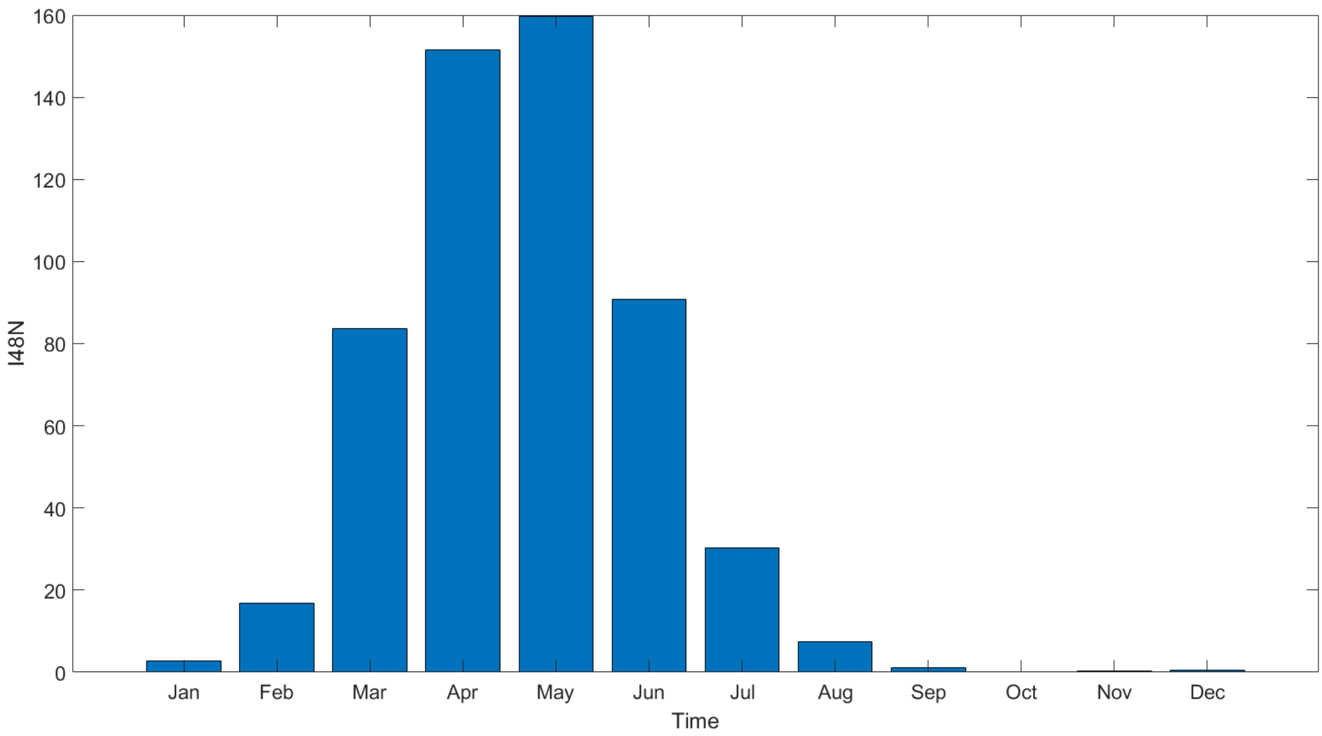

Figure 2.4 Plot of the average number of icebergs past 48°N in each month, from 1950 to 2020.

Figure 2.5 shows the main features of an iceberg year for the new prediction measures. The new measures have been outlined on the plot and can be seen to represent the main differences between one iceberg year and another. Two recent years, 2017 and 2019, have been highlighted, as they show strong characteristics of particular measures. The magenta line, representing 2019, clearly shows a multiple peak year, with a high rate of change and a high I48N. As the most significant peak that year occurs in May, this is the peak month. The blue line, showing 2017, has a much gentler increase across the year, and therefore a low rate of change. As the greatest increase was in April, this is the peak month for that year. 2017 also only has one iceberg peak, and a medium I48N. The black lines show the last 50 years of cumulative iceberg numbers across the season. It can be seen that the greatest change in iceberg numbers usually occurs between March and June. Figure 2.5 also shows that there is high variation in the total I48N, ranging from 0 to more than 2000 icebergs in a year, with the low, medium, and high divisions being clear.

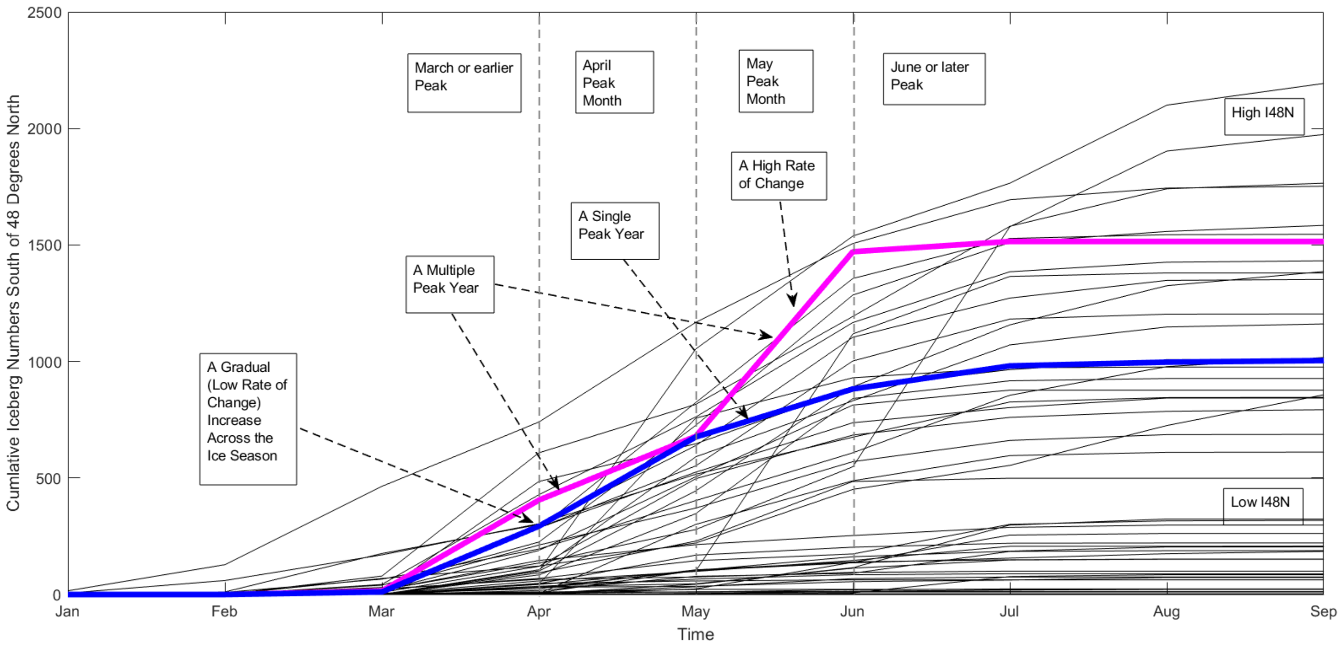

Figure 2.5 Plot of the cumulative iceberg numbers south of 48° N in the last 50 years. 2019 and 2017 have been highlighted (in magenta and blue, respectively) as they show clearly the characteristics of each new measure for prediction within the context of an iceberg season.

These new measures allow for a better understanding of iceberg behaviour in a future season, and when combined with the WERR prediction, the yearly forecast aims to aid the IIP in reducing iceberg risk in the North-West Atlantic.

2.2.2.2 The Machine Learning Models

For the new measures, three machine learning models were tested and compared: Linear Discriminant analysis, a Linear Support Vector Machine algorithm (SVM), and a Quadratic SVM algorithm. The models use knowledge of the annual means of the three environmental parameters forcing the control systems model (SMB, LSST and NAO), and allow a measure of auto-regression through having knowledge of the previous years' value of the appropriate measure of the environmental parameters and I48N. While there are other machine learning models, such as Random Forest or Gradient Boosting, that could be considered, these particular models have been selected due to their strength in classification tasks (Khondoker et al., 2016). It was found in Khondoker et al. (2016) that the Linear Discriminant approach was best for model precision, especially in circumstances with relatively few input variables. It was also suggested that the SVM method has the potential to outperform all other surveyed models when the number of input variables increases. Therefore, these approaches seem to complement each other, and were also all shown to have predictive skill beyond random chance (see Section 2.3). It should be noted that this chapter aims to demonstrate the proof-of-the-concept of machine learning for this specific application, rather than optimising their prediction performance. Further research could look at involving other relevant machine learning models for a comprehensive comparison of prediction performance.

Linear discriminant analysis, also known as the Fisher discriminant, has been used since 1936 (Fisher, 1936). While much has changed since then, the base application remains the same. Multiple variants of the theory exist, in fields ranging from earthquake-induced liquefaction (Pham & Prakash, 2019.) to text classification (AbuZeina & Al-Anzi, 2018). In general, linear discriminant analysis is a variable reduction technique, with a strong pattern recognition ability (Khondoker et al., 2016), and is therefore a useful tool for classification purposes.

Both linear and quadratic SVM algorithms are popular tools that attempt to locate an optimal boundary between classes for classification purposes (Bhuvaneswari & Kumar, 2013). A visualisation of finding the optimal linear hyperplane can be seen in Figure 2.6. While a quadratic boundary between classes is less easy to envision, the general principle remains the same: divide the data into classes by finding the best possible boundary between them. Many examples of this practice can be seen in the medical field, in analysing enzymes for liver disease (Fathi et al., 2020) or diagnosing whether a tumour is malignant or benign (Obaid et al., 2018), but examples are beginning to be encountered in environmental sciences, such as flood classification (Khan et al., 2019) or crop disease assessment (Chokey & Jain, 2019).

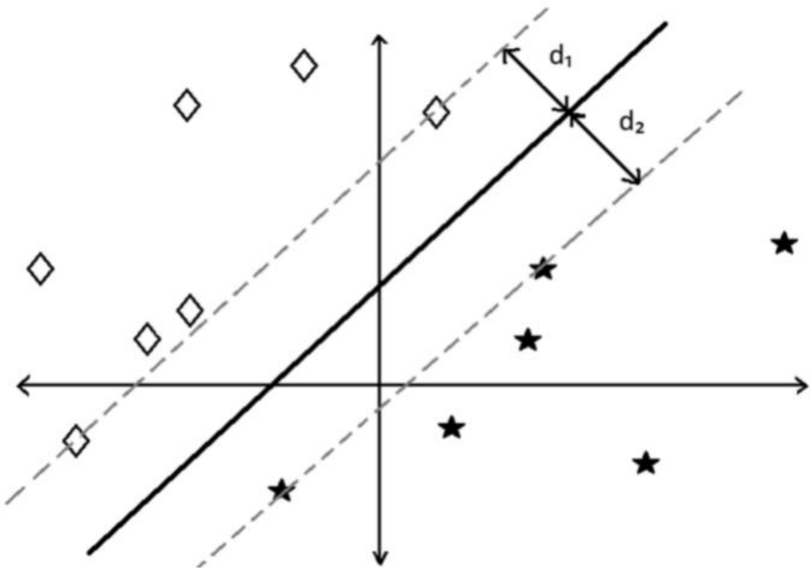

Figure 2.6 Visualisation of the optimal linear hyperplane (solid line) that classifies the data into two classes (diamonds and stars) in a support vector machine approach; inspired by Bhuvaneswari & Kumar, 2013. The support vectors are shown by the dashed lines.

The machine learning models have been run through the MATLAB Classification Learner App. All three approaches were trained on a thirty year sliding-window method in order to utilise the relatively short dataset of yearly values since 1901, and for consistency with the WERR approach (Zhao et al., 2016). They are then tested on the following year, starting at 1931, rolling forward. An average accuracy and error value can then be calculated from the 86 runs per model, as opposed to having a single accuracy value.

2.3 Sensitivity of the Machine Learning Tools

2.3.1 Model Accuracy

The average accuracy, F1 score, and root mean squared error (RMSE) of the various machine learning models can be seen in Table 1. Accuracy has been calculated simply by recording the percentage of times the model result was true, meanwhile the F1 score is a measure of precision and recall, and is commonly used to reflect machine learning model accuracy, however both are useful for assessing binary classification results (Chicco & Jurman, 2020). When forecasting the I48N annual total, the output can either be low, medium, or high. As there are three possible outcomes, an accuracy of more than 33% is desirable to show that the method has some skill beyond random chance. Similarly, for the maximum rate of increase in an ice year forecast, there are also three outcomes: either low, medium or high. However, when forecasting the number of peaks in an ice year, there are only two possible outcomes: either one or multiple. Therefore, for the prediction to show skill beyond random chance, an accuracy of more than 50% is required. Lastly, for the prediction of when the peak month will occur in an ice year, there are four possible outcomes: January to March, April, May, or June onwards. This prediction therefore has the lowest requirement, of more than 25%, of performance better than random chance.

Table 2.1 Showing the accuracy, F1 score, and root mean squared error (RMSE) of the various machine learning models over the trial period of 1931–2017. The last row shows the mean skill level for each variable predicted, defined as the mean model accuracy/(expected random accuracy).

	I48N Annual Total			**Rate of Change**			**Number of Peaks**			**Peak Month**		
	Accuracy (%)	**F1**	**RMSE**	**Accuracy (%)**	**F1**	**RMSE**	**Accuracy (%)**	**F1**	**RMSE**	**Accuracy (%)**	**F1**	**RMSE**
Linear Discriminant	54.6512	0.66	0.7924	41.8605	0.52	1	55.814	0.77	0.6647	26.7442	0.54	1.3118
Linear SVM	50	0.7	0.8627	37.2093	0.62	1.023	56.9767	0.78	0.6559	26.7442	0.59	1.2152
Quadratic SVM	50	0.71	0.9022	41.8605	0.59	1.0173	60.4651	0.77	0.6288	30.2326	0.52	1.3725
Mean Skill level	1.55			1.21			1.16			1.12		

From Table 2.1, it can be seen that the three machine learning models have similar levels of accuracy and RMSE between models when considering each new measure, however the Quadratic SVM is overall the best at predicting the peak month and the number of peaks, while the Linear Discriminant best forecasts I48N. However, the skill level, defined as the mean model accuracy/(expected random accuracy), differs between measures modelled. The model of the annual I48N total is the most skillful by some margin, while the skill levels for models of each of the other three measures are similar. The F1 score also agrees with this.

While the number of peaks prediction has a higher F1 score than I48N, reflecting high model precision, this is offset by the forecast having the lowest number of possible outcomes. Similarly, the peak month prediction has the greatest number of outcomes, and therefore has an expected lower precision.

The forecast for a particular measure is defined as a collective view of the combined models of a given measure. While the models often agree on individual measures, the likelihood of the models predicting all four measures the same is low. For the 2021 forecast, when the models predicted different outcomes for a measure, the forecast was the outcome that had been predicted more than once.

2.3.2 Machine Learning Hindcasts

Here the 2017–2021 machine learning hindcasts are presented, and can be seen in Table 2.2. Interestingly, the Linear Discriminant and Linear SVM hindcasted the same result across all measures for the years 2017–2020; however, this was not the case for the 2021 forecast, nor has this historically been the case.

Table 2.2 Machine learning hindcasts (in order Linear Discriminant, Linear SVM and Quadratic SVM) separated by commas. The observed class is shown in bold.

Year	I48N		RoC		Peak Month		No. of Peaks	
2017	1,1,1	**1**	1,1,1	**0**	2,2,2	**1**	1,1,1	**1**
2018	1,1,1	**0**	0,0,1	**1**	2,2,1	**0**	2,2,1	**2**
2019	2,2,2	**2**	0,0,1	**1**	1,1,2	**2**	1,1,1	**2**
2020	0,0,1	**0**	1,1,0	**2**	2,2,2	**1**	1,1,1	**1**
2021	1,1,1	**0**	1,0,0	**0**	3,3,1	**0**	1,1,1	**1**

The 2017 hindcast was for a medium iceberg year across all models, and this was the observed case. The three models also successfully hindcasted one peak. However, all models were incorrect in hindcasting a medium rate of change (observed low) and a peak month of May, as opposed to the true April. Overall, the hindcast was fairly successful, hindcasting both I48N and the number of peaks correctly. There was also high model unity between all measures.

For 2018, all models incorrectly hindcasted a medium iceberg year, when a low year was observed. While there is less agreement between the models for the other three measures, all incorrectly hindcasted the peak month (April and May, when January–March was observed). Only the Quadratic SVM successfully hindcasted the rate of change (medium); however, the Linear Discriminant and Linear SVM models successfully hindcasted the number of peaks (two) where the Quadratic SVM failed to do so. Overall, this hindcast was unsuccessful, with only individual models successfully hindcasting.

For the 2019 season, all models successfully hindcasted a high iceberg year; however, they all failed to hindcast a second peak. Only the Quadratic SVM successfully hindcasted both the rate of change and the peak month (medium and May). Overall, the Quadratic SVM hindcast was very good for this year; however, the two linear models were less successful.

For the 2020 hindcast, both the Linear Discriminant and the Linear SVM successfully hindcasted a low iceberg year, and all models hindcasted one peak. However, no model hindcasted a high rate of change or that the peak would occur in April. Overall, the hindcast was fairly successful when looking at the linear models.

For 2021, all models predicted a medium I48N and one peak. There was significant disagreement regarding the month in which the peak would occur, however April was selected overall for the forecast as this is the more common peak month than June onwards. A low rate of change was also chosen overall, despite the Linear Discriminant prediction of a medium rate of change. While the rate of change and number of peak predictions were successful, I48N and the peak month were not. 2021 was an extremely low year, as previously noted, with an early peak in February (the only observed iceberg past 48°N). This is potentially why there was so much disagreement over the peak month prediction.

These hindcasts show that, while the individual models often fail to predict certain measures, it is common for at least one model to successfully predict each outcome. This is true for the long-term trend, not just the four years hindcasted here. Therefore, it is in deciding which model results should take precedence that further work on this topic should focus on.

2.3.3 Properties of the Machine Learning Models

Table 2.3 shows all combinations of the four machine learning outputs that have been predicted or observed in the testing period (1931–2017). In the Table 2.3 format ([I48N, RoC, peak month, number of peaks]), the 2021 forecast is [1,0,1,1]. This combination was previously observed twice; however, it is rarely a predicted combination, only appearing once in the Linear SVM outputs and never in the Linear Discriminant or the Quadratic SVM. The most common predicted outputs for each machine learning tool, respectively, are: [1,0,2,1], [1,0,2,1], and [0,0,2,1]. The most common observed combinations are [0,0,2,1] and [1,1,1,1]. The similarity in the predicted outcomes is consistent with observed results, in that one peak in May (e.g., [x,x,2,x]) is a common scenario. Likewise, one peak in April ([x,x,1,x]) is also often predicted, as in the second common observed combination. However, it is notable that there is a wider range of observed combinations (44) than any of the models predict (43, 34, and 39, respectively). The Linear Discriminant Model appears to best reflect the range of observed combinations, and also has a similar distribution across the structure given in Table 2.3.

Table 2.3 Machine learning output combinations over 1931–2017. Here the order is: I48N, rate of change (RoC), the peak month, and the number of peaks. Therefore, a combination of [0,0,2,1] is for a low ice year, with a low rate of change, and one significant peak in May. The last row in each set shows the sub-column totals, with the total sub-set of combinations in brackets in the first column.

	Combinations with 0 I48N	**Number of Repetitions**	**Combinations with 1 I48N**	**Number of Repetitions**	**Combinations with 2 I48N**	**Number of Repetitions**
Observed Combinations	[0,0,2,1]	6	[1,1,1,1]	6	[2,1,1,1]	3
	[0,2,1,2]	3	[1,2,2,1]	3	[2,0,2,1]	2
	[0,1,2,1]	3	[1,1,2,2]	2	[2,2,3,2]	2
	[0,2,0,2]	3	[1,0,2,1]	2	[2,2,0,1]	2
	[0,2,1,1]	3	[1,2,1,2]	2	[2,2,2,2]	2
	[0,2,2,1]	3	[1,2,1,1]	2	[2,2,2,1]	1
	[0,0,1,1]	3	[1,0,1,1]	2	[2,1,3,1]	1
	[0,0,3,2]	2	[1,1,0,1]	1	[2,0,1,2]	1
	[0,1,1,1]	2	[1,1,2,1]	1	[2,0,3,1]	1
	[0,1,0,2]	2	[1,1,3,2]	1		
	[0,0,1,2]	2	[1,0,3,1]	1		
	[0,1,3,1]	2	[1,2,0,2]	1		
	[0,1,2,2]	2	[1,2,3,2]	1		
	[0,2,2,2]	2	[1,0,3,2]	1		
	[0,1,1,2]	1	[1,0,0,2]	1		
	[0,0,0,2]	1	[1,2,0,1]	1		
			[1,0,0,1]	1		
			[1,2,3,1]	1		

			[1,1,3,1]	1		
Total (44)	**16**	**40**	**19**	**31**	**9**	**15**
Linear Discriminant Output Combinations (ld)	[0,0,1,2]	5	[1,0,2,1]	6	[2,2,2,1]	2
	[0,1,2,1]	4	[1,2,2,1]	4	[2,0,2,2]	2
	[0,2,0,1]	3	[1,1,1,1]	4	[2,2,1,1]	2
	[0,2,2,1]	3	[1,2,1,1]	4	[2,2,3,2]	1
	[0,2,2,2]	3	[1,0,2,2]	3	[2,2,1,2]	1
	[0,1,1,2]	3	[1,1,3,1]	2	[2,1,1,2]	1
	[0,2,1,2]	3	[1,2,3,2]	2	[2,2,3,1]	1
	[0,0,3,2]	2	[1,0,3,2]	1	[2,0,2,1]	1
	[0,2,1,1]	2	[1,0,0,2]	1	[2,1,3,1]	1
	[0,1,2,2]	2	[1,0,1,2]	1	[2,1,2,1]	1
	[0,1,3,1]	2	[1,2,0,1]	1		
	[0,1,0,1]	2	[1,1,0,1]	1		
	[0,0,2,1]	1	[1,2,3,1]	1		
	[0,0,1,1]	1	[1,1,2,1]	1		
	[0,1,0,2]	1	[1,0,3,1]	1		
	[0,1,1,1]	1				
	[0,0,2,2]	1				
	[0,2,0,2]	1				
Total (43)	**18**	**40**	**15**	**33**	**10**	**13**
Linear SVM Output Combinations (ls)	[0,0,2,1]	5	[1,0,2,1]	6	[2,2,1,2]	3
	[0,1,2,1]	5	[1,2,2,1]	4	[2,1,2,1]	2
	[0,0,1,2]	5	[1,1,2,1]	4	[2,0,3,1]	2
	[0,2,2,1]	5	[1,0,2,2]	3	[2,1,1,2]	1

	[0,2,1,1]	5	[1,2,0,1]	3	[2,2,2,1]	1
	[0,0,2,2]	3	[1,2,1,1]	2	[2,1,2,1]	1
	[0,1,1,1]	3	[1,1,1,1]	2		
	[0,2,1,2]	3	[1,0,1,2]	2		
	[0,1,2,2]	2	[1,1,3,2]	1		
	[0,1,1,2]	2	[1,2,3,2]	1		
	[0,2,0,1]	2	[1,0,1,1]	1		
	[0,2,2,2]	2	[1,2,1,2]	1		
	[0,0,1,1]	1	[1,0,3,1]	1		
	[0,2,3,1]	1				
	[0,1,0,1]	1				
Total (34)	**15**	**45**	**13**	**31**	**6**	**10**
Quadratic SVM Output Combinations (qs)	[0,0,2,1]	7	[1,1,2,1]	5	[2,2,2,2]	2
	[0,2,2,1]	5	[1,2,0,1]	3	[2,2,0,2]	2
	[0,0,1,2]	4	[1,2,1,1]	3	[2,0,3,1]	1
	[0,2,1,2]	4	[1,2,2,1]	2	[2,2,0,1]	1
	[0,1,1,1]	4	[1,0,2,1]	2	[2,1,2,1]	1
	[0,0,0,1]	3	[1,1,2,2]	2		
	[0,1,2,2]	3	[1,1,1,1]	2		
	[0,2,1,1]	3	[1,2,1,2]	2		
	[0,2,2,2]	3	[1,2,3,1]	2		
	[0,2,3,2]	2	[1,2,2,2]	1		
	[0,0,2,2]	2	[1,0,1,2]	1		
	[0,1,2,1]	2	[1,2,0,2]	1		
	[0,2,0,1]	2	[1,1,0,2]	1		

	[0,0,3,1]	1	[1,0,2,2]	1		
	[0,1,1,2]	1	[1,0,0,1]	1		
	[0,0,3,2]	1				
	[0,1,0,1]	1				
	[0,1,0,2]	1				
	[0,2,3,1]	1				
Total (39)	**19**	**50**	**15**	**29**	**5**	**7**

Figure 2.7 attempts to show in another, more graphical way, the common patterns in the observed combinations. This clearly shows that one peak (the red circles) is significantly more common than multiple peaks (in blue). The plot also shows that the majority of observed combinations have a low or medium I48N and a peak month of April or May. This seems sensible, as the average I48N has been increasing over the last century, and the training period is 1931 to 2017. Also, as previously mentioned, the peak month is usually April or May. Figure 2.8 shows, for comparison, the Linear Discriminant model distribution which most resembles the observed results. In general, the clustering occurs at similar locations but with the main differences at times of low rate of change. The model is also more likely to predict multiple peaks; however, as previously stated, the observational results may be under-representing this aspect. For reference, the 3D scatter plots of the Linear and Quadratic SVM models have been included in the supplementary material as Figures S1 and S2.

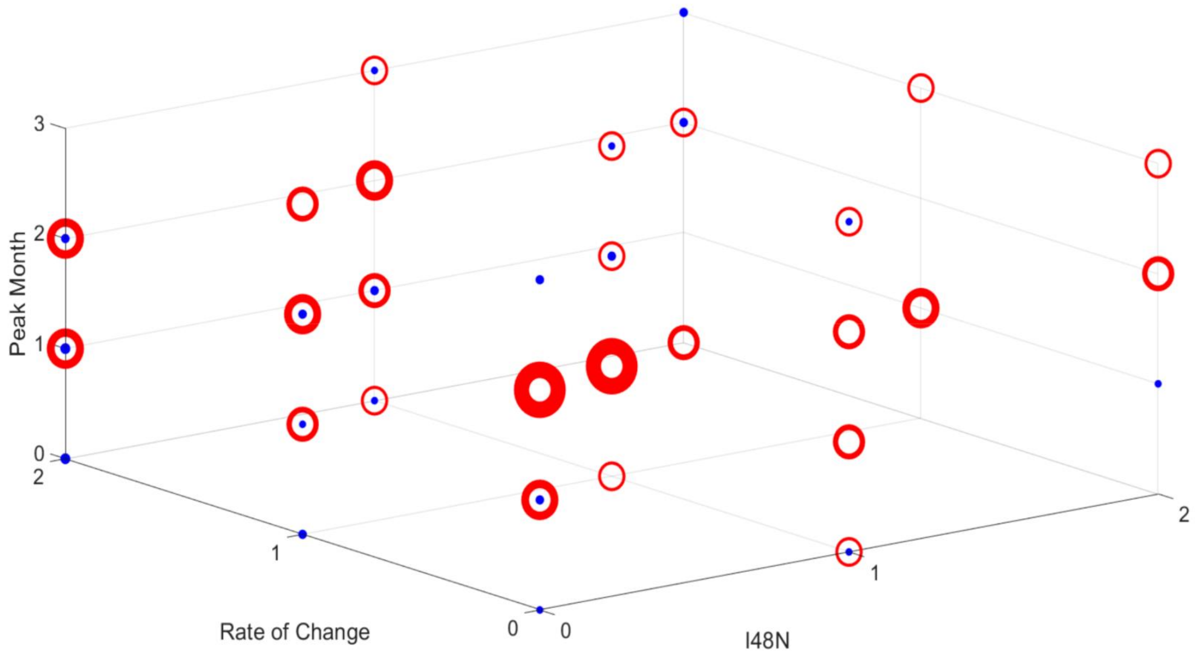

Figure 2.7 Plot of the observed combinations from the testing period of 1931–2017, where I48N, the rate of change, and the peak month are marked on the axis. A red circle corresponds to one peak, while blue represents multiple peaks. The larger the circle, the more times that combination has occurred.

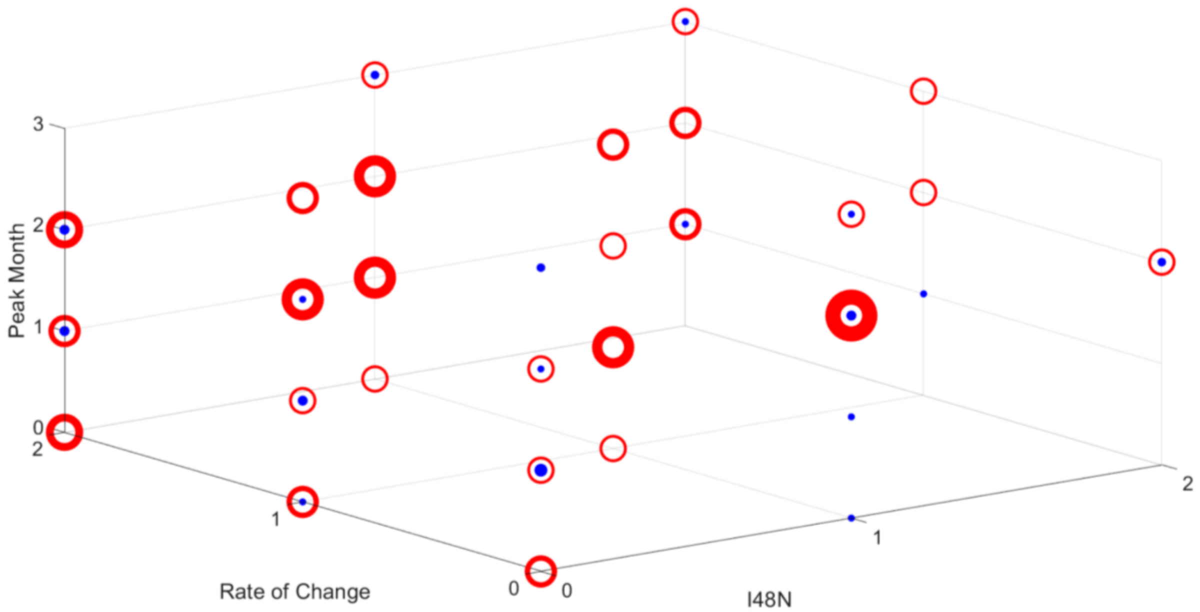

Figure 2.8 Plot of the Linear Discriminant combinations from the testing period of 1931–2017, where I48N, the rate of change, and the peak month are marked on the axis. A red circle corresponds to one peak, while blue represents multiple peaks. The larger the circle, the more times that combination has occurred.

Another question regarding how well the machine learning models perform relative to the observed states is how well they do overall for each measure. Table 2.4 attempts to show this, through a comparison of the means and standard deviation of the various models compared to observations. The prediction of the number of peaks was excluded here as there are only two possible outcomes, and it can be seen from Figure 2.6 and Figure 2.7 that one peak is overwhelmingly dominant. Table 2.4 shows that the Linear Discriminant outputs have the most similar distribution to the observed results, with a very small net difference across all three measures. The Linear Discriminant model's mean is best for two of the three measures (I48N and rate of change), and its standard deviation is best for all of the measures.

Table 2.4 Distribution of combinations. The table shows the mean and standard deviation of the predicted and observed I48N, rate of change (RoC), and the peak month over the trial period of 1931–2017. Also shown is the total difference between the unweighted means of each of the three quantities predicted and the observations. Models closest to observations are shown in bold for each measure.

Observed/Model	I48N	RoC	Peak Month	Total Diff. from Obs.
Observed	0.71 ± 0.75	1.07 ± 0.82	1.51 ± 0.94	
Linear Discriminant	**0.69 ± 0.72**	**1.06 ± 0.85**	1.58 ± 0.91	**0.1**
Linear SVM	0.58 ± 0.69	0.99 ± 0.87	**1.50 ± 0.73**	0.22
Quadratic SVM	0.50 ± 0.65	1.16 ± 0.85	1.41 ± 0.90	0.4

A final aspect of the machine learning models examined here is how successful the models are in predicting individual combinations for specific years. Table 2.3 showed that the Linear Discriminant Model had almost as many outcomes as in the observations, therefore the question is how this links to successful predictions. The successfully predicted combinations from the testing period of 1931–2017 can be seen in Table 2.5. Random chance suggests that only 1.36% of the 86 outcomes, or just one, would be expected to be predicted by a model if there were no skill in the models. However, 10 of the 44 observed combinations were successfully predicted by one or another of the models. One common combination, [0,0,2,1], which represents a low iceberg year, with a low rate of change and one peak in May, was correctly predicted multiple times. Each of the models showed levels of skill, with five, five, and nine successful predictions for the Linear Discriminant, Linear SVM, and

Quadratic SVM models, respectively. Overall, Table 2.5 shows that the Quadratic SVM approach is the most likely to predict the entire combination, with the fewest "false alarms". However, as even this tool successfully predicted only just over 10% of the years' ice states exactly, it shows that assessment of likely iceberg season risk remains exploratory. Overall, the three machine learning models help to build a more comprehensive practical idea of iceberg conditions in a given year, rather than just predicting a final total.

Table 2.5. Showing all the successfully predicted combinations over the trial period of 1931–2017, with the number of times this occurred compared to how many times it was predicted. In the list of successful combinations, the number in brackets gives the number of years in which this combination was found.

				Number of Successful Prediction			Total Number of Predictions		
Successful Combination				**Linear Discriminant**	**Linear SVM**	**Quadratic SVM**	**Linear Discriminant**	**Linear SVM**	**Quadratic SVM**
0	0	1	2 (2)	1	1	1	5	5	4
0	0	2	1 (6)	1	2	2	1	5	7
0	1	1	2 (1)	1	0	0	3	2	1
0	1	2	1 (3)	0	1	1	4	5	2
0	2	1	1 (3)	0	0	1	2	5	3
0	2	2	1 (3)	0	0	1	3	5	5
1	0	2	1 (2)	1	1	1	6	6	2
1	2	1	1 (2)	1	0	0	4	2	3
1	2	2	1 (3)	0	0	1	4	4	2
2	2	2	2 (2)	0	0	1	0	0	2
Total				5	5	9	32	39	31

2.4 The 2022 Forecast

The WERR 2022 forecast can be seen in Figure 2.9, with the machine learning forecast in Table 2.6. The WERR prediction shows a lower than average year. The figure also shows that while previously the 10 year average has been higher than the 50 year average, due to the number of very low years in the last decade the 50 year and 10 year averages are almost exactly equal. The machine learning aspect overall predicts a medium iceberg year (when the average of the three measures is taken), however when combined with the WERR forecast and noting the range in the I48N machine learning prediction, the joint forecast is for a medium year but on the lower side. A low rate of change and one peak in April is also predicted. This forecast was released to the IIP in December 2021. It was also made widely available on the University of Sheffield website in January 2022 (see https://www.sheffield.ac.uk/geography/news/forecast-2022-iceberg-season-newfoundland-canada).

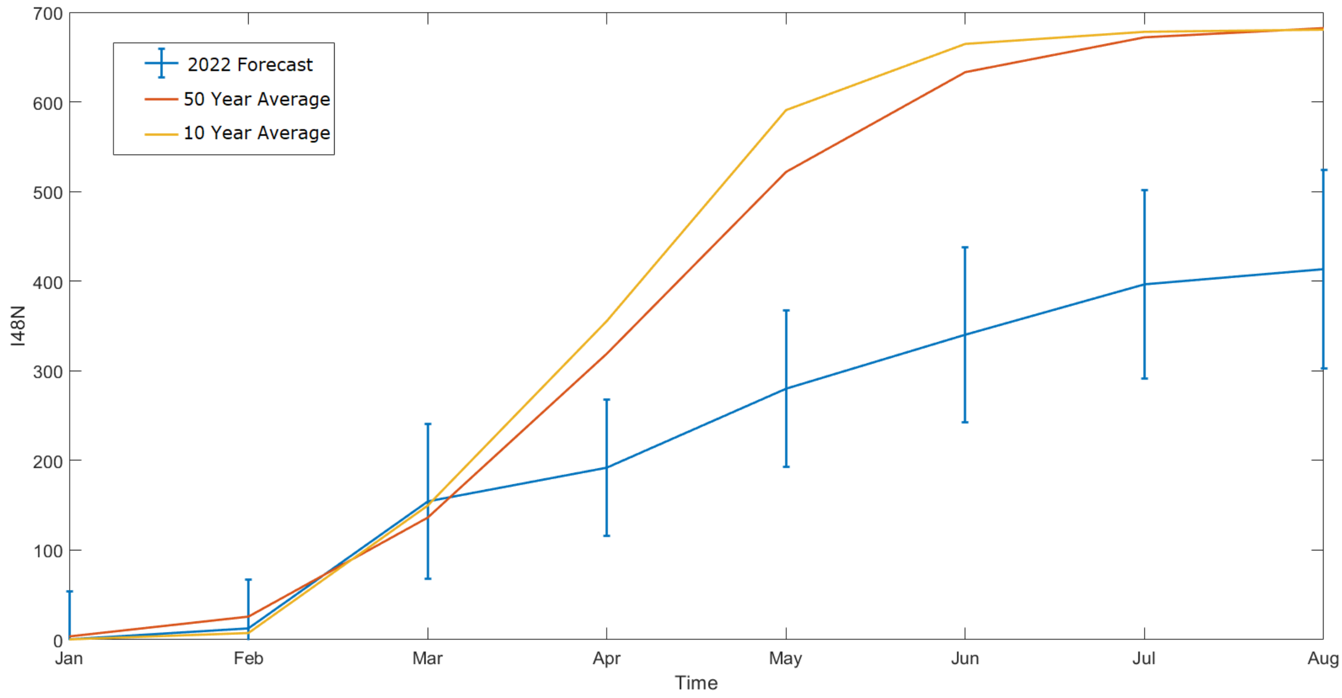

Figure 2.9 Plot of the 2022 iceberg forecast, including the average number of icebergs past 48°N by August in the last 10 and 50 years.

Table 2.6 2022 Machine Learning Model Predictions.

	I48N	RoC	Peak Month	No. of Peaks
Linear Discriminant	2	1	1	1
Linear SVM	1	0	1	1
Quadratic SVM	0	0	1	1

2.5 Bergy Bits and Growlers

The Canadian Government defines an iceberg to be ice extending 5 or more metres above the sea surface, and 15 or more metres in length (Canada, 2022). Smaller 'icebergs' than this are referred to as bergy bits, while any less than one metre above the sea surface and less than 5 metres in length are known as growlers (Canada, 2022). Despite the reduced size, they are often of a scale great enough to cause damage to ships, with collision with a bergy bit is thought to have resulted in the sinking of the Shrimp Trawler BCM Atlantic in 2000, off the Labrador Coast (Hill, 2000). However, the yearly total released by the IIP does not include bergy bits and growlers (Report of the International Ice Patrol in the North Atlantic, 2019). Therefore in this section, the aim is to determine the relationship between I48N and the number of bergy bits and growlers, in order to predict likely 2022 levels.

The iceberg data released by the IIP includes a measure of iceberg location and size (available at https://data.noaa.gov/dataset/dataset/international-ice-patrol-iip-iceberg-sightings-database). Therefore data can be used to identify both the presence and the location of observed bergy bits and growlers. However, as growlers in particular can be very small, and as they are not included in the IIP yearly total, not all bergy bits and growlers in the Newfoundland region will have been identified. However, this is still useful for looking at trends.

Figure 2.10 shows I48N compared to the yearly total number of bergy bits and growlers recorded south of 48°N. The data begins in 1998 as before this a different recording system was used, which did not include iceberg locations. It can be seen from the figure that I48N and the number of bergy bits and growlers are strongly related. This is supported by the high positive correlation between the two (0.7889 statistically significant at the 1% level).

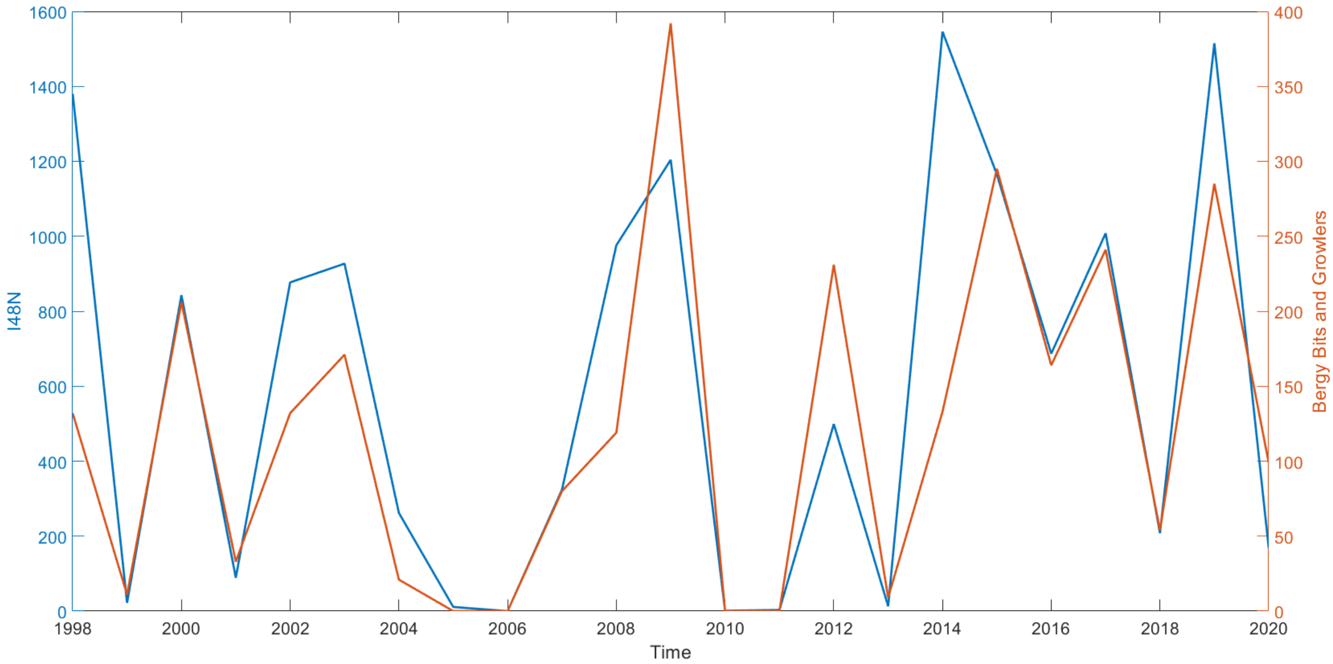

Figure 2.10 Plot showing I48N compared to the total number of bergy bits and growlers recorded south of 48°N each year between 1998-2020.

As the iceberg locations are also available, it is interesting to see whether there is also a relationship between I48N and the latitude of the furthest south bergy bit or growler in each year. This is shown in Figure 2.11, where it is clearly seen that in high I48N years, bergy bits/growlers can survive further south. However, there is little difference in latitude past around 800 icebergs (a medium-high I48N).

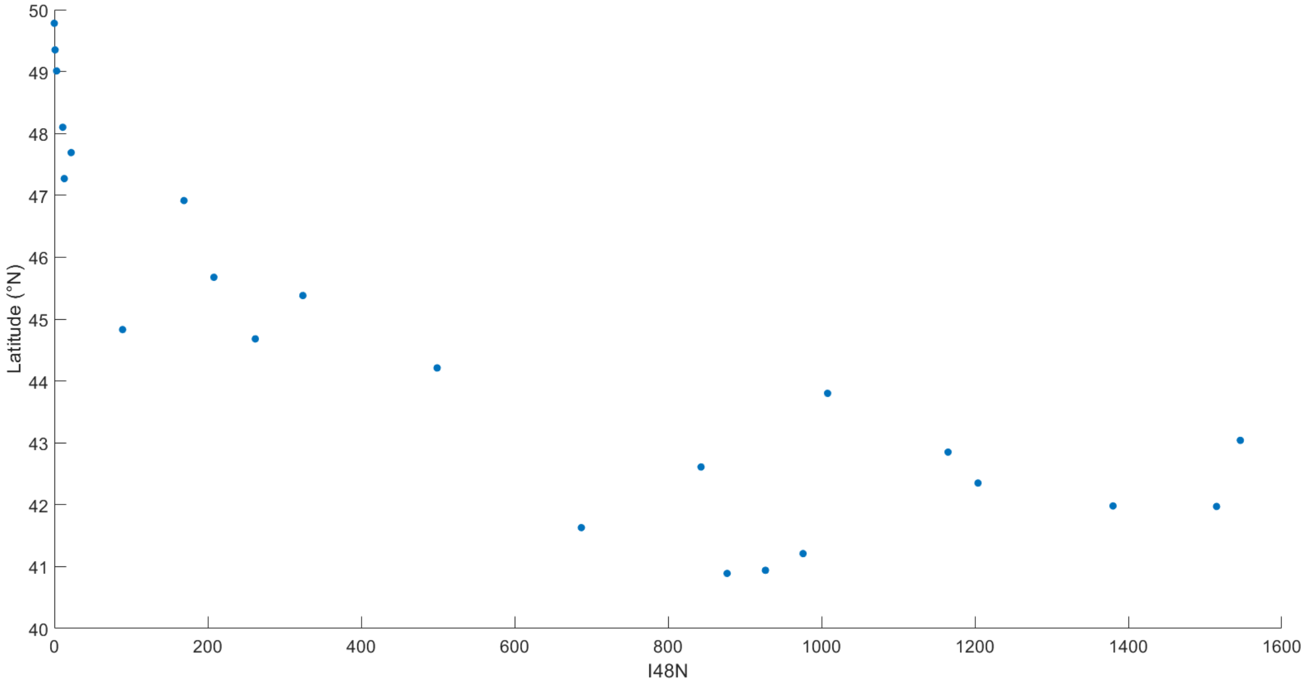

Figure 2.11 Scatter plot showing I48N compared to the latitude of the furthest south (recorded) bergy bit or growler each year between 1998-2020.

Overall, there has been shown to be a strong positive correlation between I48N and the number of recorded bergy bits and growlers. Additionally, in low I48N years the furthest south recorded bergy bit or growler is found at a significantly higher latitude than in medium-high I48N years. However, once this medium/high threshold is reached, the latitude of the bergy bit/growler does not show significant change, potentially as these small ice masses can not survive south of these latitudes. Therefore, this suggests that regarding the 2022 forecast, as a medium year, on the lower end, is predicted, that a slightly lower than average number of bergy bits and growlers are likely to be recorded south of 48°N. Similarly, the latitude of the furthest south recorded bergy bit/growler is likely to be higher than in an average I48N year.

2.6 Conclusions

Overall, this chapter presents a new machine learning approach to forecasting iceberg behaviour in the North West Atlantic. The addition of these machine learning models to an existing and updated control systems forecast has been done to supplement the WERR result and to try to predict more detailed and practically useful aspects of iceberg behaviour in the forthcoming ice year. The flexibility of the machine learning tools allows for a prediction of practically any quantity, restricted only by the available data. The four new measures in this paper were selected after end-user feedback from the IIP that these forecast aspects would be of interest for monitoring purposes. The machine learning models themselves were selected due to their established success in classification tasks in the environmental sector; however, as this a new application of these models, future work may focus on optimising the selection of machine learning approaches to achieve the best prediction performance in this field.

The WERR model forecast has been released to the IIP operationally every year since 2018, and two of the machine learning predictions—I48N and the rate of change—were also provided for the 2020 season. However, the 2021 ice season was the first to present all of the new measures and the WERR forecast. Both aspects of the forecast were also used for the 2022 season forecast. While it can be seen from the presented figures and tables that the combined iceberg forecast is statistically useful for prediction, it must also be noted that in recent years the forecast has not been as successful as might have been expected. It may be that as the models were developed using data from the last century, the dominant environmental variables affecting I48N have changed over this time. However this is difficult to prove, as only using a decade of data at a time would severely reduce the confidence in the result. The 1990's were a decade of near-consistent high I48N, which can be seen in Figure 2.12. The 5-year moving average has also been included in orange to highlight this. It can be seen that from 1999 there has been an increase in the number of extreme low years. This is likely due to reduced sea ice extent as a result of climate change, as greater sea ice extent historically facilitates iceberg survival, through reduced wave erosion on the iceberg and the associated cooler sea surface temperatures. However, there is also large natural variability in I48N.

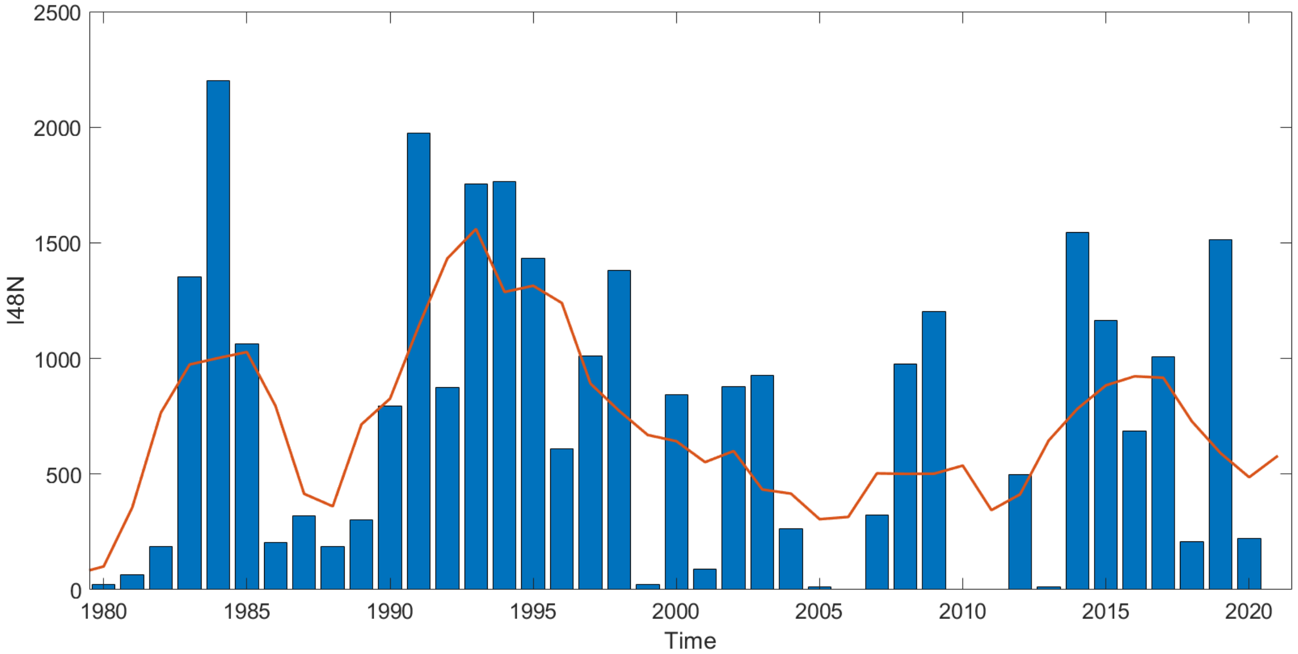

Figure 2.12. Showing I48N each year from 1980 to 2021 in blue. The 5-year moving average is plotted in orange.

Another effect of the gradually decreasing sea ice extent is allowing shipping further north. While there may be the beginnings of a decreasing trend in I48N (which is also seen from the NEMO ocean model in Chapter 4, to be discussed later), many recent years have recorded high numbers of icebergs (for example 1515 in 2019). As such, there is real practical application in long term iceberg warning. A combined forecast of iceberg severity gives the shipping industry time to adjust routes and departure times to avoid regions of high iceberg density. While this work is not currently at a stage to be crucial to the shipping sector, it shows both the predictive capacity of these machine learning tools in an area of high natural variability, and is of interest to the IIP in their continued role patrolling the region.

3. Using an Intermediate Complexity Ocean Model to Assess Meltwater Impact from the Melting Greenland Ice Sheet

3.1 Introduction and Model Overview

3.1.1 Aims and Objectives

This chapter presents the results from adding a meltwater component to the FRUGAL (the Fine Resolution Greenland and Labrador Sea) intermediate complexity coupled ocean-iceberg model in four different scenarios of increasing realism and a control run. Analysis has then been done to identify the global ocean changes that result from the differences between these runs. There is a repeated focus on sea surface salinity because this variable is a clear indicator of freshwater addition. The strength of the main ocean currents have also been included in order to understand the larger impact of the meltwater input. This plays into the main aims of this chapter – to assess the effect of meltwater input from the Greenland Ice Sheet (GrIS) on the ocean worldwide, in the context of human-induced climate change.

The structure of the chapter is as follows: an overview of the model and relevant input data, a description of the differences between model runs, model results with a particular focus on sea surface salinity and changes in ocean circulation, a discussion and analysis section, and finally an overall conclusion.

3.1.2 The Model and Input Data

The coupled ocean-iceberg model FRUGAL (Wadley & Bigg, 2002) is a modified version of the Southampton-East Anglia (SEA) ocean general circulation model that was developed in Beare (1999). The model moves the North Pole to Greenland, utilising an orthogonal curvilinear grid discussed in Madec and Imbard (1996). This allows for 20 km resolution around the coast of Greenland, but significantly coarser resolution in the Southern Hemisphere, of approximately 1.5° latitude by 2° longitude (Wilton et al., 2015). The fine resolution of the model allows the topography and bathymetry to be realistically expressed for the level of complexity of the model, most notably in globally important mixing channels (McCarron et al., 2021). FRUGAL uses a free surface which allows freshwater flux to change sea surface height, rather than a rigid lid approach (FRUGAL Model User Guide). The model has 19 vertical levels (from 30 m in thickness at the surface to 500 m for the lowest level), it includes the tracers temperature and salinity, with both allowing for horizontal, vertical and isoneutral mixing (Wilton et al., 2015).

The iceberg model was developed in Bigg et al. (1997), Gladstone et al. (2001) and Levine and Bigg (2008) and produces both iceberg flux and trajectories. The modelled icebergs are divided into size classes depending on the average observed size in each region, therefore icebergs calved from the Antarctic will be on average larger than Northern Hemisphere icebergs (McCarron et al., 2021). However, giant icebergs have not been included. Basal melting, wave erosion and buoyant convection are the dominant ways in which FRUGAL model icebergs melt (Levine & Bigg, 2008). Iceberg numbers are also scaled by the International Ice Patrol's yearly iceberg total crossing the 48th parallel (see https://nsidc.org/data/G00807/versions/1), for temporally realistic yearly variability in the North Atlantic. Icebergs are seeded so that in the Northern Hemisphere January is the peak month for any location south of 64°N and July for any North of this; in the Southern Hemisphere, October is the peak release month (FRUGAL Model User Guide). Therefore, in the Northern Hemisphere the icebergs are realistically seasonally variable as icebergs that are inputted around Greenland in July reach 48°N in March-May as is observed by the IIP (see chapter 1 for more detail on this). In the Southern Hemisphere icebergs are also seasonally variable but the annual total is constant (FRUGAL Model User Guide). This seasonality (in both hemispheres) is achieved by releasing 75% of each year's annual total in one peak month, then 15% the following month, and 10% on the following, therefore no icebergs are discharged six months after the peak (Wilton et al., 2015). There are 70 iceberg seeding locations in the Northern Hemisphere, and only 29 in the Southern Hemisphere (Wilton et al., 2015).

Regarding the model input data, gridded 3-hourly 20th Century reanalysis data: precipitation, sensible and latent heat flux, u and v wind components of momentum flux, upward and downward long wave radiation flux, and upward and downward short-wave radiation flux was accessed via Research Data Archive (available at https://rda.ucar.edu/) and transformed into daily averages. This data is derived from surface pressure observations, then observed sea-surface temperatures and sea-ice extent are used as reanalysis boundary conditions (Wilton et al., 2015). The data was then processed to be compatible with FRUGAL. The data from 1890 was used for these runs. The model is then forced with these variables: heat (sensible, latent and the radiation fluxes listed above), freshwater (where freshwater flux is the difference between precipitation and evaporation) and wind (zonal and meridional) (Wilton et al., 2015). The model does have an observed tendency to overestimate some fields, such as the strength of the AMOC, which has largely been attributed to the 20CR forcing fields used here (Wilton et al., 2015).

Greenland runoff data is courtesy of David Wilton (see Wilton et al., 2015 for how this was calculated). This data was then extended from 2008 to 2015 with ERA 5 data, available at the Copernicus Climate Change Service Climate Data Store. The Wilton data has been calculated using 20th Century reanalysis input data accessed via https://psl.noaa.gov/, and consists of surface latent heat flux, precipitation, and air temperature 2m from the surface. The evaporation rate is then calculated by dividing the surface latent heat flux per time step by either the latent heat of evaporation or sublimation, and rescaling. When the air temperature is above freezing, the latent heat of evaporation used is 2.5×10^6 J/kg. Whereas, when the air temperature is below this point, the latent heat of sublimation (equal to 2.83×10^6 J/kg) is used instead. After rescaling the variables and applying multiple ice masks, a monthly runoff total per degree latitude/longitude is outputted. A much-simplified version of this calculation is that runoff is equal to precipitation plus snowmelt, minus evaporation.

3.1.3 The Model Runs

The five model runs vary over input time and quantity, see Table 3.1 for a formal definition of each run. Note that for all runs, eleven input locations for the Greenland meltwater have been used. These locations have been chosen as they reflect the most significant regions of freshwater input around Greenland (Figure 3.1). The first non-control run (hereby denoted as Run 2) inputs a constant quantity of freshwater only over the summer months. Run 3 has monthly varying freshwater input across the whole year. Run 4 has yearly varying freshwater input. Run 5 has monthly and yearly varying freshwater input and is therefore theoretically the most realistic.

Table 3.1 Outlining the differences between FRUGAL model runs

Model Run	**Time period of freshwater input**	**Freshwater quantity**
Run 1	Control run (no inputted runoff).	Control run (no inputted runoff).
Run 2	Only during the summer months (early June to late August).	Constant input, varying only for each location. These values were the average of the period 1980-2015 over each region.
Run 3	Monthly varying input, constant for each year.	The monthly average for each location over the 1980-2015 period.
Run 4	Yearly varying input, constant across all months.	The yearly average for each location over the 1980-2015 period.
Run 5	Varying both monthly and yearly.	The average for each month at each location, changing yearly with the data.

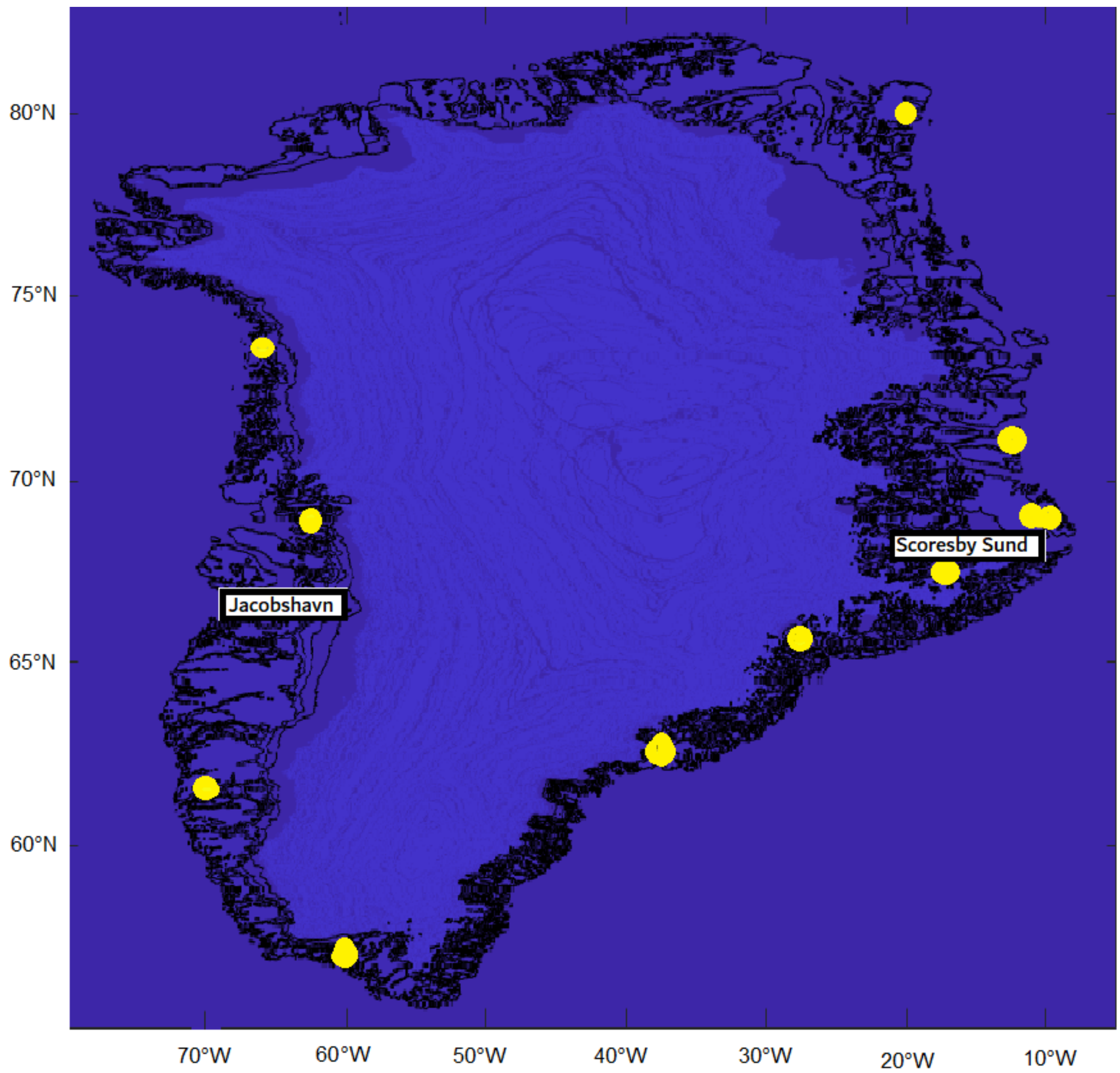

Figure 3.1 Map of Greenland showing the approximate input locations.

3.1.4 Model Run Input Data

The calculated runoff data used for the four model runs can be seen in the following tables. Note all have been rounded to 1 decimal place. Table 3.2 shows the average runoff for each input location over the summer months (June, July and August) for the 1980-2015 time period that was used for Run 2. Table 3.3 shows the runoff data used on Run 3, where the data has been averaged over the entire time period for each month and location. Table 3.4

shows the input data for Run 4, where the runoff data has been averaged for each year, across all months, for each location. The input data for Run 5 can be seen in the appendix (Table S2) due to its length and shows the input runoff varying monthly and yearly for each location.

The Greenland input locations were chosen as they were the areas of most significant surface runoff contribution. These were the areas of greatest surface runoff averaged between 1980 and 2015, from Wilton et al., 2015 data. However, as can be seen from Table 3.2, there is a large range in the size of this contribution. The input location at 72.66°N, 20.57°W adds 17 times less than that at the location 64.51°N, 51.31°W. Geographically, the largest quantities of freshwater are from Jacobshavn and the Scoresby Sund, with significant contributions from both the Helheim and Kangerdlugssuaq glaciers. The Run 4 values are lower than comparable Run 2 values as Run 4 uses the freshwater average across the whole year, whereas Run 2 only averages the summer months. From Figure 3.2, a plot of the monthly varying freshwater input of Run 3, it can be seen that the majority of runoff occurs between early May and late September. The peak is usually July or August, and as such the ‘summer’ months used for Run 2 are defined as June, July and August. From Figure 3.3, significant yearly variation exists in the Run 4 input data. No clear overall increasing trend can be seen from this plot, instead each location is individually influenced by the year.

Table 3.2 Showing the location and runoff data used for Run 2, with runoff data rounded to one decimal place. Note that ‘summer’ is defined as June, July and August.

Latitude	Longitude	Average Summer Runoff from 1980-2015 (t/yr)
64.51	-51.31	214047.2
60.94	-46.13	122585.2
72.66	-20.57	12507.4
75.03	-57.55	180667.7
80.75	-12.43	41174.6
71	-22.83	62685.4
71.29	-51.68	40511.9
65.95	-37.92	150761.6
69.98	-27.18	46125.6
68.49	-32.93	164096.4
70.95	-22.3	146195.1

Table 3.3. Input values for Run 3, showing the monthly average at each location for the years 1977-2015, in t/yr, rounded to 1 decimal place.

Location	Jan	Feb	Mar	Apr	May	Jun	Jul	Aug	Sep	Oct	Nov	Dec
(64.51, -51.31)	4586.4	4230.9	3923.2	4432.4	26172.7	135016.0	265021.3	242104.2	89800.7	14299.5	5861.0	1185.5
(60.94, -46.13)	3659.8	3457.2	3290.6	3283.1	9893.3	61176.1	149921.6	156657.9	76377.4	11432.5	4260.0	983.8
(72.66, -20.57)	3923.6	3589.8	3228.4	3699.7	5808.3	10544.2	15183.3	11794.8	6333.5	5629.9	5082.9	1057.4
(75.03, -57.55)	2612.9	2405.1	2076.7	2194.1	3300.1	60915.8	274885.1	206202.2	32182.2	5879.0	3992.0	772.3
(80.75, -12.43)	2265.3	2157.8	2107.8	2028.6	3311.8	8126.2	76191.5	39206.1	3501.0	3082.1	2741.9	602.8
(71.00, -22.83)	2318.0	2033.8	1734.2	1796.1	2599.6	16210.5	86247.8	85598.1	20664.1	4611.6	3511.4	783.3
(71.29, -51.68)	2408.1	2377.2	1875.2	1986.4	2711.2	19462.6	56873.3	45199.7	8416.7	4238.9	3337.1	758.1
(65.95, -37.92)	1773.3	1807.4	1423.3	1485.3	12948.3	88111.6	196748.5	167424.8	46832.5	6122.6	2760.9	600.1
(69.98, -27.18)	1559.4	1567.0	1271.7	1226.1	2478.8	24211.1	66333.7	47831.9	8229.5	3391.6	2542.5	562.3
(68.49, -32.93)	879.8	1003.7	785.6	915.5	3618.0	59133.4	226683.4	206472.3	36736.7	3204.7	1115.4	242.9
(70.95, -22.30)	920.9	1203.5	1024.0	839.2	5834.2	102680.7	197245.5	138659.0	26215.5	1124.1	1036.5	105.1

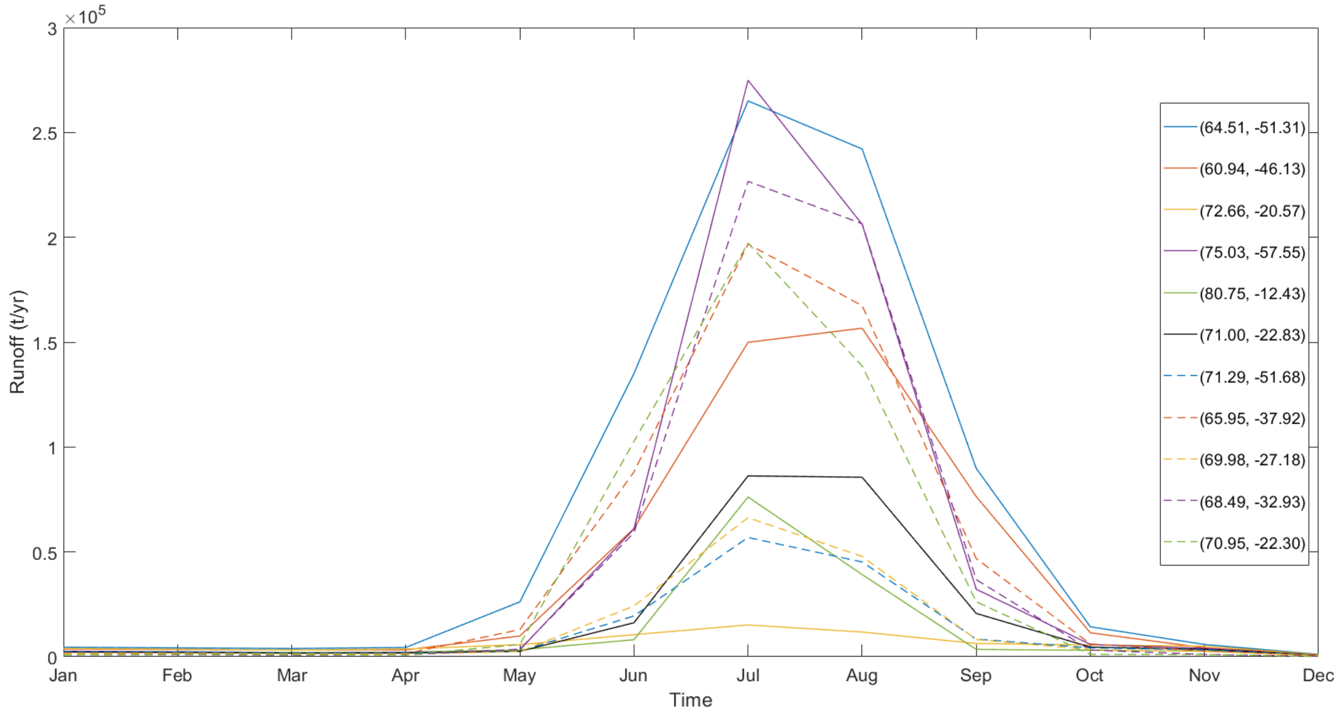

Figure 3.2 Plot of the runoff data at each input location used for Run 3, where the monthly average across all years (1980-2015) has been calculated.

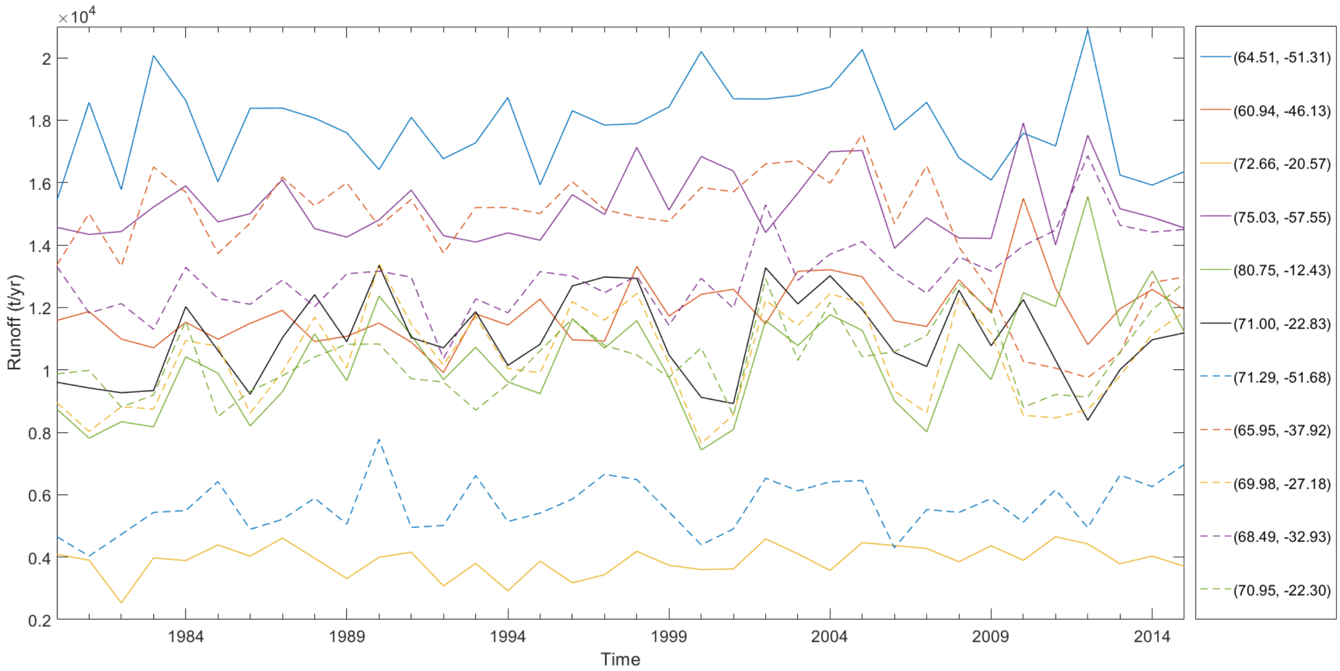

Figure 3.3 Plot of the runoff data at each input location used for Run 4, where the average runoff for each year has been calculated.

3.2 Model Results

3.2.1 Overview

The following section has been separated by location (world view, Northern Hemisphere and Southern Hemisphere) with all runs compared to the control run. A detailed look of the major seas and global passages that are likely to show the effect of meltwater input has been done. The reasoning behind choosing each location has been included in the appropriate section. These highlighted regions in the Northern Hemisphere are the Gibraltar Strait, the Bering Strait and the Labrador Sea. The strength of the Atlantic and Pacific Overturning Circulation has also been addressed. In the Southern Hemisphere, the regions are the Drake Passage and the Indonesian Throughflow (although it is noted that the Indonesian Throughflow has a Northern Hemisphere component as well). More generally, the Northern and Southern Hemisphere Overturning flow rates have also been analysed. There has been greater focus on the Northern Hemisphere as that is where the additional freshwater has been inputted, and therefore where the clearest results are expected. However, it will be shown that the inputted runoff is also having an effect in the Southern Hemisphere. Unless otherwise stated, all time-series plots use a 360-day running mean to show yearly variability.

All runs, including the control run, include yearly variable Northern Hemisphere icebergs, this means that the calving rate from the GrIS has been scaled using the IIP’s dataset. Icebergs are also present in the Southern Hemisphere. Figure 3.4 shows the yearly variability in the number of icebergs observed past the 48th parallel by the IIP (denoted I48N). From year to year, I48N can range from 0 to more than 2000 icebergs. This variability shows that while high/low iceberg years will have a local influence on the surface ocean, they are unlikely to be responsible for large-scale ocean changes. This is also historically true, with Barker et al., (2015) noting while the additional freshwater from melting icebergs may contribute to extending cold periods; they do not initiate such events.

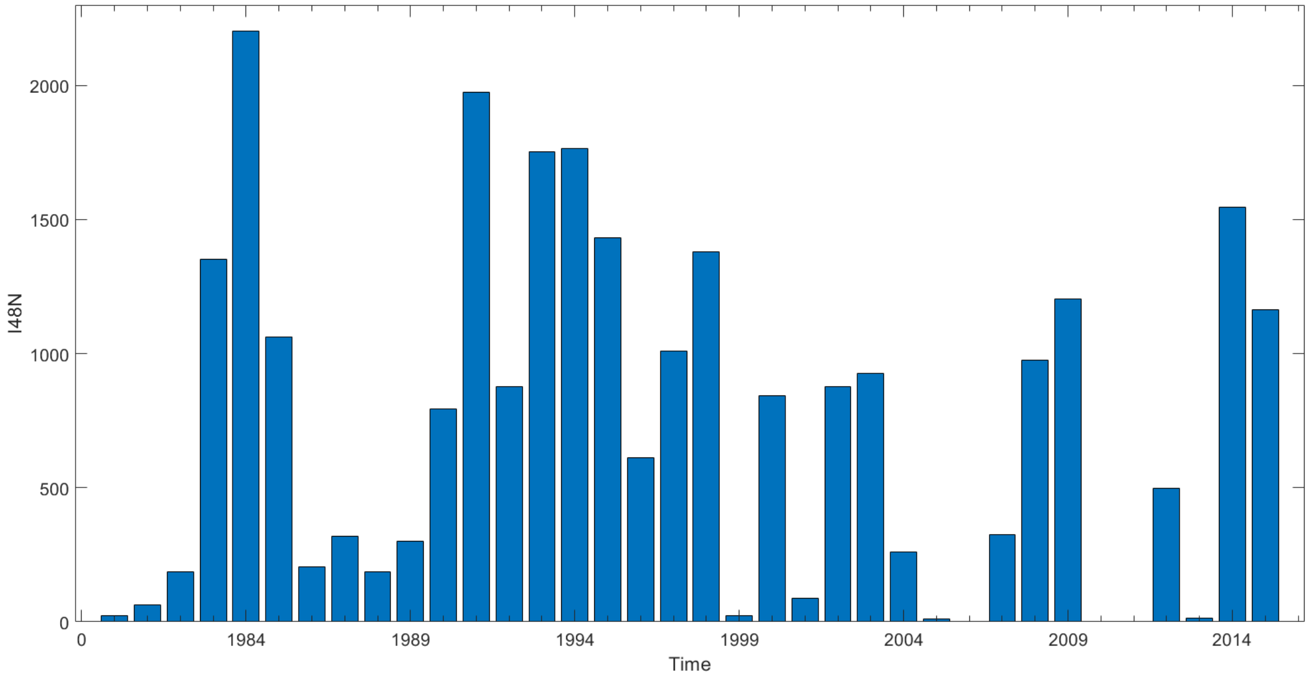

Figure 3.4 Plot of I48N from 1980-2015 as recorded by the IIP.

3.2.2 The World View

The plots of the Northern and Southern Hemisphere's overturning circulations in Run 1 can be seen in Figures 3.5 and 3.6 respectively. These plots show the background variability in the runs. The Northern Hemisphere plot shows two distinct phases: from 1987-2000 and from 2005-2015, with a transitional period in between. The Southern Hemisphere plot has a smaller range than for the Northern Hemisphere, and shows two separate troughs at 1990 and 2002-2005. Peaks in 1989, 1995 and 2013 can also be seen. This suggests the Northern Hemisphere experienced overall larger change in the time period, while the

Southern Hemisphere shows greater year-to-year variations. These regions give a good general overview of global circulation patterns.

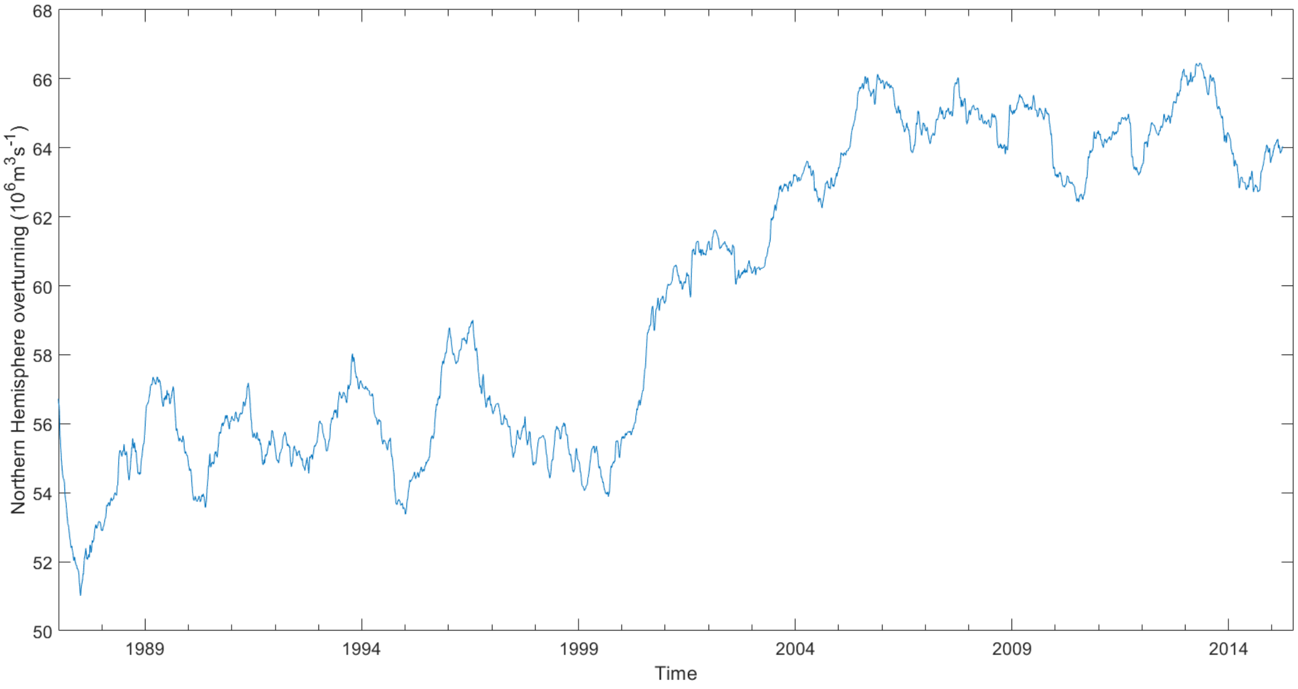

Figure 3.5 Plot of the strength of the Northern Hemisphere Overturning Circulation over time for Run 1.

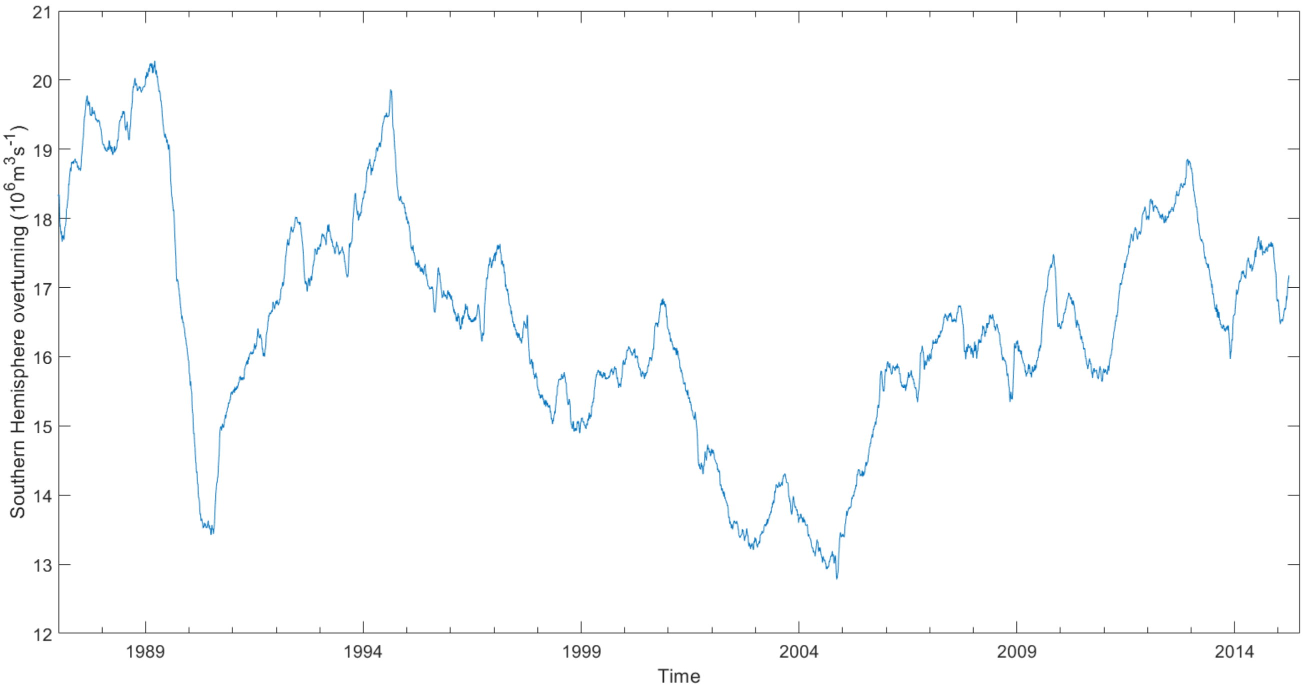

Figure 3.6 Plot of the strength of the Southern Hemisphere Overturning Circulation over time for Run 1.

The four non-control runs (2-5) have had the control run (Run 1) subtracted, in order to remove the background variations and instead see the impact of the additional freshwater. They have then been plotted with a 360-day moving average to see yearly variations. The Northern and Southern Hemisphere overturning circulations can be seen in Figure 3.7 and 3.7 respectively. The Northern Hemisphere shows that the Run 5 freshwater input has a clear and immediate impact on the overturning circulation, compared to the three other runs. However, by 1994 all of the runs (except Run 2) show a similar pattern. This continues until 2009, where Run 5 again distinguishes itself from Runs 3 and 4, and returns to values more similar to Run 2. Overall, most runs show a sustained negative impact on the Northern Hemisphere overturning circulation from inputting increased freshwater runoff, which is most strongly seen in the 20-years between 1999 and 2009. After this point, Run 5 (theoretically the most realistic run) returns to positive values, while Runs 3 and 4 remain at similar negative levels. Run 2 shows little variation over the time period, compared to the other runs, however, it does fluctuate above and below zero throughout. Figure 3.5 showed that in the control run, Northern Hemisphere overturning circulation increased significantly after 1999. This therefore suggests that the additional freshwater input acted to reduce this observed increase.

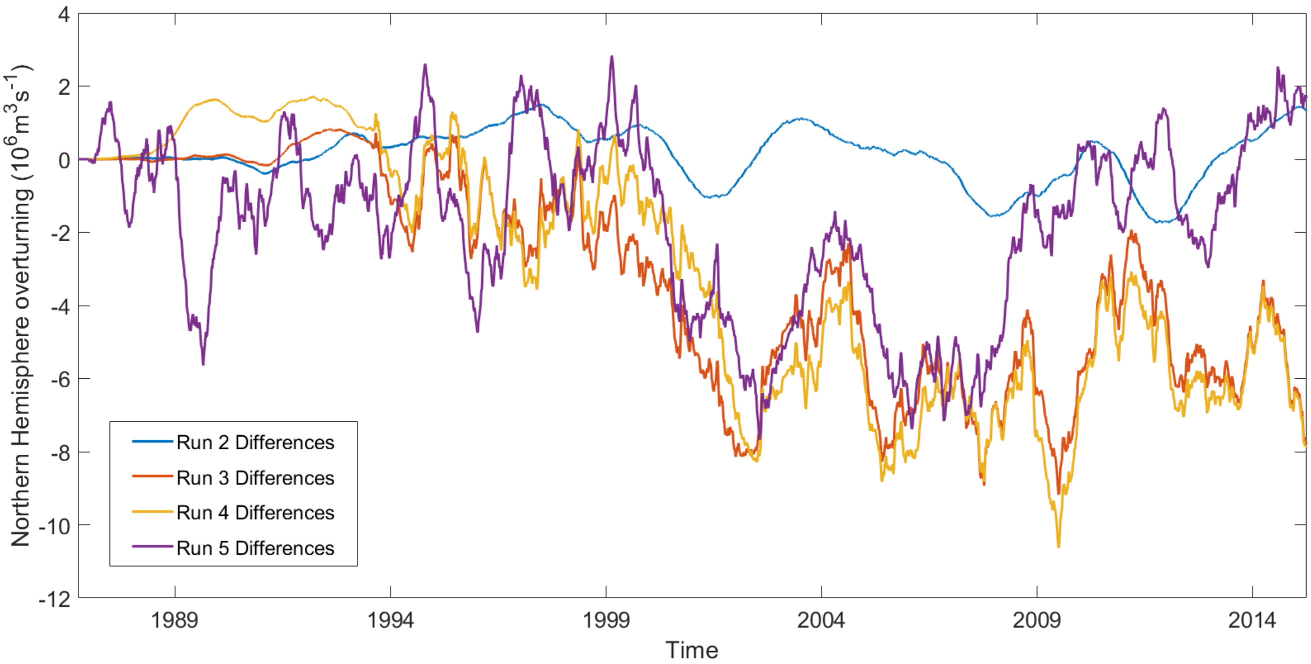

Figure 3.7 Plot of the strength of the Northern Hemisphere Overturning Circulation over time.

In the Southern Hemisphere (Figure 3.8), Run 5 again shows an immediate impact, before aligning closely to Runs 3 and 4 for much of the time period. Therefore, while all other runs take 5 years or so to affect Southern Hemisphere circulation, the freshwater in Run 5 manages to impact the Southern Hemisphere circulation before it could realistically reach these areas. Overall, this period can be considered to be the system adjusting to the large quantities of freshwater suddenly inputted, rather than a useful indication of circulation changes. This is supported by Run 5 following closely to Runs 3 and 4 after this point.

Overall, in the Southern Hemisphere, while fluctuations above and below zero are recorded, looking at the scale it can be seen that the additional freshwater tends to result in a slight positive impact on overturning circulation.

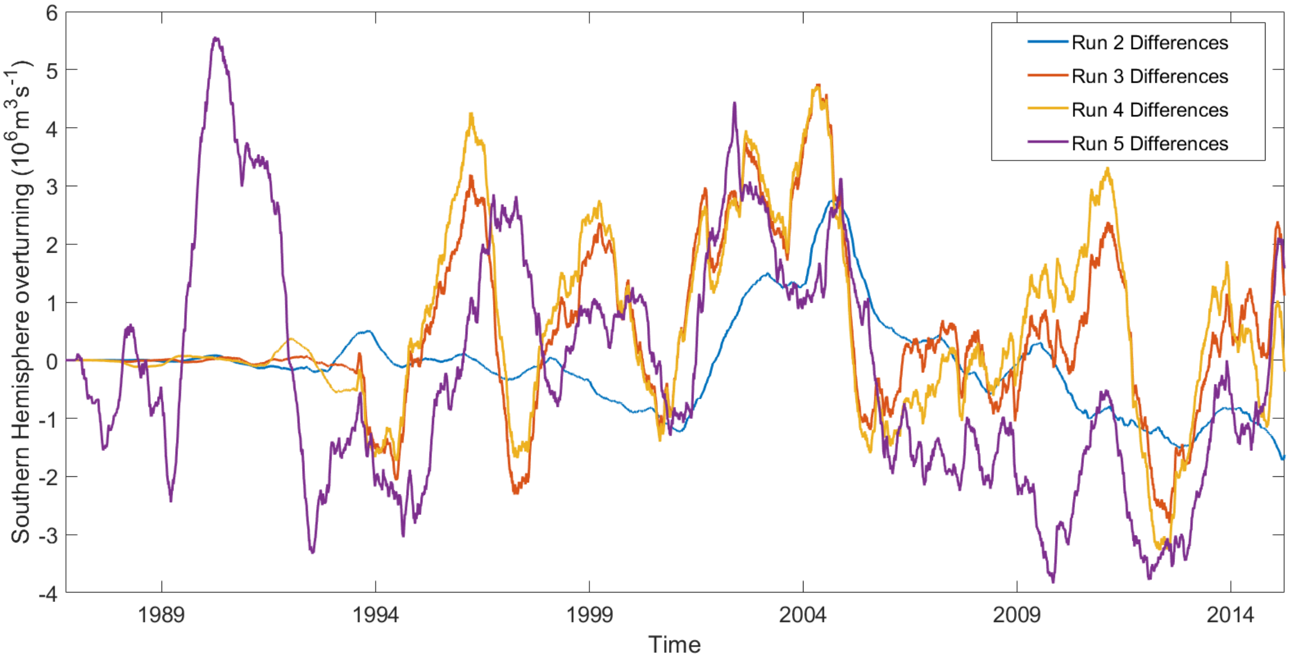

Figure 3.8 Plot of the strength of the Southern Hemisphere Overturning Circulation over time.

3.2.3 The Northern Hemisphere

Figure 3.9 shows the change in Atlantic Overturning Meridional Circulation (AMOC) over time. The trend observed in the Northern Hemisphere plot (Figure 3.5) can be seen here. Other studies also identify an increasing rate from 1995 to a peak in 2005, attributed mainly to decadal variability after a low period in the 1980s and early 1990s (Chen & Tung, 2018). The Atlantic Overturning Circulation is an important part of the global climate cycle, and a popular topic for discussion on anthropogenic climate change (Zhu & Liu, 2020).

Elsewhere in the Northern Hemisphere, the Gibraltar exchange flux shows a period of suppressed activity between 1993 and 2001 (see Figure 3.10). The Gibraltar Strait links the Atlantic Ocean to the Mediterranean Sea by narrow channel and is highly important to marine shipping (Sotillo et al., 2016). This region is heavily but indirectly influenced by the NAO and the Atlantic Multi-decadal Oscillation (AMO) (Fenoglio-Marc et al., 2013). The AMO was in a negative phase between the mid-1960s to the mid-1990s (Trenberth et al., 2021), while the yearly NAO was negative for the early 1990s and positive for much of the second half of the same decade (Jones et al., 1997).

The Bering Strait flux is shown in Figure 3.11. This shows a gradual decreasing trend before the 2009-2012 low, before increasing again. As the only ocean connection between the Arctic and the Pacific, the Bering Strait is an important region of heat and nutrient supply to the western Arctic Ocean (Zhang et al., 2020). Variability is driven by a combination of pressure differences between the Pacific and Arctic Oceans, and local wind strength and direction (Woodgate et al., 2012).

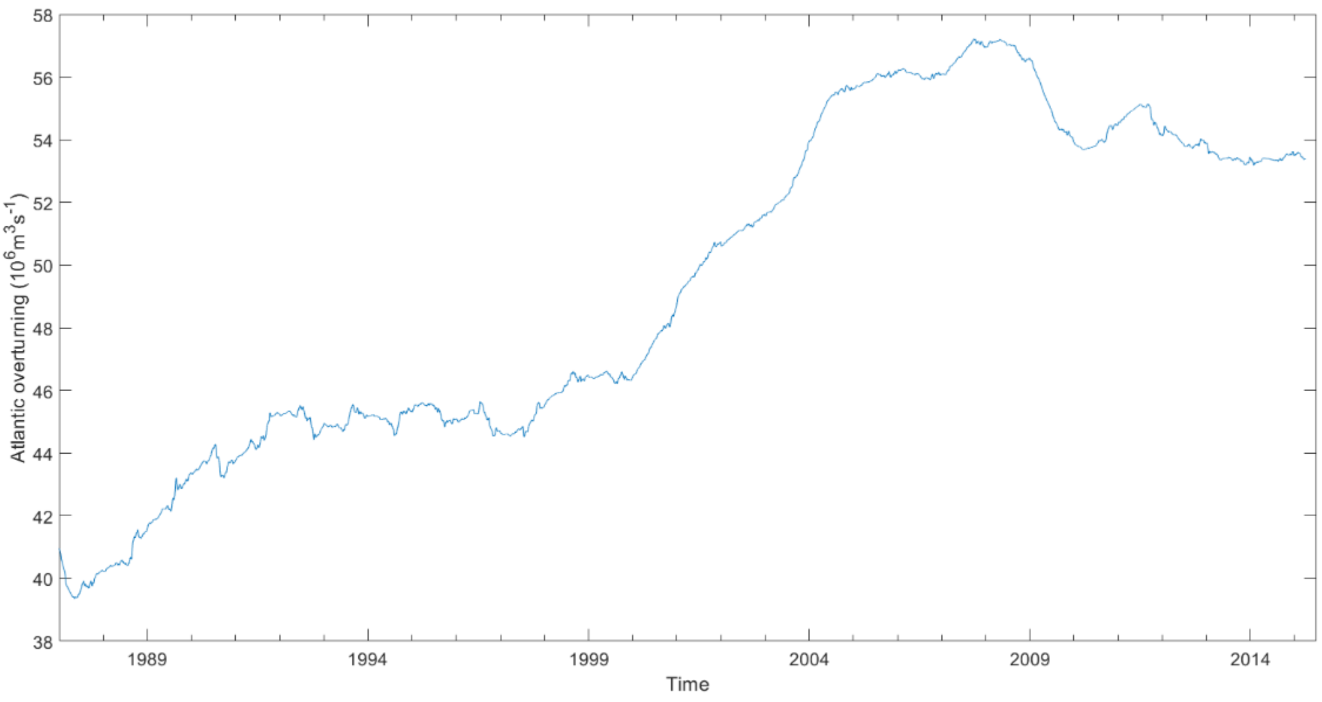

Figure 3.9 Plot of the strength of the Atlantic Overturning Circulation over time for Run 1.

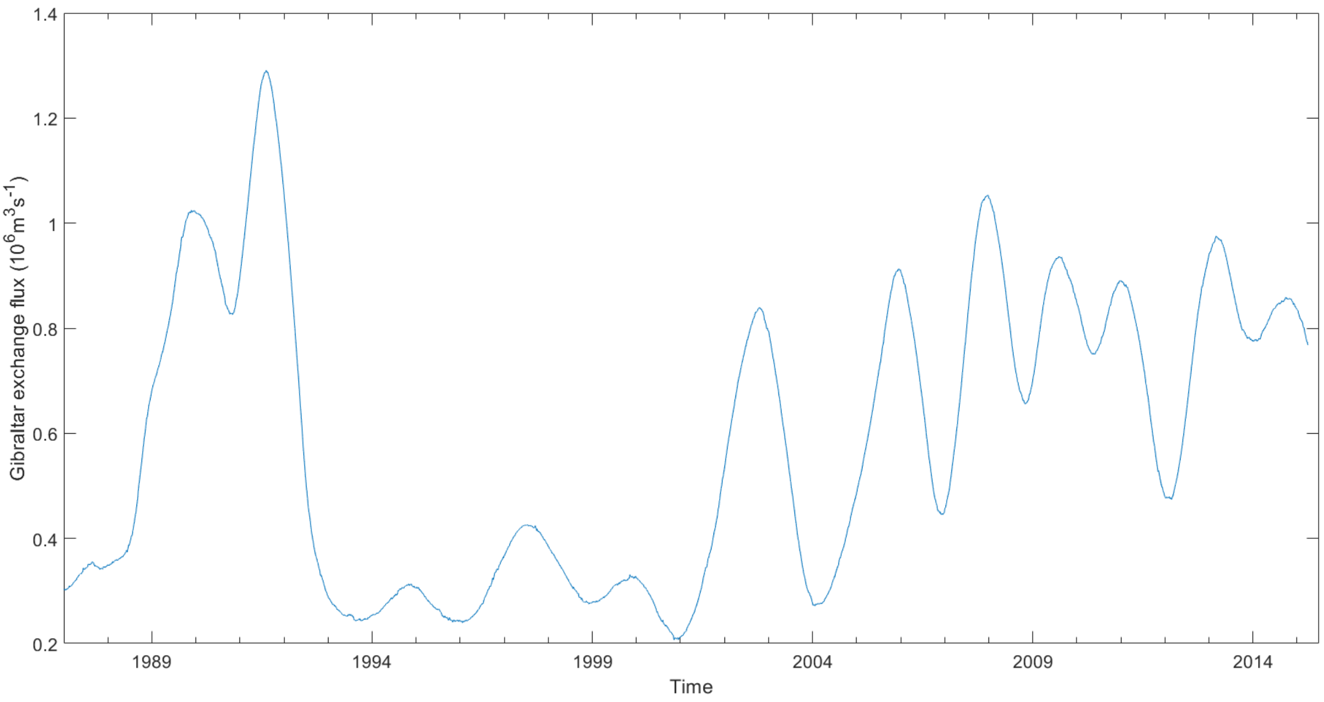

Figure 3.10 Plot of the strength of the Gibraltar Exchange flux over time for Run 1.

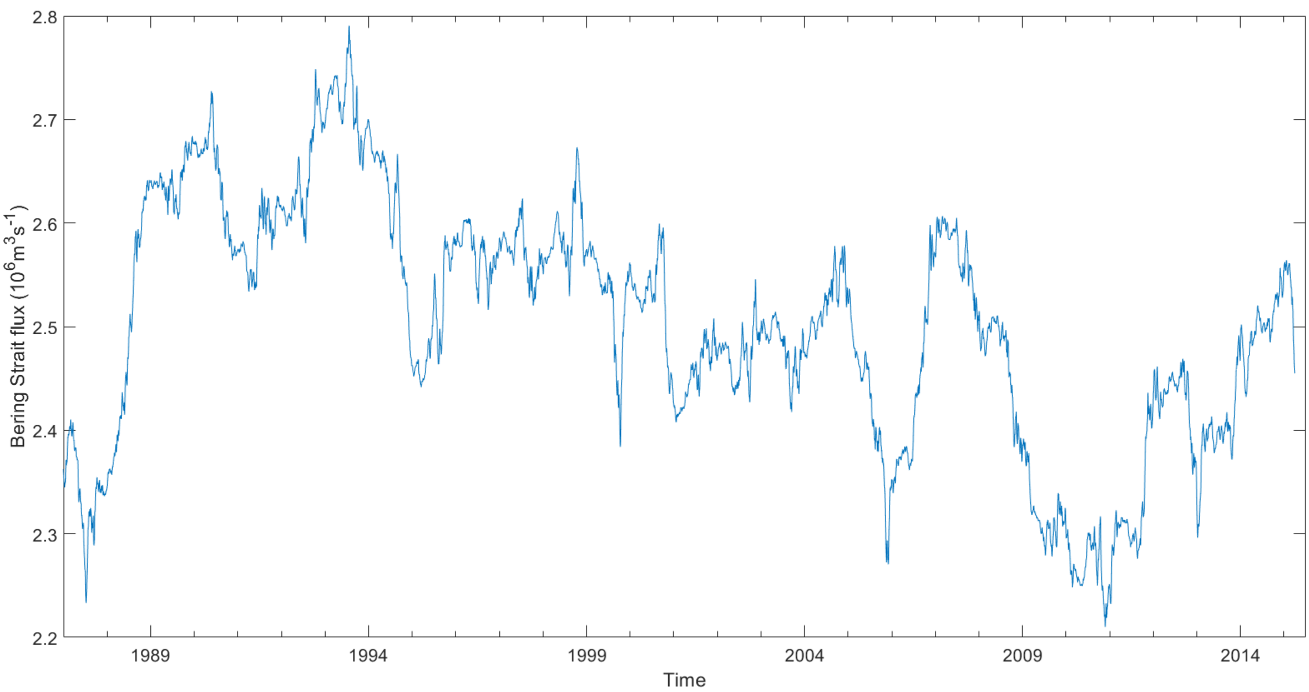

Figure 3.11 Plot of the strength of the Bering Strait flux over time for Run 1.

Sea surface salinity (SSS) is a clear indicator of freshwater, as such it is important to look at the SSS in the Labrador Sea region. The Labrador Sea is an important region of North Atlantic Deep Water formation (NADW), a significant component of the AMOC (Balaguru et al., 2018). It is also the region through which icebergs travel in order to affect the trans-Atlantic shipping lanes, monitored by the IIP (Bigg & Billings, 2014). Figure 3.12 shows the salt flux (the integral of salinity x velocity) into the Labrador Sea over the time period. As seen in Figure 3.4, of I48N, 1991-1998 was a time of high iceberg numbers passing through the Labrador Sea. After 1998, yearly variations in I48N became much greater, with seven of the next seventeen years registering very low iceberg numbers. This may explain some of the variation seen in the figure, notably the prolonged decrease seen between 1989 and 1995, however this variability cannot explain all of it. Iceberg numbers are dependent on many environmental factors, but primarily the sea temperature (Labrador Sea Surface Temperature, LSST), atmospheric temperatures (the NAO, North Atlantic Oscillation) and quantity of ice calved from the Greenland Ice Sheet (the surface mass balance, SMB) (Bigg et al., 2014; Zhao et al., 2016; Zhao et al., 2017).

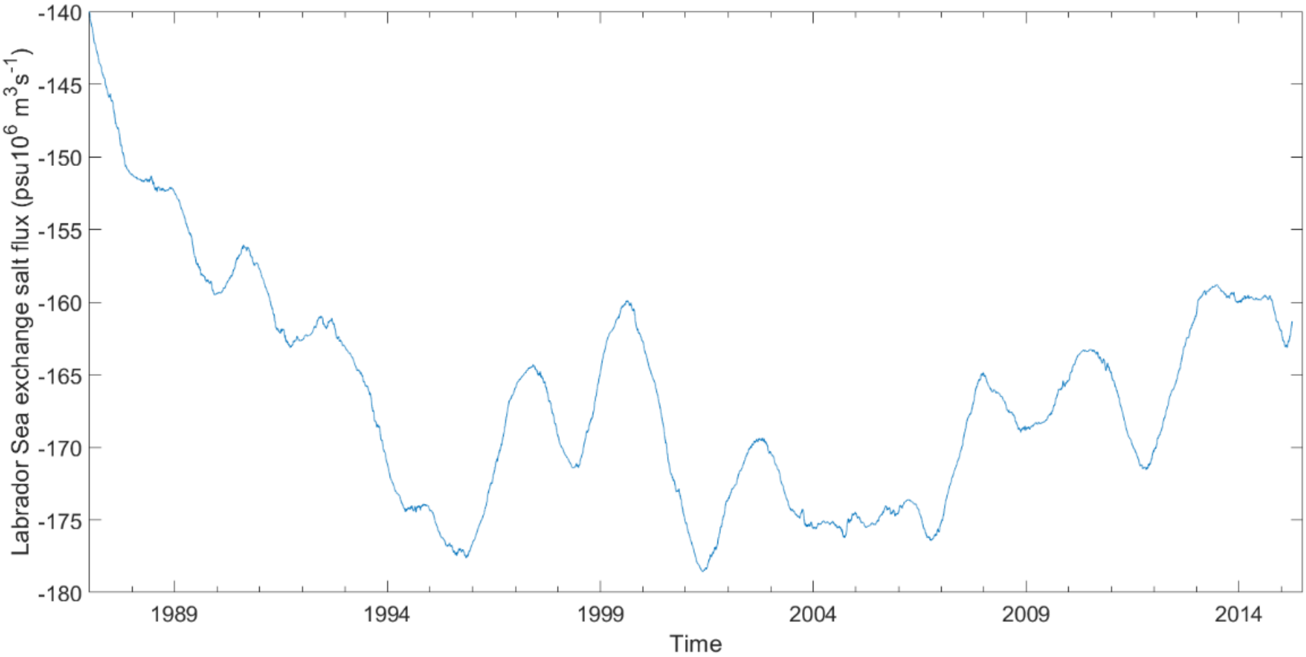

Figure 3.12 Plot of the salt flux into the Labrador Sea over time for Run 1.

As before, the four non-control runs (2-5) have had the control run (Run 1) subtracted, in order to remove the background variations and instead see the impact of the additional freshwater. They have then been plotted with a 360-day moving average to see yearly variations. Figure 3.13 shows the strength of the Atlantic Overturning Circulation in the four runs. This shows a similar pattern to the Northern Hemisphere overturning plot, as might be expected, with the significant trough in the mid-2000s. Again, here the majority of changes are negative, except for Run 5 after 2013. This suggests that the additional freshwater from all the runs is in the short term slowing the AMOC down, however as Run 5 shows an increase from 2008, this may not be the long term trend. Overall, a longer period of study would be needed here to be sure.

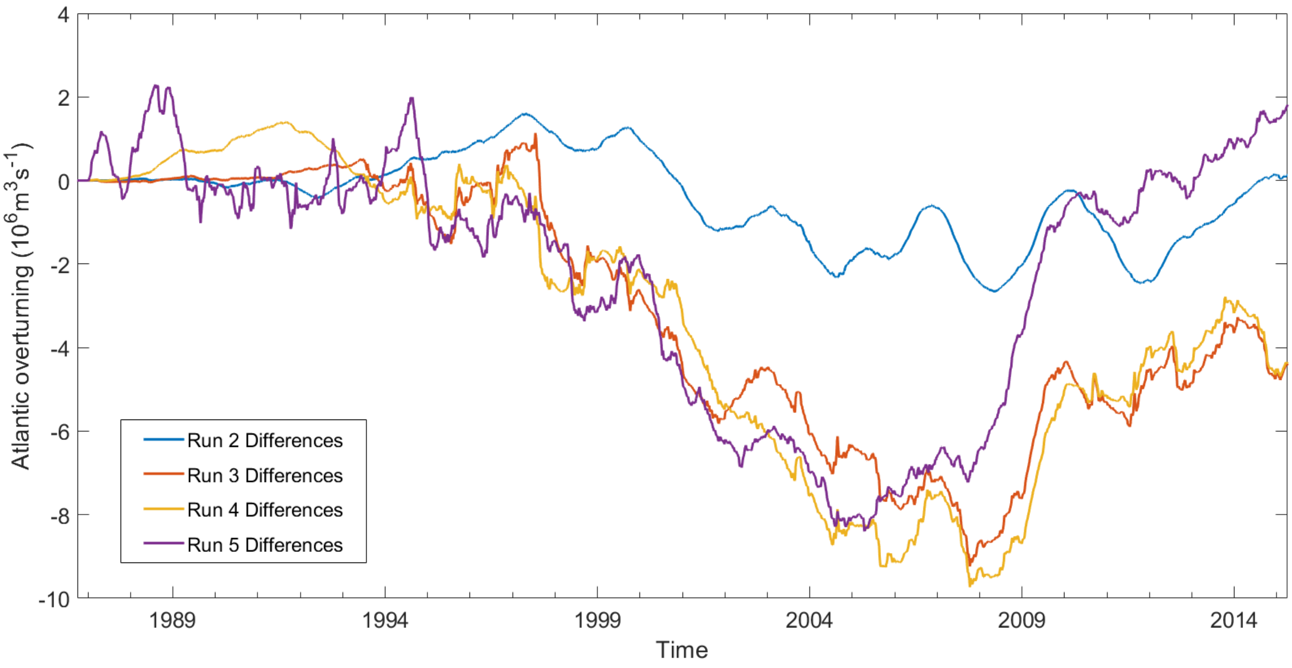

Figure 3.13 Plot of the strength of Atlantic Overturning Circulation over time.

Elsewhere, Figure 3.14 shows the Gibraltar Exchange flux over the time period. While changes here are on a much smaller scale than in the previous plots, this means that Run 2 changes are much more visible than before. In fact, Run 2 can be seen to show the most variation out of all the analysed locations, likely due to the AMOC being geographically close to the seas around Greenland. Run 3 and Run 4 as usual displaying similar patterns to each other. Figure 3.10 showed a low between 1993-2001, which can be seen here as a period of low fluctuation compared to the rest of the time period. Run 5 maintains a similar pattern of change to Runs 3 and 4, however between 1994 and 2000 it seems to act as the opposite to Run 2. While Run 2 is near zero during this time, Run 5 is distinctly positive. This suggests perhaps that the more realistic Run 5 is facilitating mixing earlier than Run 2 (which remains close to zero until 2000) allowing for the increased flux.

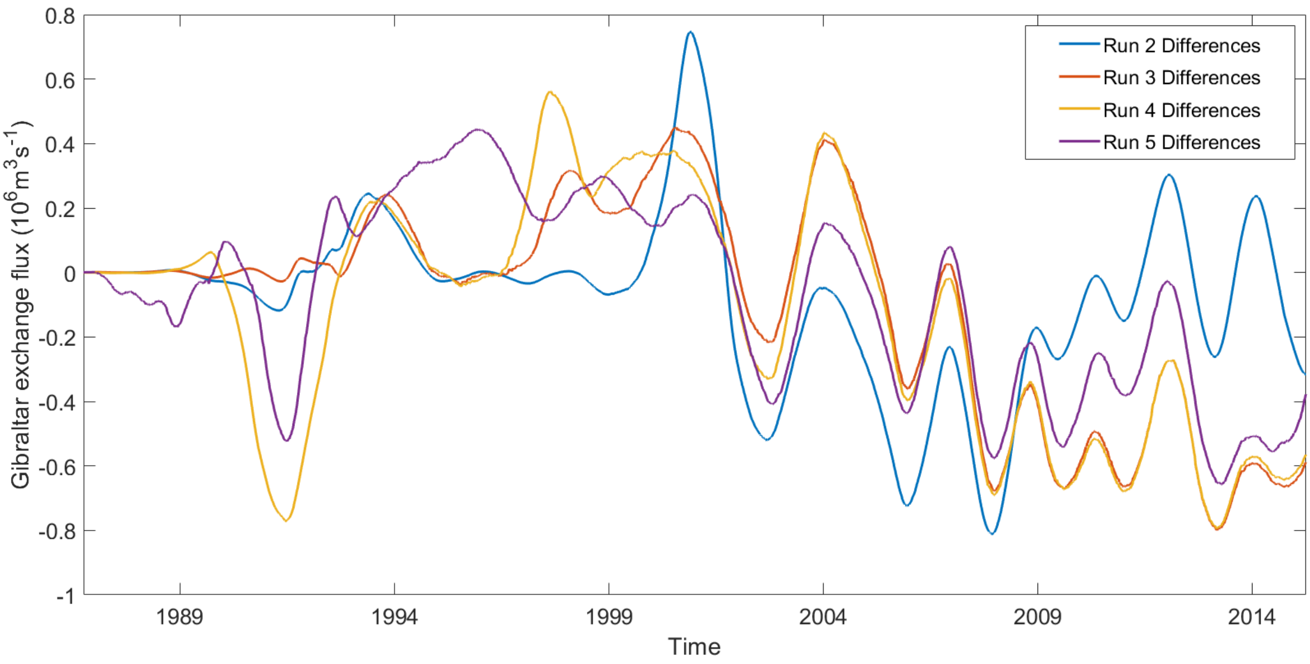

Figure 3.14 Plot of the strength of Gibraltar Exchange flux over time.

Figure 3.15 shows the Bering Strait flux over time, and here, while the scale is also reduced, Run 2 shows very little variability compared to the Gibraltar Exchange flux plot. Additionally, the three other runs are more similar than other regions have shown, after the expected variability in the Run 5 start. Overall, while the different runs are having an impact in the area, the scale of this difference is low. There is however an overall increasing trend across all runs, so perhaps on a longer timescale greater change would become apparent. The Bering Strait is, after all, not geographically close to the freshwater input locations.

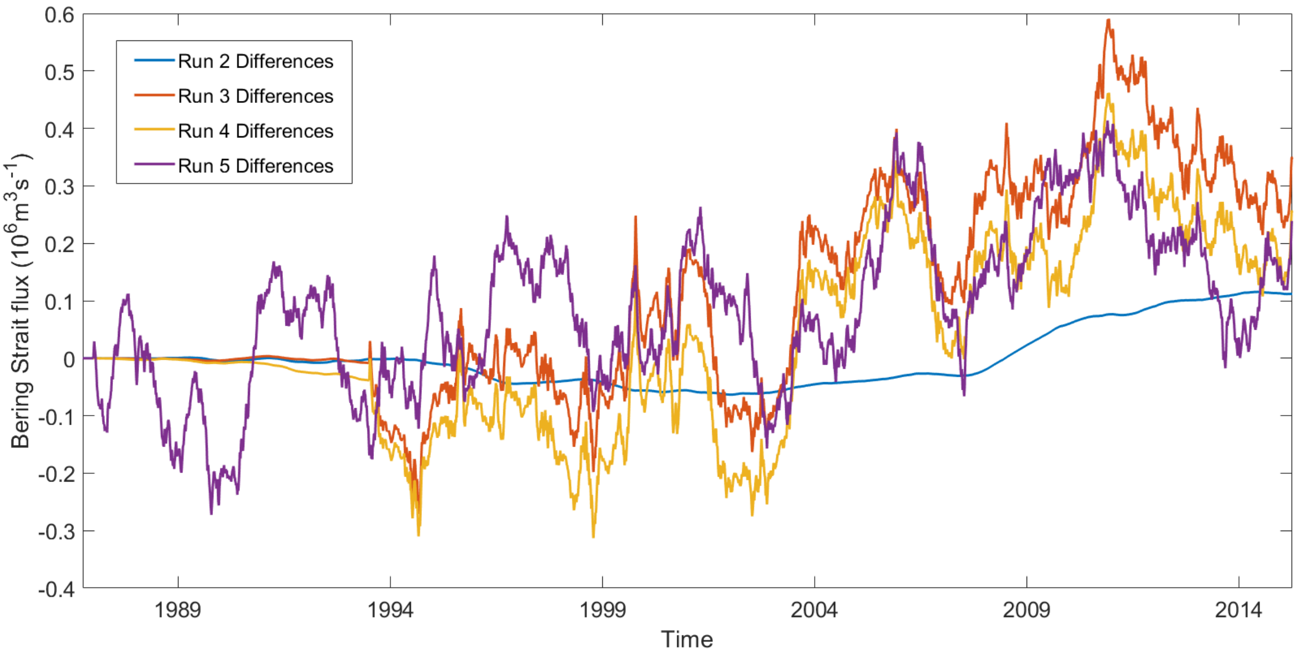

Figure 3.15 Plot of the strength of Bering Strait flux over time.

The Labrador Sea salt flux can be seen in Figure 3.16. This is an important region, not only for iceberg numbers (as seen in previous chapters) but also as it is geographically close to Greenland and the input locations. Additionally, the surface ocean currents in the region carry this freshwater directly into the area (see Chapter 1, Figure 1.2). As expected from this location, significant differences are visible in the plot, with the vast majority showing a positive reaction to the additional meltwater. This suggests that while surface salinity is decreasing, as the additional freshwater is having a negative effect on the Atlantic Overturning Circulation (see Figure 3.13) the Labrador Sea is experiencing less mixing and is therefore more stratified. As salt flux is calculated over the whole depth, a thin surface fresh layer over a high-salinity base would increase the overall flux value. This region will be considered further in Chapter 5, Section 5.3.1, where the surface layer will be analysed and compared to the NEMO model outputs (see Chapter 4).

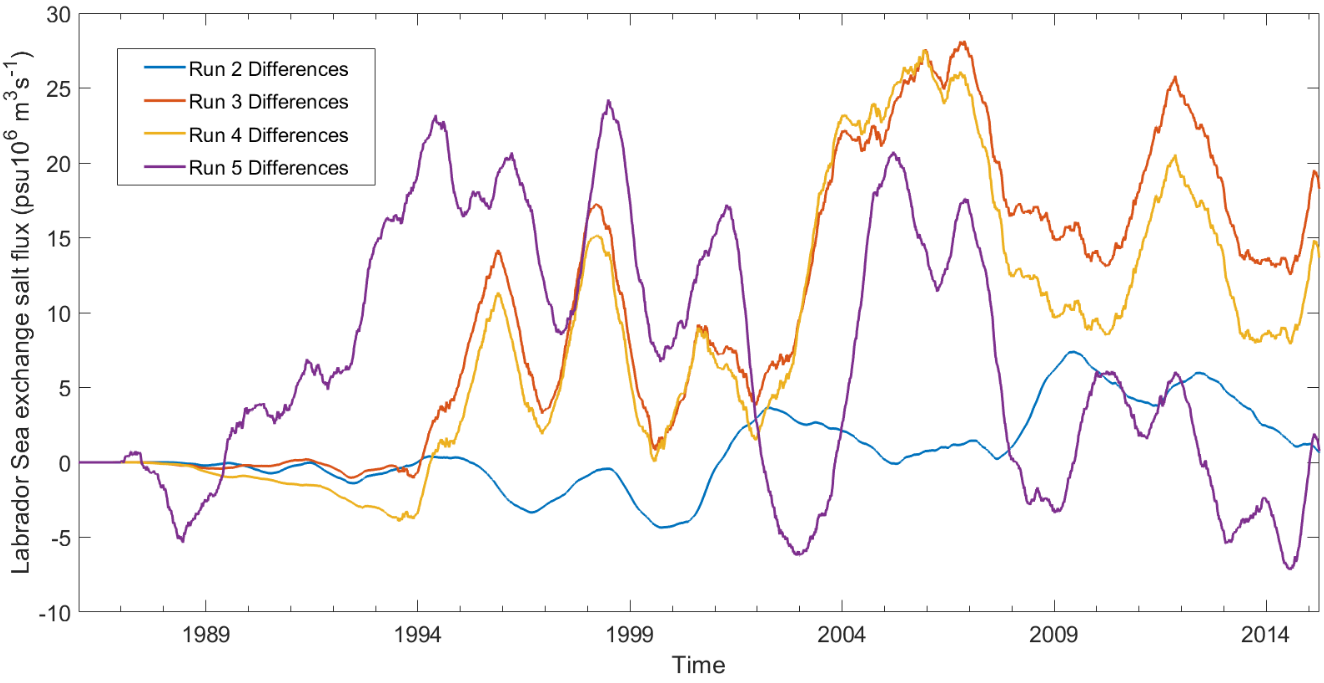

Figure 3.16 Plot of the salt flux into the Labrador Sea over time for all runs 2-5 compared to the control run.

3.2.4 The Southern Hemisphere

The strength of the Pacific Meridional Overturning Circulation (PMOC) over time can be seen in Figure 3.17. Changes in the PMOC affect marine life and carbon storage in the Pacific and may be a leading force behind interannual variability in the global Meridional Overturning Circulation (Tandon et al., 2020). After the year 2000, the flux appears to stabilise slightly and begins an increasing trend.

The Drake Passage connects the Atlantic and Pacific Oceans while extending into the Southern Ocean and is located between Cape Horn in South America and the Antarctic. This is an important region of anthropogenic carbon storage (Fay et al., 2018), and provides insight into the circulation changes occurring in the Antarctic Circumpolar Current (ACC). The ACC plays a significant role in moving freshwater, heat, and nutrients around the

Atlantic, Pacific, and Indian Oceans (Chidichimo et al., 2014). The main atmospheric variability is due to the Southern Annular Mode (SAM), which has shown a positive trend since the early 1990's (Marshall et al., 2018; Koenig et al., 2016). Figure 3.18 shows the change in Drake Passage flux over time, which is not in steady state. This is potentially associated with the steady increase in circumpolar wind forcing that is here not compensated by eddy activity. A consistent, gradual increase is observed across the whole time period, which is likely attributed to the positive SAM trend, and the associated stronger westerly winds.

Figure 3.19, the Indonesian Throughflow flux plot, shows a mid-1990s low, followed by a 2000 peak, intermittent and gradual decrease, before another peak around 2010. Interannual variations in the Indonesian Throughflow are often heavily tied to El Niño–Southern Oscillation (ENSO) phase (Feng et al., 2018). The period 1990-1995 was, barring momentary lapses, a positive ENSO phase; 1995-1997 was a negative phase; 1997-1998 was positive again (see data available at https://www.psl.noaa.gov/enso/mei). The sustained 1990-1995 positive phase is reflected in the flux being low during the same time period in the figure. Overall, there is a generally accepted strong correlation between the Indonesian Throughflow and the ENSO phase throughout the field (see England et al., 2005; Van Sebille et al, 2014).

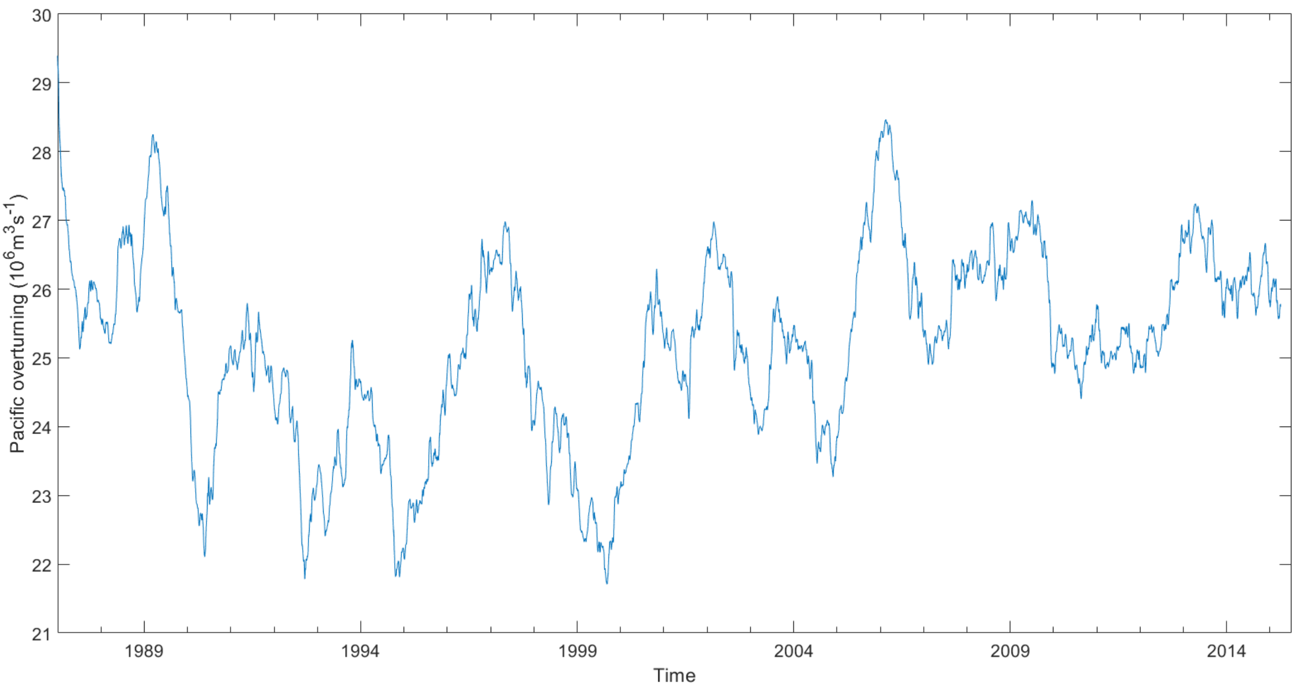

Figure 3.17 Plot of the strength of the Pacific Overturning Circulation over time for Run 1.

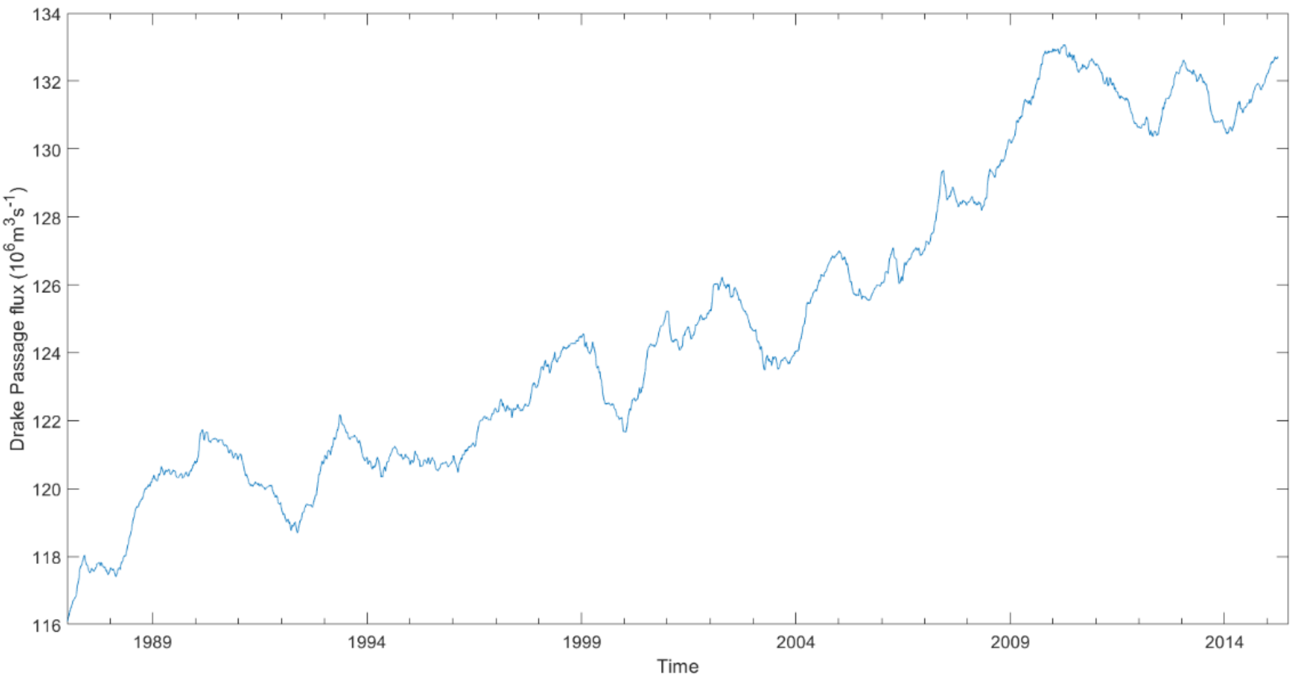

Figure 3.18 Plot of the strength of the Drake Passage flux over time for Run 1.

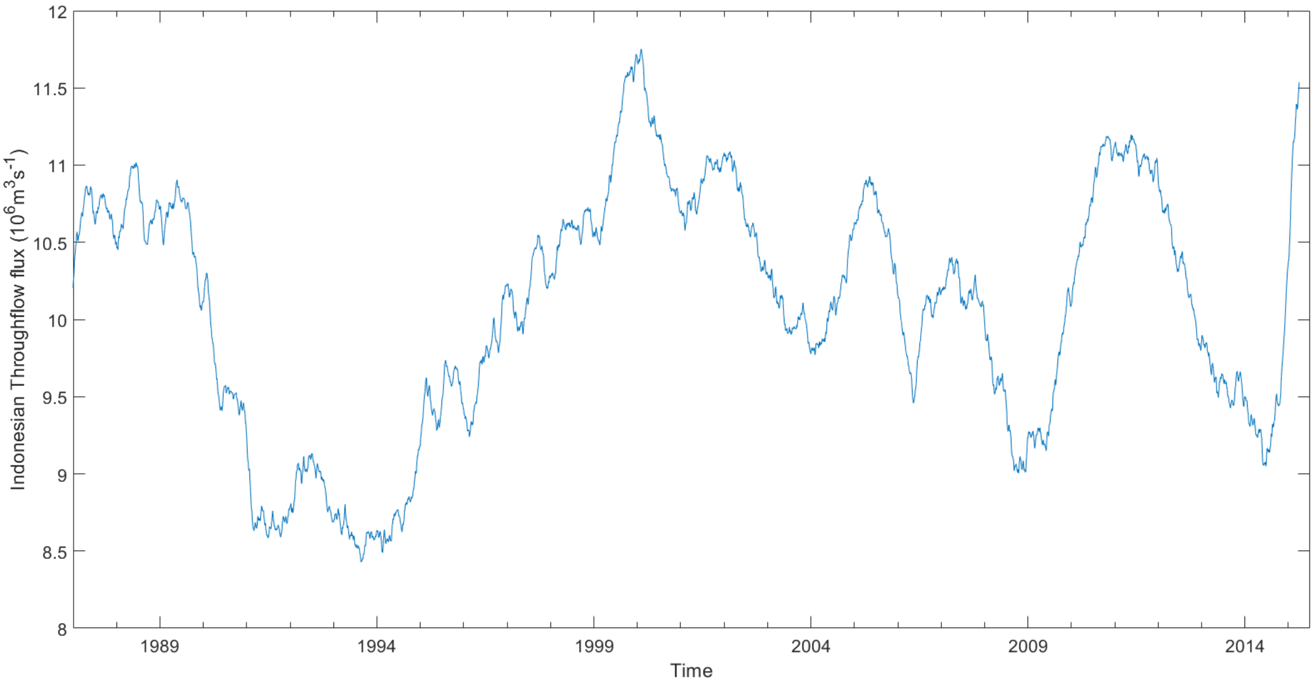

Figure 3.19 Plot of the strength of the Indonesian Throughflow flux over time for Run 1.

Again, the four non-control runs (2-5) have had the control run (Run 1) subtracted, in order to remove the background variations and instead see the impact of the additional freshwater. They have then been plotted with a 360-day moving average to see yearly variations. See Figure 3.20 for a plot of Pacific Overturning Circulation over time. As might be expected from the location of the Pacific Ocean, while all runs show some variability, the fluctuations are relatively low and focused around zero. A longer time period would identify whether any significant differences as a result of the freshwater input could be seen.

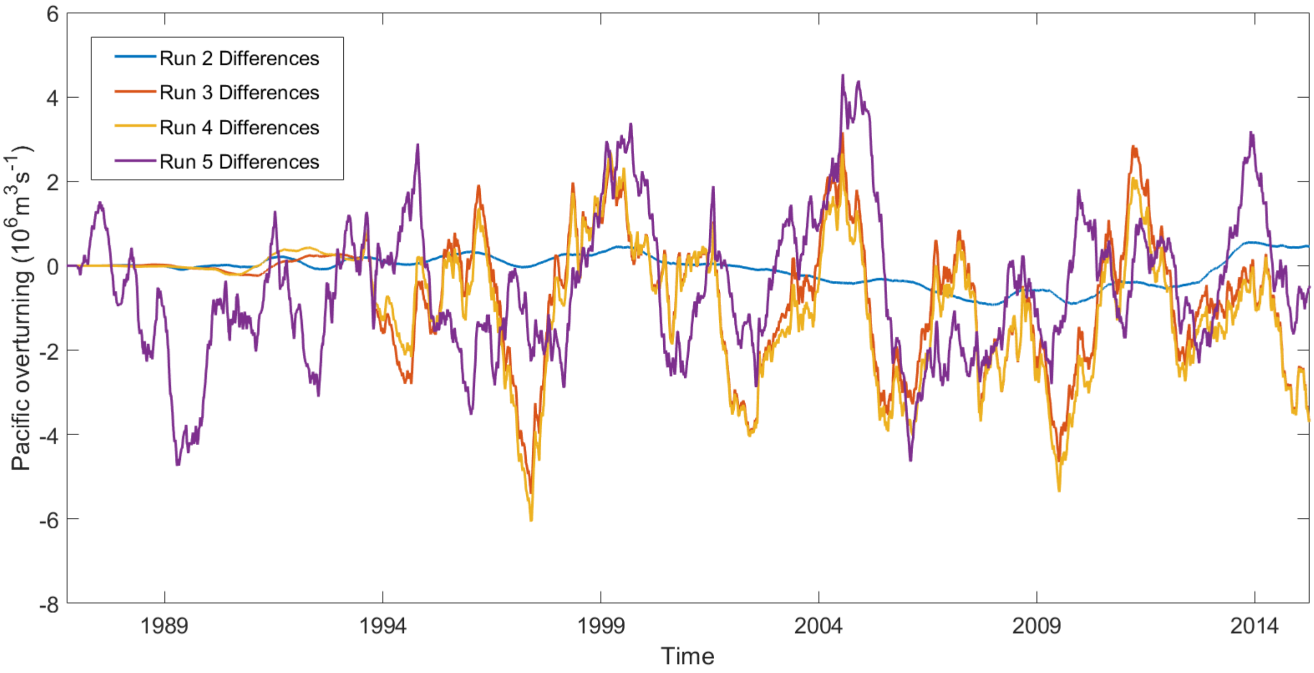

Figure 3.20 Plot of the strength of Pacific Overturning Circulation over time.

In the Drake Passage, Figure 3.21 shows flux changes over time. Here, Run 5 deviates significantly from Runs 3 and 4, remaining mainly negative as opposed to the generally positive impacts from Run 3 and Run 4. Again, Run 2 can be seen to show slight variation around zero. Run 5 represents a more realistic, and therefore variable, freshwater input than Run 3 or Run 4, which have relatively similar input patterns. Figure 3.18 showed a steady increase in Drake Passage flux over time in the control run. This is another area that will be addressed in more detail in Chapter 5 (see Section 5.2.2).

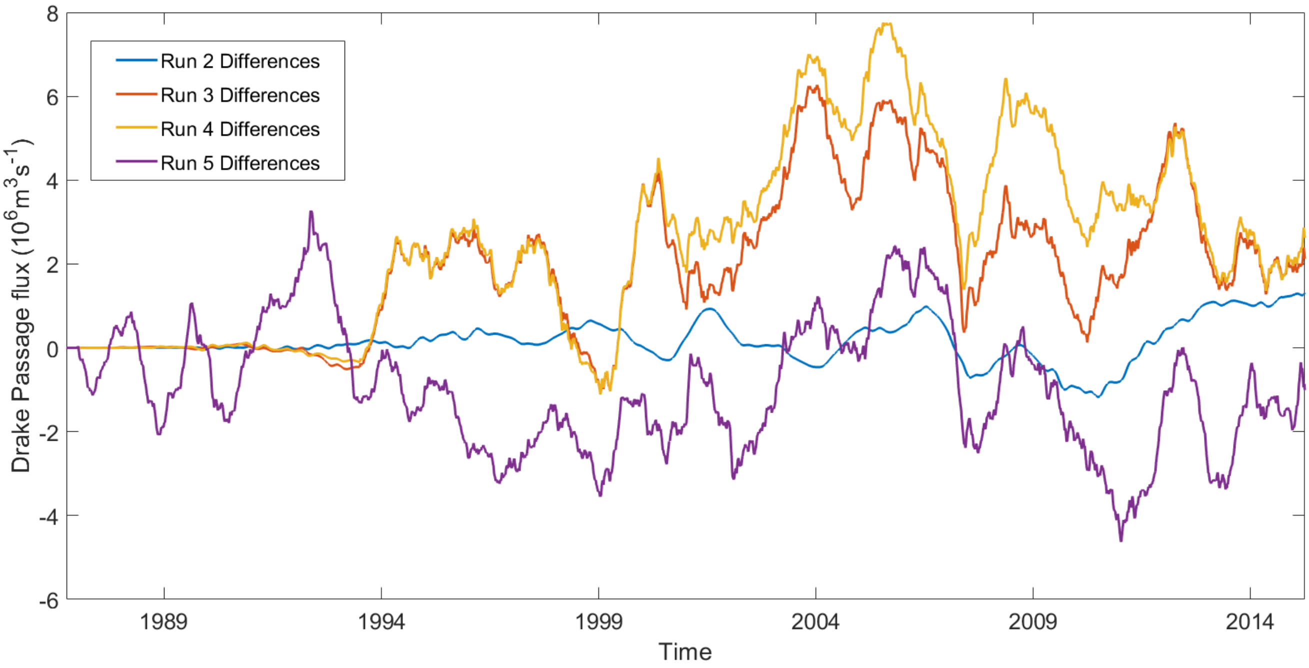

Figure 3.21 Plot of the strength of the Drake Passage flux over time.

The Indonesian Throughflow flux over time can be seen in Figure 3.22. Here, while Run 2 shows little variation, Runs 3, 4 and 5 are relatively similar for most of the time. However, towards the end of the run, Run 5 starts to show more extreme variations than the other two, while still following a similar pattern. All these three runs are negative for the majority of time. Indeed, the Indonesian Throughflow flux is reduced by 1-2 Sv in Runs 3-5, which is about 10% of the total, and is therefore significant. Overall, the plot shows that while Indonesian Throughflow flux is often heavily tied to the ENSO phase, the inputted freshwater is having an impact on this regions and generally reducing flux.

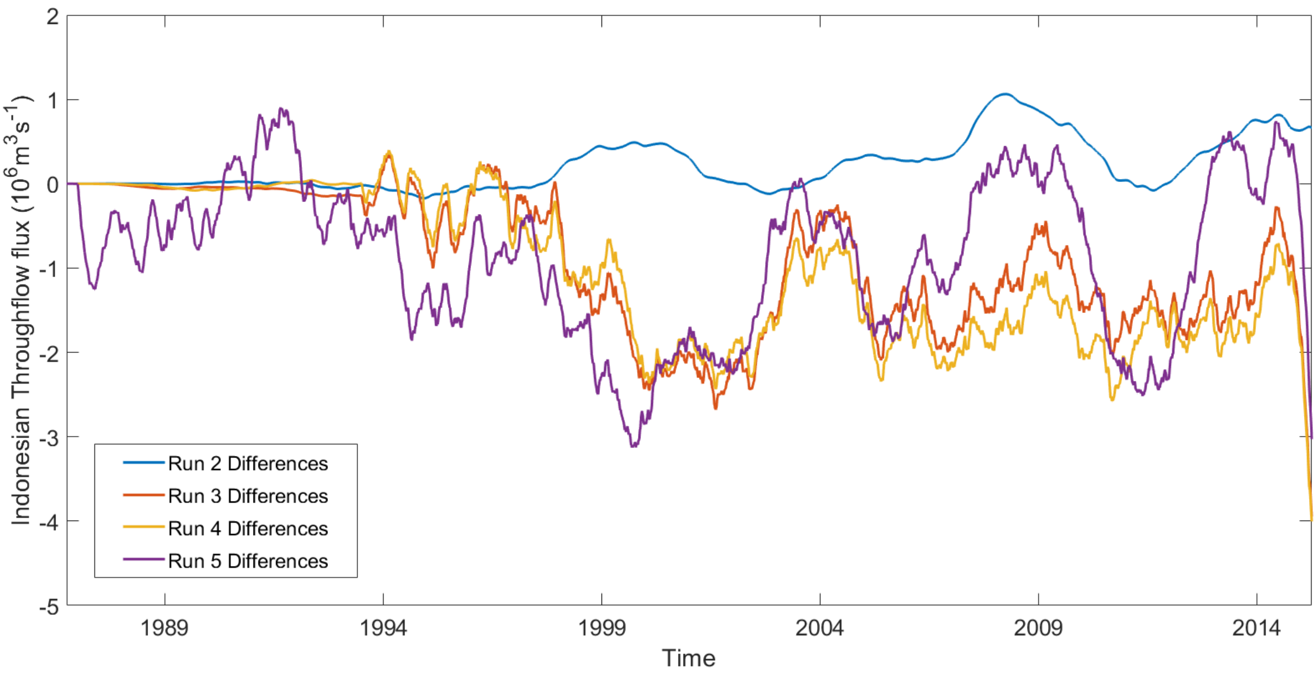

Figure 3.22 Plot of the strength of the Indonesian Throughflow flux over time.

3.3 Discussion and Conclusions

This chapter presents how four different variations of freshwater runoff input affect the world oceans, compared to the control run (Run 1). It has been shown throughout that Run 2 tends to show the least differences from Run 1, which seems sensible as additional freshwater is only inputted during the summer months. Run 3 (where runoff changes monthly) and Run 4 (where runoff varies yearly) are consistently similar. This also makes sense as they are fundamentally similar by nature - both represent an average across the time period. It is Run 5 that is theoretically the most realistic, as it varies both monthly and yearly. Therefore it is unsurprising that while Run 5 often follows a similar pattern to Runs 3 and 4, the scale of variation is usually more extreme. In the case of the Drake Passage flux, Run 5 is showing the opposite impact than Runs 3 and 4 (see Chapter 5, Section 5.2.2 for further discussion on this). Overall, from these results it seems sensible to conclude that Run 5 was the most realistic and therefore the most useful for comparison with the NEMO ocean model (see Chapter 5).

Therefore, it is interesting to consider sea surface salinity of Run 5 compared to the control run, as this is a clear indicator of freshwater. Figure 3.23 shows sea surface salinity averaged between 1995 and 2004 for the control run, while Figure 3.24 shows Run 5 sea surface salinity averaged over the same time period, but with the control run subtracted. Similarly, Figure 3.25 shows sea surface salinity averaged between 2005 and 2014 for the control run, while Figure 3.26 shows Run 5 sea surface salinity averaged over the same time period, with the control run subtracted. These plots show that while the control run has little variation between the decades, Run 5 differences from the control run are significant, with the later decade showing generally lower salinity across large parts of the world (barring the Mediterranean Sea). This seems sensible as Run 5 contains significantly more freshwater than the control run. Additionally, Figure 3.14 showed the Gibraltar Exchange flux, and suggested that Run 5 had an effect on its strength, which is then affecting mixing (and surface salinity) in the Mediterranean Sea, so this is also to be expected. Overall, these figures support that Run 5 is inputting large quantities of freshwater, and that a global impact is felt from this within two decades.

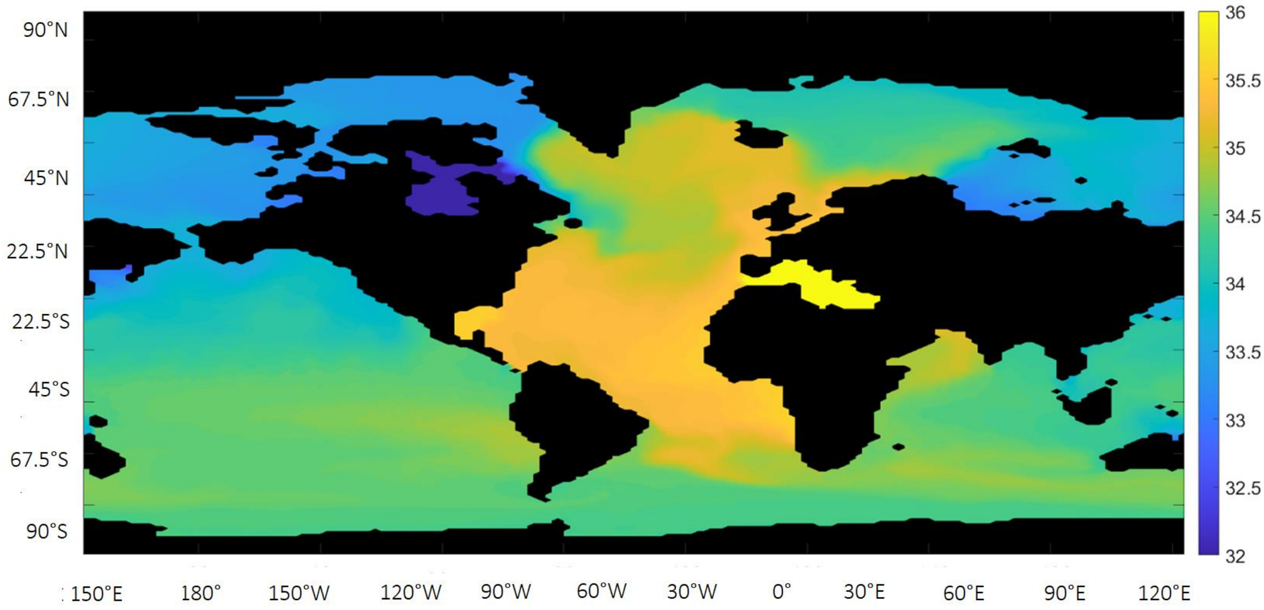

Figure 3.23 Plot of sea surface salinity averaged between 1995 and 2004 for the control run.

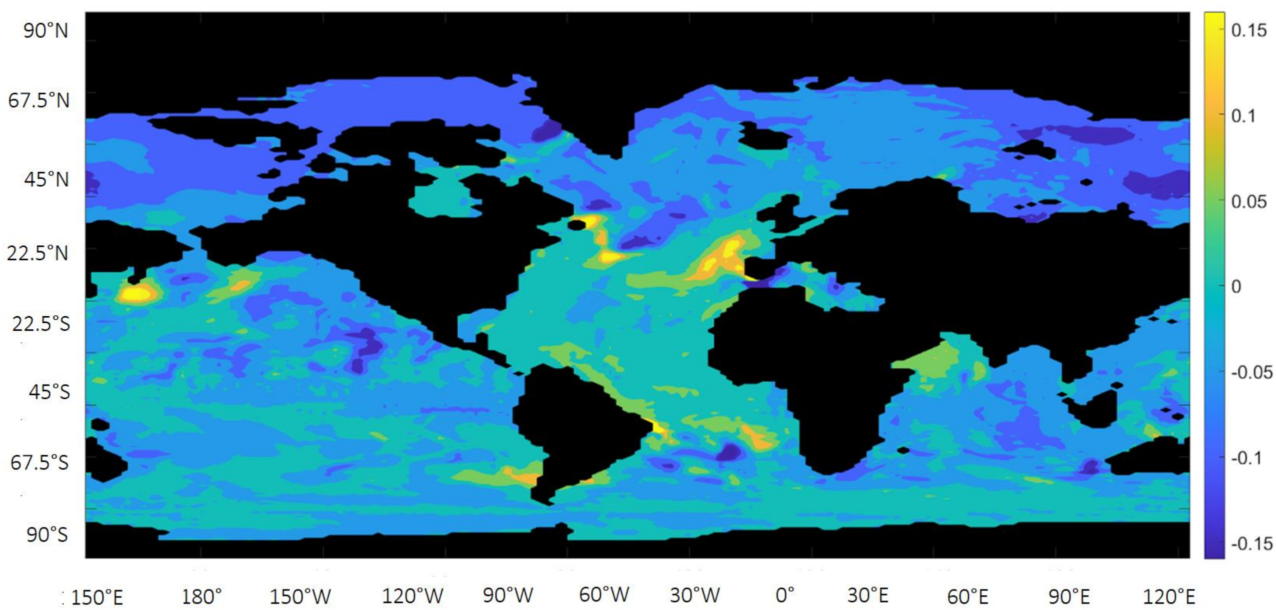

Figure 3.24 Plot of Run 5 sea surface salinity averaged between 1995 and 2004, with the control run subtracted.

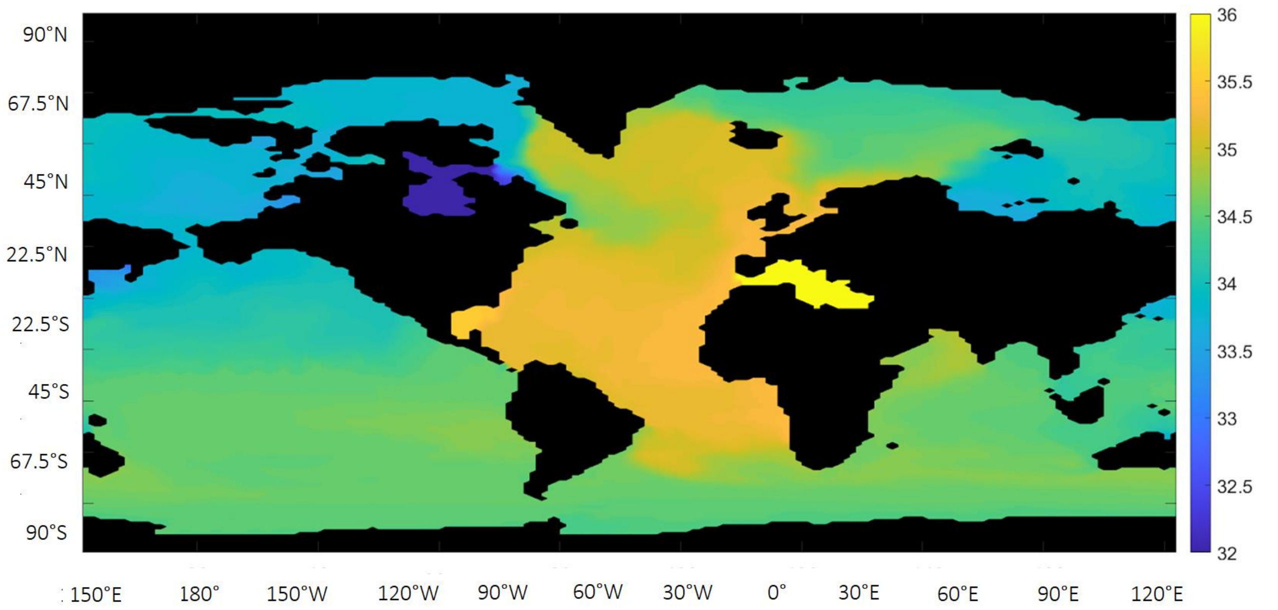

Figure 3.25 Plot of sea surface salinity averaged between 2005 and 2014 for the control run.

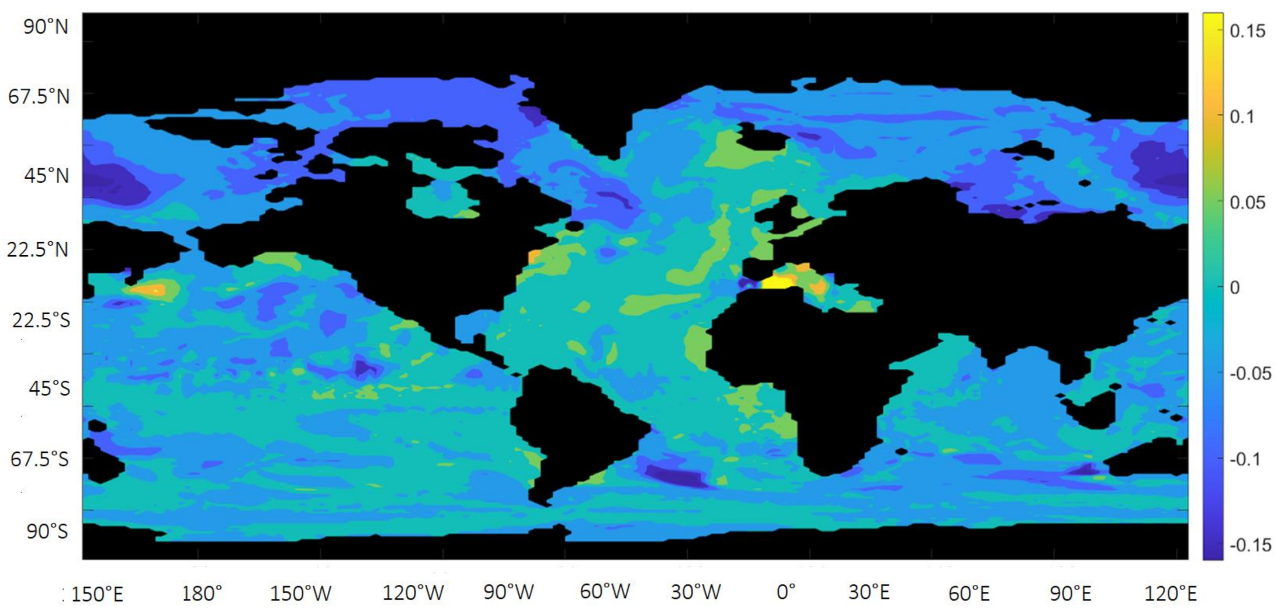

Figure 3.26 Plot of Run 5 sea surface salinity averaged between 2005 and 2014, with the control run subtracted.

Overall, the results from all the runs suggest that inputting realistic freshwater values around the Greenland coast has an impact on all major oceans and passages. Most significantly, is the observed decrease in Atlantic Overturning Circulation, however as Run 5 had increased to slightly above zero by the end of the run, it is probable that a longer time period is necessary to conclude that the additional meltwater resulted in a weakened Atlantic Overturning Circulation. Additionally, the runs suggest that the freshwater resulted in an overall decrease in Northern Hemisphere Overturning Circulation and Indonesian Throughflow flux, compared to a general increase in Bering Strait flux and Labrador Sea salt flux, and potentially in the Southern Hemisphere Overturning Circulation. Also that Run 5 is having a generally decreasing effect on global salinity, as would be expected.

4. Assessing Meltwater Impacts and Iceberg Trends to 2050 Using a High Complexity Ocean Model

4.1 Introduction

4.1.1 Model Overview

The Greenland Ice Sheet (GrIS) inputs freshwater and icebergs into the North Atlantic. This chapter aims to address how these inputs are likely to change in a high-emissions scenario by 2050, using a high complexity ocean model - the Nucleus for European Modelling of the Ocean (NEMO). While NEMO is a popular choice of ocean model, this chapter presents a first assessment of future trends in Arctic iceberg numbers using the high-resolution ORCA12-N512 run. There is also a focus on meltwater effects on major ocean currents and a discussion of whether remote sensing data can be used for iceberg detection in the North Atlantic, for comparison with NEMO outputs and observed results.

The Southampton based NEMO ocean model (see Madec et al., 2017 for in-depth documentation) is coupled with the ICB iceberg component (Marsh et al., 2015), in two runs of 1/12° global ocean resolution and 25 km atmospheric resolution, accessible through the JASMIN environment, managed by the Centre for Environmental Data Analysis (CEDA). An assessment of the advantages of the high resolution present in the ORCA12-N512 run is available in Hewitt et al. (2016). The first run is between 1950 and December 2014, the second runs into the future (to 2050) from January 2015. The future run has been forced with SSP585, a high emission scenario from the Coupled Model Intercomparison Project Phase 6 (CMIP6), with an approximate surface warming of 8.5 Wm^{-2} by 2100 (Hofer et al., 2020). Both runs include oceanic and atmospheric components (through various atmospheric general circulation models accessed via the coupling software OASIS, see Madec et al., 2017).

Therefore atmospheric pressures have an impact on the ocean and cryosphere, with the fluxes provided by the coupling software (Madec et al., 2017). The NEMO model has previously been used by the Met Office and the ECMWF as an ocean component of a climate model (Consortium, 2021). This, and the multitude of publications using this model (see Sadighrad et al.; Momin et al.; Yool et al.; etc. in 2021), promote the advantages of using ORCA12-N512 output data.

In the model, the ocean is assumed to be a fluid represented by equations including the Navier-Stokes equations and a non-linear equations of state, coupling temperature and salinity to the fluid velocity (Madec et al., 2017). Several additional assumptions are also made: the spherical earth approximation, the thin-shell approximation, the turbulent closure hypothesis, the Boussinesq hypothesis, the Hydrostatic hypothesis and the Incompressibility hypothesis (see NEMO *ocean engine*, NEMO System Team for more information on these). The surface freshwater budget has an atmosphere component (evaporation minus precipitation) and a cryosphere component (freezing minus melting of ice), and these affect the ocean through changing the volume (and so sea surface height) and surface temperature and salinity (Madec et al., 2017). Sea surface height (η_{ib}) is also affected by atmospheric pressure, defined in equation (3):

$$\eta_{ib} = -\frac{1}{g\,\rho_o}\left(P_{atm} - P_o\right) \tag{3}$$

Where P_{atm} is the atmospheric pressure, P_o is a reference atmospheric pressure defined as 101000 N/m^2 and g and ρ_o are the usual values (gravity and density of water respectively), see (Madec et al., 2017).

Concerning boundary conditions, where the land and ocean interact the major flux is freshwater input/output, primarily through river runoff; where the solid earth and ocean meet, there is no transport of heat or salt across the boundary and no momentum; when considering ocean-air interaction, the freshwater budget is maintained by considering precipitation - evaporation, horizontal momentum is also exchanged, while surface tension is not included; at the sea ice - ocean interaction, heat, salt, freshwater and momentum are exchanged (Madec et al., 2017).

Icebergs are treated as Lagrangian particles, with the equations defining their movement available in Martin & Adcroft (2010). In ORCA12-N512 simulations, the ICB module is extended to coupling via heat fluxes, whereby the ocean provides the latent heat needed to melt icebergs, amounting to a local cooling effect on the ocean. Icebergs are affected by atmospheric winds, and ocean currents and waves, and are reduced by bottom melt and erosion (Madec et al., 2017). The model assumes that icebergs are at a 45 degree angle to the wind (to the left in the Northern Hemisphere and to the right in the Southern Hemisphere) see Bigg et al. (1997). This is clearly not always the case in reality (Marsh et al., 2015). Another limitation of the model is that in real life much of the iceberg is submerged in the water, however here the iceberg is assumed to float at the surface due to the difficulties of coding this realistically (Marsh et al., 2015). Therefore, as the icebergs melt the freshwater is released only at the surface, and this additional mass is able to affect the free surface height (Marsh et al., 2015). Icebergs are calved constantly throughout time, at realistic input locations around both the Northern and Southern Hemisphere (as outlined in Levine and Bigg, 2008). The mean calving rate in the Antarctic is 1140 Gt/year, and 188 Gt/year in the Arctic; giant icebergs are under represented by the model but this is not a large consideration in the Northern Hemisphere as giant icebergs tend to be found around Antarctica (Marsh et al., 2015). The calving rates are based on calculations from around 2000, so are low in comparison to current observations; iceberg calving accounts for approximately half of the total freshwater flux into the North Atlantic from the GrIS, with runoff making up the rest (Marsh et al., 2015). An iceberg mask is applied where snow over the continents is converted to iceberg calving (personal communication with Bablu Sinha, NOC). Ice sheet melt and runoff are dependent on temperature and salinity values, and are each expressed as a volume flux (NEMO *ocean engine*, NEMO System Team).

This chapter will examine the model outputs from both of the ocean-iceberg runs. The variables considered are restricted to FICEBERG (the freshwater from melting icebergs) and SOS (sea surface salinity) for the Newfoundland region analysis. These have been selected as they are the clearest available ways of showing iceberg presence. Section 4.3 considers long-term trends in the world oceans, using sea surface salinity and sea surface temperature (TOS) to identify regions of interest for closer analysis. This chapter will also consider whether satellite data would be useful for iceberg detection in this setting, using the Aquarius (see https://aquarius.oceansciences.org/cgi/data.htm) and SMAP (see https://smap.jpl.nasa.gov/data/#:~:text=The%20SMAP%20science%20data%20products,Theoretical%20Basis%20Documents%20(ATBDs)) sources. Throughout, there is a focus on May averages as this is historically the peak iceberg month off Newfoundland, in order to be comparable to other models in this thesis (see Chapter 2, Section 2.2.2.1).

The format of the chapter is as follows. Section 4.2 will address global SOS and TOS patterns. Section 4.3 looks at Arctic regions in more depth, including an assessment of how well the SOS and FICEBERG reflect yearly iceberg severity (in terms of a high or low yearly number of icebergs). Satellite data will be used in section 4.4 to examine whether Arctic icebergs are detectable in the Labrador Sea. The chapter ends with a conclusion and discussion section. Further work comparing this model's outputs to FRUGAL (from Chapter 3) is available in Chapter 5.

4.1.2 NEMO Greenland Ice Sheet mass loss

In this high-emission run of NEMO, it is important to first assess how the Greenland Ice Sheet (GrIS) freshwater runoff and iceberg calving is changing in the model over the time period. The NEMO variables selected to best reflect these are FRIVER (the water flux into sea from rivers in kg/m²/day) and FICEBERG (the water flux into sea from icebergs, also in kg/m²/day). Here, freshwater input from rivers, icebergs and ice shelf melt is vertically distributed over depth, and the net amount of water inputted into the ocean is calculated by precipitation (including sea-ice formation and melt and iceberg calving in the Northern Hemisphere) minus evaporation, plus river runoff (FRIVER), plus iceberg melt (FICEBERG), plus ice shelf melt (Silvy et al., 2022).

Figures 4.1 and 4.2 show these monthly variables, averaged over the Greenland margin. FRIVER shows a steady increase over the time period (but still with large seasonal variability), while FICEBERG is dominated by seasonality. The rise in 2050 could be part of a multi-year trend that is repeated with similar spikes in 2037 and 2041, rather than a potential decadal pattern. For this reason, Figures 4.3 and 4.4 show the two variables with a 12-month running mean. FICEBERG can now be seen to be steady until the early 2010s, before decreasing over time. Additionally, a semi-decadal fluctuation can be detected in this overall trend. FRIVER still shows a steady increase except for a sharp rise around 2050. When the linear trend line is calculated, FRIVER (excluding the running mean) has the equation y = 0.0822x + 20.539 (not statistically significant at the 5% level), while for FICEBERG the equation is y = -0.0011x + 3.2144 (again, excluding the 12-month running mean and not statistically significant at the 5% level). These further show that FRIVER is increasing over time, while FICEBERG is decreasing. This is likely due to the high-emission scenario resulting in accelerated melt by 2050. Overall these plots show that in this model run, freshwater runoff from the GrIS is increasing by 2050, while iceberg calving is decreasing.

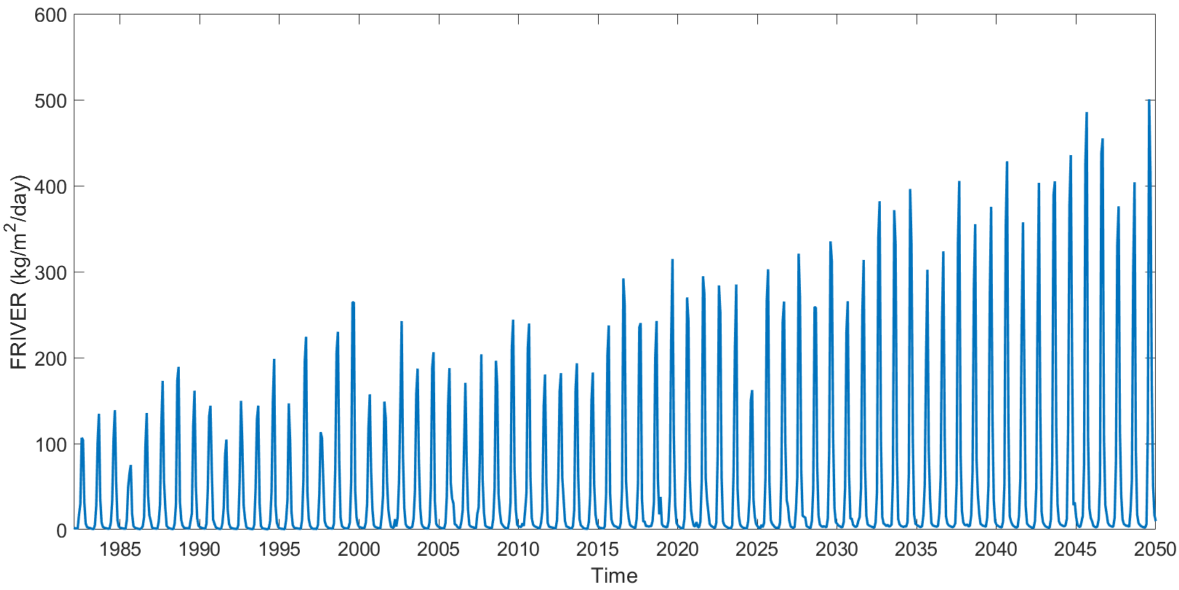

Figure 4.1 Plot of FRIVER monthly values, averaged over the Greenland margin.

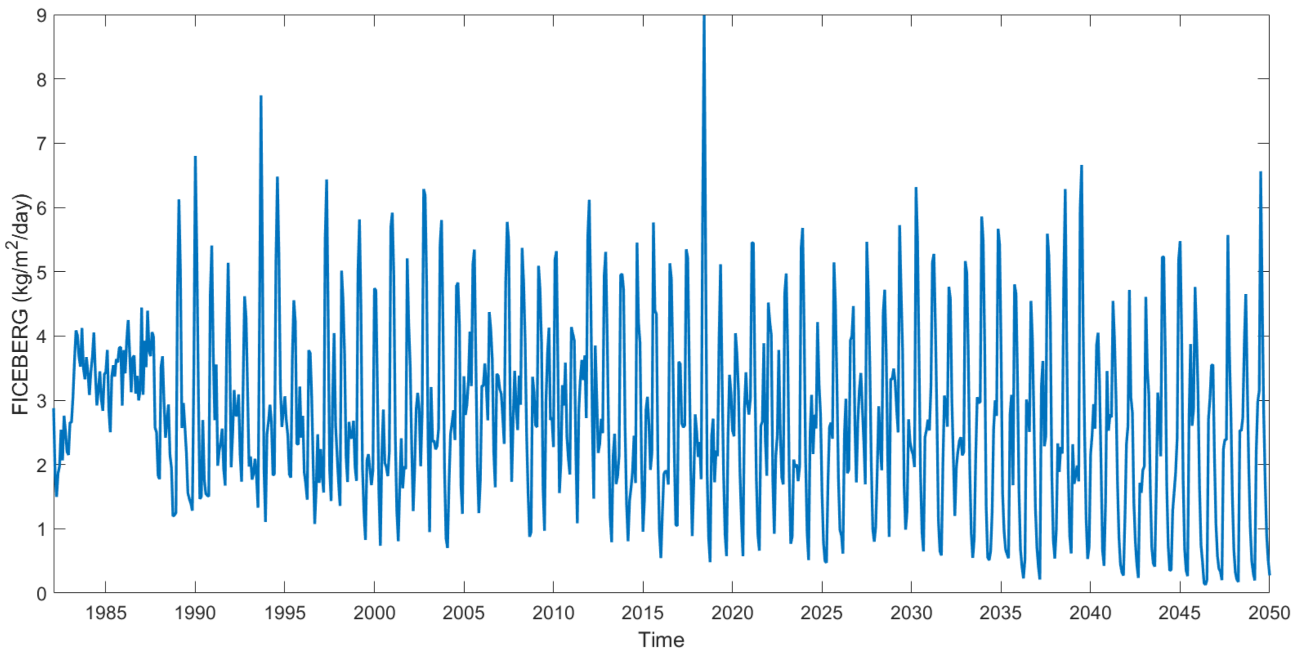

Figure 4.2 Plot of FICEBERG monthly values, averaged over the Greenland margin.

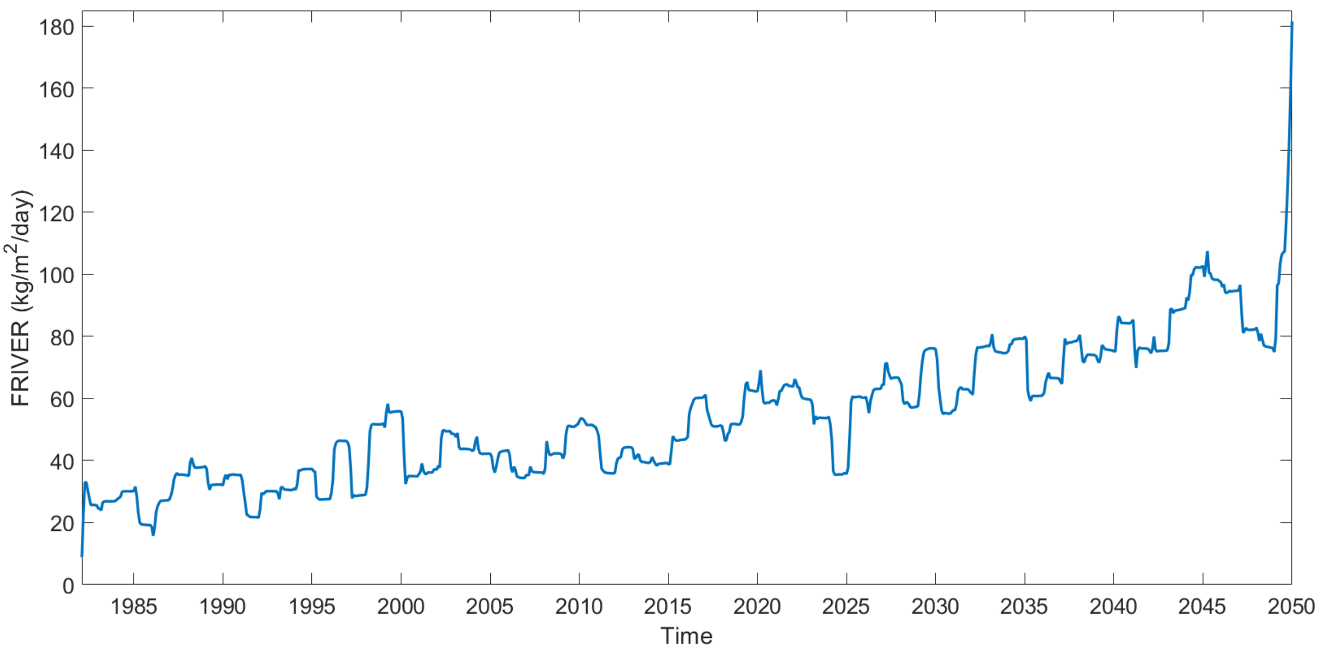

Figure 4.3 Plot of FRIVER monthly values, averaged over the Greenland margin with a 12-month moving average.

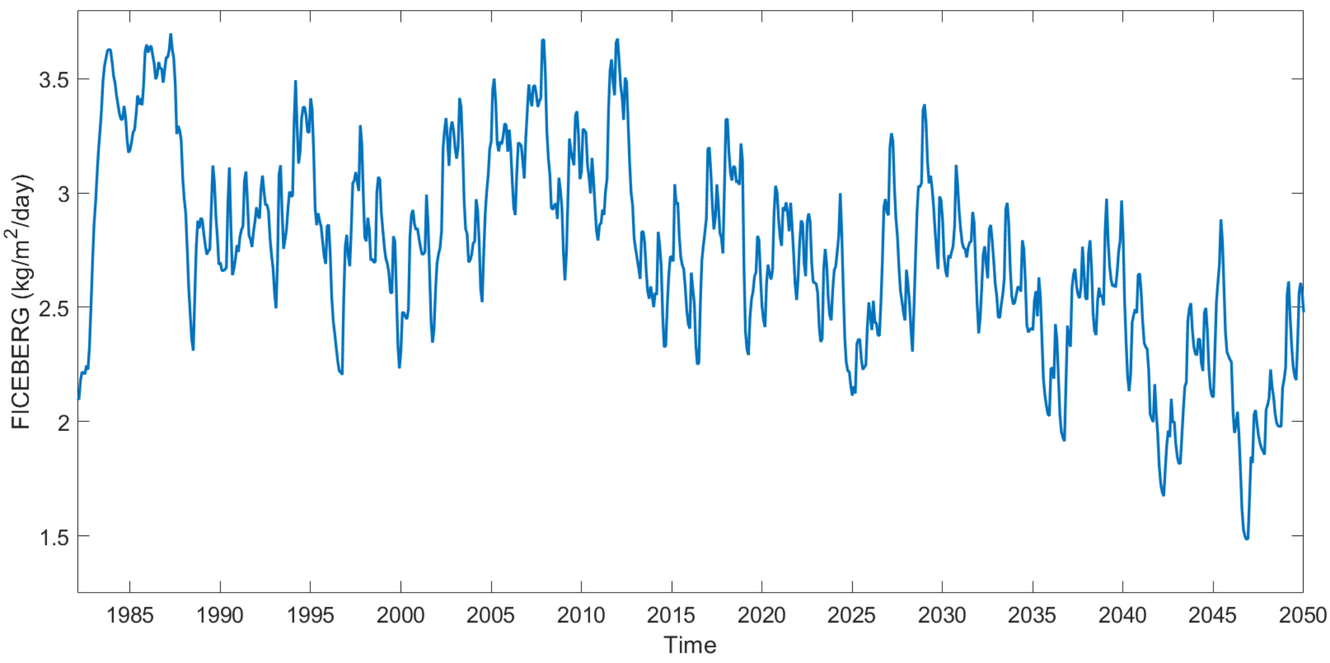

Figure 4.4 Plot of FICEBERG monthly values, averaged over the Greenland margin with a 12-month moving average.

4.2 Global Results

4.2.1 Sea Surface Salinity

The mean May SOS for the time-period 1985-95 can be seen in Figure 4.5. Later figures in this section (4.6-10) show the decadal changes in SOS compared to this initial run. Only May averages have been presented in order to be comparable to earlier sections, and to relate changes in the North Atlantic to I48N. The Arctic region around the Laptev and East Siberian Seas shows significant change in every decade, which in some sections is increased SOS. Interestingly, the Greenland region only slows slight freshening over the entire time-period. Overall, these plots show sustained slight freshening in most areas of the globe, while some Arctic regions and other large river outlets (the Amazon, the Congo etc.), show more dramatic changes. As the focus of this thesis is on changes resulting from a melting GrIS, the Arctic regions will be analysed in greater depth in Section 4.3.2.

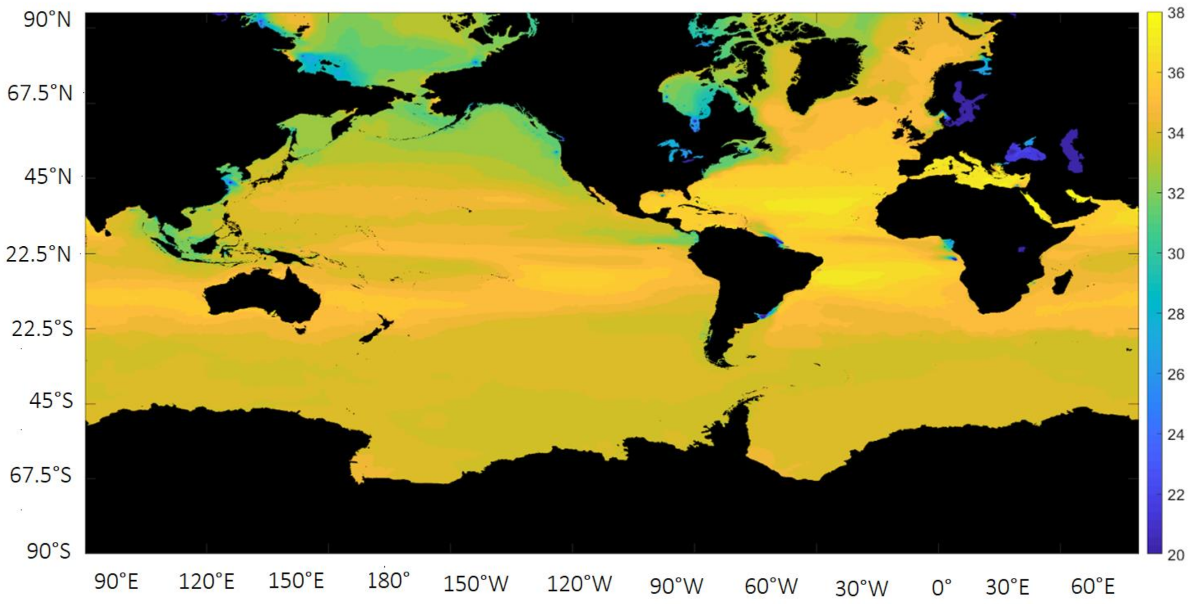

Figure 4.5 Mean May sea surface salinity (‰) between 1985 and 1995.

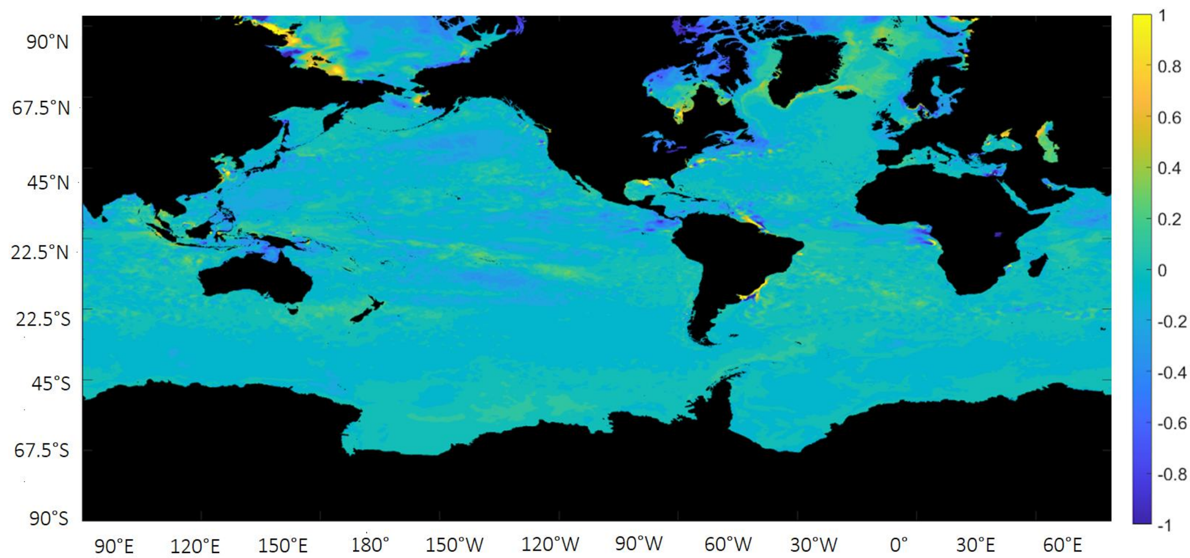

Figure 4.6 Decadal average for May sea surface salinity 1995-2005 minus 1985-95 (‰).

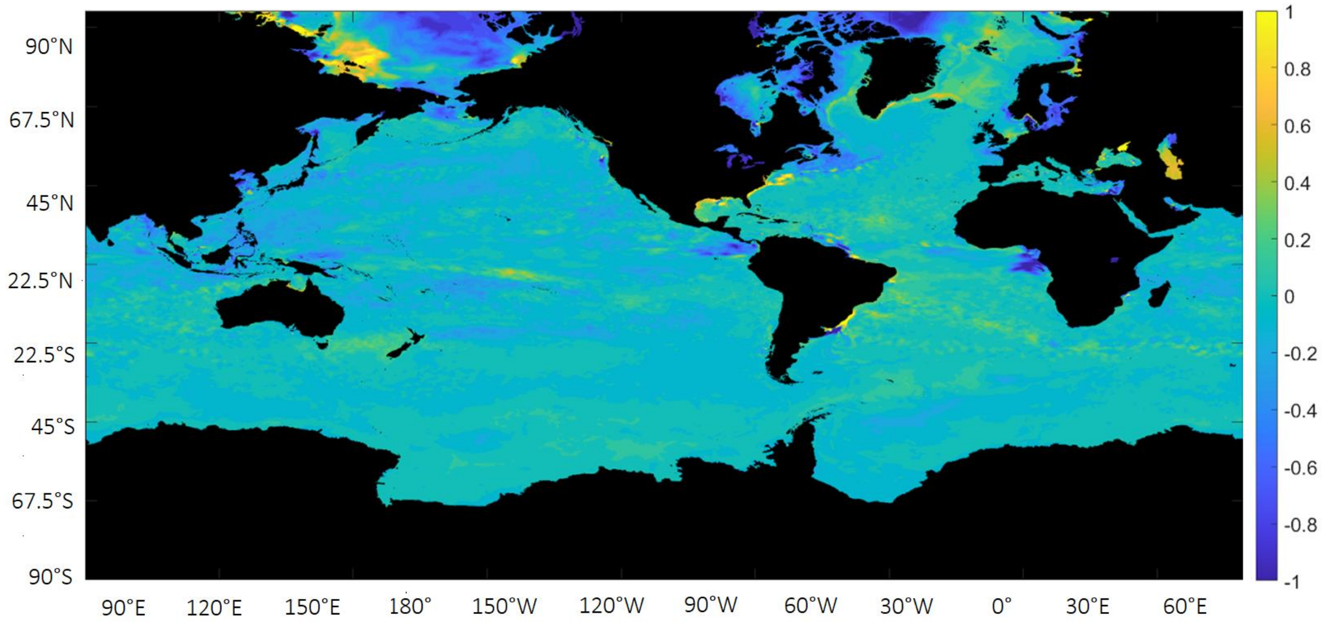

Figure 4.7 Decadal average for May sea surface salinity 2005-2015 minus 1985-95 (‰).

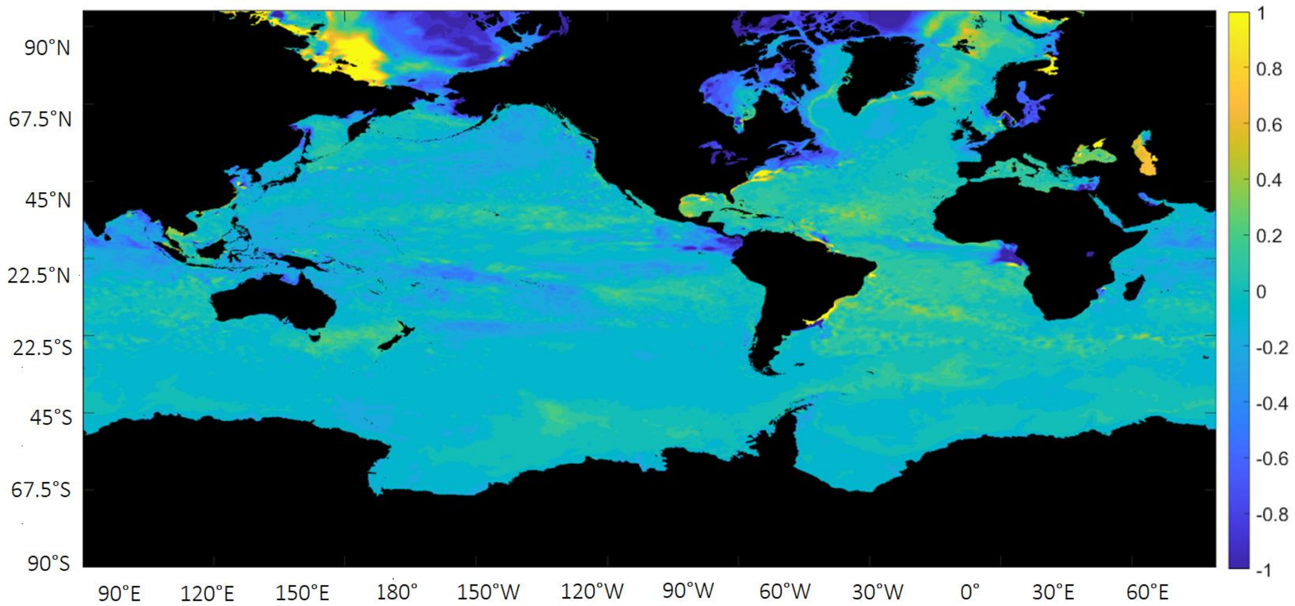

Figure 4.8 Decadal average for May sea surface salinity 2015-2025 minus 1985-95 (‰).

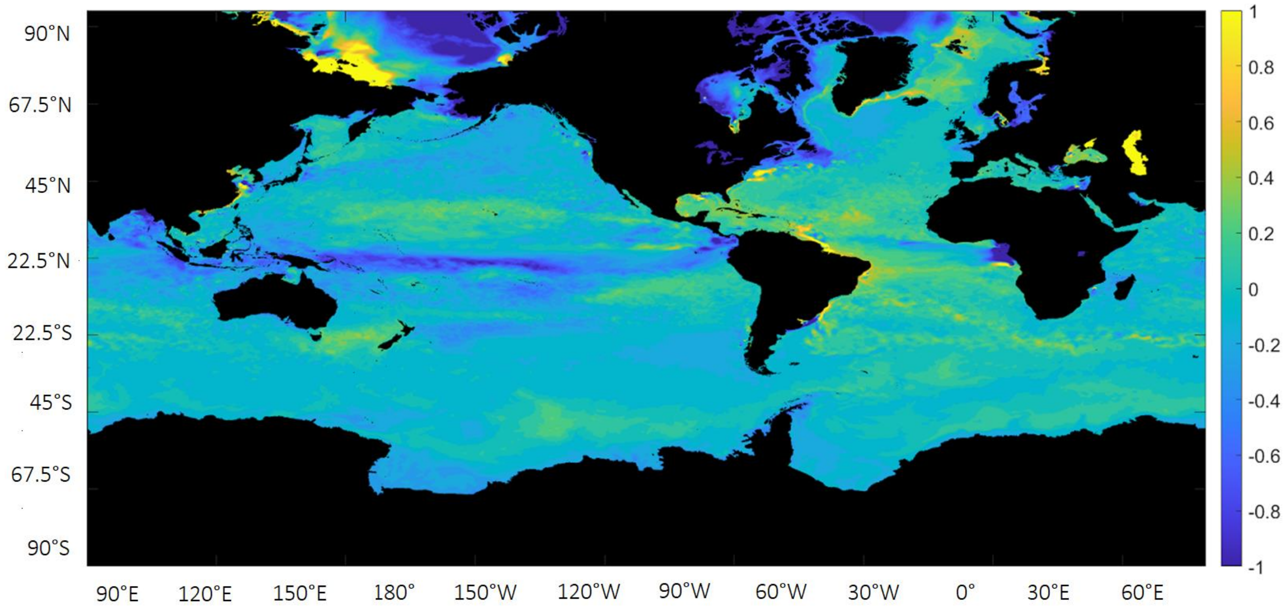

Figure 4.9 Decadal average for May sea surface salinity 2025-2035 minus 1985-95 (‰).

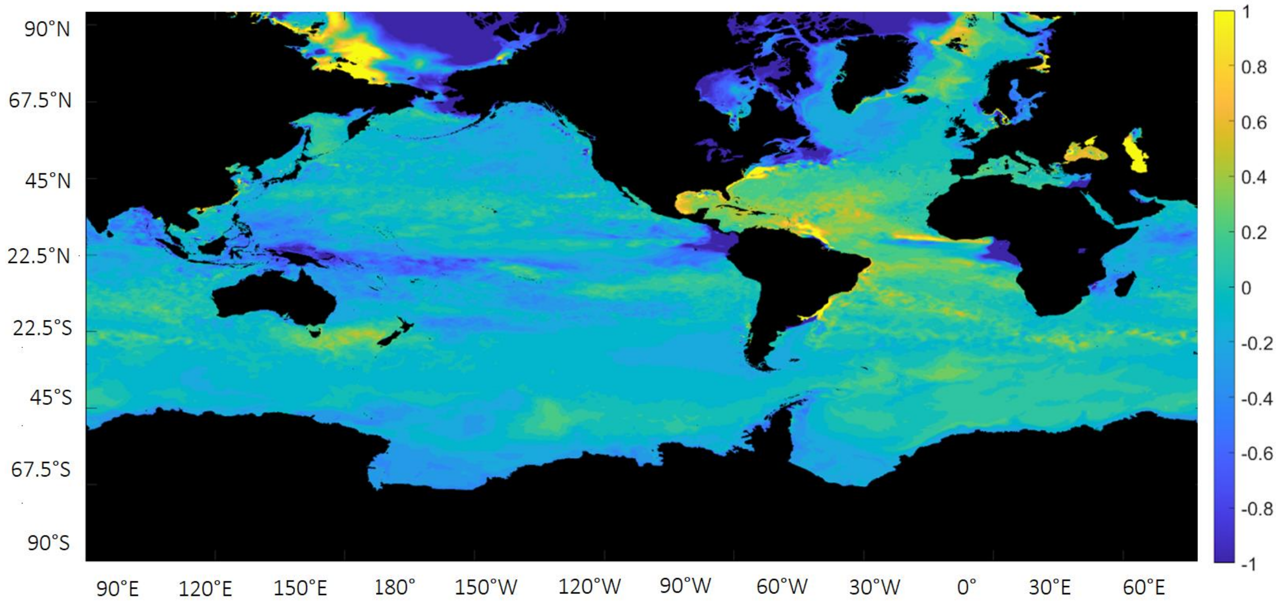

Figure 4.10 Decadal average for May sea surface salinity 2035-2045 minus 1985-95 (‰).

4.2.2 Sea Surface Temperature

The mean May TOS for the time-period 1985-95 can be seen in Figure 4.11. The following figures (4.12-16) show the decadal changes in TOS with this initial period subtracted. The May averages have been considered for the same reasons as previously stated. These figures show a steady increase in TOS for the vast majority of global regions, which is unsurprising in the high-emission scenario used. The notable exception is the mid-North Atlantic, directly south of Greenland, where a cooling effect is seen by the decade 2035-45, compared to the 1985-95 period. This area, along with Arctic regions identified in the previous section, will be directly addressed in the following section (4.3).

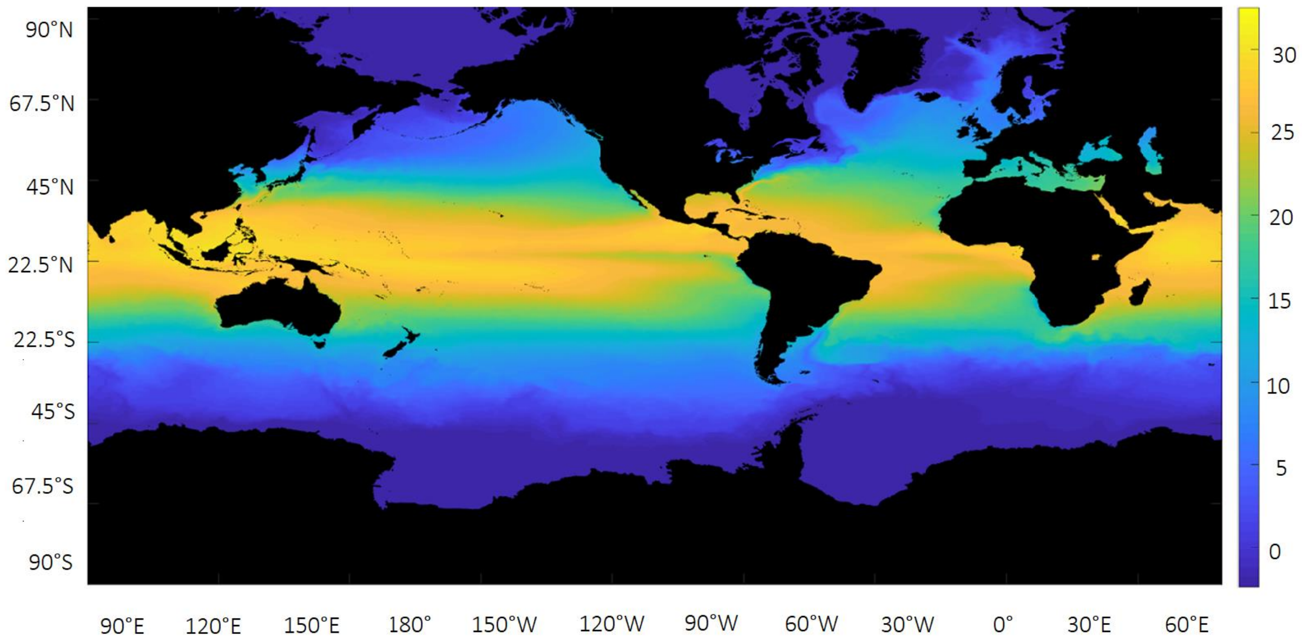

Figure 4.11 Mean May sea surface temperature (°C) between 1985 and 1995.

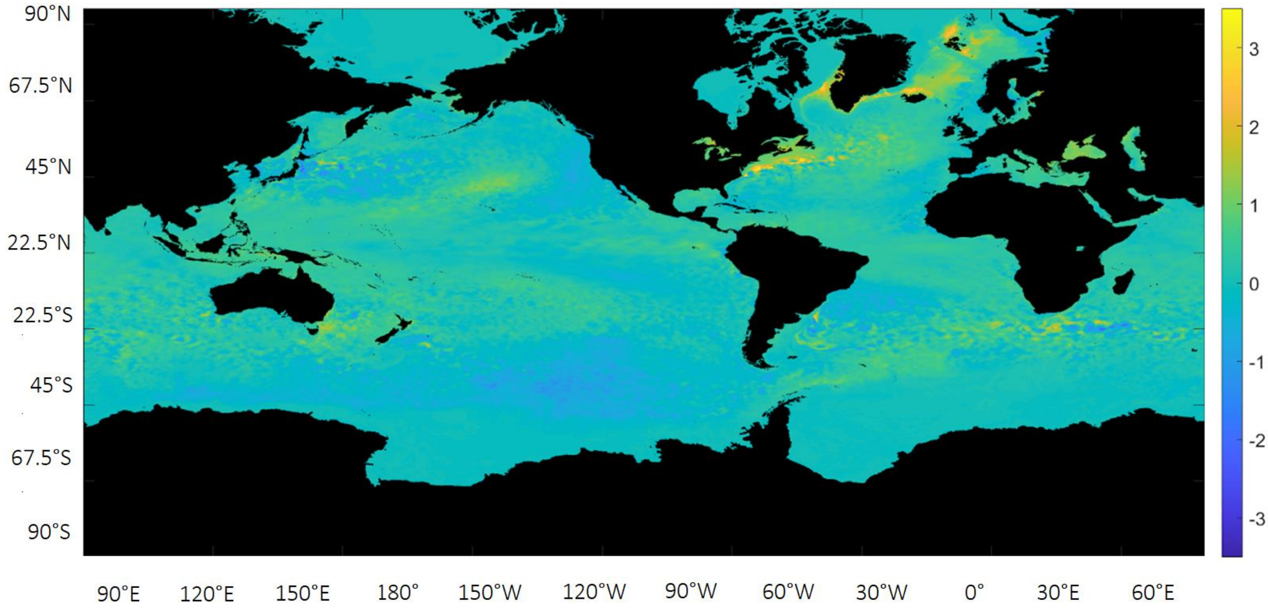

Figure 4.12 Decadal average for May sea surface temperature 1995-2005 minus 1985-95 (°C).

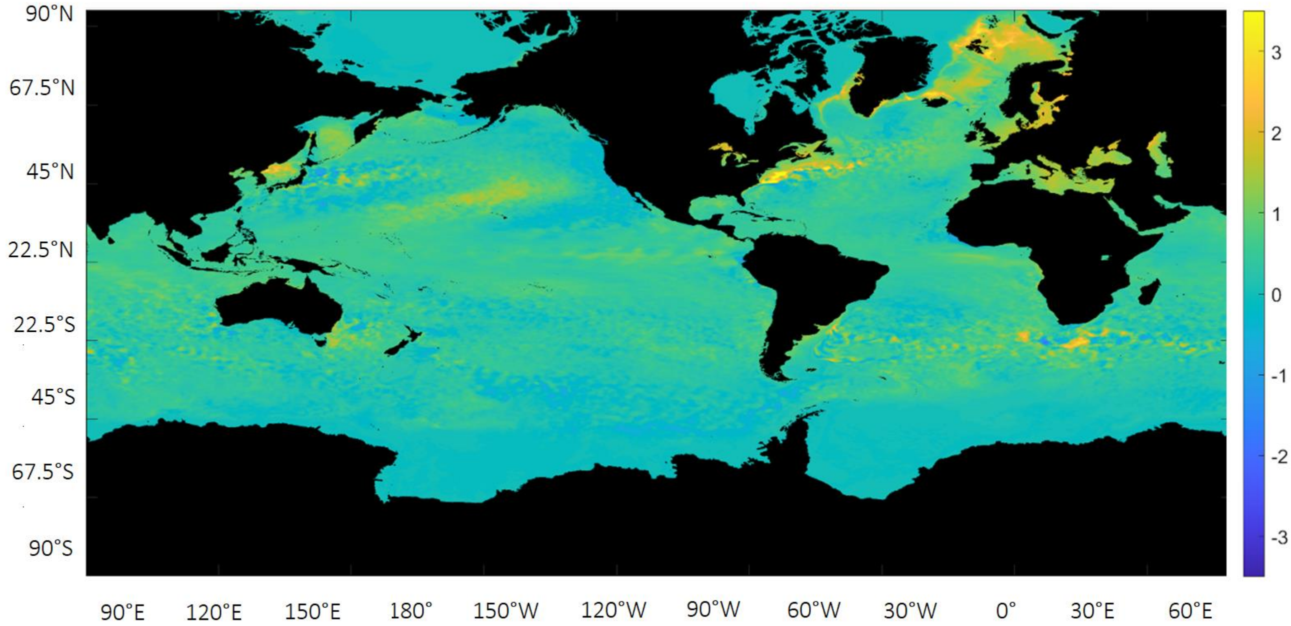

Figure 4.13 Decadal average for May sea surface temperature 2005-2015 minus 1985-95 (°C).

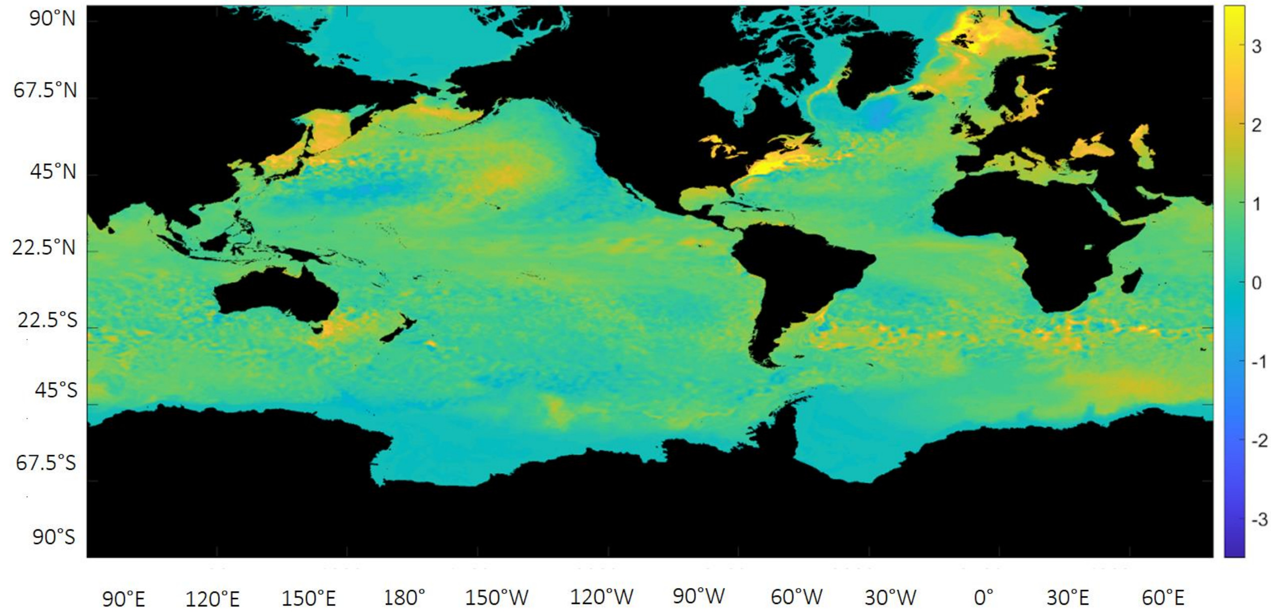

Figure 4.14 Decadal average for May sea surface temperature 2015-2025 minus 1985-95 (°C).

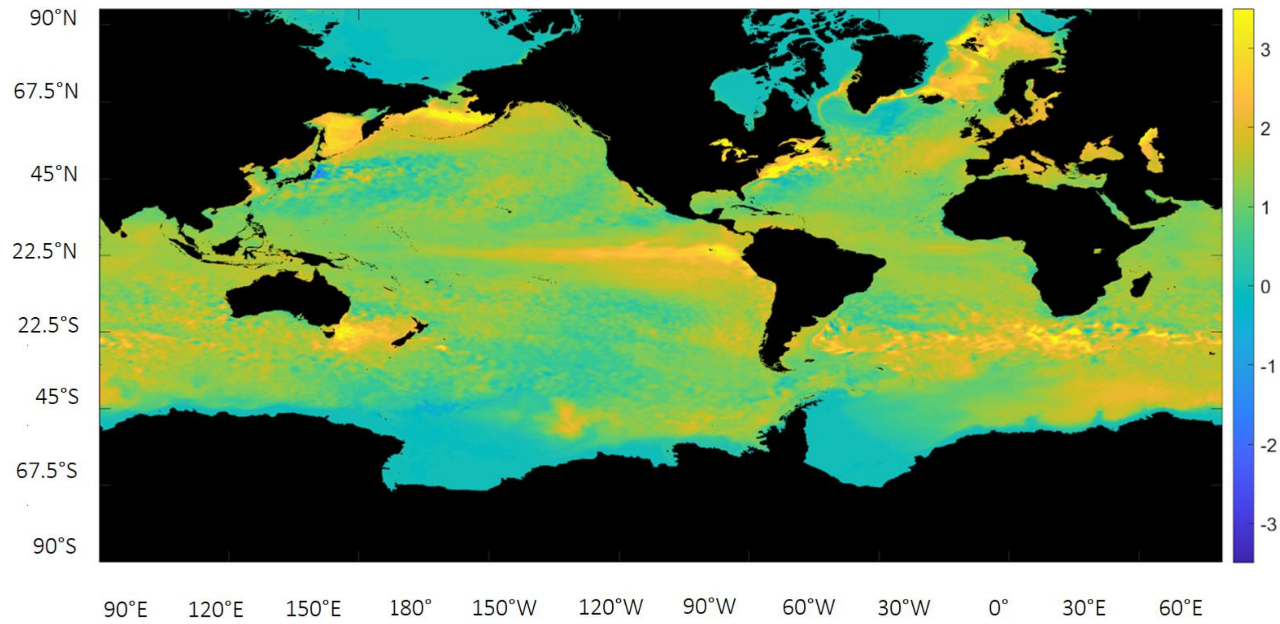

Figure 4.15 Decadal average for May sea surface temperature 2025-2035 minus 1985-95 (°C).

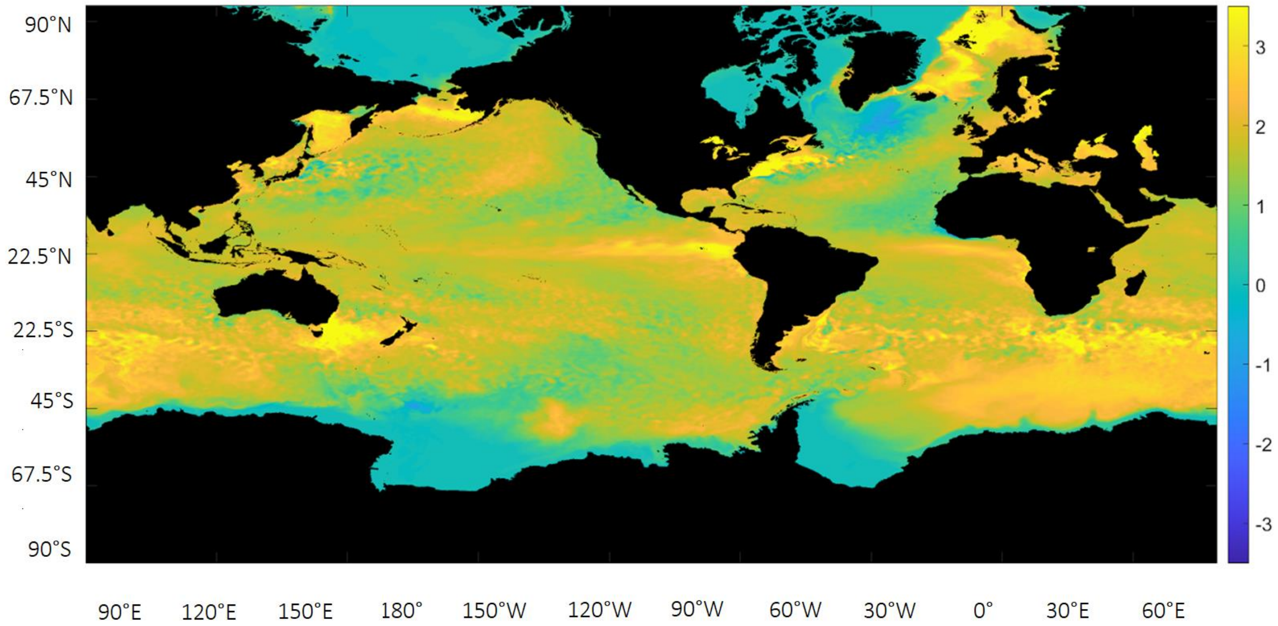

Figure 4.16 Decadal average for May sea surface temperature 2035-2045 minus 1985-95 (°C).

4.3 Arctic Regions

Regions of the Arctic identified in Section 4.2 to have shown significant changes have been marked on Figure 4.17, as Area 1, 2 and 3. Area 1 comprises the area from the Bering Strait to the Kara Sea. Area 2 covers the Barents Sea and Svalbard. Area 3 includes Iceland, Greenland and the East Canadian coast, to Newfoundland.

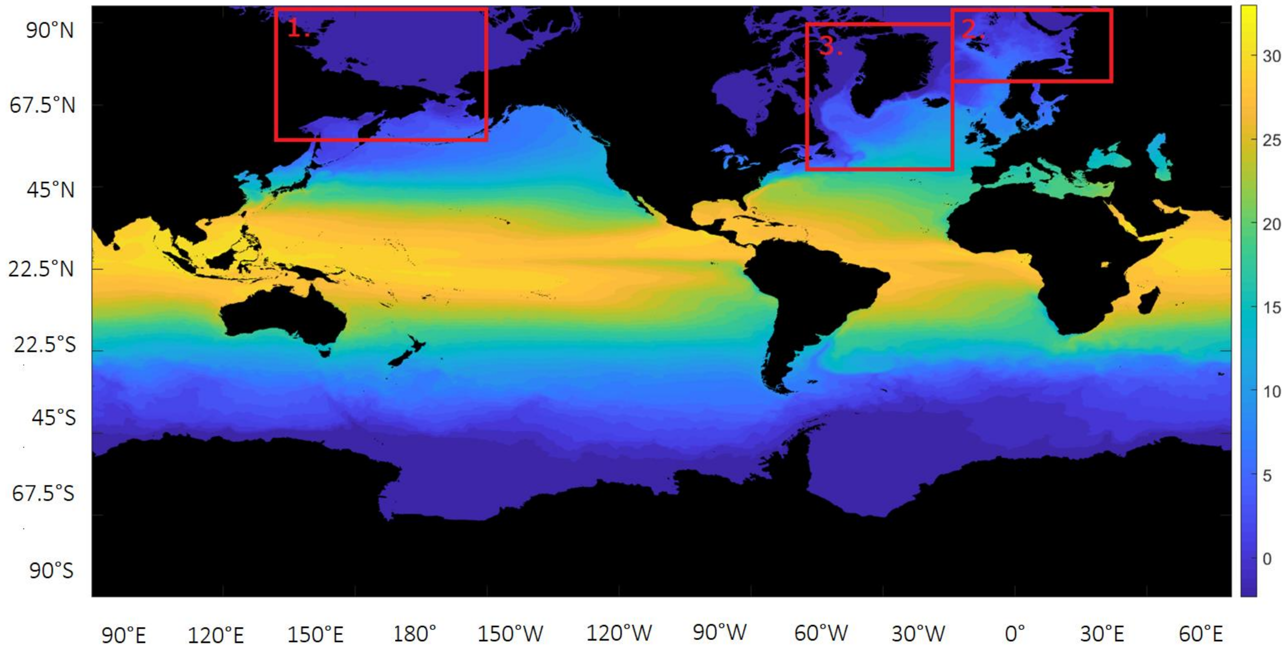

Figure 4.17 Plot showing the approximate regions detailed in section 4.3. The background plot is the average sea surface temperature for May 2015-2025.

4.3.1 Area 1 - Bering Strait to the Kara Sea

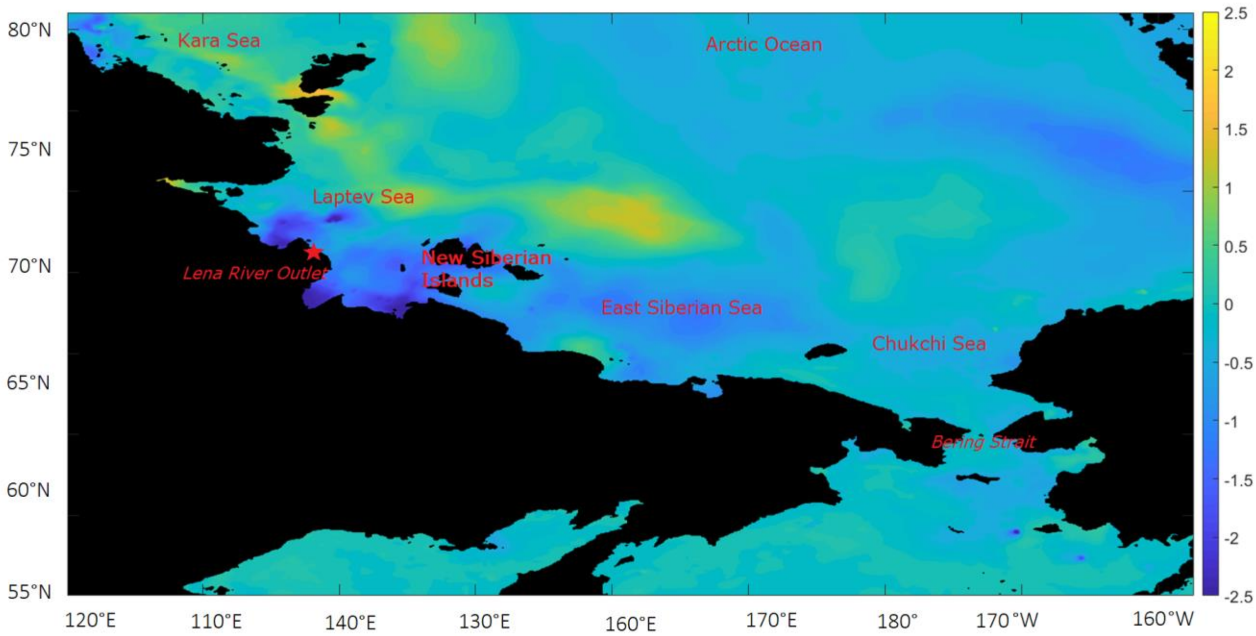

Figure 4.18 Plot of Area 1, with important locations marked in red. The background is May SOS difference between anomalies plot, averaged over the decades 2025-2035 and 2035-2045.

In Area 1, the most significant changes observed were in SOS patterns, especially between the New Siberian Islands and where the Lena River enters the Laptev Sea. Therefore, this small region has been averaged (for May only) for each decade in Figure 4.19. Note this is only the southern sector of the Laptev Sea. It can be seen from this figure that TOS shows an overall increase, excepting the 2025-35 decrease, coinciding with the peak SOS. The Laptev Sea stratification is dominated by input from the Lena River and sea ice retreat has left this susceptible to wind-driven mixing, resulting in increased SOS patterns (Janout et al., 2020). The sharp decrease in SOS after 2025-35 is potentially due to the high-emissions scenario melting the GrIS and adding freshwater to the surrounding area. It may also be a result of sea ice melting earlier in the year, as this figure focuses on May values. To address this, Figure 4.20 shows the average sea ice area fraction for May, in the same area as Figure 4.19. While a slight decreasing trend can be observed, the most significant detail is the increased variability in sea ice cover over the time-period. As the lowest trough occurs in 2043, it is likely this is swaying the decadal trend in Figure 4.19, as sea ice values in the 2025-35 decade were relatively stable compared to the previous two decades. Therefore, the 2025-35 decade, previously identified to have peak SOS and minimum TOS values, is likely a result of a combination of relatively high/stable sea ice cover and other external factors (as sea ice cover values are on a comparable scale to the 1985-95 and 1995-05 sea ice values). This is therefore brought back to the high-emissions scenario, and the increased melt of large ice masses.

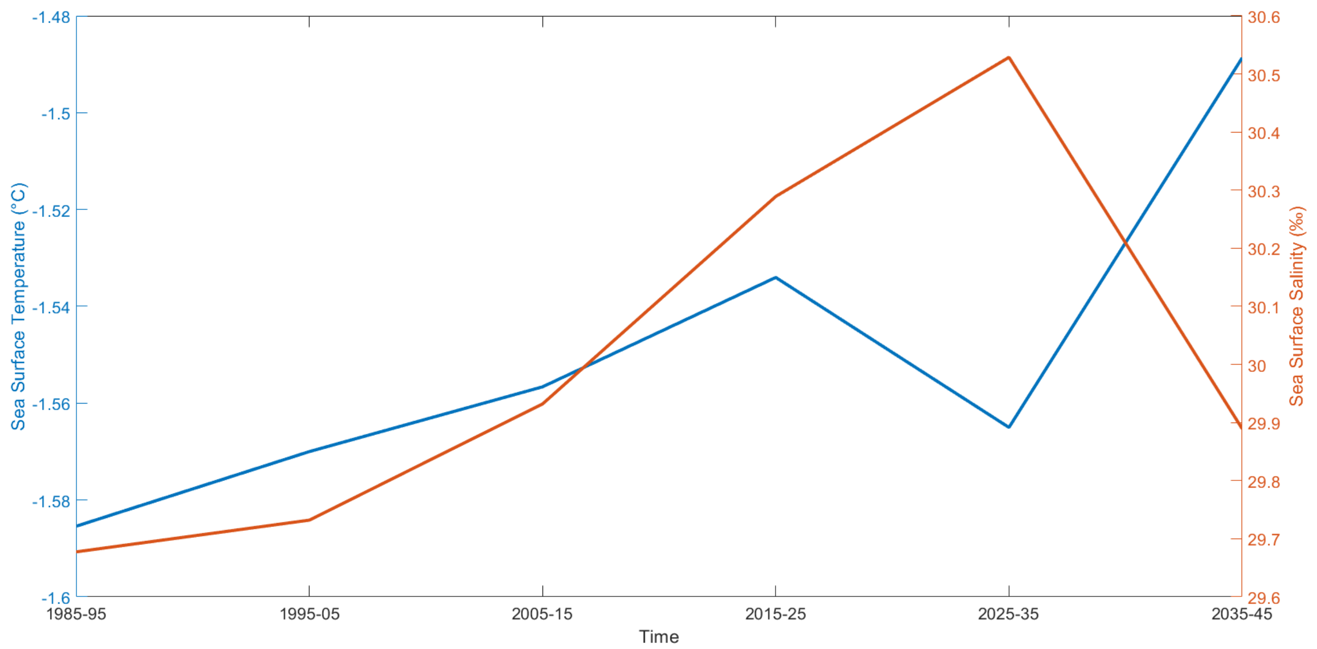

Figure 4.19 South Laptev Sea section of Area 1, May decadal averages for SOS and TOS.

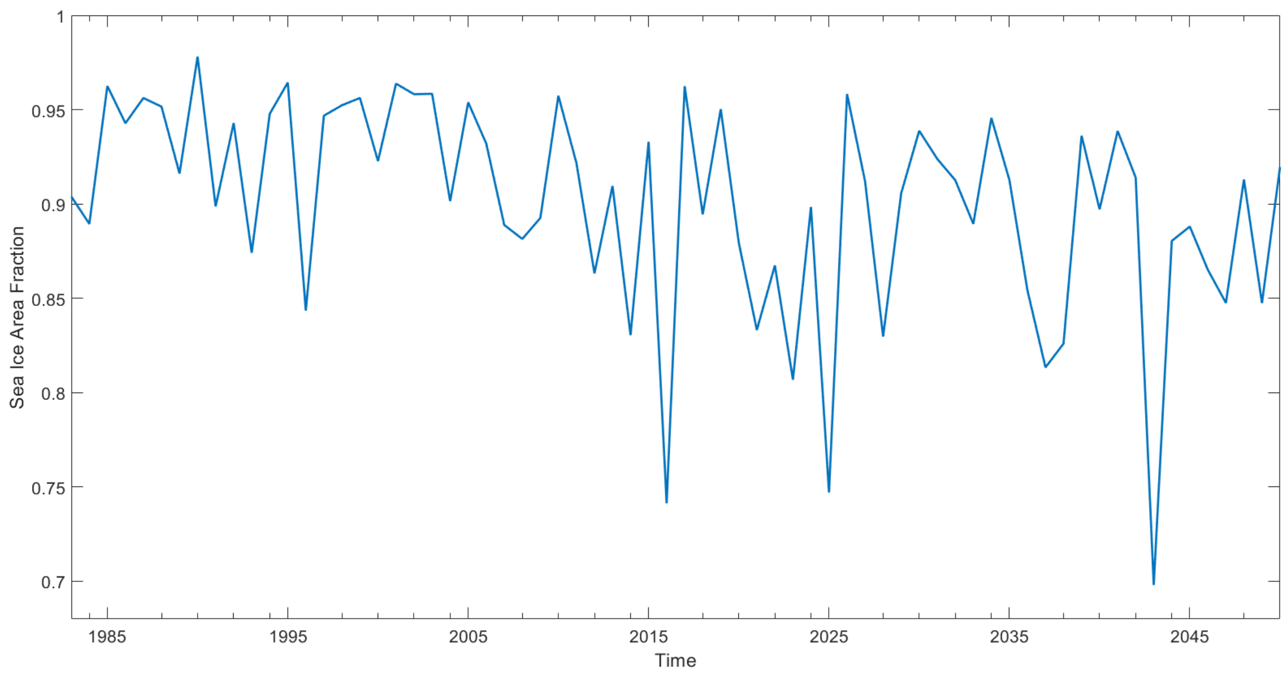

Figure 4.20 South Laptev Sea section of Area 1, average May sea ice fraction.

4.3.2 Area 2 - Barents Sea and Svalbard

In Area 2, surface temperatures showed the greatest differences, seen in Figures 4.21, with large warming areas between the Franz Josef Islands and Svalbard. Therefore, this section has been averaged, with the results seen in Figure 4.22. Both SOS and TOS show an increasing trend across the time-period, with a slight decrease in the 2025-35 decade. The average May sea ice area fraction for the same section can be seen in Figure 4.23, and shows a clear and sustained decrease in sea ice cover as early as 2007 (with a significant low in 1997). Between 2025 and 2035, there is greater sea ice cover than in the preceding or following decade, coinciding with the slightly decreasing TOS and SOS in the decade 2025-35. Perhaps this decade is showing runoff from increased ice sheet melt, resulting in decreased sea surface temperature and salinity and facilitated enhanced sea ice cover, however this is speculative at this point. Current trends support a decreasing SMB in Svalbard (Østby et al., 2017) and Franz Josef Land (Zheng et al., 2018) glaciers, however this is not an aspect included in this NEMO run. The increase in SOS and TOS in the final decade suggests that by May sea ice had significantly decreased, allowing for enhanced wind-driven mixing, and increased SOS through combination with warm, higher salinity subsurface Atlantic water.

Overall, TOS patterns are likely to increase on average in a high-emissions scenario, especially in the high-latitude Northern Hemisphere through Arctic Amplification (Serreze et al., 2009). The Barents Sea in particular is an interesting region, due to its position between the North Atlantic and the Arctic Oceans. Over recent years there has been some evidence of ‘Atlantification’, where the region experiences greater inflow of warm, Atlantic water and therefore the area of potential sea ice decreases (Lind et al., 2018). It seems likely, as this region is showing greater sea surface temperature change than the rest of the Arctic, that Atlantification is a factor here, potentially visible in Figure 4.21. Although as temperature increase occurs mostly along the shelf edge, this may be a result of stronger mixing bringing warm Atlantic water upwards instead.

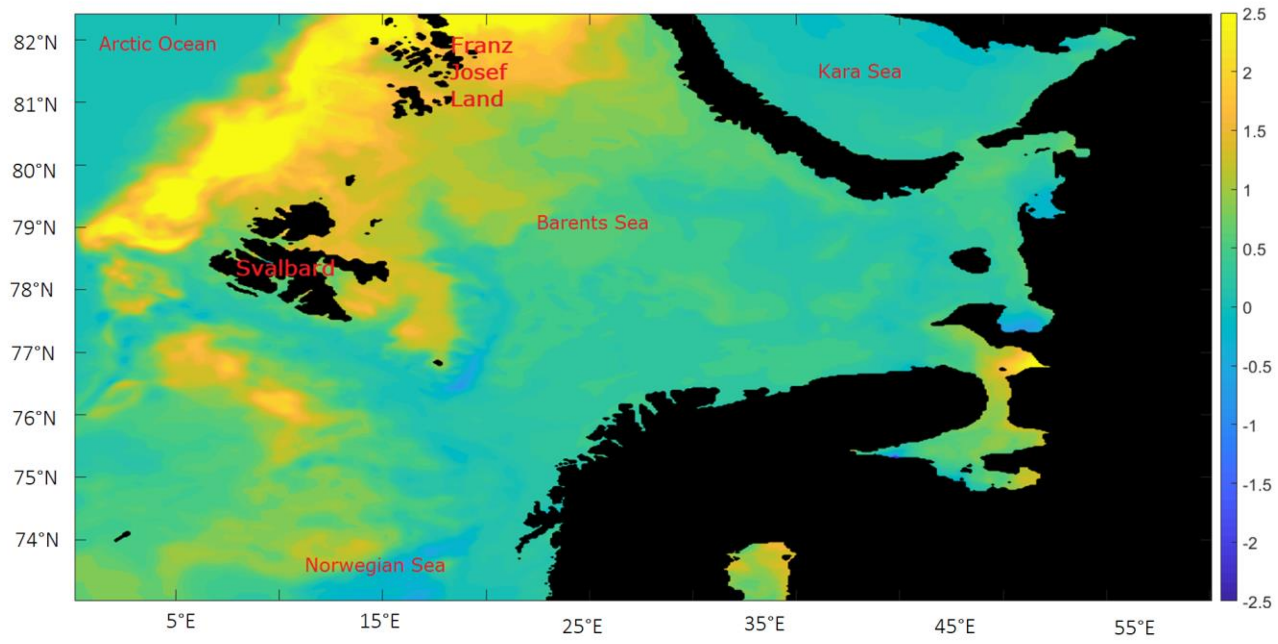

Figure 4.21 Plot of Area 2, with important locations marked in red. The background is May TOS averages difference plot for 2025-2035 and 2035-2045.

Figure 4.22 Franz Josef Islands to Svalbard section of Area 2 May decadal averages for SOS and TOS.

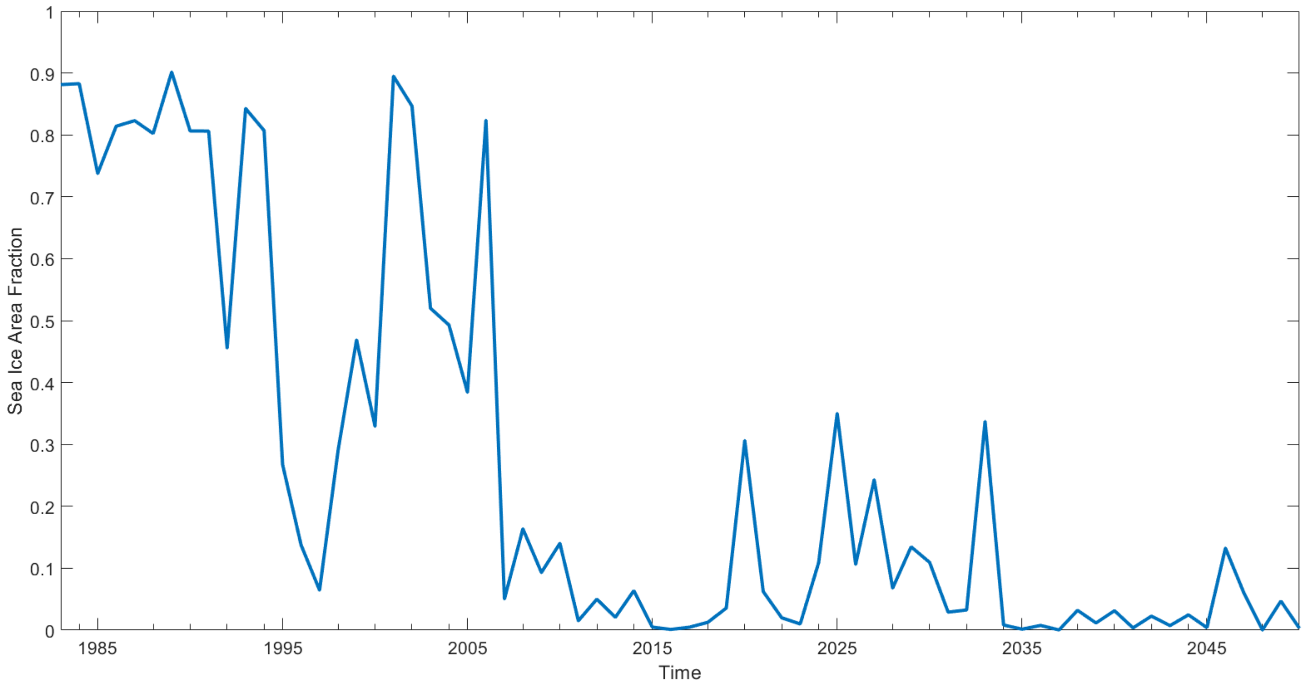

Figure 4.23 Franz Josef Islands to Svalbard section of Area 2, average May sea ice fraction.

4.3.3 Area 3 - Iceland, Greenland and the East Canadian coast, to Newfoundland

Area 3, the region around Greenland, showed less clear decadal differences than either of the two previous areas. As this is the most relevant area for this thesis, three small sections will be considered. These are the Iceland Sea, the mid-North Atlantic and the Newfoundland/Labrador Coast. Figure 4.24 shows Area 3, with important locations marked in red. The background is May TOS averages difference plot for 2025-2035 and 2035-2045, which shows significant cooling in large areas of the North Atlantic, corresponding to GrIS melt.

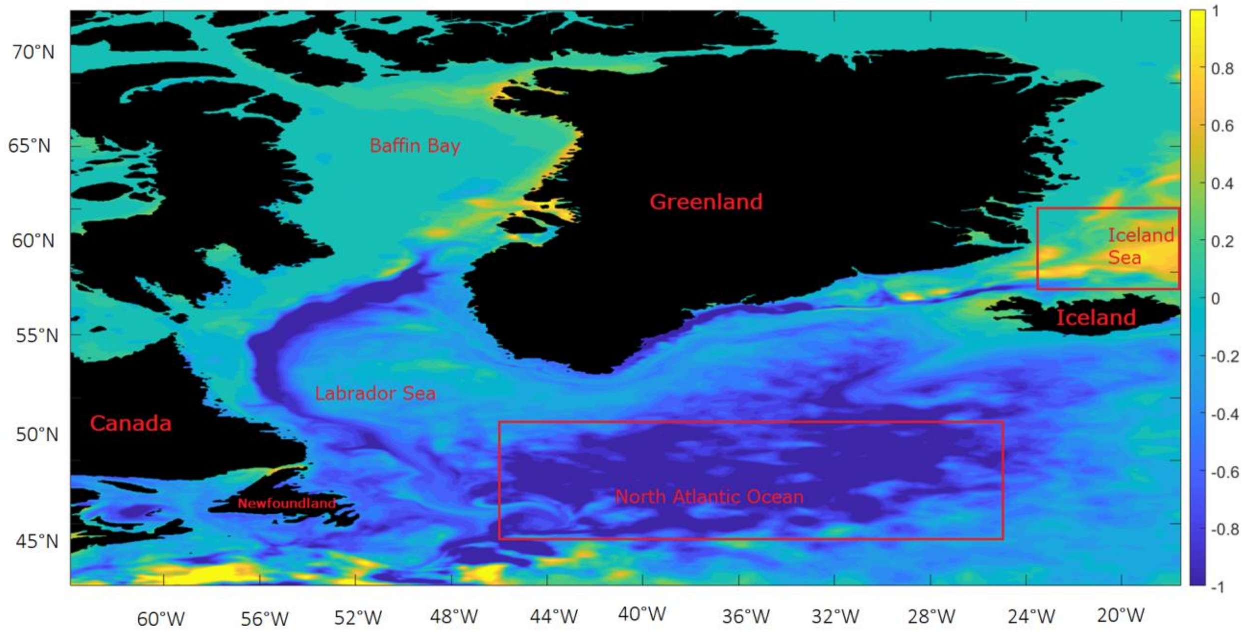

Figure 4.24 Plot of Area 3, with important locations marked in red. The background is May TOS averages difference plot for 2025-2035 and 2035-2045.

4.3.3.1 The Iceland Sea

The May average over each decade for the section north of Iceland can be seen in Figure 4.25. This shows a clear and steady increase in TOS in the Iceland Sea over each decade. SOS shows more variation between decades, and this is likely due to the interaction of the dominant ocean currents in the region. The East Iceland Current brings cold, fresh water south from the East Greenland Current, while warm, salty Atlantic water is brought north by the North Icelandic Irminger Current (Casanova-Masjoan et al., 2020). Changes in wind patterns have been previously linked to salinity anomalies in the region (Zhao et al., 2018), and it is likely these outside forces are dominating salinity here.

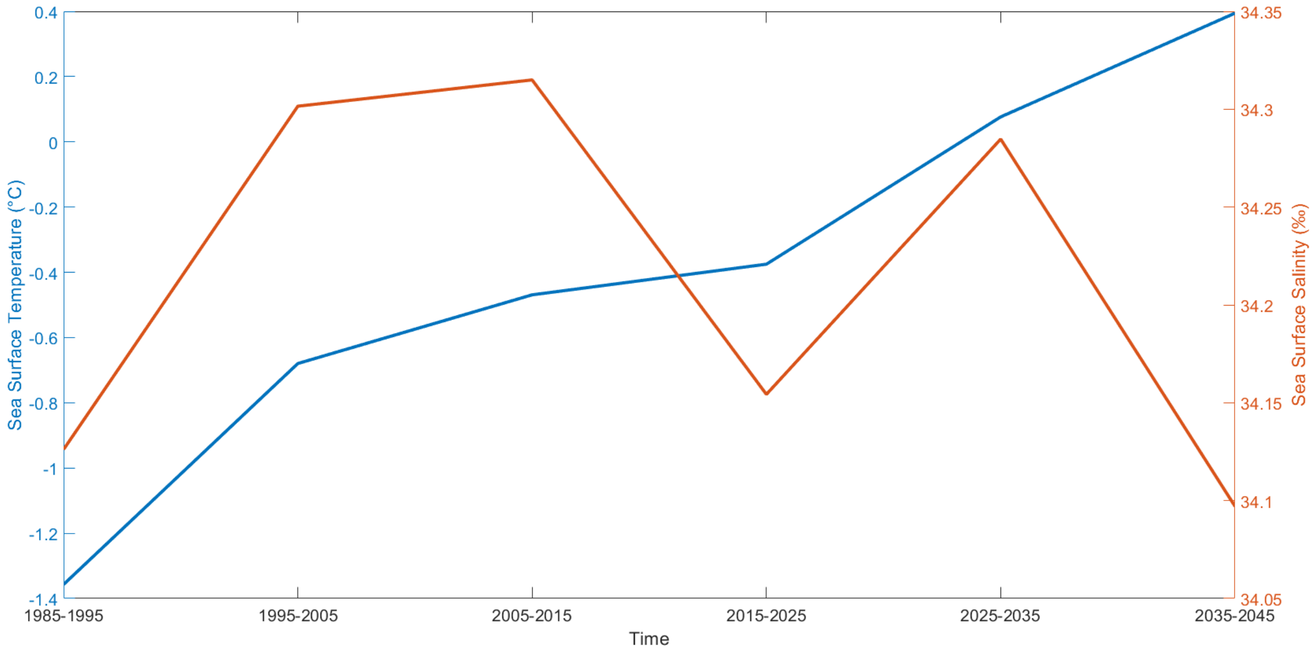

Figure 4.25 North Iceland Section of Area 3 May decadal averages for SOS and TOS.

4.3.3.2 The North Atlantic Ocean

The May average over each decade for the mid-North Atlantic section can be seen in Figure 4.26. This shows that TOS in the mid-North Atlantic section generally increases over the time-period, peaking in 2025-2035, before significantly decreasing to approximately

1985-1995 levels. This could be explained by the high-emissions scenario increasing overall TOS in the area, with the associated increasing temperatures over the GrIS resulting in increased runoff and iceberg melt, and a sharp cooling pattern (see Section 4.1.2 which shows runoff increasing over time). This pattern is also seen in SOS, where a gradual decreasing trend is seen, before a sharp decrease in 2035-45.

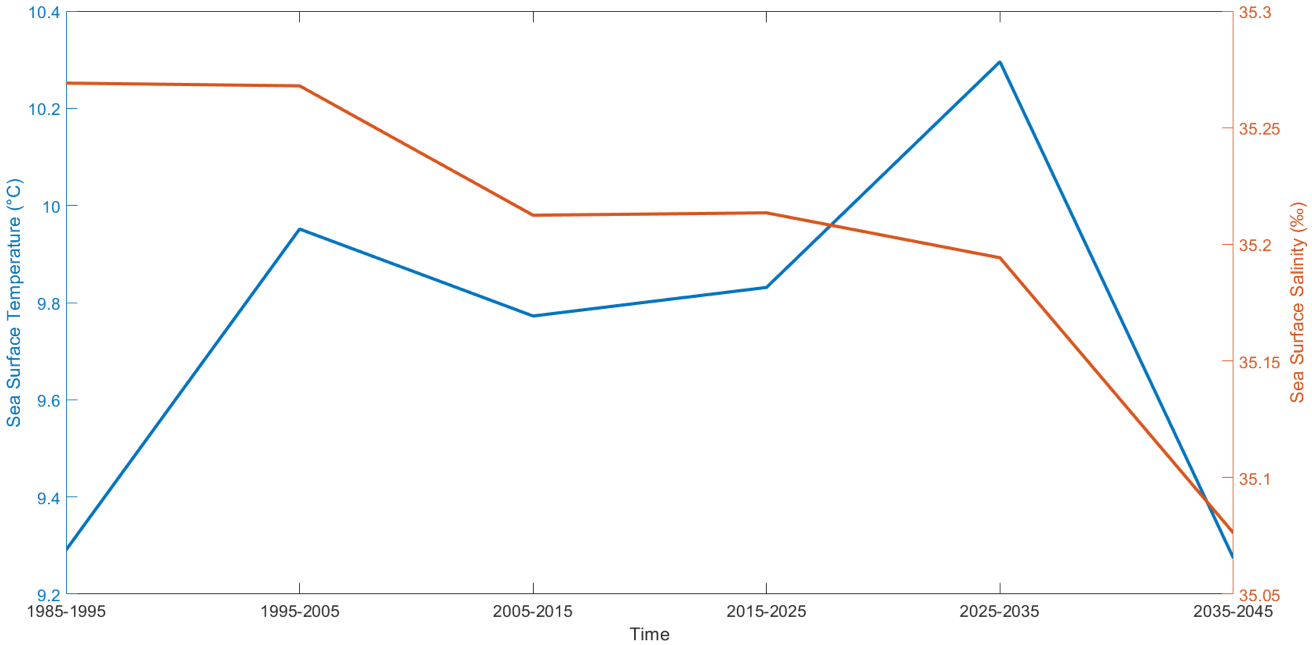

Figure 4.26 North Atlantic Section of Area 3 May decadal averages for SOS and TOS.

4.3.3.3 Newfoundland and the Labrador Sea

4.3.3.3.1 Correlation with I48N

To understand the relationship between the selected variables (SOS, TOS and FICEBERG) and I48N (the total number of icebergs reported past the 48^{th} parallel by the International Ice Patrol (see chapter 2 for more detail), five potential areas have been analysed and the correlation between the May average over the area and I48N can be seen in

Table 4.1. The approximate areas have been marked in Figure 4.27. The additional variable FICEBERG (as previously discussed in section 4.1.2) has been included in this section as it directly records the meltwater input from melting icebergs, and the aim of this section is to determine how well NEMO model results correspond to I48N values.

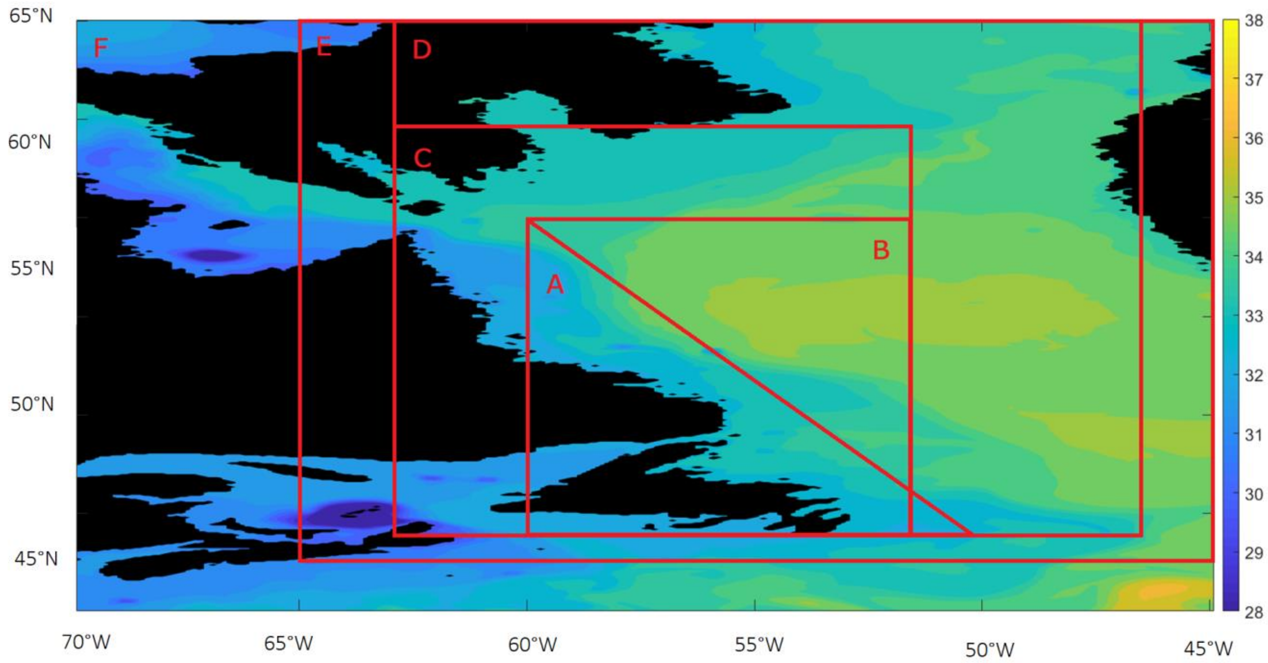

Figure 4.27 Plot showing the six regions used for comparison. Note that region A is triangular, all other areas are rectangular. The base plot (Area F) shows model SOS for May 2020.

Table 4.1 Showing the correlation between the May average FICEBERG, SOS and TOS over each area (A-E, where A is the smallest region and E is the largest) and the I48N yearly total, between 1983 and 2020. Statistically significant correlations, at the 95% level, have been highlighted in green.

	Correlation with I48N		
Region	**FICEBERG**	**SOS**	**TOS**
A	0.0083	0.4187	-0.3659
B	0.2638	0.3397	-0.387
C	0.1766	0.2846	-0.388
D	0.1356	0.2181	-0.3938
E	0.0341	0.2573	-0.3869
F	0.0363	0.3388	-0.3502

Table 4.1 shows that FICEBERG has little correlation (with no statistical significance at the 95% level) over any of the areas averaged, with I48N. SOS shows a positive correlation in all of the areas considered, with three being statistically significant. However, it is likely that Area F, the largest region, is being influenced by the freshwater input in the Gulf of St Lawrence and the Hudson Bay area. As such, the smallest regions (A and B) show the most useful correlation. Regarding TOS, all areas show similar (statistically significant) negative

correlation with I48N. As changing the area size made little difference, it seems likely that sea ice is dominating the relationship. Cold winters over Baffin Bay and the Labrador Sea will lead to an expansion of the sea cover and an associated increase in sea surface salinity resulting from brine released during sea ice formation. The presence of a sea ice cover helps to increase iceberg longevity, therefore resulting in a positive correlation between surface salinity and iceberg numbers south of 48N. Sea ice also traps icebergs north of the 48th parallel and affects the timing of the peak iceberg month off Newfoundland (Wilton et al., 2015). Overall, high winter sea ice cover, and the associated low TOS, strongly affects yearly iceberg severity (Sudom et al., 2014). Therefore, while TOS is a useful indicator of I48N, SOS appears to be most representative of iceberg numbers and will be considered before TOS and FICEBERG.

Overall, Region A will be used as the defined 'area' for the rest of this section, as the correlation is greater. It seems likely that Region A has the greatest correlation with I48N because it is the smallest area considered, and is therefore better representative of icebergs in the relatively narrow Labrador Current, rather than averaging over the warmer, more saline central Labrador Sea. It was found that using the same area averages, but with correlation with May I48N values only, produced no statistically significant results with any of the variables, suggesting seasonal accumulation of melt may be the dominant physical mechanism leading to the correlation, or that there are longer term lags between variables.

4.3.3.3.2 A Time-Series Approach

It is useful to consider the relationship between I48N and monthly river runoff (FRIVER) from southern and western Greenland. Only runoff values from south and west Greenland have been used here, as the majority of Greenland originating icebergs that reach

48°N calve off southern or western fjords (Bigg et al, 2014), however there may also be freshwater from other sources. It was previously found that icebergs take a minimum of 8 months to reach 48°N from Greenland (Bigg et al., 2021), and this can be seen in Figure 4.28, showing the lagged correlation between monthly FRIVER (averaged over southern and western Greenland) and I48N. It can be seen that a 9-month lag produces the highest similarity between the variables, and this correlation was calculated to be 0.5113, significant at the 99% level, between 1983 and 2020. This suggests that, historically, high runoff in summer and autumn tended to correspond to high iceberg numbers south of 48°N in the following spring.

Section 4.1.2 showed that by 2050, iceberg numbers around Greenland are likely to decrease, while runoff increases, probably because the glaciers have started to recede back onto land away from the ocean. When a decadal sliding-window approach to quantifying correlation between southern and western Greenland FICEBERG and FRIVER over the whole time period (1983 to 2050) was considered, no significant changes were identified. Therefore, it can only be concluded that at present, high runoff tends to align to high I48N years, and by 2050 runoff is likely to increase. However, as FICEBERG does not well represent iceberg numbers off Newfoundland (see Section 4.3.3.3.1), no conclusions can be drawn here from this variable regarding future changes in I48N. Overall in this high-emission run, increased GrIS warming results in enhanced runoff and fewer icebergs numbers around Greenland, and therefore lower iceberg flux south of 48°N. When combined with projected sea ice loss, I48N is likely to decrease further. Therefore, there is potential for the recent relationship between runoff and I48N to alter moving forward, or just for the definition of a ‘high’ I48N to reduce, but still align with high runoff years.

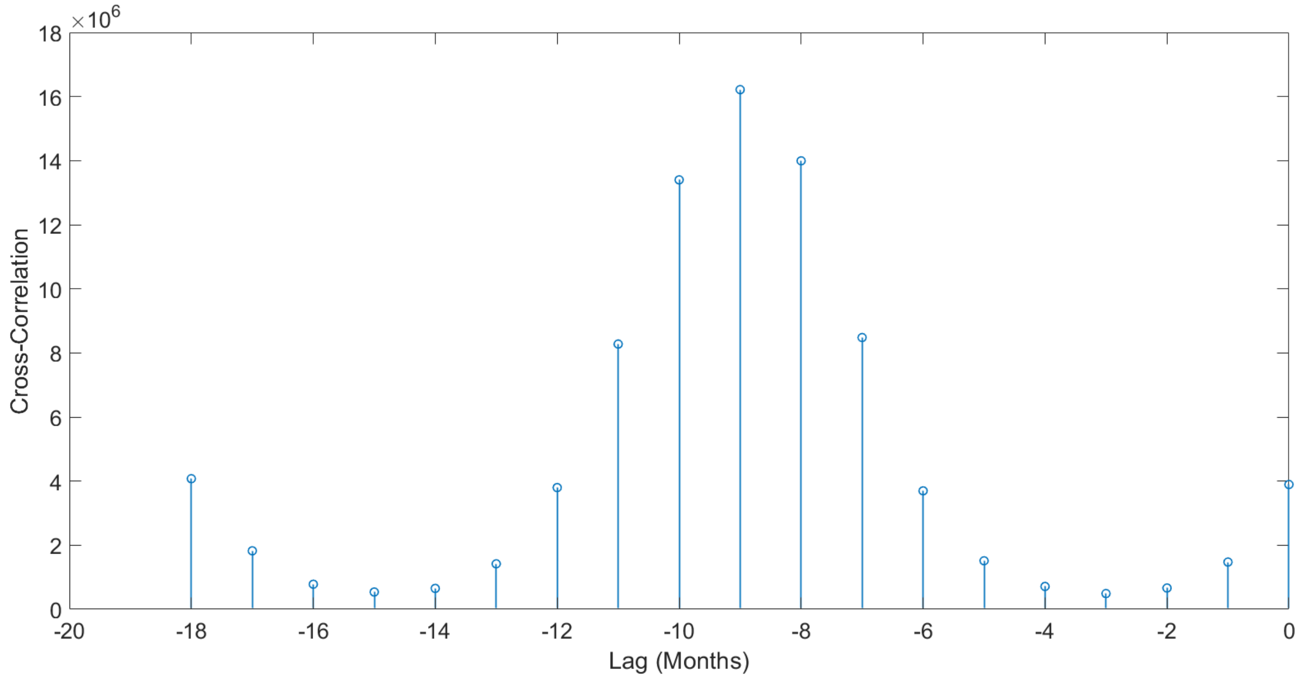

Figure 4.28 Showing the lag between southern and western Greenland FRIVER and I48N.

Consider Figure 4.29, a plot of May average SOS for Region A between 1983 and 2020, compared to the I48N yearly total. Overall, the salinity data seems a useful approximation of I48N, especially when considering the high natural variability in I48N. Looking into the future, Figure 4.30 shows the average monthly SOS values over the region up to 2050, with a 12 month moving average. This plot also includes a 9-month lagged FRIVER averaged over the same area. This lagged FRIVER shows no significant increase over time, but periods of high FRIVER do align with periods of reduced salinity, and vice versa. This supports a relationship between SOS and FRIVER, however it is noted that FRIVER values are small around Newfoundland, so it is to be expected that the graph does not show a clearly defined correlation between variables. Nevertheless, it does suggest that periods of high freshwater runoff are (after 9 months) having some impact on sea surface salinity values around Newfoundland. The plot also shows a clear decreasing trend in SOS between 1983 and 2050. This is likely due to the NEMO run (2015-2050) being forced with a high-emission scenario, resulting in rapid sea ice retreat and increased sea surface temperatures in the Labrador Sea, both of which act to reduce the number of icebergs that reach south of the 48th parallel. This also affects SOS as sea ice is made up of frozen freshwater and pockets of very salty brine. Sea ice in colder temperatures contains a small amount of high intensity brine, while in warmer conditions the sea ice has a larger quantity of lower intensity brine, and therefore affects how salt enters the water column (Widell & Haugan, 2006). This therefore suggests that while this run may be a more extreme scenario than is likely to be seen by 2050, the long-term trend in I48N is forecast to decrease overall in a warming climate.

Detrended SOS values were calculated (using the line $y = -0.0109x + 33.272$) however the resulting correlation with I48N was not statistically significant at the 95% level – the trend is an integral part of the link between the two variables. This could also indicate that there is another variable that controls both of them and that SOS and I48N are not directly linked. Therefore, only original values are considered.

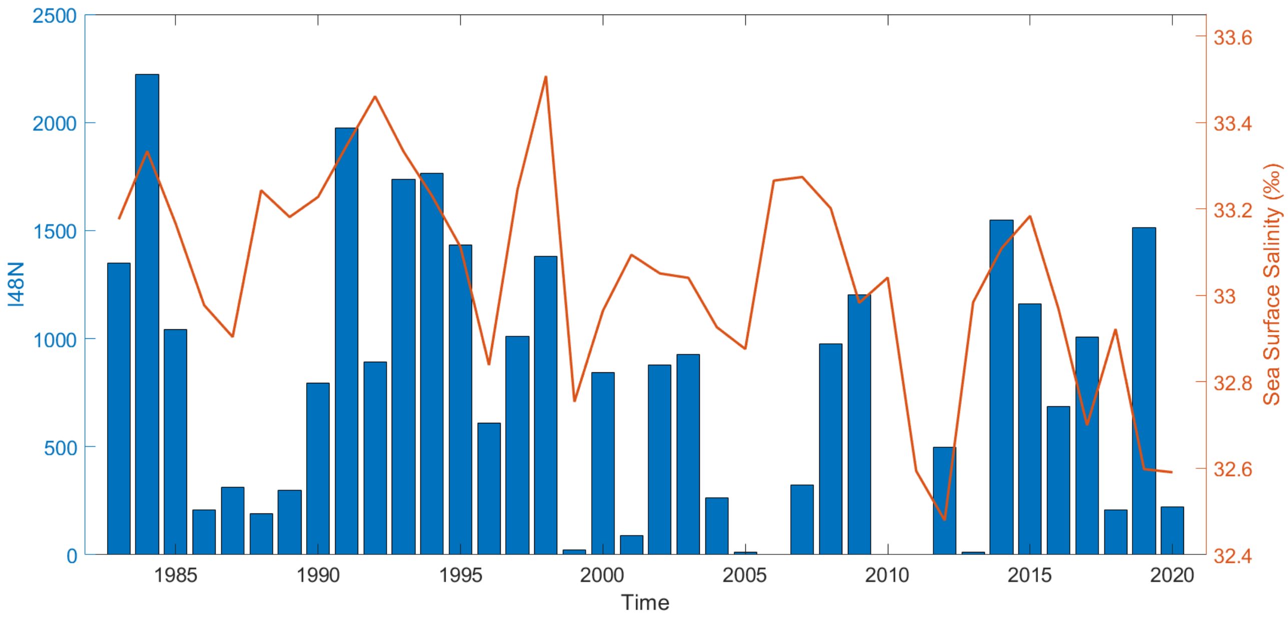

Figure 4.29 Plot of the yearly total I48N and SOS (averaged over Region A) between 1983 and 2020.

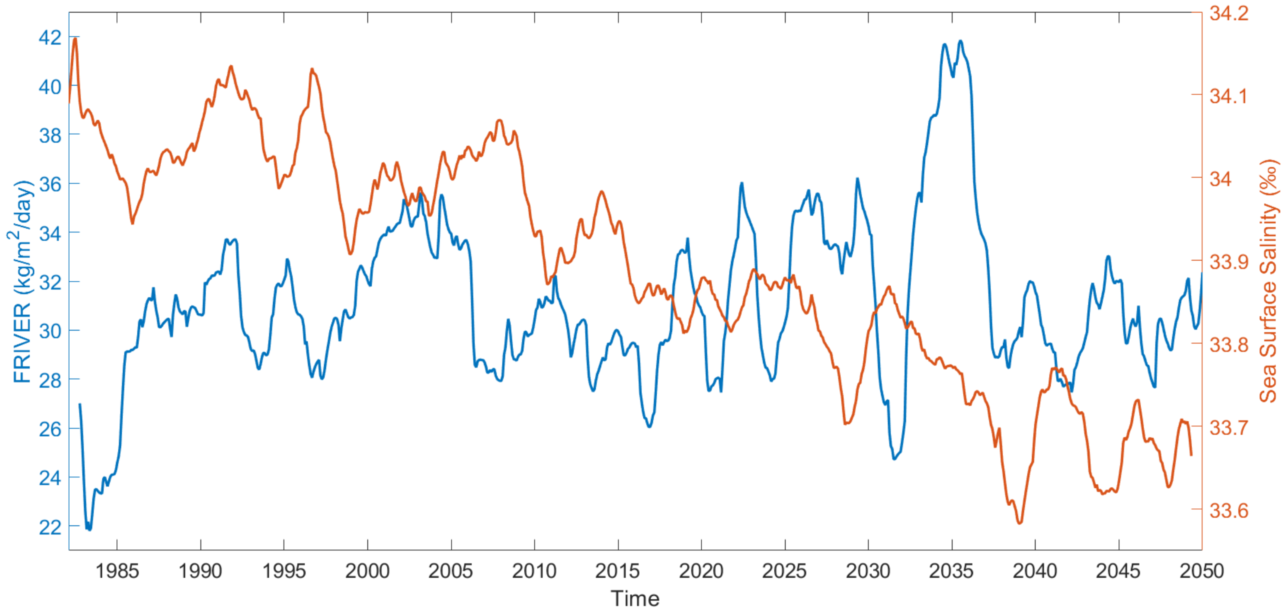

Figure 4.30 Plot of SOS compared to FRIVER (both averaged over Region A with a 12 month moving average) between 1983 and 2050. FRIVER has been lagged 9 months to allow the freshwater to reach the region from the GrIS.

4.3.3.3.3 A Discrete Approach

Another way to assess how well NEMO May SOS averages (over Region A) align with I48N is by dividing the data into the low/medium/high brackets, in the same style seen in Chapter 2 (as defined by the International Ice Patrol). Therefore, a low I48N year has less than 231 icebergs past 48°N, a medium year has between 231 and 1036, and a high year has more than 1036. SOS data has been divided using the 33rd and the 66th percentile. The results can be seen in Figure 4.31. This figure shows that high SOS years strongly relate to high I48N years, while medium and low years show less of a relationship. This suggests that high iceberg years often occur when environmental conditions result in low levels of iceberg melt (allowing icebergs to reach further south, past 48°N, before significant melting occurs). Not necessarily because iceberg melt has a strong influence on SOS, but perhaps because of the conditions associated with high iceberg year (e.g. large sea ice extent and cool sea surface temperatures). Figure 4.32 shows the same results but over time. This plot shows that this approach is dominated by the decreasing trend seen in Figure 4.29, and is therefore less useful for predicting I48N, except to reinforce the likely overall decrease in iceberg numbers south of 48°N in a warming climate.

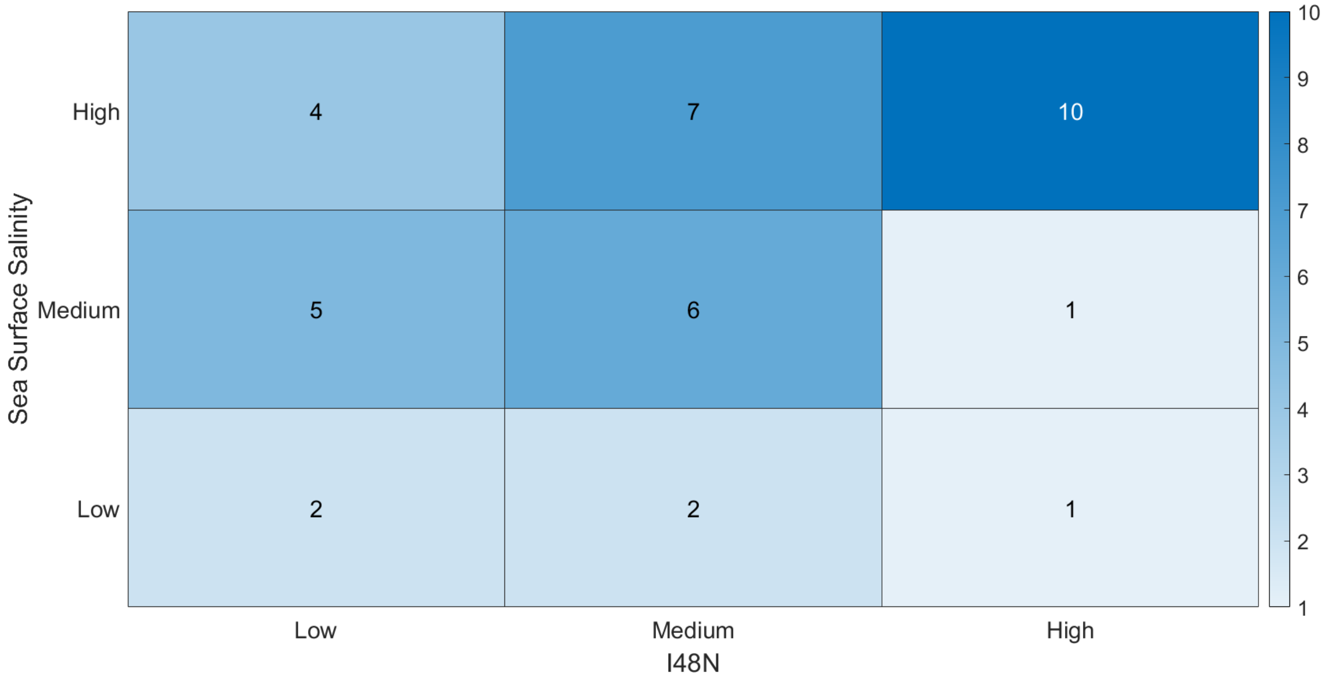

Figure 4.31 Plot showing how well low/medium/high May SOS values, averaged over Region A, coincide with low/medium/high I48N years. The numbers in each square are the number of times that combination occurred.

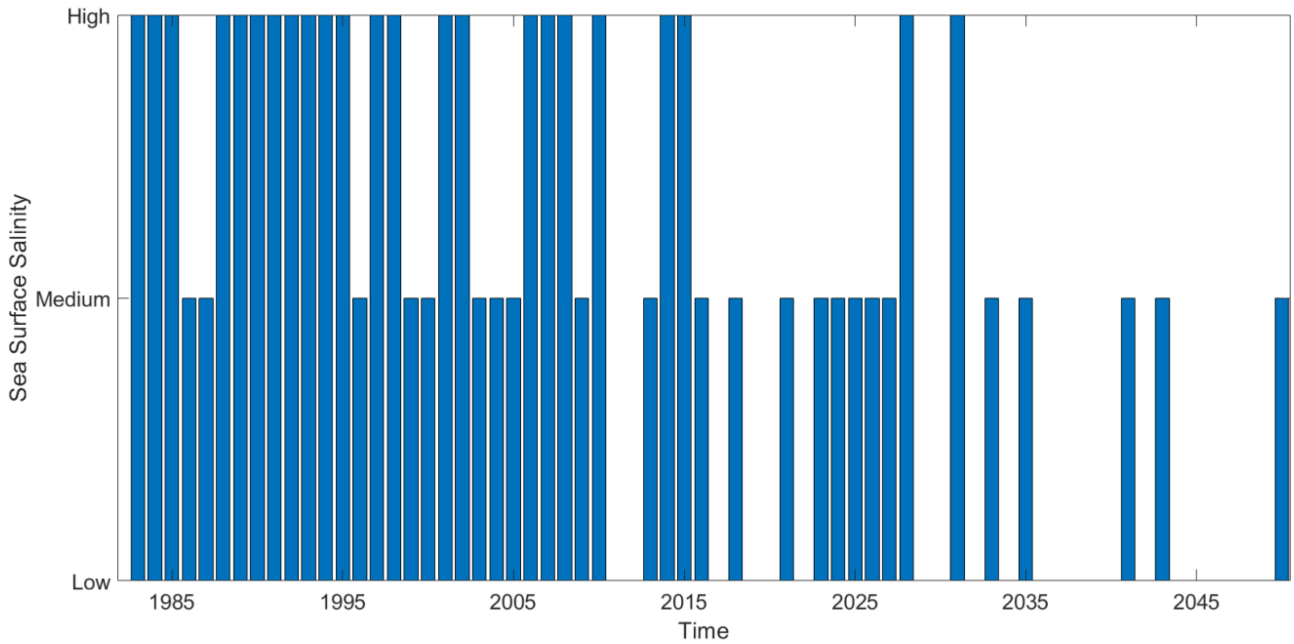

Figure 4.32 Plot showing low/medium/high May SOS from 1983-2050.

4.4 Using Remote Sensing Data to Observe Salinity Patterns

4.4.1 Introduction to satellite data

Satellite data is a useful tool for detection purposes, although often restricted by the weather (nevertheless active radar sensors can still get useful data through clouds and in darkness) and the limited timeframes they operate over. For this reason, two datasets are considered here to produce data over an eleven-year period. These are the Aquarius remote sensing data, and the Soil Moisture Active Passive (SMAP) data. Aquarius was active between August 2011 and June 2015, while SMAP overlaps the end of the Aquarius run, from early 2015 to present. Aquarius was specifically designed to monitor sea surface salinity from space. The purpose of SMAP is to continue to track changes in ocean salinity, while also monitoring soil moisture patterns, which is useful for early warning signs of a drought (Why It Matters | Mission – SMAP, 2021). The satellite data (in both cases) calculates surface salinity by considering the difference between a radiometer and radar measurements taken over the same location. As the time between measurements is short, changes can be attributed to soil moisture rather than vegetation or other surface variations (Das & Entekhabi, 2019). Both datasets have been averaged over Region A (see Figure 4.27 for a definition of this area).

The aim of this section is to determine whether these SOS satellite datasets can be used to detect yearly iceberg severity in the region off Newfoundland, Canada, and whether these results are comparable to NEMO model outputs.

4.4.2 Aquarius

The Aquarius SOS data (March-June for the years 2012-2015) has a correlation of 0.5666 (p-value = 0.02766) with March-June I48N, and is therefore statistically significant at the 95% level. However, the significance of this result is reduced by the short timeframe and the susceptibility of satellite data to cloud cover and the known poor coverage of the Aquarius data in higher latitudes, and along the coast (Kao et al., 2018). The March-June monthly averages can be seen in Figure 4.33, plotted with monthly (March-June) I48N. Note that there is no June 2015 data, as Aquarius had been discontinued by this point. Positive SOS anomalies can be seen to correspond to high I48N years, and vice versa, despite large monthly variations. It was shown in Section 4.3.3.3.1 that NEMO SOS is also positively correlated with I48N, and the same reasons are likely to apply here. High I48N years are ones in which icebergs do not experience large-scale melt before reaching Newfoundland, and therefore correspond to relatively positive SOS anomaly years. Therefore, the Aquarius dataset is shown to well represent low/high iceberg years in this short period.

GrIS runoff was also compared to SOS Aquarius data. FRIVER values were considered over variable 4-month periods (to allow for the slight lag of transporting water from southern and western Greenland to off the Newfoundland coast), however no combination produced a statistically significant correlation at the 95% level.

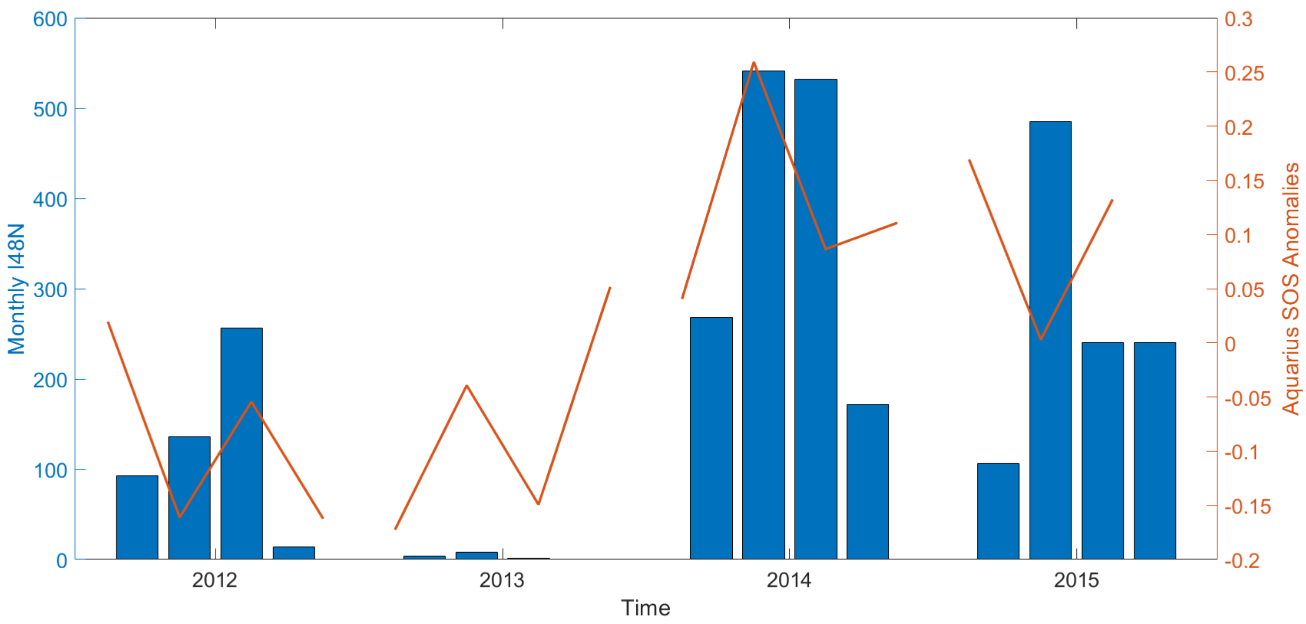

Figure 4.33 Monthly I48N totals compared to March-June monthly average Aquarius SOS anomalies.

4.4.3 SMAP

SMAP SOS March-June monthly data has a correlation of 0.2981 with monthly March-June I48N (p-value = 0.1893) and this therefore is not statistically significant at the 95% level. This aligns with other work with SMAP, where it was found that while SMAP had a higher spatial resolution than Aquarius, the data is overall less accurate (Bao et al., 2019). Note that SMAP temporarily stopped recording data from the 20th June 2019 (Yao et al., 2021), resulting in that month not being included here. Additionally, 2015 starts in May, as this is when SMAP commenced operation, therefore overlapping with the Aquarius dataset by one month only. Figure 4.34 shows the SMAP monthly SOS anomalies for March-June 2015-2020, plotted with monthly (March-June) I48N. As expected from the monthly correlation, the SMAP SOS anomalies show little relationship with I48N. It is therefore suggested that SMAP has not proven to be useful for comparison with I48N, for the examined years.

As with the Aquarius dataset, GrIS runoff was compared to SOS data. FRIVER values were considered over variable 4-month periods, again with no combination produced a statistically significant correlation at the 95% level.

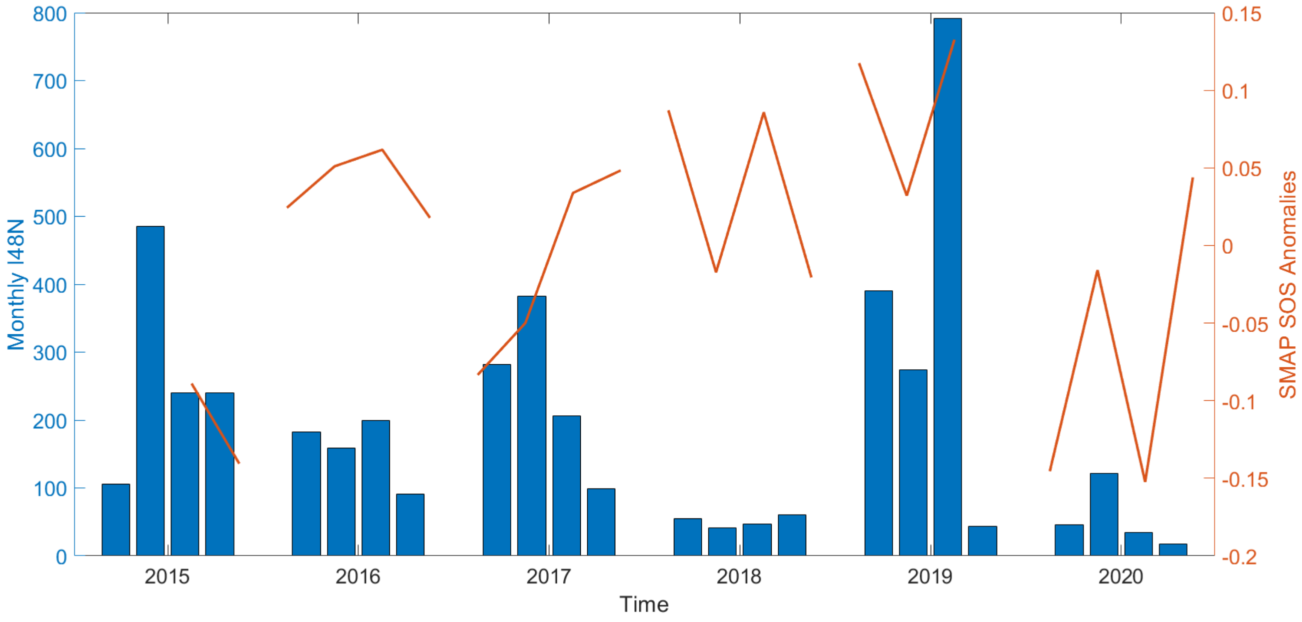

Figure 4.34 Monthly I48N totals compared to March-June monthly average SMAP SOS anomalies.

4.4.4 Conclusions and Comparisons to NEMO

A comparison of satellite (Aquarius and SMAP) data, NEMO model results and I48N can be seen in Figure 4.35. Despite the short time-period, Aquarius shows the strongest (theoretically statistically significant, however in reality there were only 4 data points) correlation with monthly I48N and can be seen from Figure 4.34 to well represent a low or high iceberg year, with positive or negative SOS anomalies. SMAP has been shown to be the least useful for the purposes here. NEMO shows a (statistically significant) correlation when considering May SOS and yearly I48N, however it can be seen from the figure (and from Figure 4.31 in Section 4.3.3.3.3) to be less accurate in the classification of high or low iceberg years.

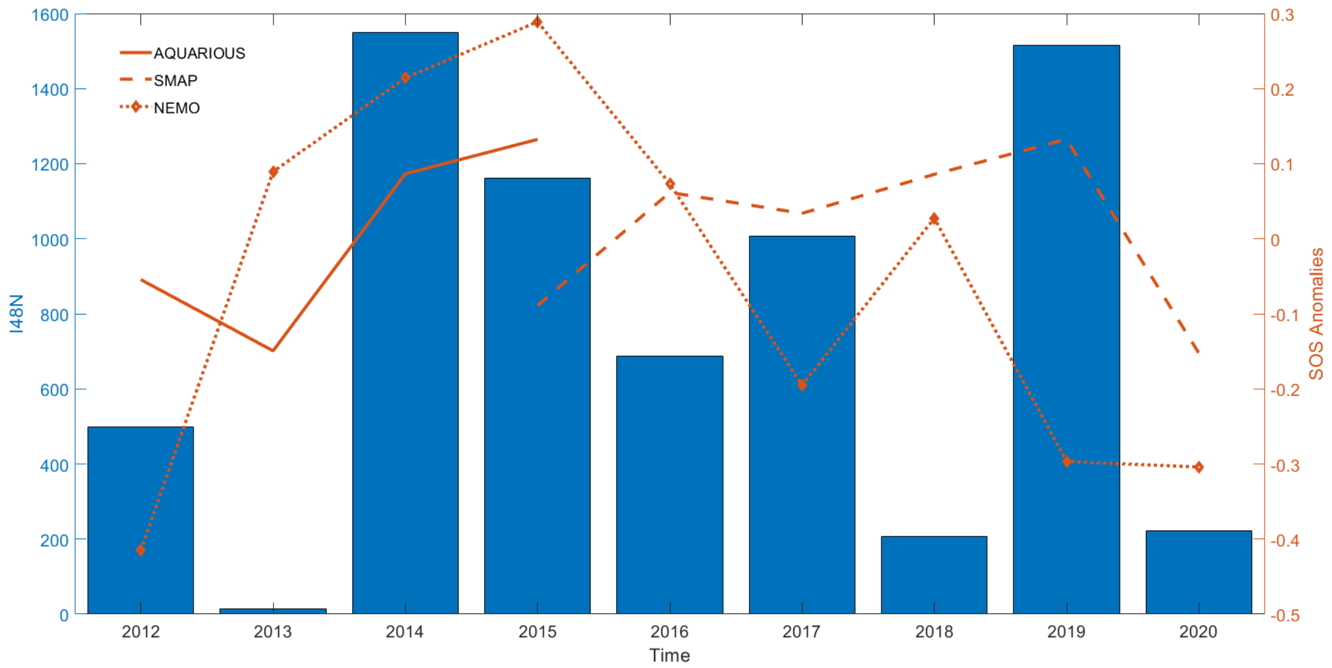

Figure 4.35 Plot of I48N and satellite May SOS anomalies (Aquarius data in solid orange; SMAP data in dashed orange) and NEMO May SOS anomalies (dotted diamond line).

4.5 Discussion and Conclusion

As NEMO model results are available to 2050, in a high-emissions scenario, it was interesting to quantify how well NEMO currently represents iceberg severity off Newfoundland, and whether this could be used to produce a general iceberg outlook by the mid-century. Interest in Arctic shipping has been increasing, and this is likely to continue into the near future (e.g. Bergström et al., 2020), thereby increasing the value of future iceberg severity prediction. At current levels, the direct risk to shipping from icebergs in the North Atlantic is very low (see Chapter 2 for further discussion on this). This is due to a combination of a good monitoring system and internationally enforced polar regulations in shipping safety, and improved navigational technology. Future risk is more complex and will be determined partially by public interest in Arctic tourism and partially by whether safety standards will make such cruises financially unviable. While a reducing GrIS is forecast to release greater quantities of ice into the surrounding ocean (Shepherd et al., 2020), the NEMO results suggest that in a high-emissions scenario, fewer icebergs would reach south of 48°N (from SOS projections), or calve from the GrIS (when considering FICEBERG). This is likely enhanced by reducing sea ice extent, which has been previously noted to be positively related to yearly I48N totals. The year 2021 is a clear example of this, with very low sea ice extent along the East Canadian Coast resulting in a very low iceberg year, with only one iceberg reaching south of 48°N (see the 2021 IIP report at Navcen.uscg.gov., 2021). This iceberg was recorded early in the ice season, in February, when the peak iceberg month is usually April or May (see Chapter 2, Section 2.2.2.1).

Increased cool, fresh meltwater input is another direct consequence of a reducing GrIS, affecting SOS and TOS as seen throughout this chapter. The majority of Arctic regions considered showed sustained TOS increase, with the exception of the mid-North Atlantic section, which saw substantial decrease in 2035-45. This is likely a result of the location of this section being the nearest to the melting GrIS, in terms of where local ocean currents would transport the freshwater (see Chapter 1 Section 1.3.1 for an overview of the relevant currents). This is likely to result in a slowdown of the AMOC due to decreased deep water production in the Labrador Sea (and other important regions). SOS patterns varied on a more localised scale; however, the majority of sub-regions had seen large decreases by 2035-45, excepting the Svalbard-Franz Josef Islands section. This section has already experienced significant sea ice retreat, and correspondingly showed large increases in TOS in May, which facilitates wind-driven mixing thereby increasing SOS through mixing of the fresh surface layer with the higher salinity subsurface Atlantic Water.

Overall, changing freshwater fluxes from the GrIS in the ORCA12-N512 simulation has clear implications for the Arctic and further afield in the next 30 years. While this chapter has focused on a high-emission scenario with the NEMO ocean model, this level of global warming has not presently been ruled out. Even in a more realistic emissions scenario, the changing SOS, TOS and iceberg patterns are likely to hold true, just on a slower timescale. Retreating sea ice extent has been a recurring theme throughout this chapter and is a clear indicator of the ocean changes already taking place. This chapter also suggests that freshwater runoff from the GrIS is likely to increase in the future, with an intensifying hydrological cycle (higher runoff rates linked to heavier snowfall and higher air temperatures), while iceberg calving decreases. Therefore, while at present iceberg calving is a major contributor to GrIS mass loss (Bigg et al., 2014), in the near future runoff is likely to significantly dominate. This was supported by a decreasing trend in SOS by 2050, in the Newfoundland region. This has interesting consequences for shipping, with decreasing sea ice extent and iceberg numbers seemingly making Arctic regions far more traversable.

5. Comparing a High and a Medium Complexity Ocean Model for Sea Level Analysis and Verification Purposes

5.1 Introduction

The ocean models considered here, FRUGAL and NEMO, have been individually analysed in chapters 3 and 4 respectively. However, to briefly summarise, the coupled ocean-iceberg model FRUGAL moves the North Pole to Greenland, allowing for a 20 km resolution around the coast of Greenland, with a much coarser resolution in the Southern Hemisphere. The model runs from the winter of 1987 to spring 2015, due to restrictions in available input data. A control run and four runs of variable freshwater input were produced, with the differences highlighted in Table 5.1 (as seen in Chapter 3, Section 3.1.3). While it was concluded in Chapter 3 that Run 5 (where freshwater input varies monthly and yearly) was the most realistic, it is interesting in some instances in this chapter to review all the FRUGAL runs. Meanwhile, the ocean model NEMO has been coupled with the iceberg module (see Marsh et al., 2015), in two runs of 1/12° global ocean resolution. The first run is between January 1950 and December 2014, while the second runs to December 2050 from January 2015. This second run has been forced with a high emission scenario from the Coupled Model Intercomparison Project Phase 6 (CMIP6), with an approximate surface warming of 8.5 Wm^{-2} by 2100 (Hofer et al., 2020). As the NEMO runs are significantly more complex, they can be used to verify aspects of the FRUGAL run (when the timescales overlap).

Table 5.1 Outlining the differences between FRUGAL model runs

Model Run	**Time period of freshwater input**	**Freshwater quantity**
Run 1	Control run (no additional runoff).	Control run (no additional runoff).
Run 2	Only during the summer months (early June to late August).	Constant input, varying only for each location. These values were the average of the period 1980-2015 over each region.
Run 3	Monthly varying input, constant for each year.	The monthly average for each location over the 1980-2015 period.
Run 4	Yearly varying input, constant across all months.	The yearly average for each location over the 1980-2015 period.
Run 5	Varying both monthly and yearly.	The average for each month at each location, changing yearly with the data.

The chapter begins with a global assessment of change, using variables that may be used to reflect sea level. This aspect has been highlighted here due to the wider thesis focus on ocean risk, where sea level rise is a major socio-economic threat. In this context, risk is produced from the physical impacts of global warming and the associated human response (IPCC, 2019). This section has been divided into discussion of two decades: 1995-2004 and 2005-2014. The following section addresses small areas identified in earlier chapters as regions of interest. These include the Labrador Sea and the Drake Passage, and focus on the changing strength of the major ocean currents in each region. An assessment of the Gulf Stream strength has also been included, as this is shown to be an important region regarding dynamically-driven sea level change. The final section provides the chapter conclusions and discusses the potential for sea level rise on the east coast of the USA.

5.2 Global Differences in Sea Level

This section addresses the global differences in sea level between the most realistic FRUGAL run (Run 5) and the control run (Run 1), NEMO model outputs and satellite data. Therefore, only the decades 1995-2004 and 2005-2014 have been selected for direct comparison, as FRUGAL runs from 1987 to 2015. However, the NEMO outputs have been included up to 2035-2044 in order to assess likely future changes in sea level. The variables considered are the 'sea level height above geoid' in the NEMO run and a sea surface height variable in the FRUGAL runs. Additionally, a FRUGAL surface stream function variable has also been included, as it reflects the changes in ocean circulation, and therefore implies the sea level slope changes. This is due to the uneven nature of global sea level, as a result of ocean circulation patterns (Sasaki et al., 2014.). This is naturally regionally dependent, with, for example, Domingues et al. (2018) estimating that a 1 Sv decrease in transport through the Gulf Stream aligns with a 0.5 to 3 cm rise in sea level, along the northeast coast of the USA. For comparison, absolute sea level data from satellite altimetry measurements has also been plotted. This data is available at https://cds.climate.copernicus.eu/cdsapp#!/dataset/satellite-sea-level-global?tab=overview and has been plotted for the comparable decades 1995-2004 and 2005-2015, and referenced hereafter as the CMEMS sea level dataset, from the Copernicus Marine Environment Monitoring Service.

5.2.1 The decade 1995-2004

For comparison between models, sea level data from CMEMS, the FRUGAL control run and Run 5, and NEMO for the period 1995-2004 are shown in Figures 5.1-4 respectively. All plots use the same scale and therefore show that while NEMO closely matches the overall pattern of global sea level, there is a tendency for the CMEMS data to show stronger positive change, while the NEMO (in this decade) has a greater area of negative sea surface height above geoid. This is partly due to the satellite path of the CMEMS dataset resulting in reduced coverage in polar regions, however the data does have full availability in 81% of the globe (with full data evaluation available via https://cds.climate.copernicus.eu/cdsapp#!/dataset/satellite-sea-level-global?tab=eqc). Therefore, it is likely that NEMO is marginally under-representing positive sea level differences, especially in the low-latitudes. On the other hand, FRUGAL appears to be marginally over-estimating negative sea level height in the North Atlantic, and under-estimating positive sea level height south of the Gulf Stream. However, considering the FRUGAL control run is a lower resolution model, the overall pattern of positive/negative sea surface height is similar to the CMEMS data. However, as this is the control run it is interesting to see how this differs from Run 5 (see Figure 5.3). It can be seen that the additional freshwater that Run 5 is inputting is significantly altering sea surface height in the North Atlantic, specifically showing a strong positive change in the Newfoundland to UK region, where the CMEMS data suggests the FRUGAL control run is over-estimating the negative sea level height. The Gulf Stream region is another area of significant difference, with Run 5 having a decreasing effect in the southern Gulf Stream and an increasing effect in the northern Gulf Stream. This would create a clearer defined Gulf Stream response in the FRUGAL results. Therefore, these changes would produce a North Atlantic with a more similar sea level height pattern to the CMEMS data than the FRUGAL control run. FRUGAL Runs 2-4 plots for sea surface height for both discussed decades are available in the Appendices Section, S3-8.

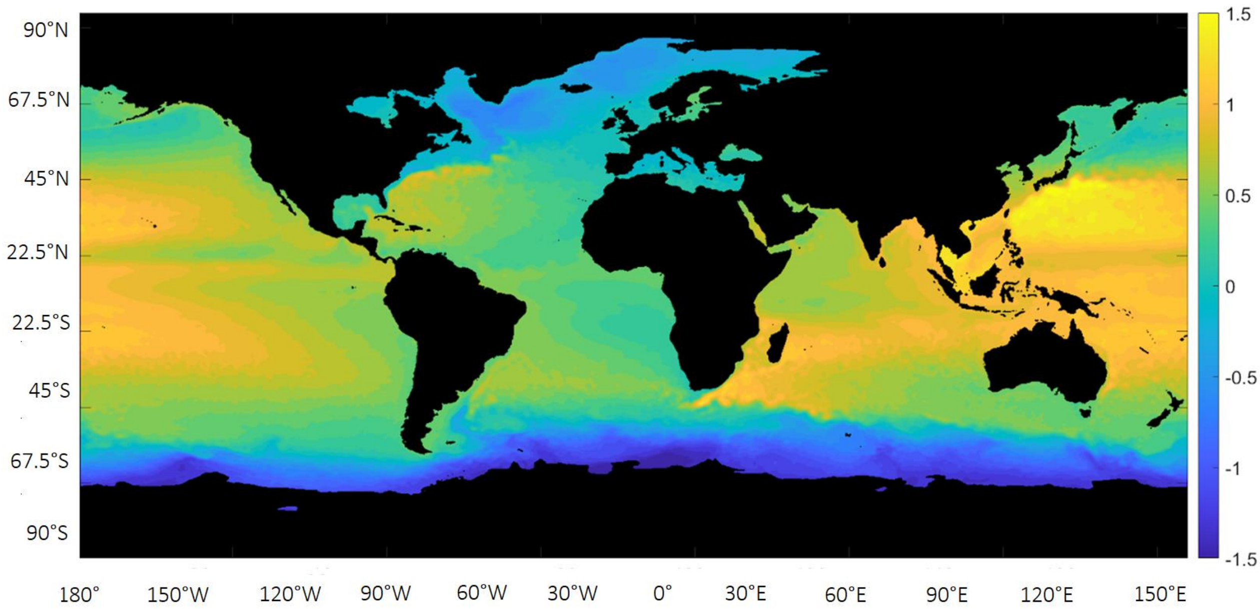

Figure 5.1 Plot of average absolute sea level relative to the geoid from the CMEMS dataset, in m, 1995-2004.

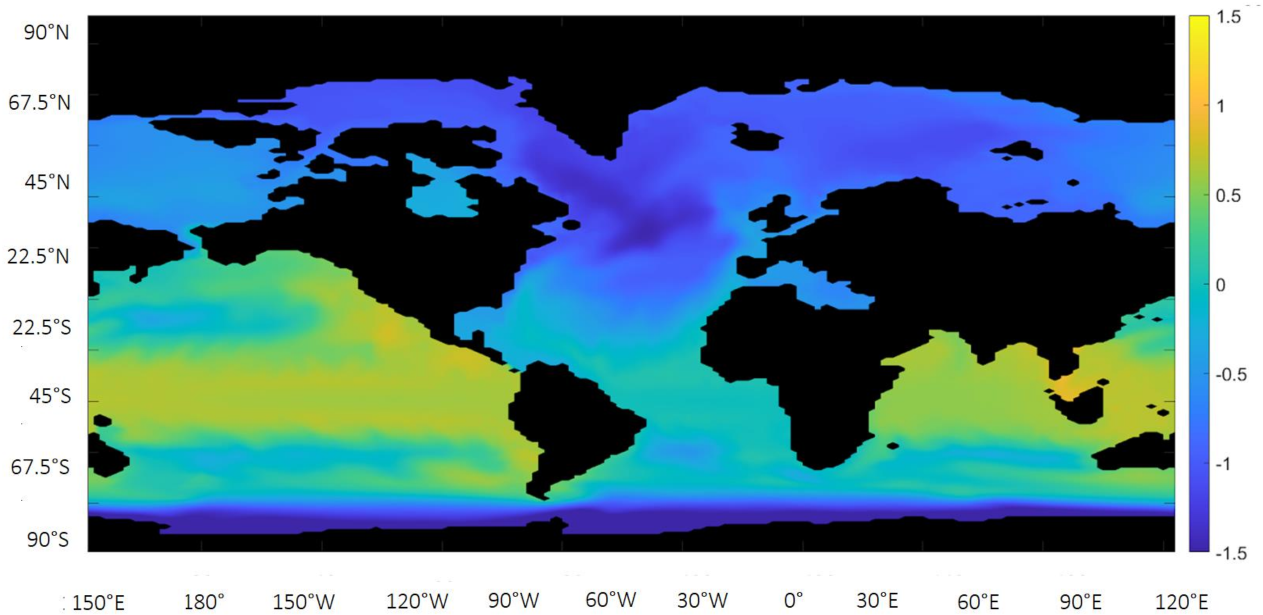

Figure 5.2 Plot of the FRUGAL control run (Run 1) surface height, in m, 1995-2004.

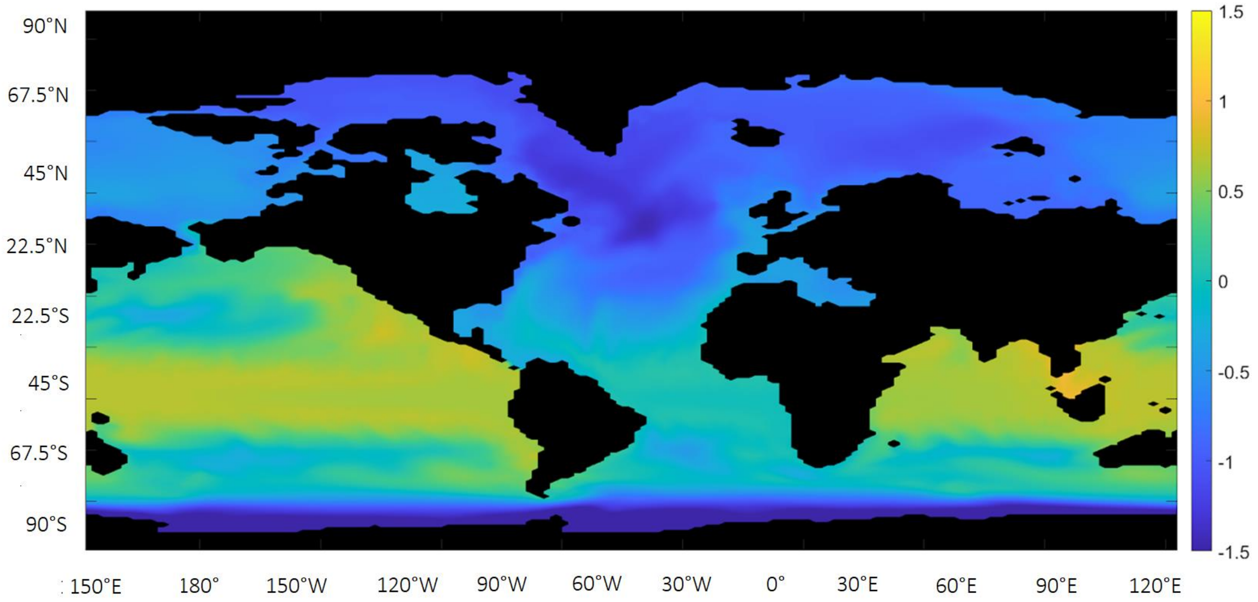

Figure 5.3 Plot of the FRUGAL Run 5 surface height, in m, 1995-2004.

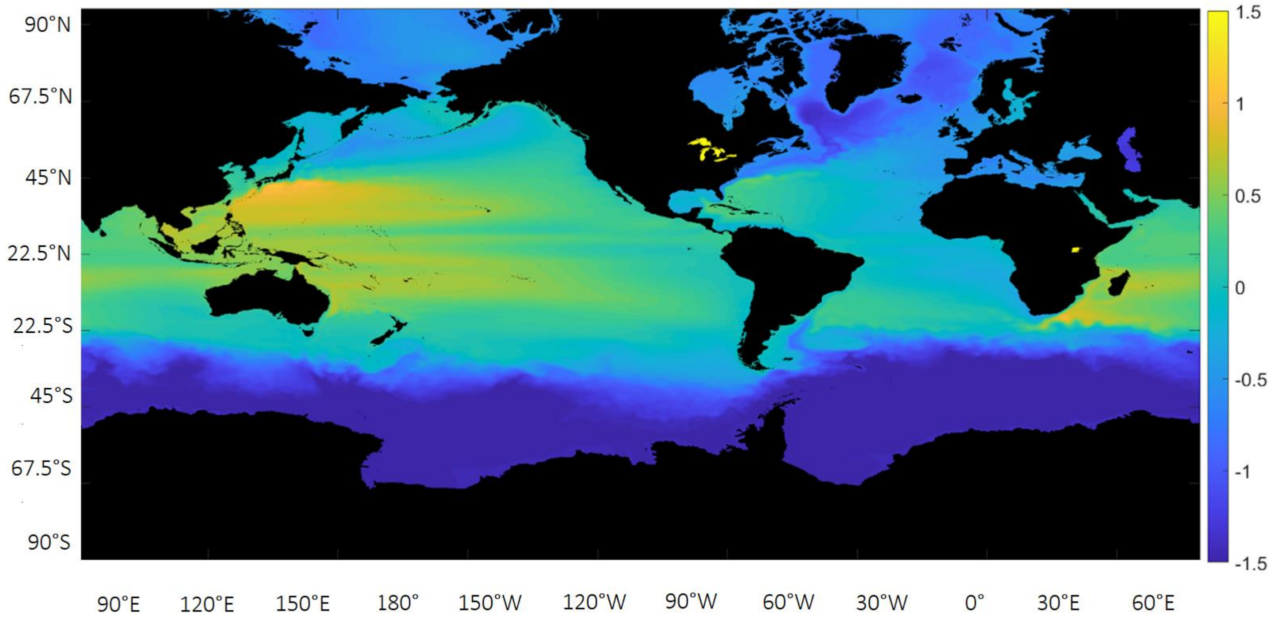

Figure 5.4 Plot of NEMO sea surface height above geoid for the period 1995-2004 in m.

The Gulf Stream has been introduced as a region of significant change. In fact, the increase/decrease above/below the Gulf Stream respectively, may suggest a weakening current strength, in line with observed results (see Dong et al., 2019) of a southward shift resulting in a weakening of the Gulf Stream, and an increase in sea surface height north of the current. To assess this, and the impact on other major ocean currents, further, Figure 5.5 shows the control run FRUGAL stream function, while Figure 5.6 shows the Run 5 FRUGAL stream function, with the control run subtracted. This has been done to highlight changes between the runs. In the control run, the large north-to-south variation in the Southern Ocean reflects a strong eastward Antarctic Circumpolar Current (ACC), while the difference between the low Gulf Stream region and the high mid-North Atlantic reflect the location of the Atlantic Meridional Overturning Circulation (AMOC). From Run 5, a large negative effect can be seen in the North Atlantic, in the subpolar gyre, acting to reduce the high-positive values found in this area in the control run, therefore implying a reduced AMOC strength. Additionally, patches of the Southern Ocean show an increase from the control run, while the region south and east of New Zealand show a decrease. This implies a marginal decrease in ACC strength in that region, due to reduced gradient differences. The FRUGAL runs 2-4 surface stream functions are available in the Appendices, Figures S9-14, for both discussed decades.

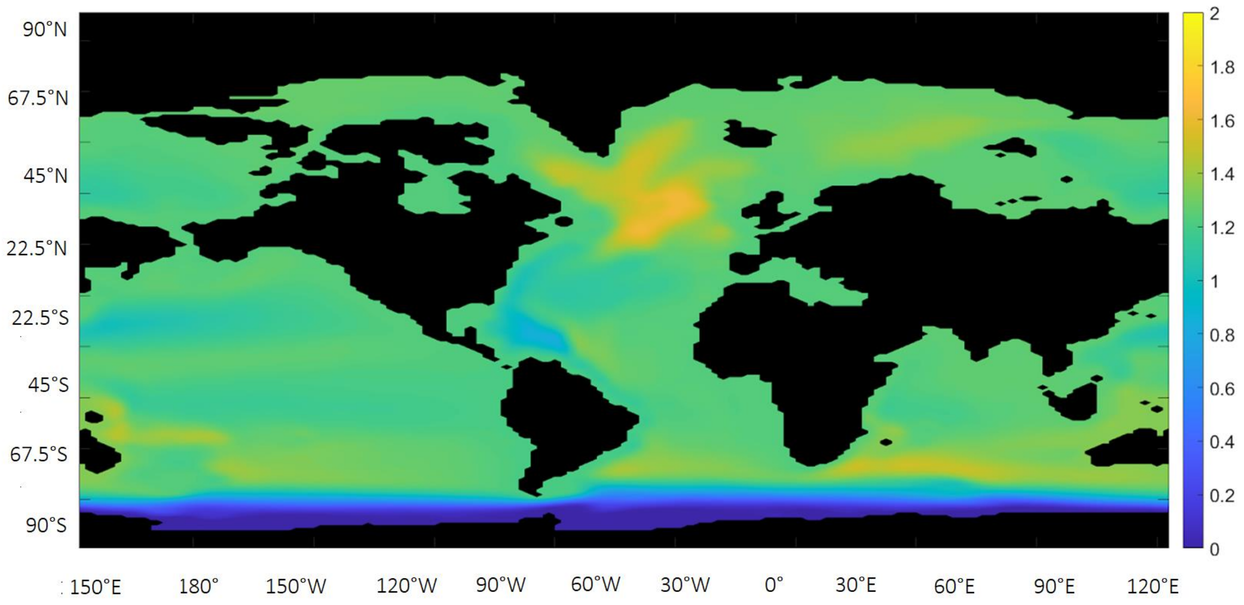

Figure 5.5 Plot of the FRUGAL control run surface stream function for the decade 1995-2004 in m (relative to zero at Antarctica).

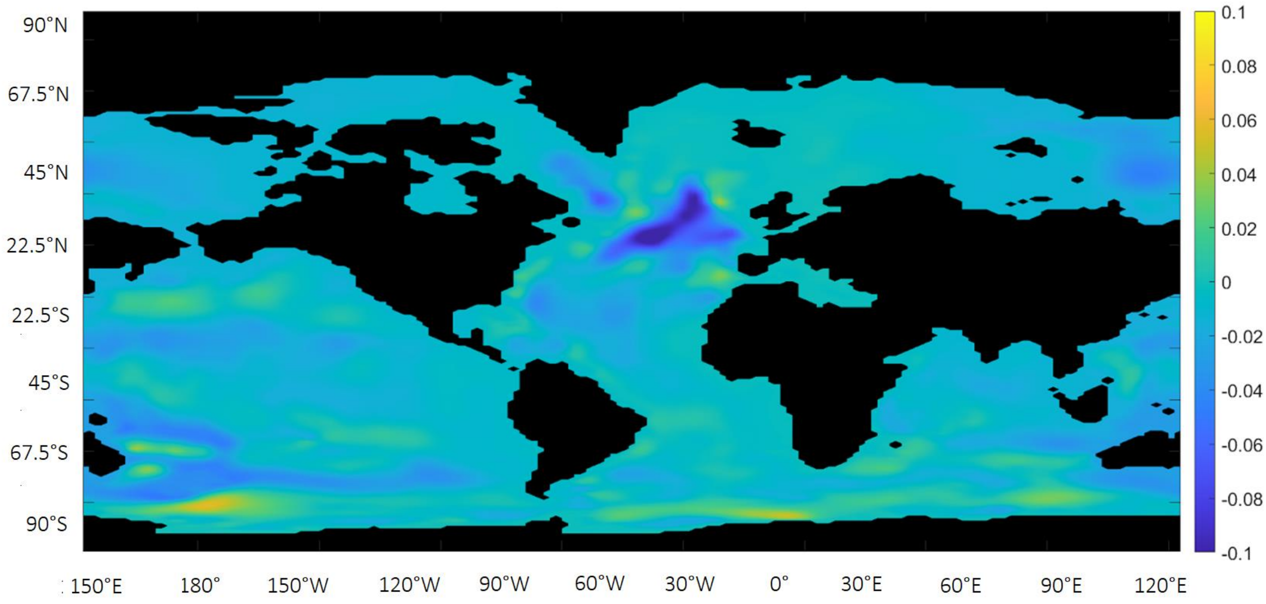

Figure 5.6 Plot of the FRUGAL Run 5 surface stream function for the decade 1995-2004, minus the control run for the same decade, in m.

5.2.2 The decade 2005-2014

Similar to the previous section, Figures 5.7-10 show the sea level height data from CMEMS, the FRUGAL control run and Run 5, and NEMO for the period 2005-2014 respectively. However this time, each plot has had the respective average for the decade 1995-2004 subtracted. All figures have again been plotted on the same scale to aid comparison. As such, it can be seen that the Gulf Stream area is showing significant and similar change in both the CMEMS and NEMO plots, while the FRUGAL runs show more extreme differences in the region. Additionally, the North Pacific region is showing large change between decades, and this is stronger in the CMEMS data than in the NEMO results, with the FRUGAL runs showing marginal change here. Some change can also be seen around the Aghulas retroflection in all plots, again this is stronger in the FRUGAL runs, but clearly visible in the CMEMS and NEMO results. The Drake Passage is showing minor decadal variation in the CMEMS data, and slight negative change in the NEMO results. The FRUGAL runs show clear negative effects, with the pattern of significant change along the ACC. Differences can also be seen between FRUGAL Run 1 and Run 5, with the control run showing greater positive change over Europe, while Run 5 shows larger negative change over the Newfoundland region. As Run 5 includes additional meltwater input compared to the control run, this suggests that even over relatively short timescales, increased freshwater input from the GrIS is affecting North Atlantic sea level height, through changes in ocean circulation (see stream function plots, Figures 5.11 and 5.12). However, while up to 0.2 m of sea level change can be easily seen between decades in some regions, the FRUGAL scale of change is larger than was seen in the satellite CMEMS data. The CMEMS and NEMO plots (FRUGAL to less clear) show the same pattern of change for the North Pacific and North

Atlantic suggesting a weakening of the western boundary currents during this decade compared to 1995-2004. The Pacific western boundary current is strongly related to the ENSO phase however over decadal timescale the Pacific Decadal Oscillation (PDO), and the cold PDO phase after 1990 has been linked to intensified current strength in the western Pacific (Hu et al., 2015) and is likely the dominant factor here as to why the decade 2005-2014 is shown to be weaker than the period 1995-2004. In the North Atlantic, a warming of the subpolar gyre in the mid 1990's was attributed to a strengthening of the AMOC, which weakened after 2005 with a cooling of the upper North Atlantic Ocean (Robson et al., 2016), therefore again the decade 2005-2014 is shown to be weaker than the period 1995-2004 in the CMEMS plot.

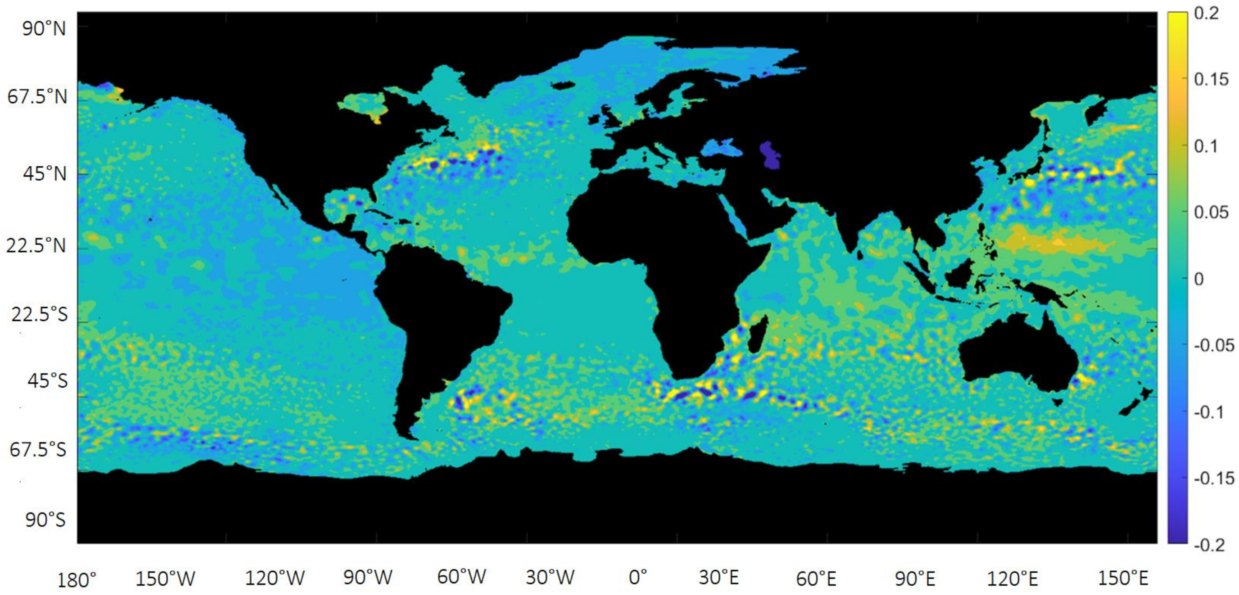

Figure 5.7 Plot of the average absolute sea level from the CMEMS dataset, in m, for the decade 2005-2014 minus the average for the decade 1995-2004, m.

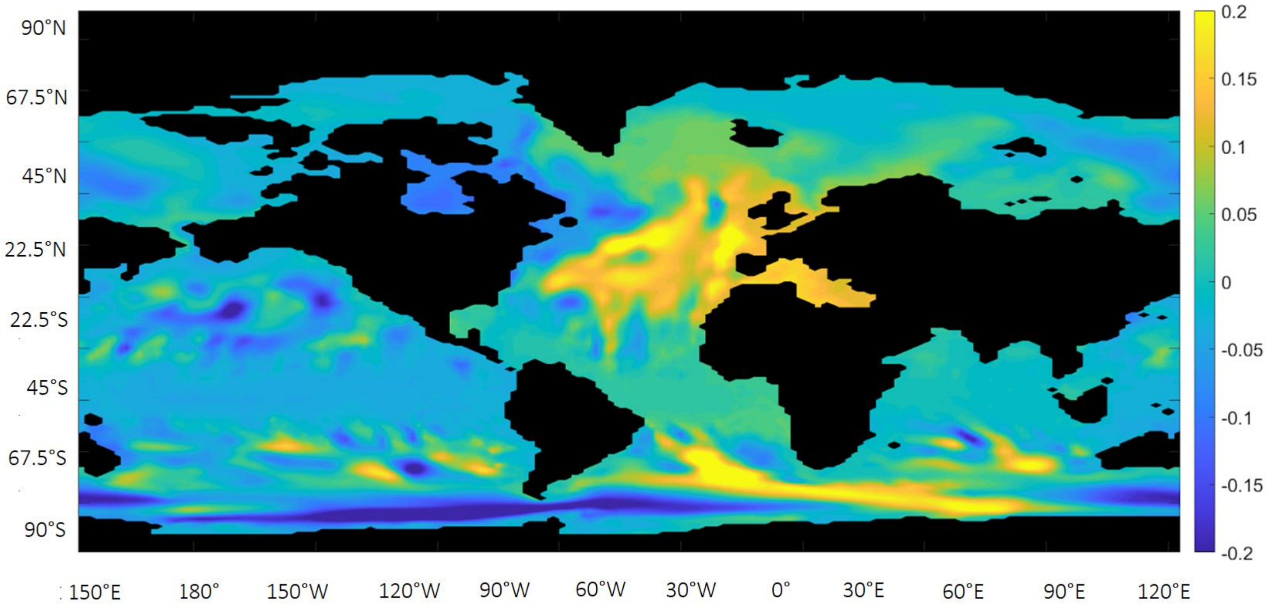

Figure 5.8 Plot of the FRUGAL control run (Run 1) surface height for the decade 2005-2014 minus the average for the decade 1995-2004, m.

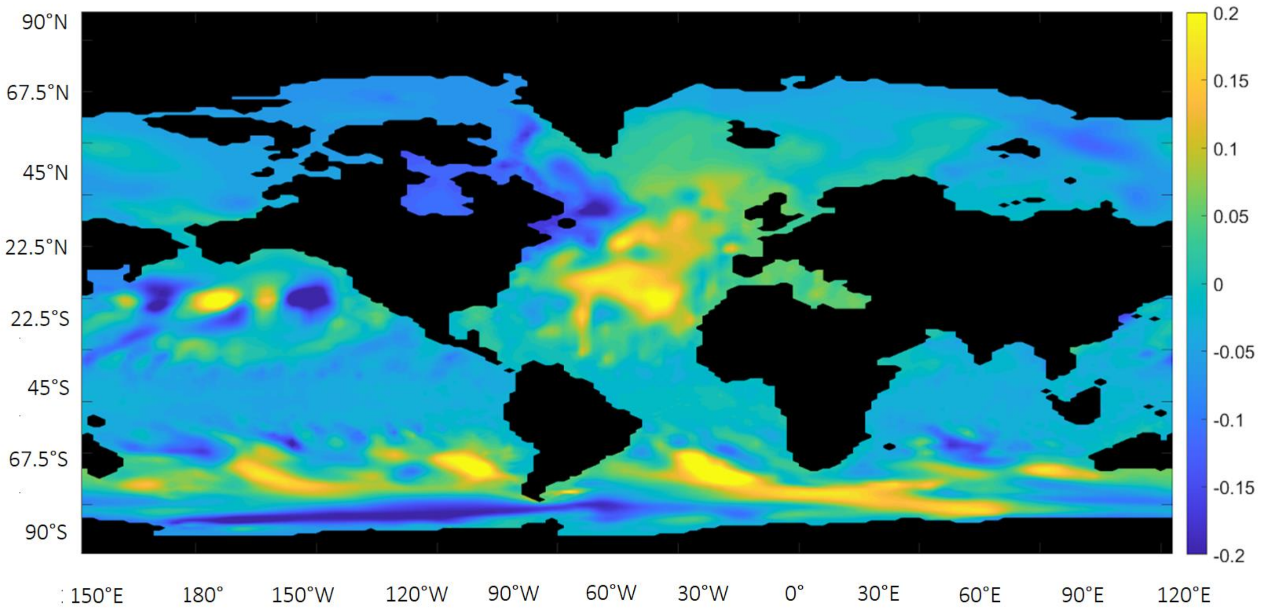

Figure 5.9 Plot of the FRUGAL Run 5 surface height for the decade 2005-2014 minus the average for the decade 1995-2004, m.

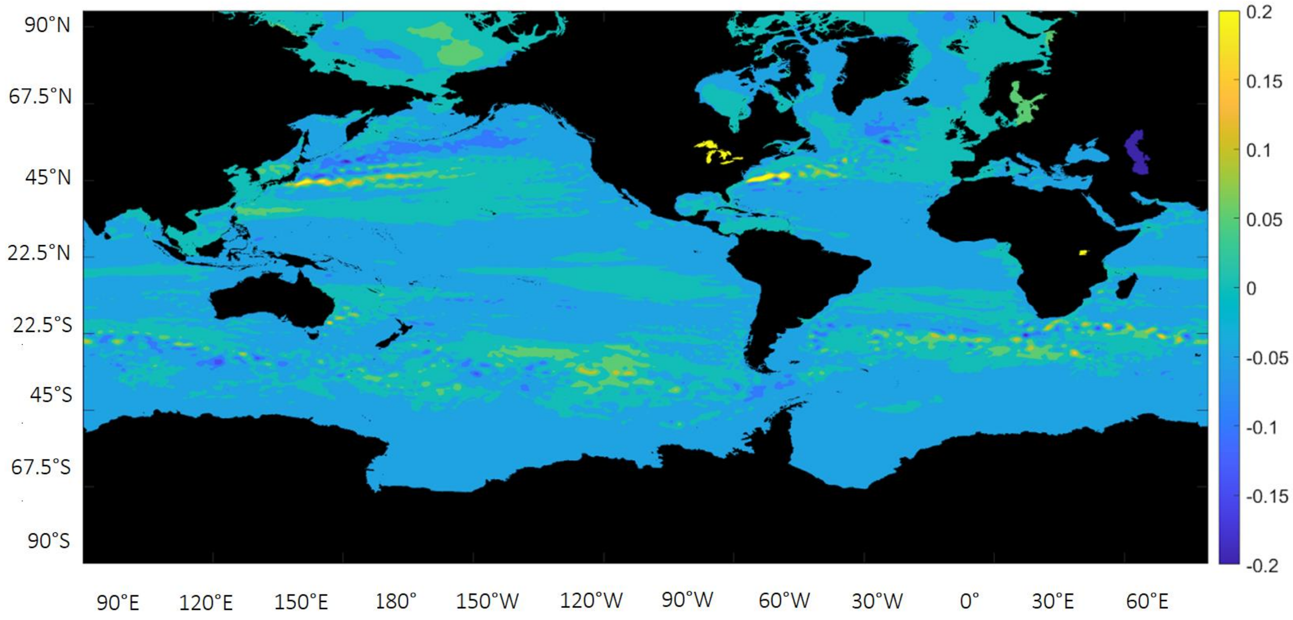

Figure 5.10 Plot of NEMO sea surface height above geoid (in m) for the decade 2005-2014, minus the average for the decade 1995-2004.

The control run FRUGAL surface stream function can be seen in Figure 5.11, while Figure 5.12 shows the Run 5 FRUGAL surface stream function, with the control run subtracted. This has been done to make freshwater input changes clear, rather than the plot being dominated by underlying decadal variations that are already visible from the control run. As discussed in the previous section, the North Atlantic Ocean shows the most significant change in these plots, aligning to regions of increased/decreased sea surface height in the previous figures. The additional freshwater in Run 5 acts to strengthen changes seen in the control run in the subpolar gyre, so in this instance is increasing the decadal variation. This may suggest a strengthening of surface currents around Greenland, e.g the Labrador Current, and an increased northern component of the AMOC, however note the reduced scale on Figure 5.12. Overall, the control run shows significant decadal change in the North

Atlantic, compared to the rest of the globe, and the additional freshwater in Run 5 is acting to strengthen some of the decadal changes visible in the control run.

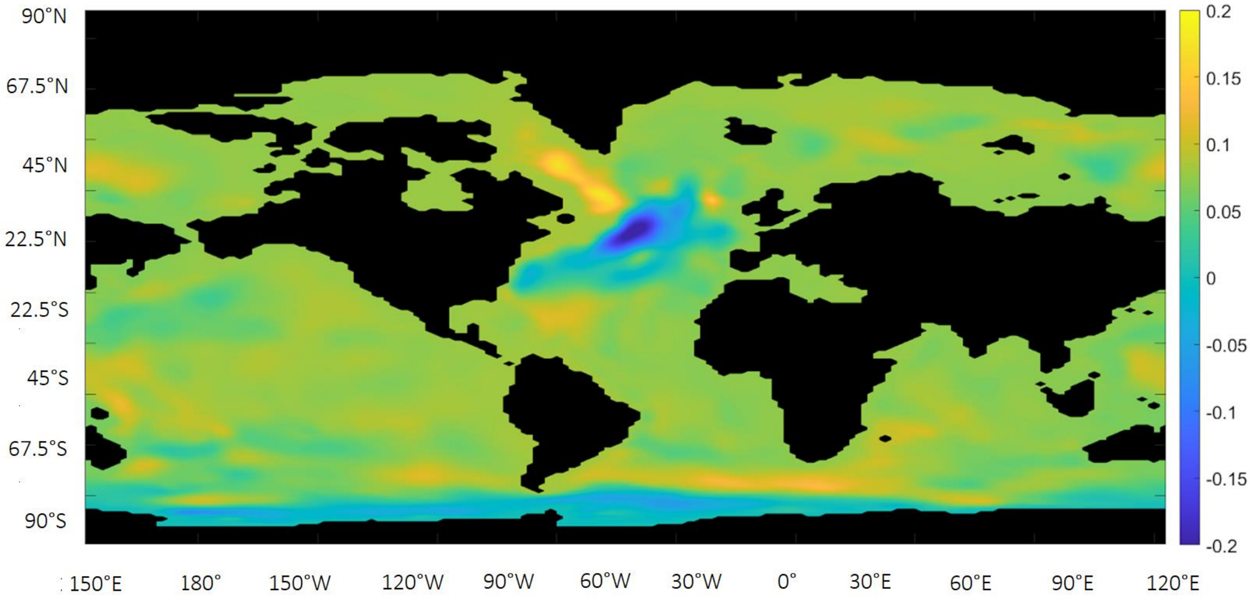

Figure 5.11 Plot of the FRUGAL control run (Run 1) surface stream function for the decade 2005-2014, minus the average for the decade 1995-2004, in m.

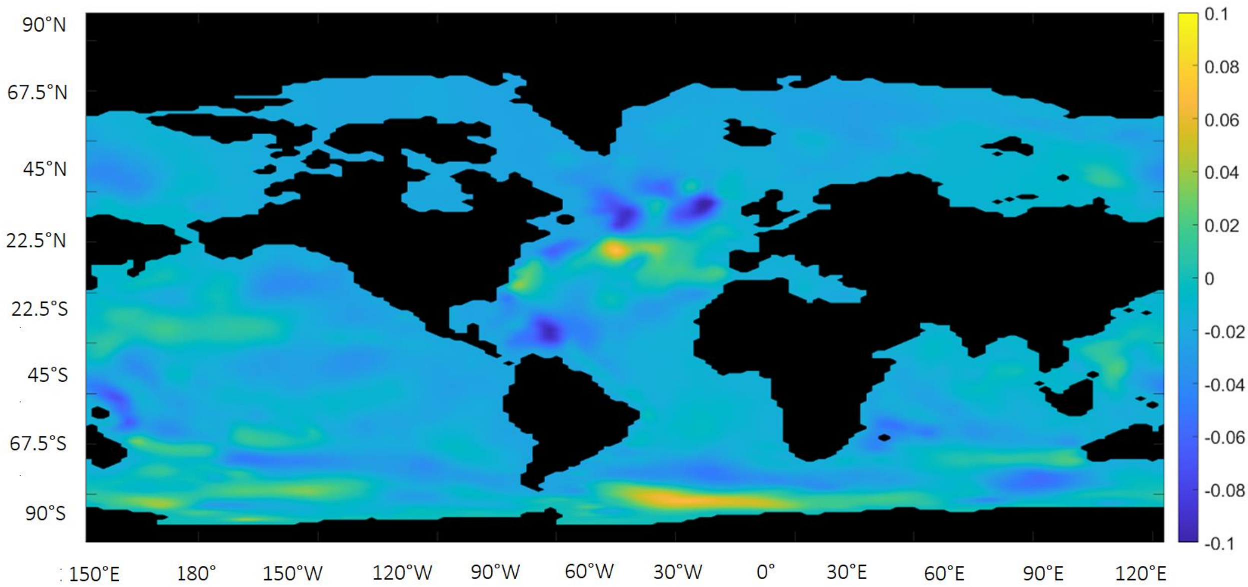

Figure 5.12 Plot of the FRUGAL Run 5 surface stream function minus the control run for the decade 2005-2014 in m.

5.2.3 The period 2015 to 2050

While this section goes beyond the FRUGAL timescale, it is interesting to assess likely sea level changes in the high-emission NEMO scenario, especially as the previous sections showed that the inputted meltwater is having some impact on sea level already. Figures 5.13-15 show the NEMO sea level variable, again minus the initial value, for increasing decades up to 2035-2044. These do not show wide-spread sea level rise, instead an uneven reaction is observed, with a steady increase across the time-period in the magnitude of this change. This is most clearly seen in Figure 5.15, where, while many areas do show an increase in sea surface height, many regions show an equally significant decrease, due to the changes being dynamic with a small overall change to sea surface height. This suggests that the increased runoff and global warming has an impact on the strength of ocean circulation, which in turn controls relative sea level, rather than just producing an overall increase directly linked with runoff. Overall, the Gulf Stream region and the Newfoundland area have been repeatedly highlighted as areas of significant change. The figures in this section support this while also showing how much the Southern Ocean is likely to change over time as well. Therefore, the following section is dedicated to analysing these selected regions in more depth: the Labrador Sea, the Drake Passage, and the Gulf Stream.

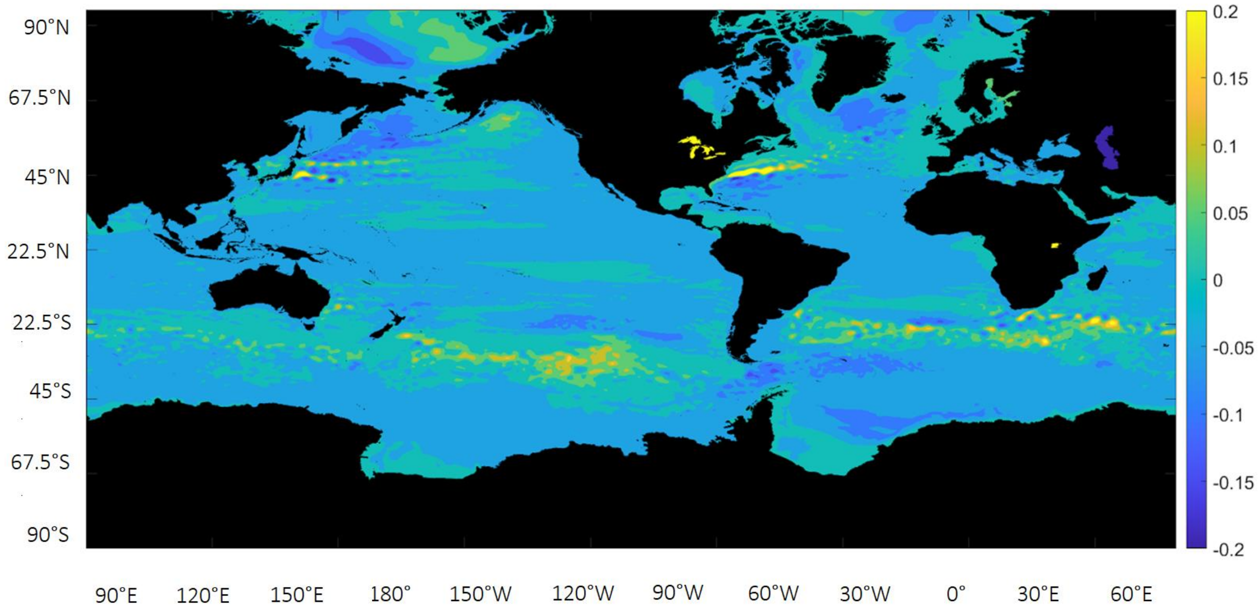

Figure 5.13 Plot of NEMO sea surface height above geoid (in m) for the decade 2015-2024, minus the average for the decade 1995-2004.

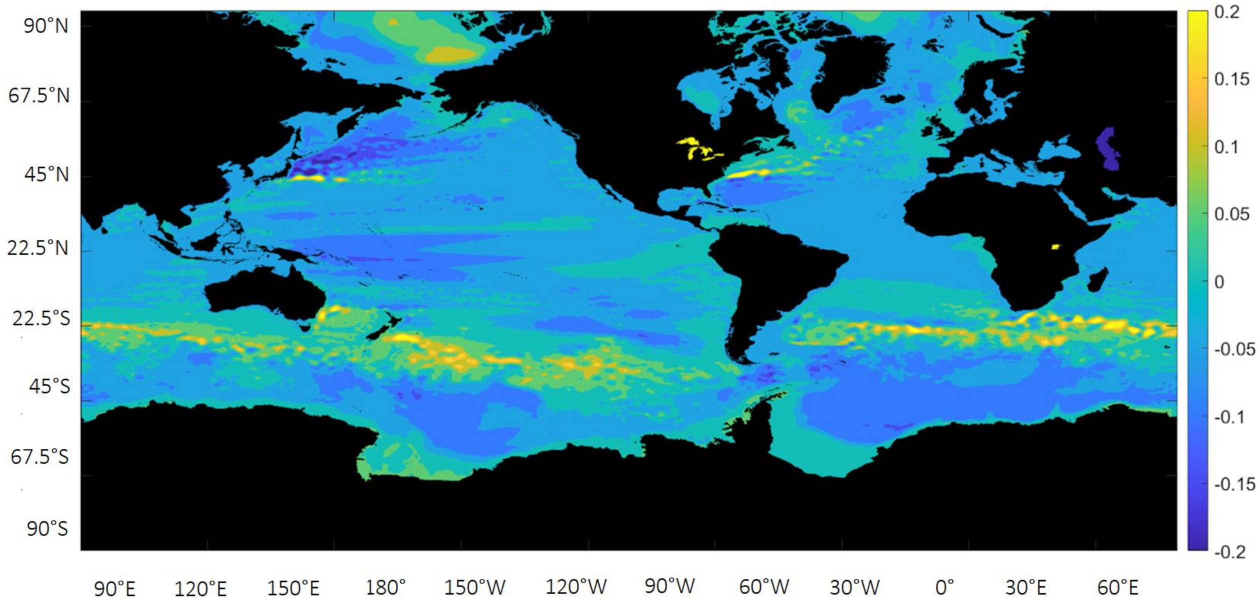

Figure 5.14 Plot of NEMO sea surface height above geoid (in m) for the decade 2025-2034, minus the average for the decade 1995-2004.

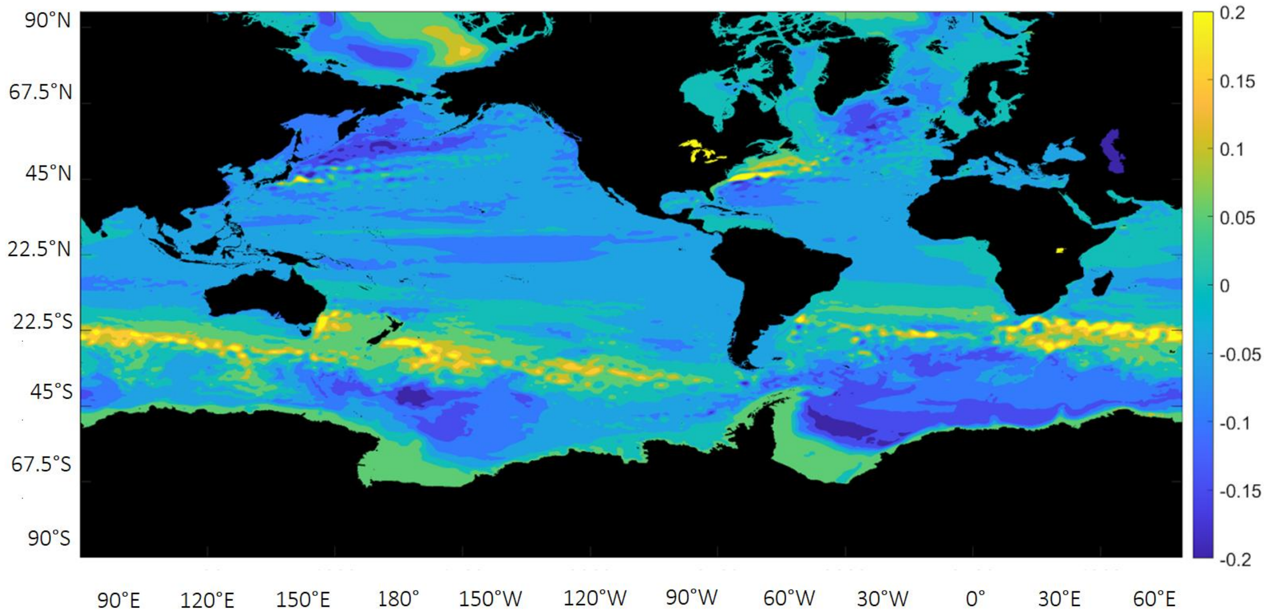

Figure 5.15 Plot of NEMO sea surface height above geoid (in m) for the decade 2035-2044, minus the average for the decade 1995-2004.

5.3. Regional Ocean Currents

5.3.1 The Labrador Sea

As discussed in previous chapters, the Labrador Sea is an important region of North Atlantic Deep Water (NADW) formation, a significant component of the Atlantic Meridional Overturning Circulation (AMOC). It is also a region of high iceberg-ship interaction. In this section, the hypothesis that was introduced in Chapter 3, Section 3.2.3.2 is tested. That is, while surface salinity is decreasing, as the additional freshwater is having a negative effect on the Atlantic Overturning Circulation the Labrador Sea is experiencing less mixing and is therefore more stratified. As this was identified in the FRUGAL run, the NEMO model outputs have been used in Figure 5.16, to show the vertical ocean mass transport at the surface in the Labrador Sea for January 1983. The marked black line shows the transect, the timeseries of which can be seen in Figure 5.17. This shows a slight reduction between the late 1990’s and 2015, excluding peaks in 2009-10. This is potentially linked to the 2000’s warming hiatus (see Fyfe et al., 2016), which was concluded to be a result of decadal scale ocean variation, including a negative phase of the Interdecadal Pacific Oscillation decreasing tropical Pacific sea surface temperatures, however this can not be proven here. Overall, these figures support the suggested theory, by showing that vertical mixing is reduced by 2015 compared to 1983. This decreasing trend continues to 2050, suggesting that vertical mixing will halve by 2050 compared to the early 1980’s. This is likely to have an effect on the AMOC, through decreased NADW formation (see section 5.2.4 for current AMOC trends). However, transport variability over the shelf is not obviously linked to the formation of deep, dense water in the Labrador Sea, which usually occurs away from the shelves. Therefore, perhaps the decreased vertical transport is related to the (likely very) reduced sea ice cover by 2050. While this may act to increase vertical mixing, as the sea surface is more exposed to wind driven mixing, perhaps with warming (from current) Labrador Current waters travelling south, the smaller temperature difference in the water column is overall reducing vertical mixing.

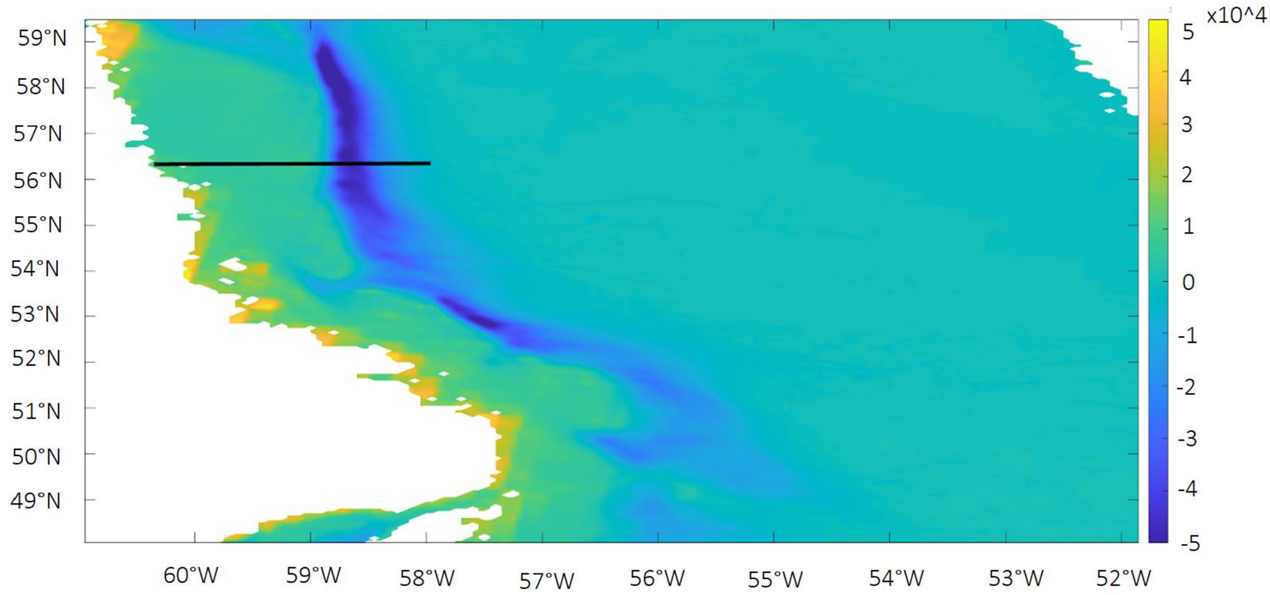

Figure 5.16 Plot of the NEMO vertical ocean mass transport (integrated over the length and width of the transect) at the surface in the Labrador Sea for January 1983, with the transect marked with a black line (kg/m2/s).

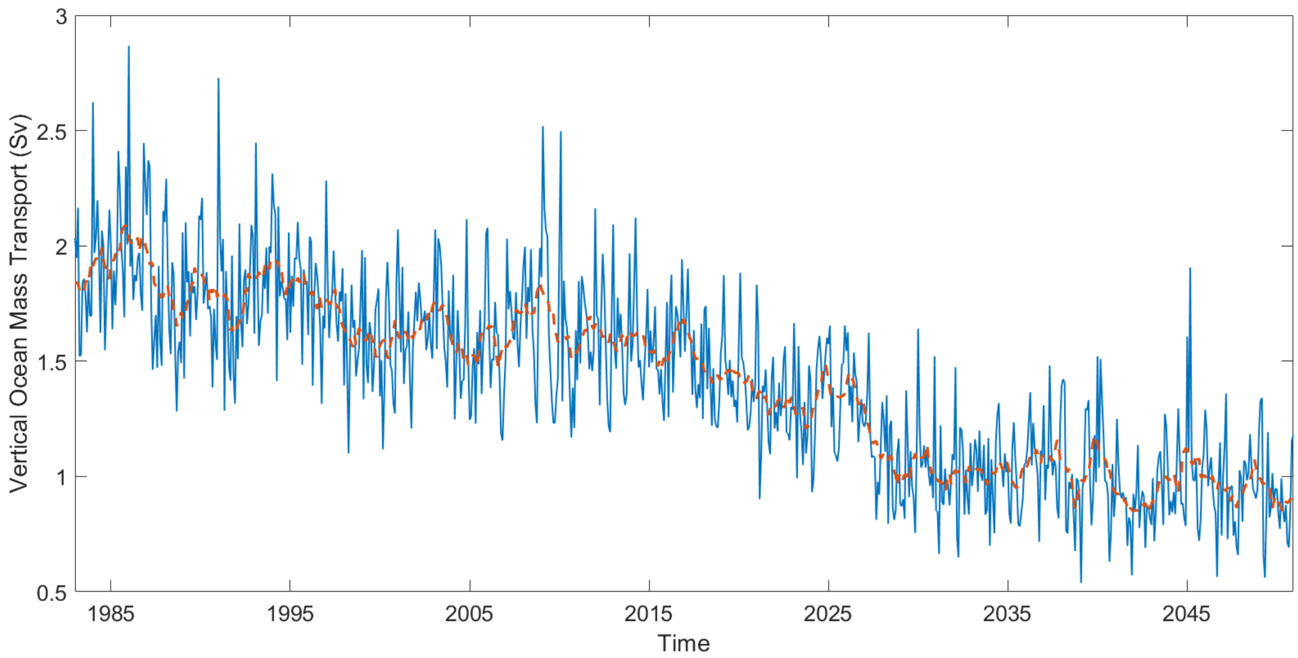

Figure 5.17 Plot of the average vertical ocean mass transport from the Labrador Sea transect over time (Sv), in the NEMO run, with a 12-month moving average overlaid in orange.

5.2.2 The Drake Passage

The Drake Passage plot in the FRUGAL chapter (see Chapter 3, Figure 3.21) showed that Run 5 deviated significantly from Runs 3 and 4. This was identified as unusual, as in previous location plots, while the runs did deviate from each other, they followed similar patterns. It seems useful to try and identify what is causing this difference, especially as the Southern Ocean was found to show significant change in the sea level plots. To achieve this, the NEMO run has been used to plot the average horizontal ocean mass transport of the transect from South America to the Antarctic over time. This transect can be seen in Figure 5.18, which is also showing the surface ocean mass transport for January 1983. The horizontal mass transport has been considered here, rather than the upward transport seen in the previous section, as the main ocean current in the region is the horizontal Antarctic Circumpolar Current (ACC). Figure 5.19 shows horizontal ocean mass transport averaged over the whole depth profile between 1983 and 2050. This shows a consistent positive transport, with a slight decadal oscillation from 1983 to 2015, followed by a slight decrease to 2045, with a subsequent sharp decrease to 2050. Overall, this suggests that this is a region that is not showing significant change by 2015, and that variable ocean current strength here is not responsible for the anomalous Run 5 result. However, longer term the plot is showing a decrease in transport through the Drake Passage, suggesting an overall weakening of the ACC on a similar percentage scale of decrease as that seen in Figure 5.17 and NADW formation. This suggests a potential connection between the two, but more analysis would need to be done to be sure. However, as 2015 is the point at which the NEMO runs switch, this may be a modelling quirk rather than a useful result. As the Drake Passage is a very well observed region of the Southern Ocean, it is worth noting that total transport through the Drake Passage tends to be slightly higher than the NEMO output suggests, including an estimated 123 Sv from Whitworth and Peterson (1985) and 157 Sv from Xu et al. (2020). This is likely a result of only considering the horizontal mass transport from the NEMO model, due to the ACC (travelling eastwards) dominating transport in the region.

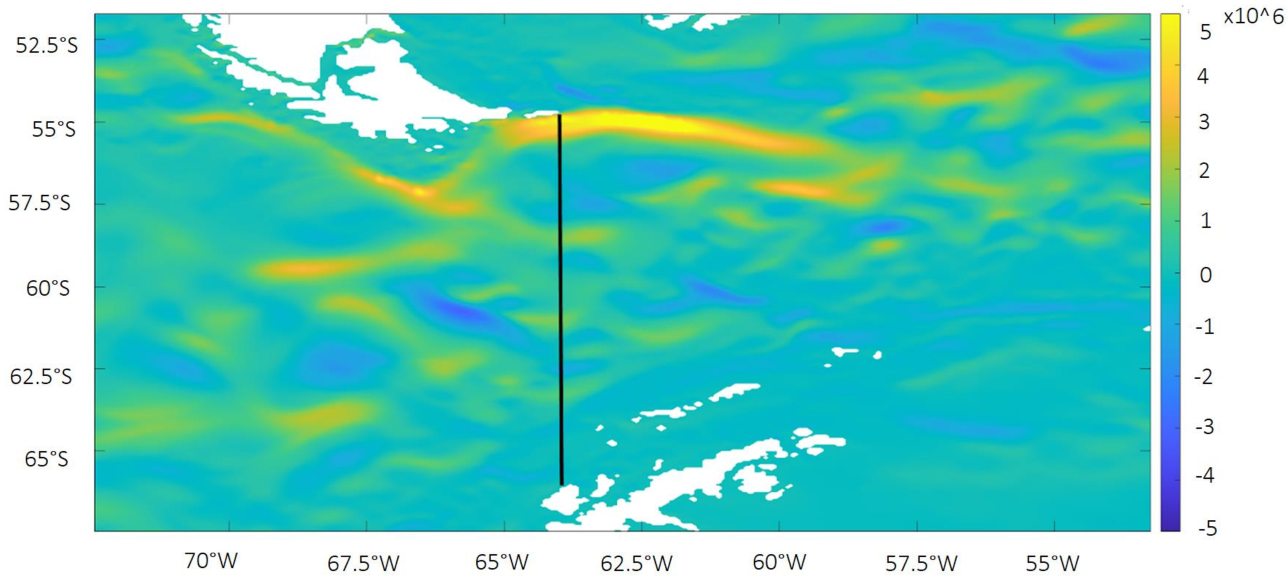

Figure 5.18 Plot of the horizontal ocean mass transport (integrated over the whole depth profile) but shown at the surface for January 1983 to visualise the transect location, with the transect marked with a black line (kg/m2/s), in the NEMO run.

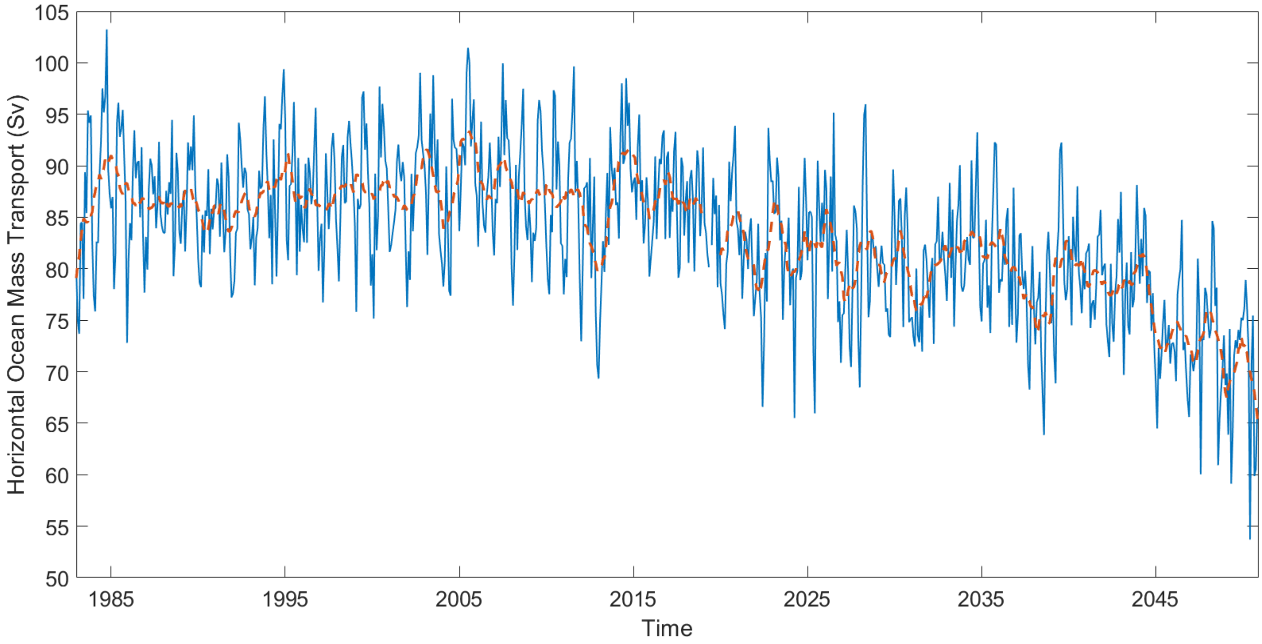

Figure 5.19 Plot of the average horizontal ocean mass transport from the Drake Passage transect over time (Sv), in the NEMO run, with a 12-month moving average overlaid in orange.

5.2.3 The Gulf Stream

The Gulf Stream, located along the East American coast, is responsible (along with the Florida Current, the North Atlantic Current and Norwegian currents) for carrying warm, sub-tropical water northwards towards the Arctic and significantly affects Northern Hemisphere climate (Palter, 2015). Section 5.1.2 first identified this region as showing a strong signal in the sea surface height above the geoid. Figure 5.20 shows the location of three transects across the Gulf Stream separation region, while Figure 5.21 shows the integrated (across the whole depth profile) horizontal ocean mass transport from these Gulf Stream transects between January 1983 and December 2050, applying a 12-month moving average. This clearly shows a decrease after 2010, excluding a peak in 2028, for the B transect. Additionally, after a sharp decrease, the magnitude of transport remains consistently low from the mid 2010's onwards. After 1995, the A transect remains consistently around zero across the rest of the time period (likely due to enough recirculation to cause the net transport to be small), whereas the C (which is closer to the Florida Current that detaches at Cape Hatteras) transect shows a clear increase during the period of decrease for the B transect, between 2013 and 2023. However, overall the inputted meltwater and global warming is appearing to have an overall weakening effect, as the A and B transects show a significant decrease from earlier in the time period. Transect C shows an increase from 2030 onwards in line with transect B decrease, in a similar way to the late-2010's and early 2020's. This suggests a weakening/slowdown of the Florida Current/Gulf Stream and an associated reorientation towards the north, with a weaker detachment at Cape Hatteras. This is supported by Andres (2016) who suggests a weaker Gulf Stream is more easily unstable near Cape Hatteras than when it is stronger. Overall, it is likely to be this effect observed here, rather than a northward shift of the current.

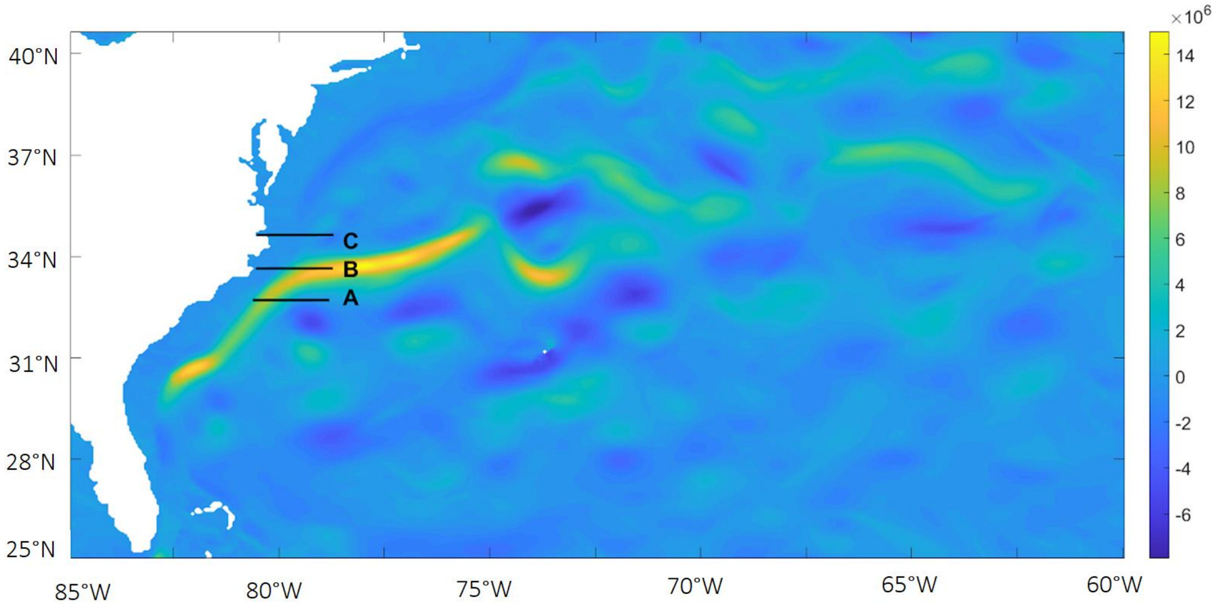

Figure 5.20 Plot of the horizontal (east-west) ocean mass transport (integrated over the whole depth profile) but shown at the surface for January 1983 to visualise the transect location, with the three transects marked with black lines (kg/s), for the NEMO run.

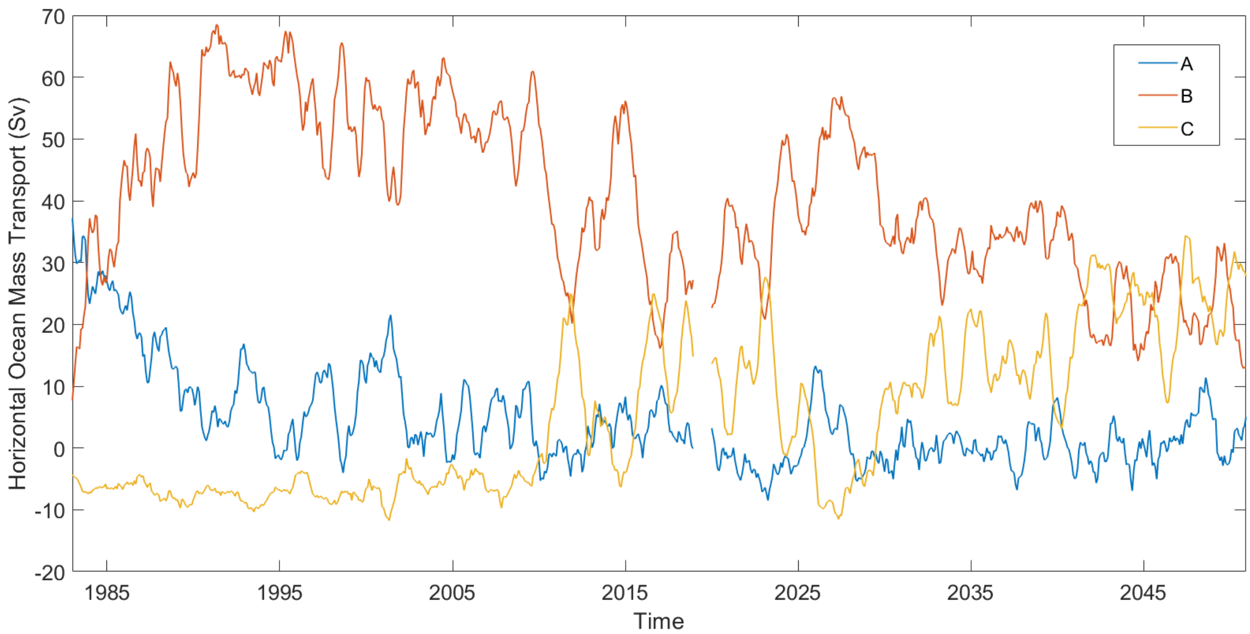

Figure 5.21 Plot of the average horizontal ocean mass transport for the three Gulf Stream transects over time, with a 12-month moving average applied (Sv), for the NEMO run. Note the missing data for June 2020.

As the Gulf Stream can be identified by large warm-cold sea surface temperature gradients (Siqueira & Kirtman, 2016), it is interesting to test whether the FRUGAL and NEMO models show sea surface temperature changes in the Gulf Stream region. The NEMO sea surface temperature for each transect in Figure 5.20 can be seen in Figure 5.22. Region A, shown to have the most consistent transport across the time period, also has little yearly variation in temperature, but does show a general and sustained increase overall. Region B shows an increasing temperature between 1983 and 2015, followed by a relative 'flattening'. Region C shows a 10°C increase in sea surface temperature between 1983 and 2050, and therefore supports a northern reorientation of the Gulf Stream. As this region is normally supplied by cold water coming in from the Labrador Sea, if waters there warm, so will the waters south of Delmarva Peninsula (to the east of Washington, DC). All regions show a steep increase at 2050, but this is likely a model reaction rather than a realistic result. Overall, the NEMO sea surface temperature results suggest a reorientation northward rather than a clear increase/decrease in Gulf Stream strength. The FRUGAL runs have been plotted in Figures 5.24-26, with the box locations (that have been averaged over) visible in Figure 5.23. Here all FRUGAL runs have been included for completeness. Box C shows a steady decrease in all runs across the time period, while box A shows a peak temperature around 2003, followed by a marginal decrease. Box B shows variations between runs, however overall the control Run 1 can be seen to show generally lower temperatures than the other runs, with additional freshwater. However, when compared to the NEMO plot, Region A and B are showing significantly lower sea surface temperatures: close to 14°C in FRUGAL and 18-

24°C in the same time period in NEMO. Additionally no statistically significant correlation was found between the FRUGAL runs and the NEMO results, in any region. Nevertheless, the Gulf Stream region is shown to exhibit visible change in both models.

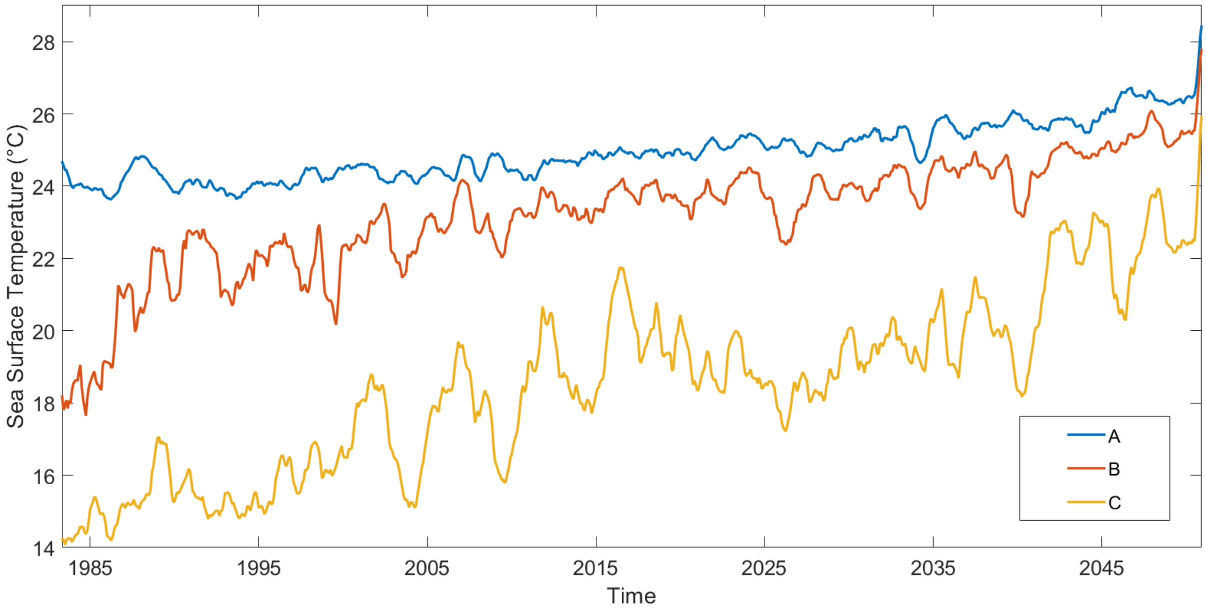

Figure 5.22 Plot of NEMO sea surface temperature for the three transects marked in Figure 5.20, applying a 12-month moving average.

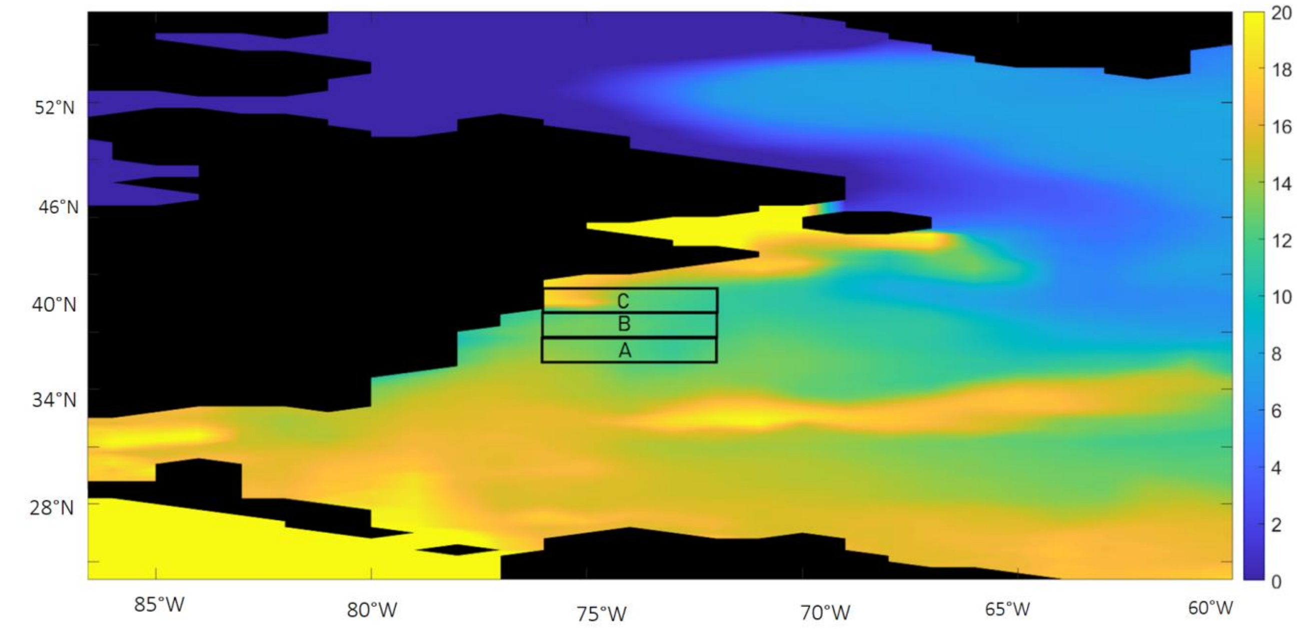

Figure 5.23 Plot of FRUGAL sea surface temperature with the boxes used in this section marked in black. The background is the control run for spring 1983.

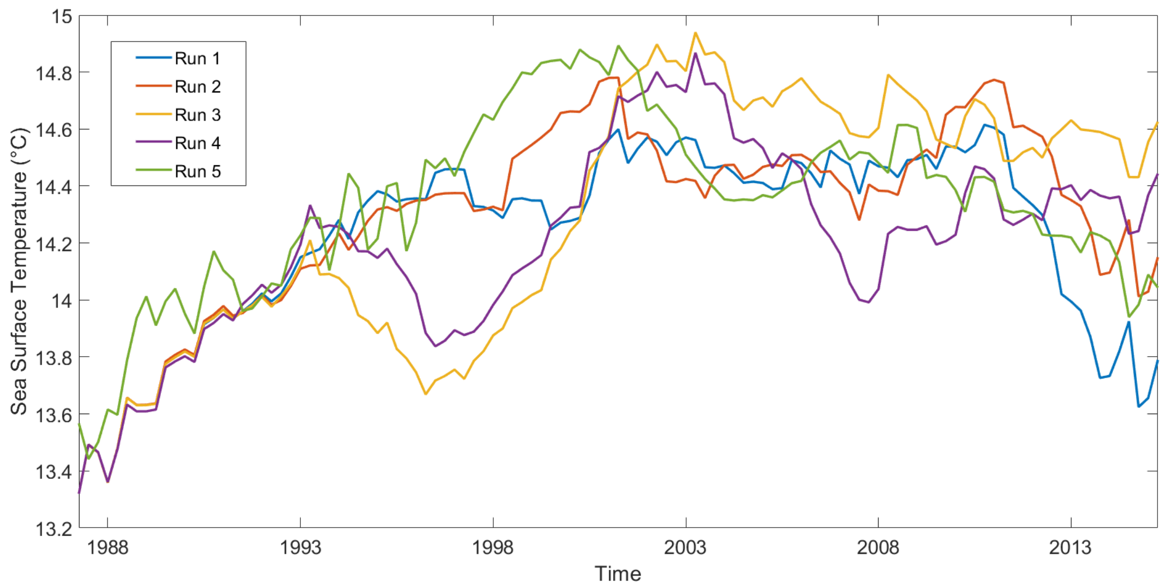

Figure 5.24 Plot of the FRUGAL runs averaged over box A, for sea surface temperature (°C).

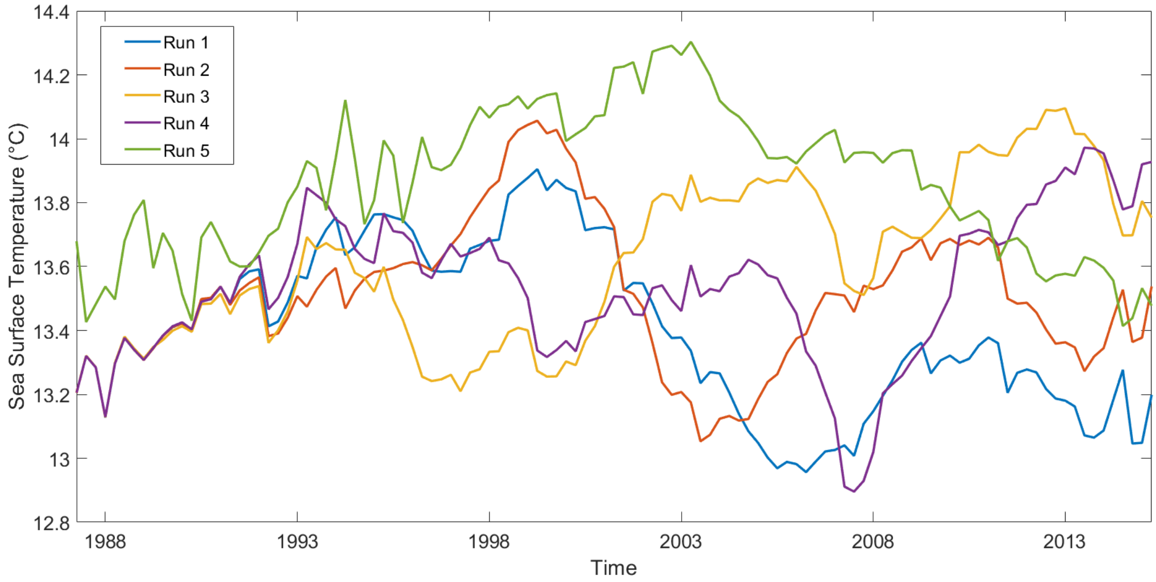

Figure 5.25 Plot of the FRUGAL runs averaged over box B, for sea surface temperature (°C).

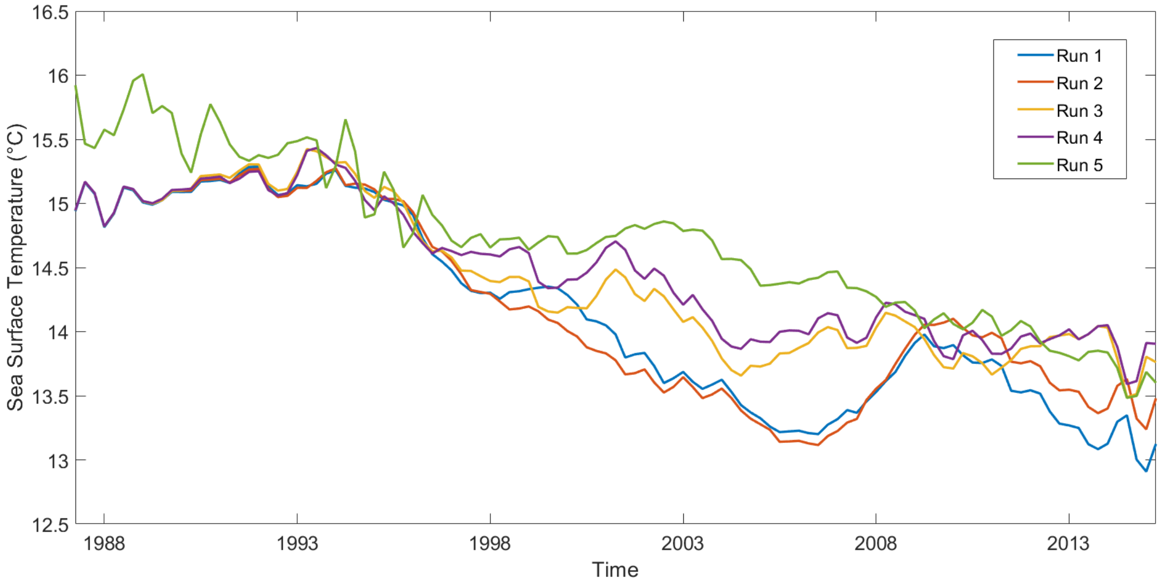

Figure 5.26 Plot of the FRUGAL runs averaged over box C, for sea surface temperature (°C).

5.2.4 The Atlantic Meridional Overturning Circulation

Due to the focus throughout this chapter on the North Atlantic and the Gulf Stream, it is interesting to try and quantify how the AMOC has varied from 1983-present. The NEMO model includes an overturning heat transport variable, at 26°N, between 1983-2015, while the RAPID dataset (Frajka-Williams et al., 2021) records Meridional Overturning Strength (MOC) at 26°N between 2004 and 2020 (see McCarthy et al., 2015), data available at https://rapid.ac.uk/rapidmoc/rapid_data/datadl.php, as well as heat transport data (Johns et al., 2011) available at https://rapid.ac.uk/rapidmoc/rapid_data/heatflux.php. Figure 5.27 shows the RAPID MOC in blue, with a 12-month moving average in orange, to remove the strong seasonal cycle. In section 5.3.1, Figure 5.17 showed a gradual decrease in upward ocean mass transport from the Labrador Sea between 2015 and 2030, which can not be confirmed here due to the short timescale and lack of directly comparable data. However, there is a suggestion of a 'flattening' of the MOC between 2014 and 2018, and potential decrease beyond this point. Figure 5.28 shows the RAPID and NEMO heat transports; these variables have a correlation of 0.45 (significant at the 1% level). It can be seen that while the values of the 12-month moving average are very similar, the NEMO data shows significantly greater seasonal variation. Overall, the NEMO data is shown to be interesting for comparison with the RAPID dataset, but ultimately not useful in directly predicting changes in the AMOC by 2050, due to restricted timescales.

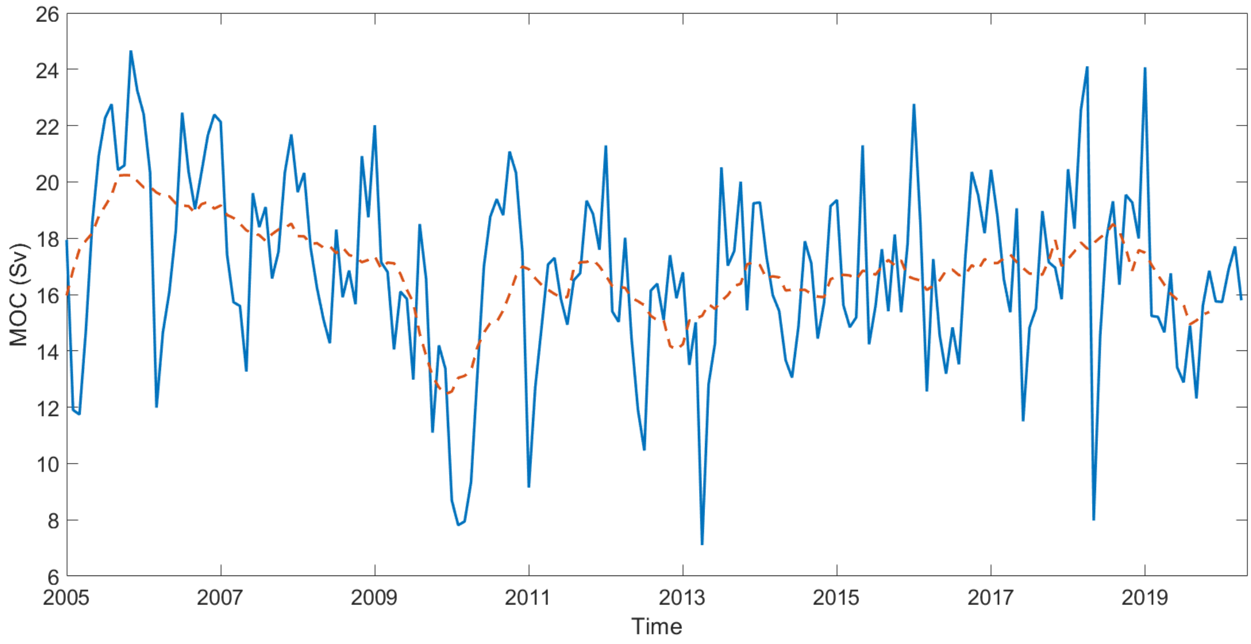

Figure 5.27 Plot of RAPID Meridional Overturning Circulation (MOC) at 26°N (in blue) with a 12-month moving average in orange.

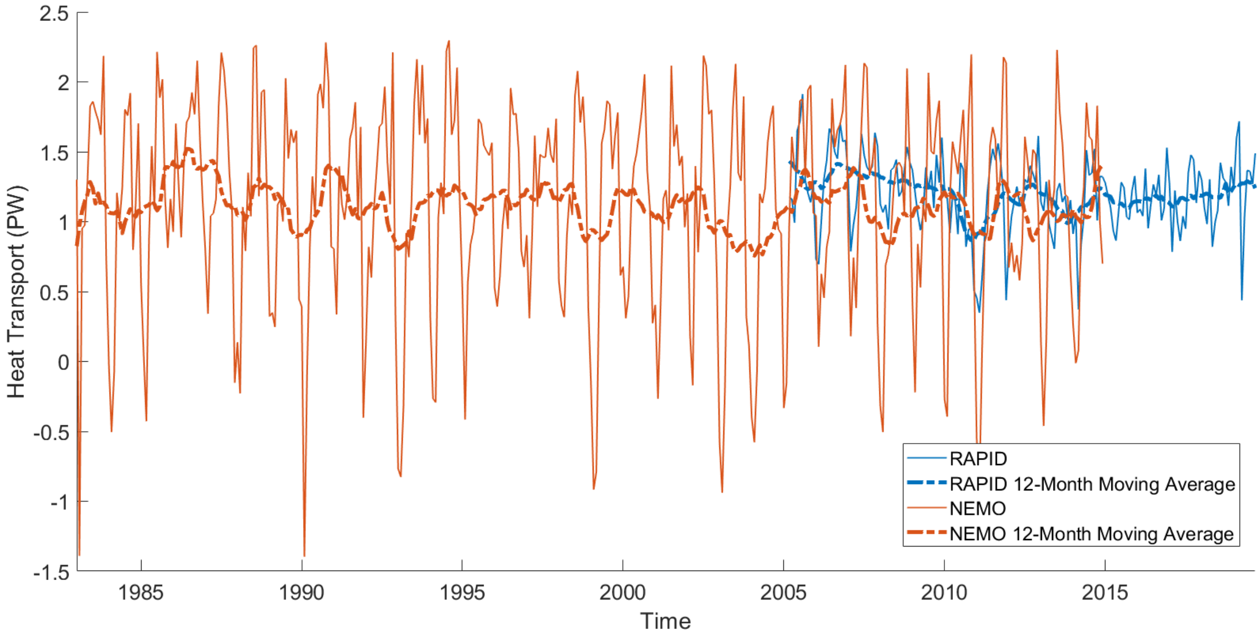

Figure 5.28 Plot of RAPID heat transport (blue) and NEMO overturning heat transport (orange) at 26°N, with a 12-month moving average applied.

5.3 Discussion and conclusions

This chapter has in part used the high-complexity NEMO model to verify and answer questions from the FRUGAL runs, while also combining these model results to produce an overview of likely global sea level changes by 2050. Additionally, the CMEMS sea level dataset has been included to verify that both the models produce realistic patterns of sea level change between 1995 and 2014, and are therefore valid in this context. While there is inevitably some difficulty in comparing different modes, with different available variables, it does add significance to the reached findings.

The NEMO run was used to show that in the Labrador Sea, while sea surface salinity decreases, the additional freshwater has a negative effect on the overturning circulation, and therefore experiences less mixing and becomes more highly stratified. The Drake Passage findings were less conclusive, only suggesting that it is unlikely that changes in ocean circulation in the region were contributing to the variations in FRUGAL Run 5 results (see Chapter 3, Figure 3.21). Therefore, either the run is being influenced by another external variable, or it is misrepresenting this particular region (or both models could be misrepresenting the dynamics here). This seems possible as the model is specifically designed to best represent the North Atlantic and has a lower resolution in the Southern Ocean. The Gulf Stream region, which has been repeatedly highlighted throughout this chapter, appears to show an overall decrease in strength by 2050, in the major transect selected.

Regarding sea level, the combination of model outputs and the comparison with the CMEMS dataset allows some significance to be attributed to the findings that increased meltwater input will not necessarily result in wide-scale sea level rise (although a net sea level rise is expected). Instead the dominant factor influencing sea level will be the changing strength of ocean circulation patterns, which may therefore result in greater annual variation in sea level, with the associated difficulties in protecting coastlines from storm surges. When combined with enhanced extreme weather events associated with climate change, large scale flooding is highly likely. A major example of this is that the changing strength in the Gulf Stream is likely to affect the North-East American coastline, in an area which is already highly susceptible to (likely increasing) hurricane damage. Hurricane Sandy, in 2012, resulted in around US$ 20 billion losses in New York alone (Hinkel et al., 2018). As a leading economy, the USA is theoretically well placed to adapt to such levels of environmental hazards, however this has not been historically true. When rising sea levels are included, the potential repercussions are clear. With this in mind, it is interesting to assess how well the NEMO model captures sea level rise in the regions marked in Figure 5.29. Figure 5.30 shows the NEMO average sea level height compared to the CMEMS average between January 1995 and December 2015. This shows how closely the NEMO model fits to the satellite data during the observation period, and this is further confirmed when the correlation is included. All regions had statistically significant correlation, at the 1% level, with Region A recording 0.51, Region B 0.53, and Region C 0.55. Therefore, while the scale of results is unlikely to be accurate, the trend is useful to consider to 2050. This has been plotted in Figure 5.31, with the seasonal noise removed. This shows that regions A and B, New York and Washington, are likely to see gradual sustained increases in sea level, while Region C, between Jacksonville and Miami, is showing greater yearly variation, but does ultimately appear to increase over time. Overall, all three regions, chosen due to their significant population size, are shown in the NEMO outputs to experience an increasing trend in sea level. Although it is worth noting that in all regions, there is not shown to be a significant difference in sea level between 2025 and 2050. However there does appear to be an increase in interannual variation, which would still have significant effects on flooding risk if accurate.

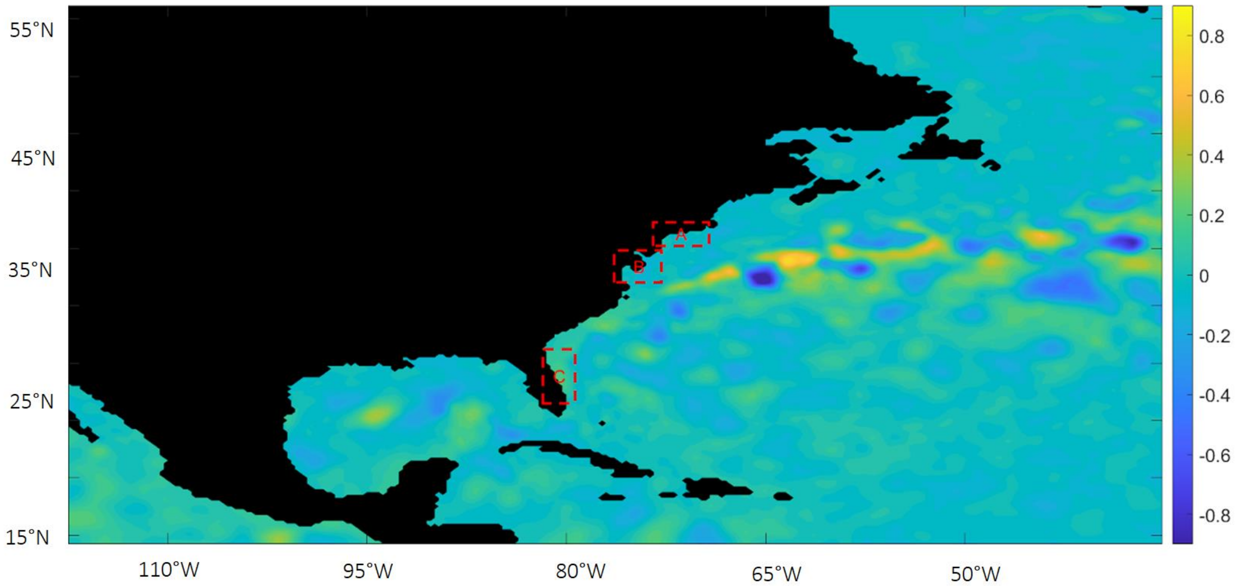

Figure 5.29 Showing the 3 considered regions, marked on the sea surface height above geoid plot for January 1983.

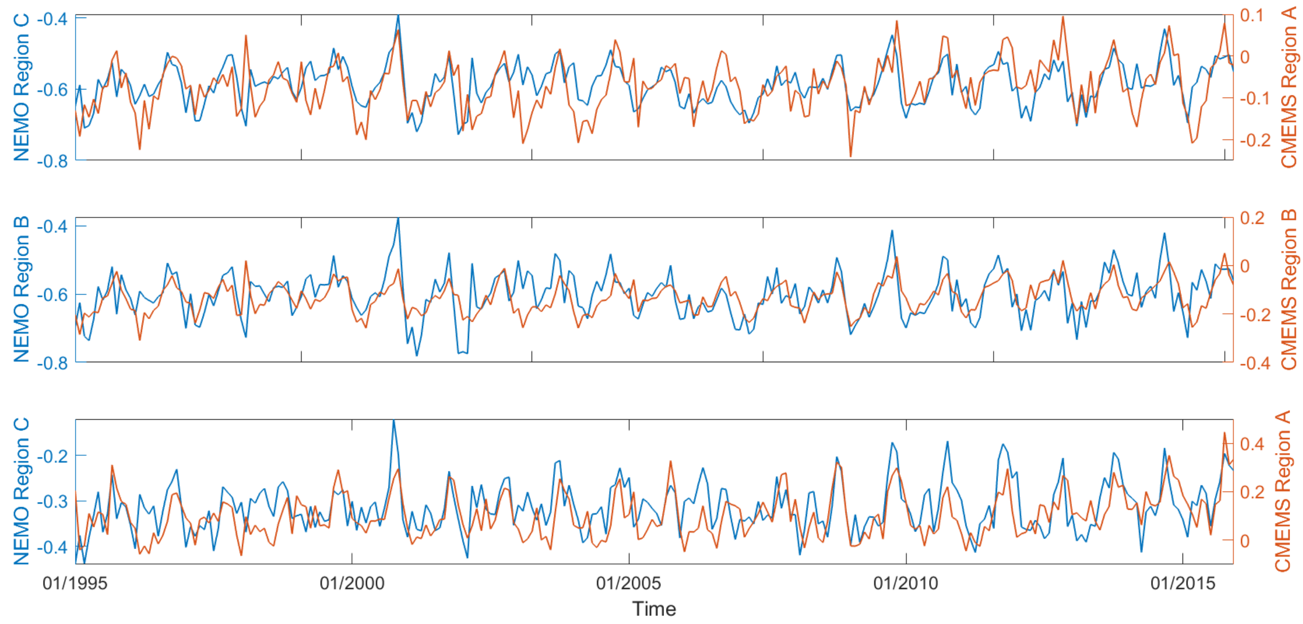

Figure 5.30 Plot of NEMO (blue) and CMEMS (orange) sea surface height region averages.

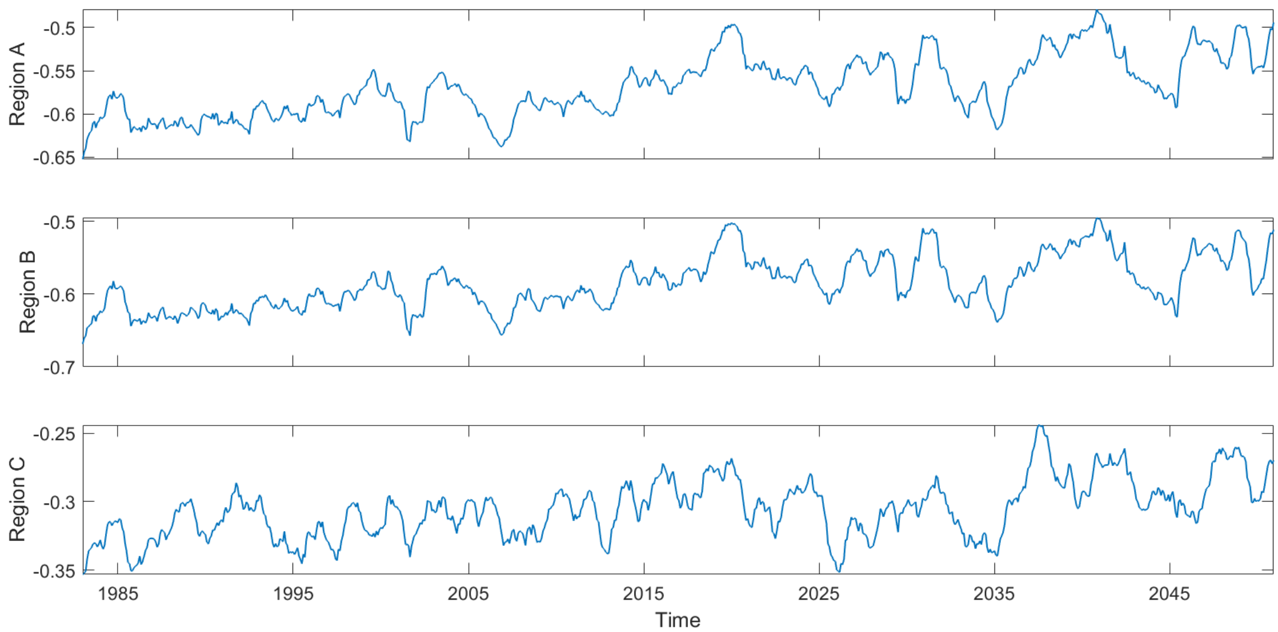

Figure 5.31 Plot of NEMO region sea surface height averages smoothed with a 12-month moving average.

6. Discussion of Risk

6.1 Background

As part of the PhD process, a 6-week secondment was conducted at the London office of AXA XL, the leading global (re)insurer. This was completed in order to place this research in the practical context of ocean risk, where risk is defined as a function of a hazard, and the exposure and vulnerability to said hazard (Niehörster & Murnane, 2018). In the context of climate change, risks can be generated from the physical impacts of global warming or the human response to it (IPCC, 2021). As it pertains to the ocean, risk can be further defined as the potential for a changing ocean to trigger major socio-economic casualties (Niehörster & Murnane, 2018). While this research does not seek to quantify these losses, it does attempt to address the potential impacts a warming climate may have on iceberg behaviour and Greenland meltwater input, notably in regard to shipping and changes in ocean circulation patterns.

The effects of anthropogenic climate change on global oceans are well documented and have been under sharp focus over the last few decades (Barnet et al., 2001; IPCC, 2021). This thesis aims to contribute to the field through enhancing the Newfoundland iceberg prediction model and assessing the impacts of increased GrIS meltwater input on major ocean currents and sea level. Its findings have contributed to the readiness and response capabilities of the International Ice Patrol (IIP) in managing iceberg hazards since December 2018, and suggest future changes in iceberg behaviour which directly affects the functional operation and economics of the shipping industry. When combined, these approaches are critical tools with which to understand future iceberg risk in the Arctic. From a meltwater perspective, an assessment of ocean circulation patterns changes as a result of increased freshwater input, and the links to sea level variations, is of direct interest to insurers and governmental sectors. This is compounded by the general agreement that extreme climatic events will increase, either in strength or quantity, under global warming (Marsooli et al., 2019; Mukherjee et al., 2018; IPCC, 2022 etc.). Therefore, this thesis will be of direct benefit to relevant industries, institutions and vulnerable communities not only in the Arctic, but internationally.

This chapter discusses the main results of the thesis from an ocean risk perspective.

6.2 Iceberg Risk

Iceberg risk to the shipping industry in the wider Arctic is different to that in the relatively small International Ice Patrol (IIP) patrolled region (see Chapter 1.3.2), as there is a greater hazard (more icebergs) but currently lower exposure (less shipping). In response to increasing interest in Arctic shipping (e.g. Bergström et al., 2020), the 2017 International Code for Ships Operating in Polar Waters (the Polar Code) was established to regulate safety and environmental standards in polar waters (Bai, 2015). Particular focus has been on the two main potential shipping routes across the Arctic: the Northern Sea Route (NSR) and the Northwest Passage. The NSR is the more popular and direct route, along the Russian coast, while the Northwest Passage takes a less defined path through the Canadian archipelago (Tseng & Cullinane, 2018). The NSR could remove 40% of the distance between Europe and Asia as opposed to passing through the Suez Canal (Hansen et al., 2016). Shorter shipping routes would also use less fuel, and therefore would theoretically act to decrease shipping emissions (Melia et al., 2016).

Discussions with marine hull underwriters at AXA XL have highlighted vessels using the Northwest Passage today are specifically constructed for Polar waters. This implies they have been strengthened with double hulls and engines that are built to survive the freezing temperatures, as mandated by the Polar Code (DNV, 2021). It was thought unlikely that significant shipping would be passing through the Northwest Passage in the near future, as the NSR is the more direct passage. It is therefore the tourist industry that is likely to see the most movement through this region, as Polar tourism continues to increase in popularity (Rantala et al., 2019), therefore increasing exposure in the Arctic and potentially contributing to emissions in the region.

Future risk is more complex and will be determined partially by public interest in Arctic tourism and partially by whether safety standards will make such cruises financially unviable. It is worth noting that part of the reason the *Titanic* sank was that demand for trans-Atlantic luxury travel outweighed the safety standards of the time. The *Great Eastern*, built fifty years earlier, incorporated every safety feature imaginable for the time period, however, she proved to be hard to manoeuvre and expensive to run (Lord, 2012). When faced with a comparable puncture in the hull (with a rock rather than an iceberg), the *Great Eastern* successfully made it to the nearest port (Lord, 2012).

Iceberg risk can be mitigated through increased funding for ice-class ships, as most ships currently operating in the North Atlantic Ocean are not designed to withstand iceberg interaction and instead aim to avoid them by following IIP advice. This is mainly due to the economic implications of strengthening a vessel's hull and modifying a ship's engine, and the associated fuel budget. Current estimates suggest that building an ice-class ship requires a 9% increase in overall costs (Solakivi et al., 2019). As there are currently limited rescue facilities in the Arctic, any ship that does run into difficulty (e.g. colliding with an iceberg or suffering engine failure) has a higher chance of major loss than in many other regions of the world, thereby increasing the associated risk (Benz et al., 2021).

The UK Government noted in 2017 that in order for Arctic shipping routes to be financially viable on the scale of current international routes, a number of significant investments would have to be made (Government Office, 2017). The focus of such investment would be on developing infrastructure and ports along the proposed route(s), constructing vessels designed for Polar waters operated by appropriately trained crew and securing adequate insurance for such journeys (Government Office, 2017). Currently, Arctic shipping is 19 times more likely to be involved in incidents than when in the open ocean, with human failings the most common cause (Fedi et al., 2018). Overall, large-scale insurance of Arctic shipping would require a specific framework in this high-risk region. Nevertheless, the benefits of shorter travel times, and the monetary returns of Arctic tourism make near-term and regular passage through the Arctic a seemingly likely scenario. However it is worth noting that this is a geo-political topic, not just an economic one. It may prove to be difficult or undesirable to traverse Russian waters, depending on the nationality of the ship and/or crew. Recent Russian actions have also highlighted a European reliance on oil and gas resources (Liadze et al., 2022) that may make Arctic sources a more intriguing option than before.

6.3 Freshwater Input

Meltwater input has a direct result on sea level rise. By 2100, Moon et al. (2018) estimates that sea level rise from the GrIS (only) would be approximately 92 ± 45 mm under the same strength emissions scenario that forced the NEMO model (RCP8.5), however this estimate does not include reactions to changes in ocean circulation. When the rest of the Arctic, and the wider World, is included, this would place millions of people currently in low-lying coastal locations at risk of flooding at high tide, or during a storm surge (Kulp & Strauss, 2019).

In the UK alone, it is estimated that the annual cost from river and coastal flooding to property is £1 billion (Environment Agency, 2009). Still, the UK is likely one of the least at-risk island countries as a result of its geographical location and the available financial resources to mitigate and/or rebuild after a flood event. The success of current strategies are shown when past events are highlighted. Around 2000 people were killed in 1607 when flooding occurred in the Bristol Channel, while lives on the scale of 10,000 were lost on the east coast in 1099, 1421 and 1446 (Haigh et al., 2017). While this scale of human loss would be unthinkable now, this is a result of sustained forecasting and mitigation approaches brought in after the devastating 1953 event, where approximately £5 billion (in today's money) was lost along with 307 lives (Lumbroso & Vinet, 2011). This was a result of a North Sea storm surge and was felt across the UK, the Netherlands and Belguim (Wadey et al., 2015). Figure 6.1 shows an estimate of the UK if sea level were to rise 0.9 m, a realistic estimate by 2100 under a high-emission scenario. It can be seen that large areas of the east coast are underwater at high tide. When the map is focused on Greater London, significant flooding is visible in much of the capital, as seen in Figure 6.2. However note the Thames Barrier that was built after the 1953 event and would potentially negate such flooding. While these maps give a coarse picture of UK coastal flooding, they are still interesting tools when considering the potential wide-scale effects of sea level rise.

Figure 6.1 An estimated map of the UK under 0.9 m of sea level rise (Coastal.climatecentral.org. 2022).

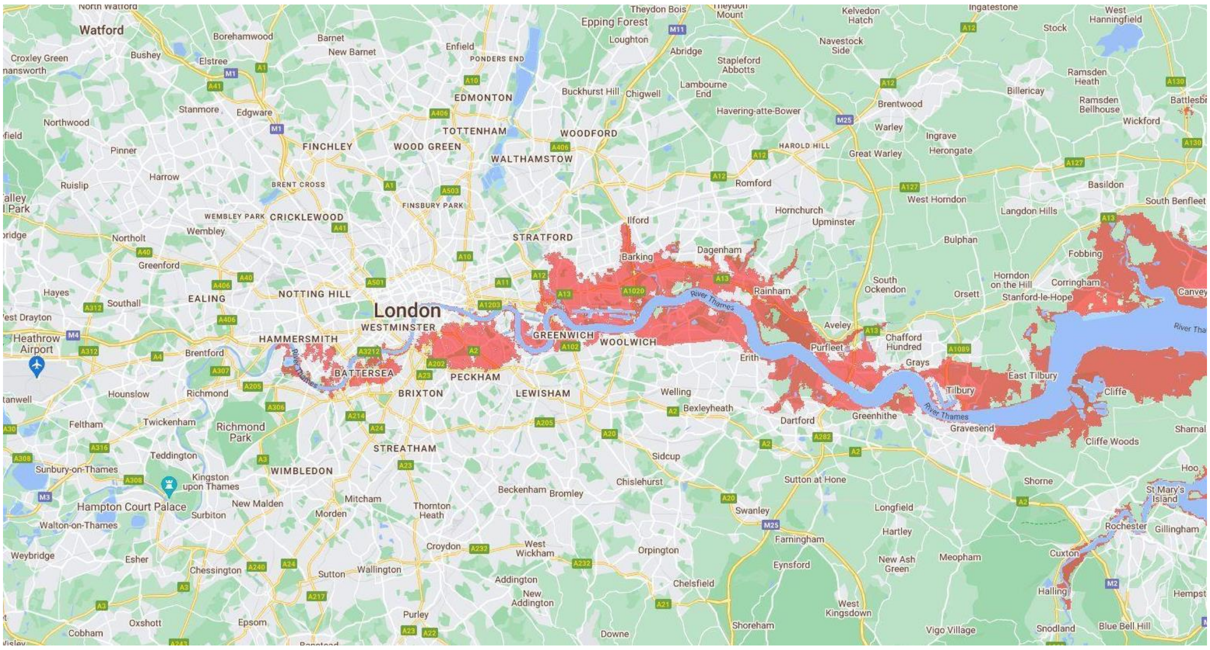

Figure 6.2 An estimated map of London under 0.9 m of sea level rise (Coastal.climatecentral.org. 2022).

6.4 Conclusion

While iceberg numbers are forecast to decrease with climate change, iceberg risk is dependent in part on the number of ships entering the ice-zone. Additionally, the IIP has significantly reduced the risk of iceberg collision in the region off Newfoundland due to extensive patrolling of the area for a century. As sea ice retreat makes Arctic shipping routes more accessible, the lack of continuous iceberg data may prove disastrous in an area of low rescue facilities. Even in the Southern Hemisphere, the effects of anthropogenic climate change are shown in this thesis to be significant in terms of ocean circulation patterns and sea level rise. As the global climate is regulated by ocean currents, changes here will have lasting effects on human life, variable at the regional level. Sea level rise is a popular effect of climate change, in part due to the easily envisioned disaster of cities sinking beneath the waves, but more realistically as property flooding is a common occurrence around the world, and the associated monetary and personal costs widely known. As such, it is an important area of research not only due to the wide-scale effects of coastal flooding, but also as a means of convincing governments to implement the changes required to limit climate change to below the IPCC goal of 1.5°C.

7. Conclusion

7.1 Overview

This thesis has used a range of models to try and quantify the changes that a melting Greenland Ice Sheet (GrIS) is likely to have on the world's oceans. The focus has been on changing iceberg behaviour and the effects of additional meltwater input on ocean currents. The WERR model (when combined with machine learning techniques) offers a seasonal iceberg warning system (Chapter 2), while NEMO model results have been analysed to produce an estimate of iceberg numbers up to 2050, in a high-emission scenario, with an approximate surface warming of 8.5 Wm^{-2} by 2100 (Chapter 4). The FRUGAL ocean model has been used to assess meltwater impact between 1987 and 2015, in five simulations of varying freshwater forcing (Chapter 3). NEMO outputs were then compared to these results, with comparative variables extended to 2050 (Chapter 5), with a focus on sea level rise. Chapter 6 was a discussion of the impacts of increased meltwater input and iceberg presence in the Arctic, from an insurance perspective.

This chapter discusses the main findings from the thesis, before addressing the limitations of this research and highlighting potential areas for future work.

7.2 Iceberg Prediction

The monthly WERR model was shown in Bigg et al. (2014) to produce an output that had a correlation of 0.84 with the annual variation in the number of icebergs passing 48°N between 1900 and 2008. However, when considering the yearly result between 1970 and 2020, this correlation drops to 0.46 (significant at the 1% level). It seems likely that this is either a result of climate change altering the relationship between the environmental variables and I48N, or a suggestion that the WERR model better represents monthly, rather than yearly, variations. Nevertheless, this is still a strong correlation, especially when considering the high natural variation in I48N, but it must be noted that the WERR model has not been very successful at predicting icebergs numbers over the last few years.

Regarding the addition of machine learning tools, it was shown in Chapter 2 that the I48N forecast was a valid application of these models, however, the selected models were not optimised from all existing machine learning tools. It is also worth considering whether selecting a single model would have produced more reliable forecasts, as the three models used often predicted a range of outcomes that was averaged in the final forecast. For example, for the 2022 I48N forecast, the three models each predicted a different outcome. Therefore, the decision was made to take the average prediction (medium) as the forecast. Figures 7.1, 7.2 and 7.3 show the success (true) or failure (false) of the three machine learning models, for the I48N prediction, between 1935 and 2020.

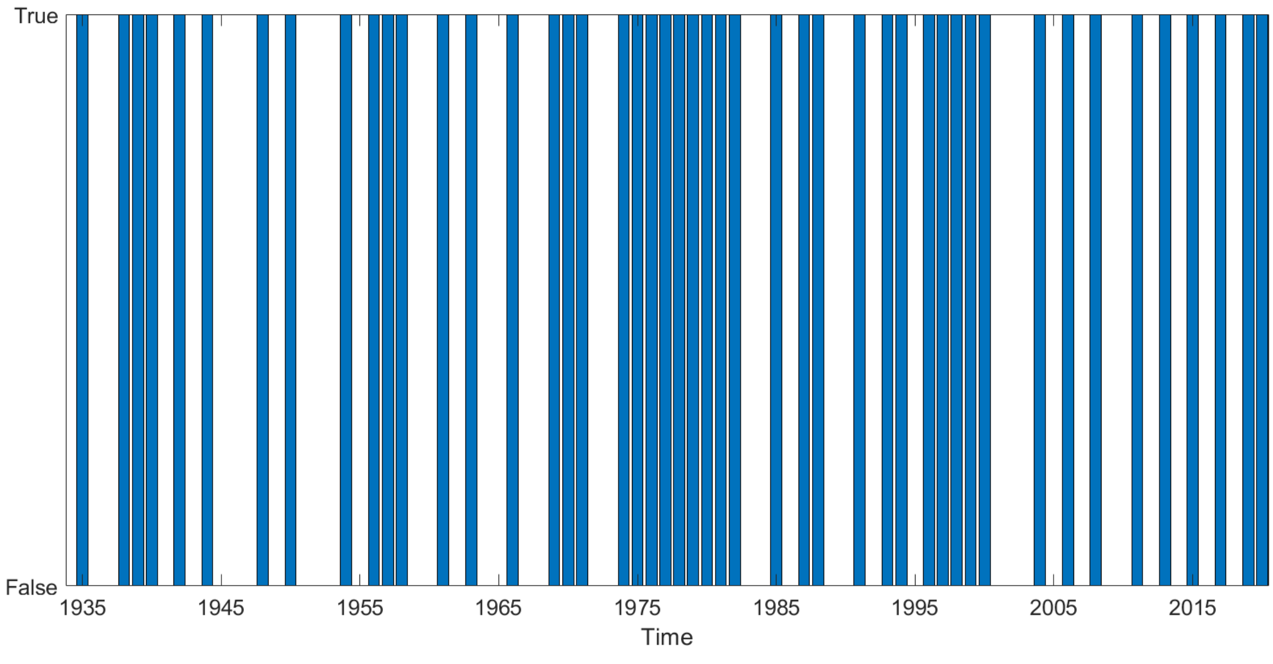

Figure 7.1 Showing the success (true) or failure (false) of the Linear Discriminant model prediction over the test period, for I48N.

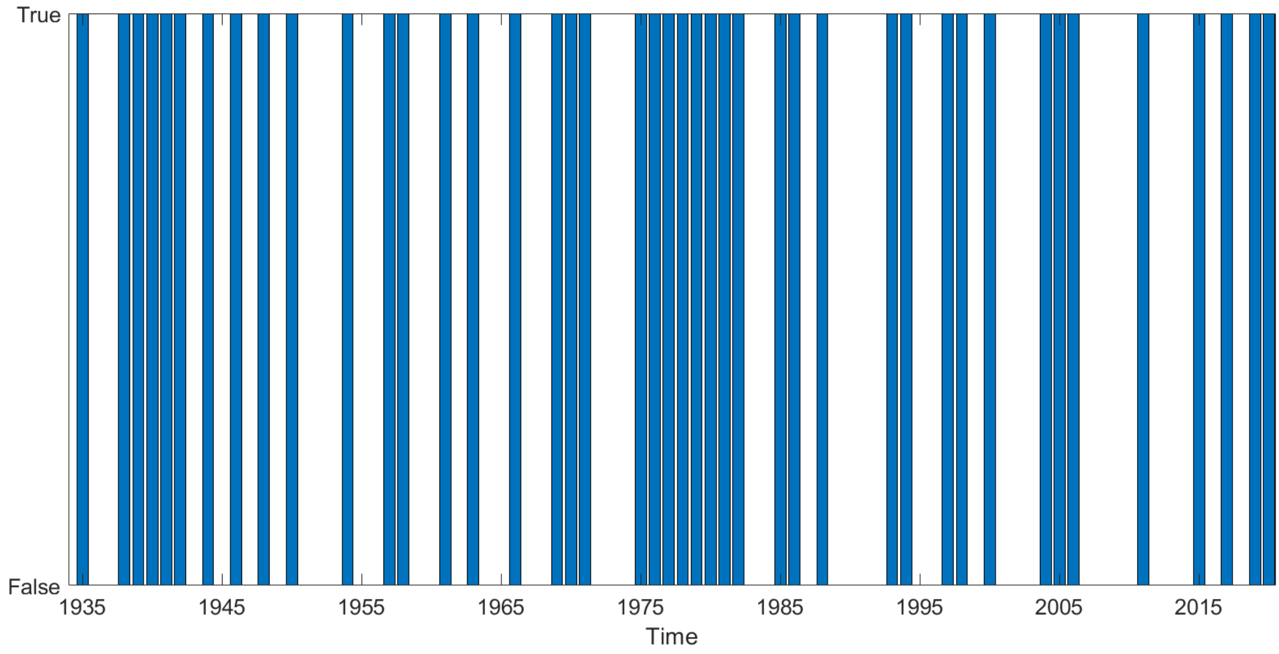

Figure 7.2 Showing the success (true) or failure (false) of the Linear SVM model prediction over the test period, for I48N.

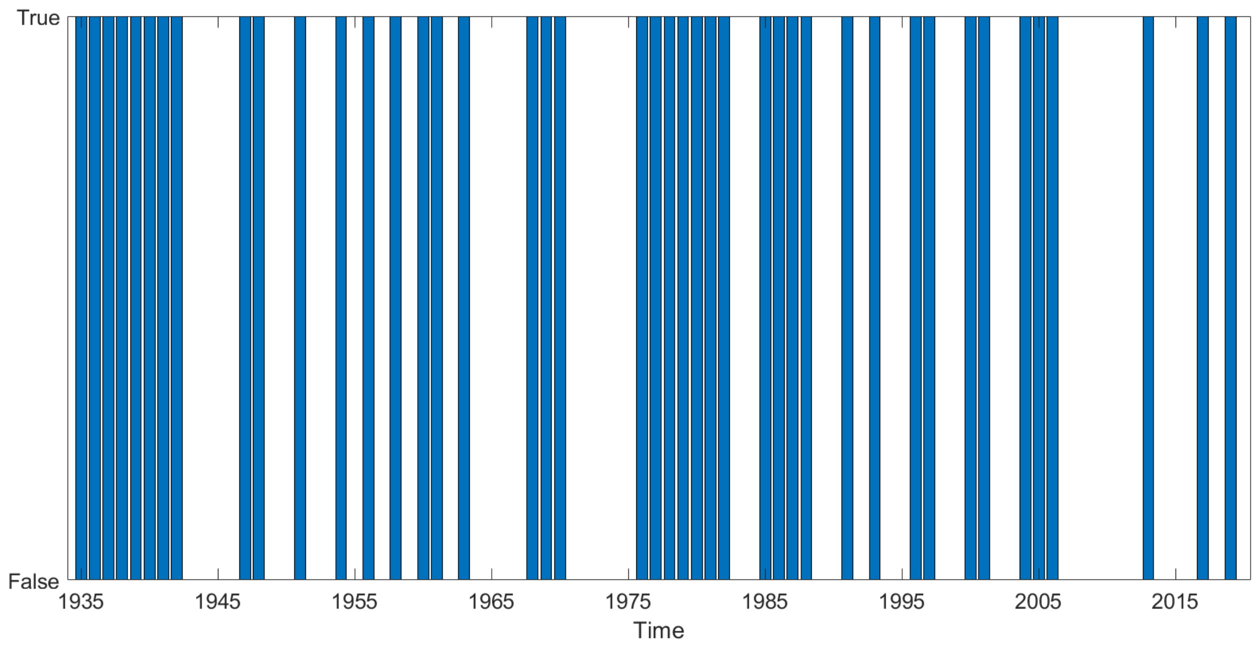

Figure 7.3 Showing the success (true) or failure (false) of the Quadratic SVM model prediction over the test period, for I48N.

These show that the Quadratic SVM model, in particular, may not be the most useful at present, as since 2006, the success rate has been low compared to earlier in the time period. Sustained successful prediction between 1935 and 1942 will increase the percentage accuracy of the model, but may not well represent the chance of success in the 2020's. The Linear SVM model does a better job of successful prediction in the 2000s onwards than the Quadratic SVM, however large gaps in its success can still be seen in this period, compared to relative success before 1980. The Linear Discriminant model can be seen to have the most success in recent decades, compared to the other two models. However, regarding the 2022 forecast, the Linear Discriminant model predicted a 'high' year, while early indicators suggest a lower than average year (see below).

All models show prolonged success in the mid-late 1970's. This was a time of continuous low I48N (this can be seen in Figure 7.4) which suggests that the models either better predict low iceberg years, or (due to the element of auto-regression through having knowledge of the previous years' value) have a higher likelihood of success if the forecast is the same as the previous years. However, it is worth noting that the Linear Discriminant model also successfully predicted 1974, which was a 'high' year, unlike the other two models. Overall, as the Linear Discriminant model was potentially found to be the most realistic in Chapter 2 (Section 2.3.3), and due to the reasons discussed in this chapter, perhaps this model's prediction should be selected as the forecast, without input from the SVM models.

The 2022 iceberg season was forecast to be a low/medium year, with one peak in April and a low rate of change. The daily iceberg numbers south of 48°N by 1st May can be seen in Figure 7.4. A low year has a maximum of 230 icebergs recorded in the season, with peak iceberg numbers usually found in April or May. Therefore, the 2022 iceberg season is currently looking like it will be a low year, however this cannot be confirmed before the end of the season. For comparison, 2021 had 1 iceberg in total, recorded in late February, while in the 2019 season, which was the most recent 'high' iceberg year, by the end of April 679 icebergs had been recorded south of 48°N. Therefore, while it is too early to be certain, current iceberg numbers suggest a lower than average season, as the WERR model predicted.

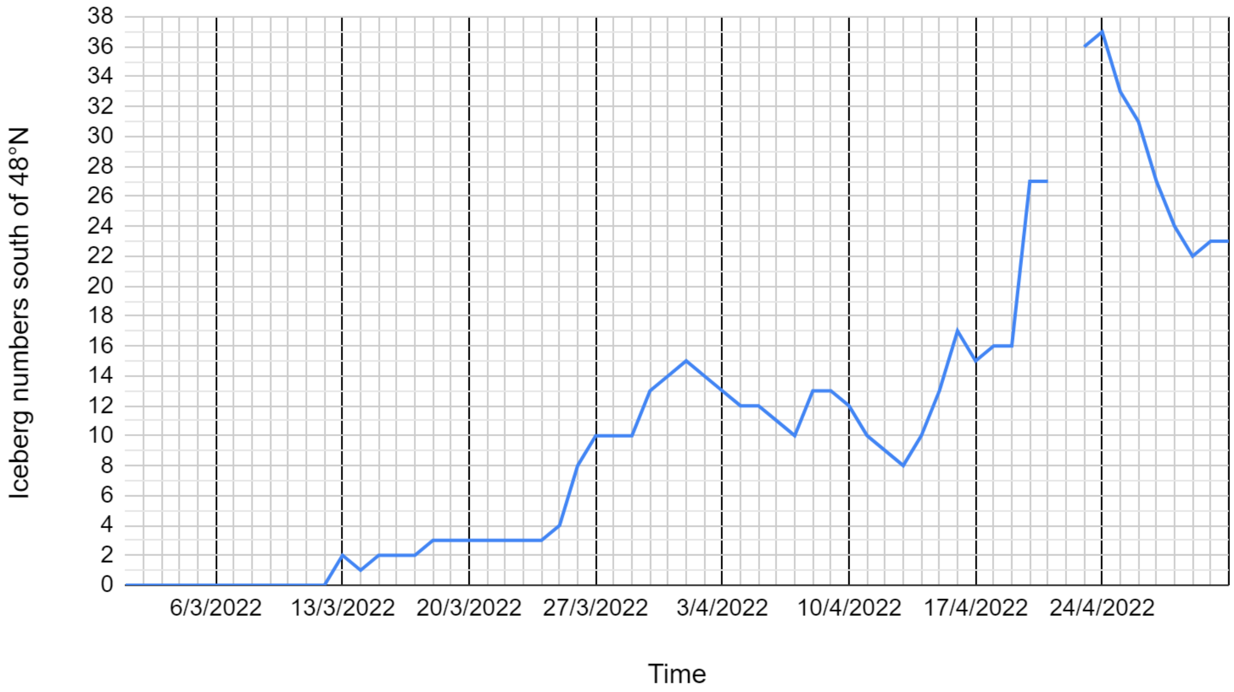

Figure 7.4 Plot of daily iceberg numbers south of 48°N, from the 1st March to the 1st May 2022. Note the missing data for the 22nd April.

7.3 Meltwater Input

Inputting large quantities of freshwater into the North Atlantic from melting of the Greenland ice sheet has repercussions for the global climate. These implications have been analysed using the FRUGAL and NEMO models throughout the thesis. While Arctic regions have been seen in Chapters 3 and 4 to represent the areas with the most extreme responses, changes were detected in all analysed regions. FRUGAL showed a likely decrease in the Atlantic Overturning Circulation as a result, however as FRUGAL historically overestimates the AMOC there can not be a large amount of confidence in this finding. Additionally, an overall decrease in Northern Hemisphere Overturning Circulation as a result of increased meltwater input was seen, and a decreasing Labrador Sea salt flux was suggested. A decreasing Labrador Sea salt flux is attributed to reduced vertical mixing as a result of increased stratification due to increased meltwater input. A general increase in Bering Strait flux was seen, and variability here is normally driven by a combination of pressure differences between the Pacific and Arctic Oceans and wind patterns, so the increase could be attributed to freshwater input in the Arctic Ocean resulting in greater pressure differences with the Pacific Ocean, however this is not explored in the thesis and so no solid remarks can be made.

The NEMO ocean model showed a general pattern of reduction in Arctic salinity and temperature. There was also a large focus on retreating sea ice extent, and how this interacts with ocean circulation and iceberg movement. The Franz Josef Islands to Svalbard region showed significant sea surface temperature and salinity changes beyond that seen in much of the rest of the Arctic region. May surface temperatures were expected to rise from a decadal average of -1.6 to 2.3 °C between 1985-95 and 2035-45, with salinity rising at a similar rate.

This is likely as a result of ‘Atlantification’, the associated decrease in areas of potential sea ice (see Figure 4.23 for the average May sea ice fraction decrease).

Meltwater input also has a direct impact on sea level. While this thesis has a focus on large-scale ocean circulation patterns, rather than individual case studies (e.g. that evaluate flooding risk) Chapter 5 used NEMO and FRUGAL results to assess likely changes in sea level by 2050. This has been achieved by using a direct sea surface height variable for both models, and by analysing the FRUGAL stream function. This variable reflects the changes in ocean circulation, and by implication, the sea level slope changes, as a result of meltwater input. While the FRUGAL model only runs to 2015, the inputted runoff was significant enough to produce a change visible in the stream function and sea surface height directly (see Chapter 5, Section 5.2.1), on a decadal scale. The most notable changes were in the North Atlantic in both models, and in the CMEMS sea surface height (from satellite data) which was used for comparison. However, significant variations were also recorded in the Pacific and the Southern Ocean when the difference between the decade 2005-2014 and 1995-2004 was considered. These plots suggest that increased runoff will have an impact on the strength of ocean circulation, but this will not necessarily result in wide-scale sea level rise (at least by 2050). Rather, the relative increase/decrease in the strength of major ocean currents, such as an increasing Gulf Stream, will cause a physically variable reaction in sea level, but with the associated exacerbation of extreme climatic events, that would still produce increased global flooding.

7.4 Conclusion

The NEMO model suggests that by 2050, meltwater runoff is likely to significantly dominate iceberg calving from the GrIS. That is, runoff is forecast to increase, while iceberg calving is expected to decrease. However there are some caveats to this, namely that NEMO has been forced with icebergs from around the year 2000 (which are potentially lower than current values, although there is a large amount of yearly variability in I48N and 2020-2023 have seen low numbers of icebergs - compared to those seen in 2000 - past the 48th parallel). Additionally, the NEMO run used here is a high-emission scenario, and therefore produces a more extreme reaction than may be seen. While it would have been interesting to compare this run to a ‘realistic’ emissions NEMO run, this was not practical due to limited access to the model, and the inability to run it for other scenarios. Nevertheless, the NEMO run that was used is the most useful for creating a (realistic) worst-case scenario, ideal for considering future risk, and had the option been there to select a single run, this would have been the one chosen. This is a limitation of the NEMO chapter. Future work with NEMO would therefore include a comparison to a low-emissions scenario run, and in an ideal scenario, would allow for more access to the model (potentially being able to actually run it) and/or would include visiting Southampton in person, which was not an option here, due to Covid restrictions.

The FRUGAL ocean model was a useful tool in understanding how increased runoff is likely to affect ocean currents, primarily because it was possible to access and physically alter the models scripts in order to produce a result tailored to the thesis question. This did have some drawbacks, mainly in terms of programming errors and computational time, but has still produced some interesting results that are comparable to NEMO outputs. Future work could focus on extending the run past 2015, as this was the upper limit for data availability in this thesis. Additionally, the FRUGAL runs input meltwater at the surface, when recent work from Slater et al. (2022) suggests that peak freshwater influx is at 100 m depth, with a range of 0 – 400 m, therefore future work could look at implementing this into the runs.

While iceberg calving is forecast to decrease by 2050, and therefore iceberg numbers south of 48°N, there is still value in a yearly iceberg forecast. This is partly a result of high-yearly variability in the iceberg season and the likely increase in Arctic shipping due to oil and gas exploration and tourism ventures. This variability can be seen in Figure 7.5, which shows the yearly I48N between 1950 and 2021, with a 10-year running mean. A fairly consistent high iceberg count can be seen in the 1990s, producing a peak in the running mean. The 2000's showed comparatively low numbers, while the 2010's had a couple of high years but were still overall lower values than in the 1990s. As previously discussed, it is suggested that I48N is likely to decrease in the future, and therefore it seems possible that an overall peak in iceberg numbers in the region has already occurred, between 1980 and 2000. This may be a result of changes at Jakobshavn Isbrae on the west coast of Greenland, which sped up dramatically during this period (Van Der Veen et al., 2011). Nevertheless, due to the complex nature of I48N, it is likely that while a general decrease will be seen, some years will still show 'extreme' high numbers.

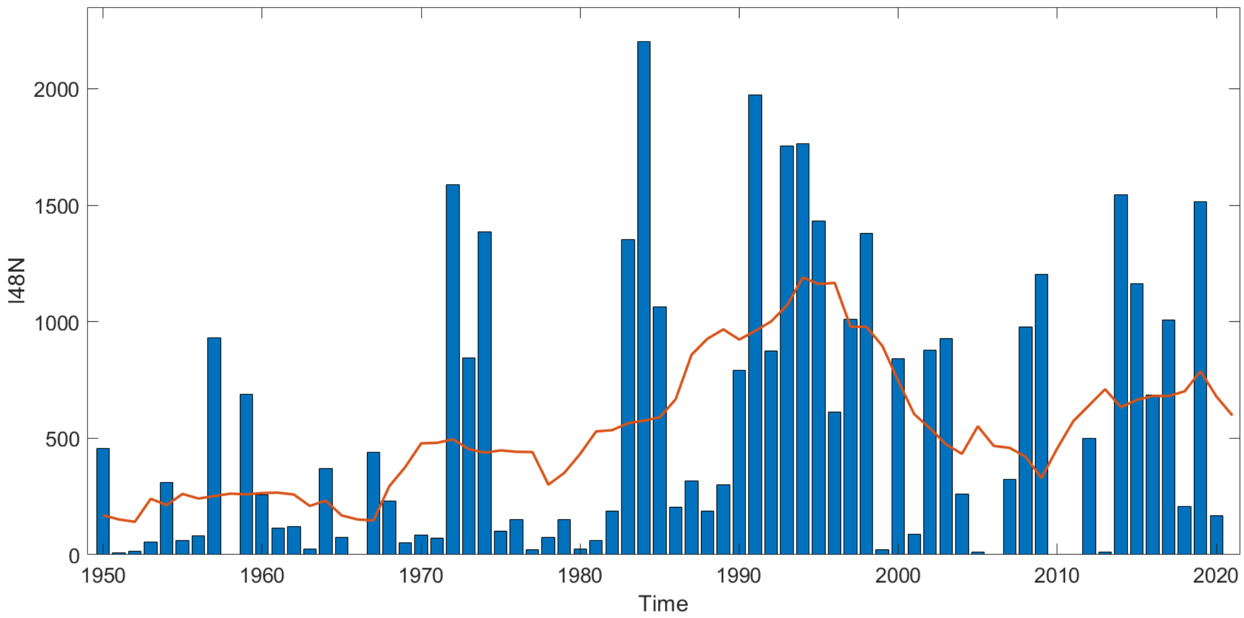

Figure 7.5 Yearly iceberg totals south of 48°N, with a 10-year moving average overlaid in orange.

As discussed in this chapter, while the WERR forecast may be less useful for yearly prediction than was found in the Bigg et al. (2021) paper, it still shows significant correlation, and therefore has real practical application in this complex field. The machine learning aspect was also shown to be useful, however future work should either highlight the Linear Discriminant model prediction for the forecast or analyse a wider range of machine learning models, to produce a quantitative result to determine which is the most successful/skilful. One way in which the WERR model could be further improved would be to use solid ice discharge estimates for the Greenland Ice Sheet (available from 1986 to present, see Mankoff et al., 2019). This could be a better predictor than SMB, when an appropriate lag was included. The machine learning models could be improved by testing further input variables. One such potential could be a measure of surface currents in the North Atlantic (responsible for transporting the icebergs south) or sea ice cover around Greenland (however previous experimentation with sea ice extent around Newfoundland found no correlation). Further analysis on whether the relationship between environmental variables and I48N has changed enough to warrant a different model approach would also be a useful area of future research. This was discussed when the WERR model terms were shifted closer to the forecast year, as this was shown to improve the model result. However, due to the short time period of the PhD project, this could only be extended by a couple of years, and therefore can not fully test the evolution over time. It has previously been shown in Zhao et al. (2017) that the dominant factor influencing I48N alternates on a decadal scale throughout the 21st Century between the environmental variables considered in Chapter 2. Therefore, the success of current models over this period suggests that they are able to adapt to some level of variability; however, if further global warming in the future alters the relationship beyond an unknown tipping point, it may be that the model approach discussed here is no longer relevant.

Overall, all models considered in this thesis contributed a unique element to the wider picture of climate change impacts discussed here. The WERR model and the machine learning approach combine to present a practical forecast of iceberg hazard in the Newfoundland region. The WERR model presents a higher-accuracy I48N total, while the machine learning models give an idea of iceberg behaviour in the following season. The FRUGAL and NEMO ocean models act to verify the findings of the other, in regard to ocean circulation changes and the effect on sea level, while both include an iceberg component. The FRUGAL model was useful as direct access to the code was possible, and therefore near total control over the outputs were available. Whereas, the more complex NEMO model outputs were only accessible in one high-emission run and had Covid related restrictions to its use.

Nevertheless, interesting insights were found from all models and future work would look to expand on these further.

References

2019. Report of the International Ice Patrol in the North Atlantic. [PDF] Available at: <https://www.navcen.uscg.gov/pdf/iip/2019_Annual_Report_FINAL.PDF> [Accessed 5 January 2022].

2021. Report of the International Ice Patrol in the North Atlantic. [PDF] Available at:

<https://www.navcen.uscg.gov/pdf/iip/2021_Annual_Report_FINAL.PDF>

[Accessed 11 January 2022].

20th Century Reanalysis data provided by the NOAA/OAR/ESRL PSL, Boulder, Colorado, USA, from their Web site at /https://psl.noaa.gov/data/gridded/data.20thC_ReanV3.monolevel.html

AbuZeina, D. and Al-Anzi, F.S., 2018. Employing fisher discriminant analysis for Arabic text

classification. Computers & Electrical Engineering, 66, pp.474-486.

Amundson, J.M., Truffer, M., Lüthi, M.P., Fahnestock, M., West, M. and Motyka, R.J., 2008. Glacier, fjord, and seismic response to recent large calving events, Jakobshavn Isbræ, Greenland. Geophysical Research Letters, 35(22).

Anderson, I., 1993. International Ice Patrol Iceberg Sighting Data Base 1960-1991. Appendix D in Report of the International Ice Patrol in the North Atlantic, Bulletin, (79).

Andres, M., 2016. On the recent destabilization of the Gulf Stream path downstream of Cape Hatteras. Geophysical Research Letters, 43(18), pp.9836-9842.

Bai, J., 2015. The IMO Polar Code: The emerging rules of Arctic shipping governance. The International Journal of Marine and Coastal Law, 30(4), pp.674-699.

Balaguru, K., Doney, S.C., Bianucci, L., Rasch, P.J., Leung, L.R., Yoon, J.H. and Lima, I.D., 2018. Linking deep convection and phytoplankton blooms in the northern Labrador Sea in a changing climate. PloS one, 13(1), p.e0191509.

Bao, S., Wang, H., Zhang, R., Yan, H. and Chen, J., 2019. Comparison of satellite-derived sea surface salinity products from SMOS, Aquarius, and SMAP. Journal of Geophysical Research: Oceans, 124(3), pp.1932-1944.

Bai, J., 2015. The IMO Polar Code: The emerging rules of Arctic shipping governance. The International Journal of Marine and Coastal Law, 30(4), pp.674-699.

Barker, S., Chen, J., Gong, X., Jonkers, L., Knorr, G. and Thornalley, D., 2015. Icebergs not the trigger for North Atlantic cold events. Nature, 520(7547), pp.333-336.

Barnett, T.P., Pierce, D.W. and Schnur, R., 2001. Detection of anthropogenic climate change in the world's oceans. Science, 292(5515), pp.270-274.

Barrette, P., McGonigal, D. and Pike, K., 2018, June. Risks to Marine Pipelines From Drifting Ice: Gathering the Evidence. In International Conference on Offshore Mechanics and Arctic Engineering (Vol. 51241, p. V005T04A064). American Society of Mechanical Engineers.

Beare, M.I., 1999. The southampton-east anglia (sea) model: A general purpose parallel ocean circulation model. In High-Performance Computing (pp. 337-346). Springer, Boston, MA.

Benz, L., Münch, C. and Hartmann, E., 2021. Development of a search and rescue framework for maritime freight shipping in the Arctic. Transportation Research Part A: Policy and Practice, 152, pp.54-69.

Bergström, M., Leira, B.J. and Kujala, P., 2020, August. Future Scenarios for Arctic Shipping. In International Conference on Offshore Mechanics and Arctic Engineering (Vol. 84393, p. V007T07A006). American Society of Mechanical Engineers.

Bhuvaneswari, P. and Kumar, J.S., 2013. Support vector machine technique for EEG signals. International Journal of Computer Applications, 63(13).

Bigg, G.R., 2015. Icebergs: their science and links to global change. Cambridge University Press.

Bigg, G.R., Wadley, M.R., Stevens, D.P. and Johnson, J.A., 1997. Modelling the dynamics and thermodynamics of icebergs. Cold Regions Science and Technology, 26(2), pp.113-135.

Bigg, G.R., Wei, H.L., Wilton, D.J., Zhao, Y., Billings, S.A., Hanna, E. and Kadirkamanathan, V., 2014. A century of variation in the dependence of Greenland iceberg calving on ice sheet surface mass balance and regional climate change. Proceedings of the Royal Society A: Mathematical, Physical and Engineering Sciences, 470(2166), p.20130662.

Bigg, G.R., Zhao, Y. and Hanna, E., 2021. Forecasting the severity of the Newfoundland iceberg season using a control systems model. Journal of Operational Oceanography, 14(1), pp.24-36.

Bigg, G.R.; Billings, S.A. The iceberg risk in the Titanic year of 1912: Was it exceptional? Significance 2014, 11(3), pp.6-10.

Bigg, G.R.; Wei, H.; Wilton, D.J.; Zhao, Y.; Billings, S.A.; Hanna, E.; Kadirkamanathan, V. A century of variation in the dependence of Greenland iceberg calving on ice sheet surface mass balance and regional climate change. Proc. Roy. Soc Ser. A 2014, 470, 20130662, doi:10.1098/rspa.2013.0662.

Bügelmayer, M., Roche, D.M. and Renssen, H., 2015. How do icebergs affect the Greenland ice sheet under pre-industrial conditions?–a model study with a fully coupled ice-sheet–climate model. The Cryosphere, 9(3), pp.821-835.

Canada, E., 2022. Iceberg shapes, sizes and colours - Canada.ca. [online] Canada.ca. Available at: <https://www.canada.ca/en/environment-climate-change/services/ice-forecasts-observations/latest-conditions/educational-resources/icebergs/shapes-sizes-colours.html> [Accessed 5 January 2022].

Casanova-Masjoan, M., Pérez-Hernández, M.D., Pickart, R.S., Valdimarsson, H., Ólafsdóttir, S.R., Macrander, A., Grisolía-Santos, D., Torres, D.J., Jónsson, S., Våge, K. and Lin, P., 2020. Along-stream, seasonal, and interannual variability of the North Icelandic Irminger Current and East Icelandic Current around Iceland. Journal of Geophysical Research: Oceans, 125(9), p.e2020JC016283.

Chen, X. and Tung, K.K., 2018. Global surface warming enhanced by weak Atlantic overturning circulation. Nature, 559(7714), pp.387-391.

Chidichimo, M.P., Donohue, K.A., Watts, D.R. and Tracey, K.L., 2014. Baroclinic transport time series of the Antarctic Circumpolar Current measured in Drake Passage. Journal of Physical Oceanography, 44(7), pp.1829-1853.

Chokey, T. and Jain, S., 2019, February. Quality assessment of crops using machine learning techniques. In 2019 Amity International Conference on Artificial Intelligence (AICAI) (pp. 259-263). IEEE.

Church, J.A., P.U. Clark, A. Cazenave, J.M. Gregory, S. Jevrejeva, A. Levermann, M.A. Merrifield, G.A. Milne, R.S. Nerem, P.D. Nunn, A.J. Payne, W.T. Pfeffer, D. Stammer and A.S. Unnikrishnan, 2013: Sea Level Change. In: Climate Change 2013: The Physical Science Basis. Contribution of Working Group I to the Fifth Assessment Report of the Intergovernmental Panel on Climate Change [Stocker, T.F., D. Qin, G.-K. Plattner, M. Tignor, S.K. Allen, J. Boschung, A. Nauels, Y. Xia, V. Bex and P.M. Midgley (eds.)]. Cambridge University Press, Cambridge, United Kingdom and New York, NY, USA.

Chicco, D. and Jurman, G., 2020. The advantages of the Matthews correlation coefficient (MCC) over F1 score and accuracy in binary classification evaluation. BMC genomics, 21(1), pp.1-13.

Coastal.climatecentral.org. 2022. *Sea level rise and coastal flood risk maps -- a global screening tool by Climate Central*. [online] Available at:<https://coastal.climatecentral.org/map/5/6.7489/53.6501/?theme=water_level&map_type=water_level_above_mhhw&basemap=roadmap&contiguous=true&elevation_model=best_available&refresh=true&water_level=0.9&water_unit=m> [Accessed 7 April 2022].

Compo, G. P., et al. 2015, updated yearly. NOAA/CIRES Twentieth Century Global Reanalysis Version 2c. Research Data Archive at the National Center for Atmospheric Research, Computational and Information Systems Laboratory.

Connolly, R., Connolly, M. and Soon, W., 2017. Re-calibration of Arctic sea ice extent datasets using Arctic surface air temperature records. Hydrological Sciences Journal, 62(8), pp.1317-1340.

Consortium, E., 2021. History of the NEMO European Consortium. [online] www.nemo-ocean.eu. Available at: <https://www.nemo-ocean.eu/consortium/history/> [Accessed 11 November 2021].

Copernicus Climate Change Service (C3S) (2017): ERA5: Fifth generation of ECMWF atmospheric reanalyses of the global climate . Copernicus Climate Change Service Climate Data Store (CDS), 12/04/2021. https://cds.climate.copernicus.eu/cdsapp#!/home

Das, N. and Entekhabi, D., 2019. Algorithm theoretical basis document SMAP-Sentinel L2 radar/Radiometer soil moisture (active/passive) data products: L2 _ SM _ sP. Jet Propuls. Lab., pp.1-62.

Dima, M. and Lohmann, G., 2011. Causes and consequences of the late 1960s great salinity anomaly. In Planet Earth 2011-Global Warming Challenges and Opportunities for Policy and Practice (pp. 213-230). InTech.

DNV. 2021. IMO Polar Code - DNV. [online] Available at: <https://www.dnv.com/maritime/polar/index.html> [Accessed 21 October 2021].

Domingues, R., Goni, G., Baringer, M. and Volkov, D., 2018. What caused the accelerated sea level changes along the US East Coast during 2010–2015?. Geophysical Research Letters, 45(24), pp.13-367.

Dong, S., Baringer, M.O. and Goni, G.J., 2019. Slow down of the Gulf Stream during 1993–2016. Scientific Reports, 9(1), pp.1-10.

England, M.H. and Huang, F., 2005. On the interannual variability of the Indonesian Throughflow and its linkage with ENSO. Journal of Climate, 18(9), pp.1435-1444.

Environment Agency, 2009. Flooding in England: a national assessment of flood risk.

Fathi, M., Nemati, M., Mohammadi, S.M. and Abbasi-Kesbi, R., 2020. A machine learning approach based on SVM for classification of liver diseases. Biomedical Engineering: Applications, Basis and Communications, 32(03), p.2050018.

Fay, A.R., Lovenduski, N.S., McKinley, G.A., Munro, D.R., Sweeney, C., Gray, A.R., Landschützer, P., Stephens, B.B., Takahashi, T. and Williams, N., 2018. Utilizing the Drake Passage Time-series to understand variability and change in subpolar Southern Ocean pCO 2. Biogeosciences, 15(12), pp.3841-3855.

Feng, M., Zhang, N., Liu, Q. and Wijffels, S., 2018. The Indonesian throughflow, its variability and centennial change. Geoscience Letters, 5(1), pp.1-10.

Fenoglio-Marc, L., Mariotti, A., Sannino, G., Meyssignac, B., Carillo, A., Struglia, M.V. and Rixen, M., 2013. Decadal variability of net water flux at the Mediterranean Sea Gibraltar Strait. Global and Planetary Change, 100, pp.1-10.

Fisher, R.A., 1936. The use of multiple measurements in taxonomic problems. Annals of eugenics, 7(2), pp.179-188.

Frajka-Williams E.; Moat B.I.; Smeed D.A.; Rayner D.; Johns W.E.; Baringer M.O.; Volkov, D.; Collins, J. (2021). Atlantic meridional overturning circulation observed by the RAPID-MOCHA-WBTS (RAPID-Meridional Overturning Circulation and Heatflux Array-Western Boundary Time Series) array at 26N from 2004 to 2020 (v2020.1), British Oceanographic Data Centre - Natural Environment Research Council, UK. doi:10.5285/cc1e34b3-3385-662b-e053-6c86abc03444

Fuglem, M., Stuckey, P., King, T. and Brown, M., 2015, May. Iceberg Drift Forecast Requirements for Offshore Platforms Utilizing Facility Side-Tracking to Avoid Impacts. In ASME 2015 34th International Conference on Ocean, Offshore and Arctic Engineering (pp. V008T07A039-V008T07A039). American Society of Mechanical Engineers.

Fyfe, J.C., Meehl, G.A., England, M.H., Mann, M.E., Santer, B.D., Flato, G.M., Hawkins, E., Gillett, N.P., Xie, S.P., Kosaka, Y. and Swart, N.C., 2016. Making sense of the early-2000s warming slowdown. Nature Climate Change, 6(3), pp.224-228.

Gelderloos, R., Straneo, F. and Katsman, C.A., 2012. Mechanisms behind the temporary shutdown of deep convection in the Labrador Sea: Lessons from the Great Salinity Anomaly years 1968–71. Journal of Climate, 25(19), pp.6743-6755.

Gladstone, R.M., Bigg, G.R. and Nicholls, K.W., 2001. Iceberg trajectory modeling and meltwater injection in the Southern Ocean. Journal of Geophysical Research: Oceans, 106(C9), pp.19903-19915.

Government Office for Science document: Future of the sea: implications from opening arctic sea routes, 2017 [online] Available at<publishing.service.gov.uk> [accessed 22nd September 2021].

Haigh, I.D., Ozsoy, O., Wadey, M.P., Nicholls, R.J., Gallop, S.L., Wahl,

T. and Brown, J.M., 2017. An improved database of coastal flooding in the United Kingdom from 1915 to 2016. Scientific data, 4(1), pp.1-10.

Hanna, E., Huybrechts, P., Cappelen, J., Steffen, K., Bales, R.C., Burgess, E., McConnell, J.R., Peder Steffensen, J., Van den Broeke, M., Wake, L. and Bigg, G., 2011. Greenland Ice

Sheet surface mass balance 1870 to 2010 based on Twentieth Century Reanalysis, and links with global climate forcing. Journal of Geophysical Research: Atmospheres, 116(D24).

Hanna, E., Jones, J.M., Cappelen, J., Mernild, S.H., Wood, L., Steffen, K. and Huybrechts, P., 2013. The influence of North Atlantic atmospheric and oceanic forcing effects on 1900–2010 Greenland summer climate and ice melt/runoff. International Journal of Climatology, 33(4), pp.862-880.

Hansen, C.Ø., Grønsedt, P., Graversen, C.L. and Hendriksen, C., 2016. *Arctic shipping: commercial opportunities and challenges*. CBS Maritime.

Hansen, J., Sato, M., Hearty, P., Ruedy, R., Kelley, M., Masson-Delmotte, V., Russell, G., Tselioudis, G., Cao, J., Rignot, E. and Velicogna, I., 2016. Ice melt, sea level rise and superstorms: evidence from paleoclimate data, climate modeling, and modern observations that 2 C global warming could be dangerous. Atmospheric Chemistry and Physics, 16(6), pp.3761-3812.

Hawkings, J.R., Wadham, J.L., Tranter, M., Raiswell, R., Benning, L.G., Statham, P.J., Tedstone, A., Nienow, P., Lee, K. and Telling, J., 2014. Ice sheets as a significant source of highly reactive nanoparticulate iron to the oceans. Nature communications, 5(1), pp.1-8.

Hewitt, H.T., Roberts, M.J., Hyder, P., Graham, T., Rae, J., Belcher, S.E., Bourdallé-Badie, R., Copsey, D., Coward, A., Guiavarch, C. and Harris, C., 2016. The impact of resolving the Rossby radius at mid-latitudes in the ocean: Results from a high-resolution version of the Met Office GC2 coupled model. Geoscientific Model Development, 9(10), pp.3655-3670.

Hill, B.T., 2000. Database of ship collisions with icebergs. Institute for Marine Dynamics, St. John’s.

Hinkel, J., Aerts, J.C., Brown, S., Jiménez, J.A., Lincke, D., Nicholls, R.J., Scussolini, P., Sanchez-Arcilla, A., Vafeidis, A. and Addo, K.A., 2018. The ability of societies to adapt to twenty-first-century sea-level rise. Nature Climate Change, 8(7), pp.570-578.

Hodson, D.L., Robson, J.I. and Sutton, R.T., 2014. An anatomy of the cooling of the North Atlantic Ocean in the 1960s and 1970s. Journal of Climate, 27(21), pp.8229-8243.

Hofer, S., Lang, C., Amory, C., Kittel, C., Delhasse, A., Tedstone, A. and Fettweis, X., 2020. Greater Greenland Ice Sheet contribution to global sea level rise in CMIP6. Nature communications, 11(1), pp.1-11.

Hofer, S., Tedstone, A.J., Fettweis, X. and Bamber, J.L., 2017. Decreasing cloud cover drives the recent mass loss on the Greenland Ice Sheet. Science Advances, 3(6), p.e1700584.

Hopwood, M.J., Carroll, D., Höfer, J., Achterberg, E.P., Meire, L., Le Moigne, F.A., Bach, L.T., Eich, C., Sutherland, D.A. and González, H.E., 2019. Highly variable iron content modulates iceberg-ocean fertilisation and potential carbon export. Nature communications, 10(1), pp.1-10.

Hu, D., Wu, L., Cai, W., Gupta, A.S., Ganachaud, A., Qiu, B., Gordon, A.L., Lin, X., Chen, Z., Hu, S. and Wang, G., 2015. Pacific western boundary currents and their roles in climate. Nature, 522(7556), pp.299-308.

International Ice Patrol. Report of the International Ice Patrol in the North Atlantic Season of 2019; CG-188-74; U.S. Coast Guard: Washington, DC, USA, 2019.

IPCC, 2013: Climate Change 2013: The Physical Science Basis. Contribution of Working Group I to the Fifth Assessment Report of the Intergovernmental Panel on Climate Change [Stocker, T.F., D. Qin, G.-K. Plattner, M. Tignor, S.K. Allen, J. Boschung, A. Nauels, Y.

Xia, V. Bex and P.M. Midgley (eds.)]. Cambridge University Press, Cambridge, United Kingdom and New York, NY, USA, 1535 pp.

IPCC, 2019: Technical Summary [H.-O. Pörtner, D.C. Roberts, V. Masson-Delmotte, P. Zhai, E. Poloczanska, K. Mintenbeck, M. Tignor, A. Alegría, M. Nicolai, A. Okem, J. Petzold, B. Rama, N.M. Weyer (eds.)]. In: IPCC Special Report on the Ocean and Cryosphere in a Changing Climate [H.- O. Pörtner, D.C. Roberts, V. Masson-Delmotte, P. Zhai, M. Tignor, E. Poloczanska, K. Mintenbeck, A. Alegría, M. Nicolai, A. Okem, J. Petzold, B. Rama, N.M. Weyer (eds.)]. In press. Ipcc.ch. 2021. [online] Available at: <https://www.ipcc.ch/site/assets/uploads/2021/01/The-concept-of-risk-in-the-IPCC-Sixth-Assessment-Report.pdf> [Accessed 18 October 2021].

IPCC, 2022: Summary for Policymakers [H.-O. Pörtner, D.C. Roberts, E.S. Poloczanska, K. Mintenbeck, M. Tignor, A. Alegría, M. Craig, S. Langsdorf, S. Löschke, V. Möller, A. Okem (eds.)]. In: Climate Change 2022: Impacts, Adaptation, and Vulnerability. Contribution of Working Group II to the Sixth Assessment Report of the Intergovernmental Panel on Climate Change [H.-O. Pörtner, D.C. Roberts, M. Tignor, E.S. Poloczanska, K. Mintenbeck, A. Alegría, M. Craig, S. Langsdorf, S. Löschke, V. Möller, A. Okem, B. Rama (eds.)]. Cambridge University Press. In Press

Jackson, L.C., Kahana, R., Graham, T., Ringer, M.A., Woollings, T., Mecking, J.V. and Wood, R.A., 2015. Global and European climate impacts of a slowdown of the AMOC in a high resolution GCM. Climate dynamics, 45(11-12), pp.3299-3316.

Janout, M., Hölemann, J., Laukert, G., Smirnov, A., Krumpen, T., Bauch, D. and Timokhov, L., 2020. On the variability of stratification in the freshwater-influenced Laptev Sea Region. Frontiers of Marine Science.

Janssens, I. and Huybrechts, P., 2000. The treatment of meltwater retention in mass-balance parameterizations of the Greenland ice sheet. Annals of Glaciology, 31, pp.133-140.

Johns, W. E., Baringer, M. O., Beal, L. M., Cunningham, S. A., Kanzow, T., Bryden, H.L., Hirschi, J.J.-M., Marotzke, J., Meinen, C.S., Shaw, B., and Curry, R.: Continuous, array-based estimates of Atlantic Ocean heat transport at 26.5 N, J. Climate, 24, 2429 - 2449, 2011.

Jones, P.D., Jónsson, T. and Wheeler, D., 1997: Extension to the North Atlantic Oscillation using early instrumental pressure observations from Gibraltar and South-West Iceland. Int. J. Climatol. 17, 1433-1450.

Jongma, J.I., Driesschaert, E., Fichefet, T., Goosse, H. and Renssen, H., 2009. The effect of dynamic–thermodynamic icebergs on the Southern Ocean climate in a three-dimensional model. Ocean Modelling, 26(1-2), pp.104-113.

Joyce, T.M. and Zhang, R., 2010. On the path of the Gulf Stream and the Atlantic meridional overturning circulation. Journal of Climate, 23(11), pp.3146-3154.

Kao, H.Y., Lagerloef, G.S., Lee, T., Melnichenko, O., Meissner, T. and Hacker, P., 2018. Assessment of aquarius sea surface salinity. *Remote Sensing*, *10*(9), p.1341.

Khan, T.A., Alam, M., Kadir, K., Shahid, Z. and Mazliham, M.S., 2019. A Comparison Review based on Classifiers and Regression Models for the Investigation of Flash Floods. Editorial Preface From the Desk of Managing Editor…, 10(9).

Khondoker, M., Dobson, R., Skirrow, C., Simmons, A. and Stahl, D., 2016. A comparison of machine learning methods for classification using simulation with multiple real data examples from mental health studies. Statistical methods in medical research,

25(5), pp.1804-1823.

Kim, W.M., Yeager, S. and Danabasoglu, G., 2021. Revisiting the causal connection between the Great Salinity Anomaly of the 1970s and the shutdown of Labrador Sea deep convection. Journal of Climate, 34(2), pp.675-696.

Koenig, Z., Provost, C., Park, Y.H., Ferrari, R. and Sennéchael, N., 2016. Anatomy of the Antarctic Circumpolar Current volume transports through Drake Passage. Journal of Geophysical Research: Oceans, 121(4), pp.2572-2595.

Kulp, S.A. and Strauss, B.H., 2019. New elevation data triple estimates of global vulnerability to sea-level rise and coastal flooding. Nature communications, 10(1), pp.1-12.

Liadze, I., Macchiarelli, C., Mortimer-Lee, P. and Juanino, P.S., 2022. The economic costs of the Russia-Ukraine conflict. *NIESR Policy Paper*, *32*.

Lind, S., Ingvaldsen, R.B. and Furevik, T., 2018. Arctic warming hotspot in the northern Barents Sea linked to declining sea-ice import. Nature climate change, 8(7), pp.634-639.

LINDSEY, R., 2022. *Climate Change: Global Sea Level*. [online] Available at: <https://www.climate.gov/news-features/understanding-climate/climate-change-global-sea-level> [Accessed 7 April 2022].

Lord, W., 2012. *The Night Lives On: The Untold Stories and Secrets Behind the Sinking of the "Unsinkable" Ship—Titanic* (Vol. 2). Open Road Media.

Lozier, M.S., Li, F., Bacon, S., Bahr, F., Bower, A.S., Cunningham, S.A., De Jong, M.F., De Steur, L., Deyoung, B., Fischer, J. and Gary, S.F., 2019. A sea change in our view of overturning in the subpolar North Atlantic. Science, 363(6426), pp.516-521.

Lumbroso, D.M. and Vinet, F., 2011. A comparison of the causes, effects and aftermaths of the coastal flooding of England in 1953 and France in 2010. *Natural Hazards and Earth System Sciences*, *11*(8), pp.2321-2333.

Madec, G. and Imbard, M., 1996. A global ocean mesh to overcome the North Pole singularity. Climate Dynamics, 12(6), pp.381-388.

Madec, G., Bourdallé-Badie, R., Bouttier, P.A., Bricaud, C., Bruciaferri, D., Calvert, D., Chanut, J., Clementi, E., Coward, A., Delrosso, D. and Ethé, C., 2017. NEMO ocean engine.

Margold, M., Stokes, C.R., Clark, C.D. and Kleman, J., 2015. Ice streams in the Laurentide Ice Sheet: a new mapping inventory. Journal of Maps, 11(3), pp.380-395.

Marsh, R., Bigg, G., Zhao, Y., Martin, M.J., Blundell, J.R., Josey, S.A., Hanna, E. and Ivchenko, V., 2018. Prospects for seasonal forecasting of iceberg distributions in the North Atlantic. Natural Hazards, 91(2), pp.447-471.

Marsh, R., Ivchenko, V.O., Skliris, N., Alderson, S., Bigg, G.R., Madec, G., Blaker, A.T., Aksenov, Y., Sinha, B., Coward, A.C. and Sommer, J.L., 2015. NEMO–ICB (v1. 0):

interactive icebergs in the NEMO ocean model globally configured at eddy-permitting resolution. *Geoscientific Model Development*, *8*(5), pp.1547-1562.

Marshall, Gareth & National Center for Atmospheric Research Staff (Eds). Last modified 19 Mar 2018. "The Climate Data Guide: Marshall Southern Annular Mode (SAM) Index (Station-based)." Retrieved from https://climatedataguide.ucar.edu/climate-data/marshall-southern-annular-mode-sam-index-station-based.

Mankoff, K. D., Solgaard, A., Colgan, W., Ahlstrøm, A. P., Khan, S. A., and Fausto, R. S.: Greenland Ice Sheet solid ice discharge from 1986 through March 2020, Earth Syst. Sci. Data, 12, 1367–1383, https://doi.org/10.5194/essd-12-1367-2020, 2020.

Mackie, S., Smith, I.J., Ridley, J.K., Stevens, D.P. and Langhorne, P.J., 2020. Climate response to increasing Antarctic iceberg and ice shelf melt. Journal of Climate, 33(20), pp.8917-8938.

Marsooli, R., Lin, N., Emanuel, K. and Feng, K., 2019. Climate change exacerbates hurricane flood hazards along US Atlantic and Gulf Coasts in spatially varying patterns. *Nature communications*, *10*(1), pp.1-9.

Marson, J.M., Myers, P.G., Hu, X. and Le Sommer, J., 2018. Using vertically integrated ocean fields to characterize Greenland icebergs' distribution and lifetime. Geophysical Research Letters, 45(9), pp.4208-4217.

Martin, T. and Adcroft, A., 2010. Parameterizing the fresh-water flux from land ice to ocean with interactive icebergs in a coupled climate model. Ocean Modelling, 34(3-4), pp.111-124.

Marzocchi, A., Hirschi, J.J.M., Holliday, N.P., Cunningham, S.A., Blaker, A.T. and Coward, A.C., 2015. The North Atlantic subpolar circulation in an eddy-resolving global ocean model. Journal of Marine Systems, 142, pp.126-143.

McCarron, A.P., Bigg, G.R., Brooks, H., Leng, M.J., Marshall, J.D., Ponomareva, V., Portnyagin, M., Reimer, P.J. and Rogerson, M., 2021. Northwest Pacific ice-rafted debris at 38° N reveals episodic ice-sheet change in late Quaternary Northeast Siberia. Earth and Planetary Science Letters, 553, p.116650.

McCarthy, G.D., Smeed, D.A., Johns, W.E., Frajka-Williams, E., Moat, B.I., Rayner, D., Baringer, M.O., Meinen, C.S., Collins, J. and Bryden, H.L., 2015. Measuring the Atlantic meridional overturning circulation at 26 N. Progress in Oceanography, 130, pp.91-111.

McMillan, M., Leeson, A., Shepherd, A., Briggs, K., Armitage, T.W., Hogg, A., Kuipers Munneke, P., Van Den Broeke, M., Noel, B., van de Berg, W.J. and Ligtenberg, S., 2016. A high-resolution record of Greenland mass balance. Geophysical Research Letters, 43(13), pp.7002-7010.

Medvedev, S., Souche, A. and Hartz, E.H., 2013. Influence of ice sheet and glacial erosion on passive margins of Greenland. Geomorphology, 193, pp.36-46.

Melia, N., Haines, K. and Hawkins, E., 2016. Sea ice decline and 21st century trans-Arctic shipping routes. Geophysical Research Letters, 43(18), pp.9720-9728.

Melia, N., Haines, K. and Hawkins, E., 2016. Sea ice decline and 21st century trans-Arctic shipping routes. Geophysical Research Letters, 43(18), pp.9720-9728.

Momin, I.M., Mitra, A.K. and Bhatla, R., 2021. Assessment of NEMO simulated surface current with HF radar along Andhra Pradesh coast. Journal of Earth System Science, 130(2), pp.1-11.

Moon, T., Ahlstrøm, A., Goelzer, H., Lipscomb, W. and Nowicki, S., 2018.

Rising oceans guaranteed: Arctic land ice loss and sea level rise. Current climate change reports, 4(3), pp.211-222.

Mukherjee, S., Mishra, A. and Trenberth, K.E., 2018. Climate change and drought: a perspective on drought indices. *Current Climate Change Reports*, *4*(2), pp.145-163.

Murphy, D.L.; Cass, J.L. The International Ice Patrol, safeguarding life and property at sea. Coast Guard Proc.Mar. Safety Sec. Coun. 2012, 69, 13-16.

Navcen.uscg.gov. (2019). ABOUT INTERNATIONAL ICE PATROL (IIP). [online] Available at: https://www.navcen.uscg.gov/?pageName=IIPHome [Accessed 16 Feb. 2021].

Navcen.uscg.gov. 2022. Iceberg Locations. [online] Available at: <https://www.navcen.uscg.gov/?pageName=IcebergLocations> [Accessed 16 Feb. 2021].

Navcen.uscg.gov. 2021. Ice Patrol Charts & Chart Archives. [online] Available at: <https://www.navcen.uscg.gov/?pageName=iipCharts&year=2020> [Accessed 15 February 2021].

Navcen.uscg.gov. 2021. Report of the International Ice Patrol in the North Atlantic. [online] Available at: <https://navcen.uscg.gov/pdf/iip/2021_Annual_Report_FINAL.pdf> [Accessed 9 December 2021].

NEMO ocean engine, NEMO System Team, Scientific Notes of Climate Modelling Center, 27, ISSN 1288-1619 Institut Pierre-Simon Laplace (IPSL), doi:10.5281/zenodo.1464816

Neumann, B., Vafeidis, A.T., Zimmermann, J. and Nicholls, R.J., 2015. Future coastal population growth and exposure to sea-level rise and coastal flooding-a global assessment. PloS one, 10(3), p.e0118571.

Niehörster, F. and Murnane, R.J., 2018. Ocean risk and the insurance industry. Pub. by XL Catlin Services SE, UK.

Noël, B., van de Berg, W.J., Lhermitte, S. and van den Broeke, M.R., 2019. Rapid ablation zone expansion amplifies north Greenland mass loss. Science advances, 5(9), p.eaaw0123.

Normandeau, A., MacKillop, K., Macquarrie, M., Richards, C., Bourgault, D., Campbell, D.C., Maselli, V., Philibert, G. and Clarke, J.H., 2021. Submarine landslides triggered by iceberg collision with the seafloor. Nature Geoscience, 14(8), pp.599-605.

Norris, S.L., Garcia-Castellanos, D., Jansen, J.D., Carling, P.A., Margold, M., Woywitka, R.J. and Froese, D.G., 2021. Catastrophic drainage from the northwestern outlet of glacial Lake Agassiz during the Younger Dryas. Geophysical Research Letters, 48(15), p.e2021GL093919.

Nsidc.org. (2019). bergy bit | National Snow and Ice Data Center. [online] Available at: https://nsidc.org/cryosphere/glossary/term/bergy-bit [Accessed 22 May 2019].

Obaid, O.I., Mohammed, M.A., Ghani, M.K.A., Mostafa, A. and Taha, F., 2018. Evaluating the performance of machine learning techniques in the classification of Wisconsin Breast Cancer. International Journal of Engineering & Technology, 7(4.36), pp.160-166.

Oppo, D.W., Curry, W.B. and McManus, J.F., 2015. What do benthic δ13C and δ18O data tell us about Atlantic circulation during Heinrich Stadial 1?. Paleoceanography, 30(4), pp.353-368.

Oppenheimer, M., B.C. Glavovic , J. Hinkel, R. van de Wal, A.K. Magnan, A. Abd-Elgawad, R. Cai, M. Cifuentes-Jara, R.M. DeConto, T. Ghosh, J. Hay, F. Isla, B. Marzeion, B. Meyssignac, and Z. Sebesvari, 2019: Sea Level Rise and Implications for Low-Lying Islands, Coasts and Communities. In: IPCC Special Report on the Ocean and Cryosphere in a Changing Climate [H.-O. Pörtner, D.C. Roberts, V. Masson-Delmotte, P. Zhai, M. Tignor, E. Poloczanska, K. Mintenbeck, A. Alegría, M. Nicolai, A. Okem, J. Petzold, B. Rama, N.M. Weyer (eds.)]. Cambridge University Press, Cambridge, UK and New York, NY, USA, pp. 321-445. https://doi.org/10.1017/9781009157964.006.

Østby, T.I., Schuler, T.V., Hagen, J.O., Hock, R., Kohler, J. and Reijmer, C.H., 2017. Diagnosing the decline in climatic mass balance of glaciers in Svalbard over 1957–2014. The Cryosphere, 11(1), pp.191-215.

Palter, J.B., 2015. The role of the Gulf Stream in European climate. Annual review of marine science, 7, pp.113-137.

Peterson, C. D. and Lisiecki, L. E.: Deglacial carbon cycle changes observed in a compilation of 127 benthic δ13C time series (20–6 ka), Clim. Past, 14, 1229-1252.

Pham, B.T. and Prakash, I., 2019. Evaluation and comparison of LogitBoost Ensemble, Fisher’s Linear Discriminant Analysis, logistic regression and support vector machines methods for landslide susceptibility mapping. Geocarto International, 34(3), pp.316-333.

Pörtner, H.-O., D.M. Karl, P.W. Boyd,W.W.L. Cheung, S.E. Lluch-Cota, Y. Nojiri, D.N. Schmidt, and P.O. Zavialov, 2014: Ocean systems. In: Climate Change 2014: Impacts, Adaptation, and Vulnerability. Part A: Global and Sectoral Aspects. Contribution of Working Group II to the Fifth Assessment Report of the Intergovernmental Panel on Climate Change

[Field, C.B., V.R. Barros, D.J. Dokken, K.J. Mach, M.D. Mastrandrea, T.E. Bilir, M. Chatterjee, K.L. Ebi, Y.O. Estrada, R.C. Genova, B. Girma, E.S. Kissel, A.N. Levy, S. MacCracken, P.R. Mastrandrea, and L.L.White (eds.)]. Cambridge University Press, Cambridge, United Kingdom and New York, NY, USA, pp. 411-484.

Raiswell, R., Benning, L.G., Tranter, M. and Tulaczyk, S., 2008. Bioavailable iron in the Southern Ocean: the significance of the iceberg conveyor belt. Geochemical transactions, 9(1), pp.1-9.

Rantala, O., Barre, S.D.L., Granås, B., Jóhannesson, G.Þ., Müller, D.K., Saarinen, J., Tervo-Kankare, K., Maher, P.T. and Niskala, M., 2019. Arctic tourism in times of change: Seasonality. Nordic Council of Ministers.

Renssen, H., Mairesse, A., Goosse, H., Mathiot, P., Heiri, O., Roche, D.M., Nisancioglu, K.H. and Valdes, P.J., 2015. Multiple causes of the Younger Dryas cold period. Nature Geoscience, 8(12), p.946.

Robson, J., Ortega, P. and Sutton, R., 2016. A reversal of climatic trends in the North Atlantic since 2005. Nature Geoscience, 9(7), pp.513-517.

Sadighrad, E., Fach, B.A., Arkin, S.S., Salihoğlu, B. and Hüsrevoğlu, Y.S., 2021. Mesoscale eddies in the Black Sea: Characteristics and kinematic properties in a high-resolution ocean model. Journal of Marine Systems, 223, p.103613.

Sasaki, Y.N., Minobe, S. and Miura, Y., 2014. Decadal sea-level variability along the coast of Japan in response to ocean circulation changes. Journal of Geophysical Research: Oceans, 119(1), pp.266-275.

Serreze, M.C., Barrett, A.P., Stroeve, J.C., Kindig, D.N. and Holland, M.M., 2009. The emergence of surface-based Arctic amplification. The Cryosphere, 3(1), pp.11-19.

Slater, D.A., Carroll, D., Oliver, H., Hopwood, M.J., Straneo, F., Wood, M., Willis, J.K. and Morlighem, M., 2022. Characteristic depths, fluxes and timescales for Greenland's tidewater glacier fjords from subglacial discharge-driven upwelling during summer. Geophysical Research Letters, p.e2021GL097081.

Shepherd, A., Ivins, E., Rignot, E., Smith, B., van Den Broeke, M., Velicogna, I., Whitehouse, P., Briggs, K., Joughin, I., Krinner, G. and Nowicki, S., 2020. Mass balance of the Greenland Ice Sheet from 1992 to 2018. Nature, 579(7798), pp.233-239.

Silvy, Y., Rousset, C., Guilyardi, E., Sallée, J.B., Mignot, J., Ethé, C. and Madec, G., 2022. A modeling framework to understand historical and projected ocean climate change in large coupled ensembles. Geoscientific Model Development, 15(20), pp.7683-7713.

Siqueira, L. and Kirtman, B.P., 2016. Atlantic near-term climate variability and the role of a resolved Gulf Stream. Geophysical Research Letters, 43(8), pp.3964-3972.

SMAP. 2021. *Why It Matters | Mission – SMAP*. [online] Available at:<https://smap.jpl.nasa.gov/mission/why-it-matters/> [Accessed 13 October 2021].

Solakivi, T., Kiiski, T. and Ojala, L., 2019. On the cost of ice: estimating the premium of Ice Class container vessels. Maritime Economics & Logistics, 21(2), pp.207-222.

Sotillo, M.G., Amo-Baladrón, A., Padorno, E., García-Ladona, E., Orfila, A., Rodríguez-Rubio, P., Conti, D., Madrid, J.J., De los Santos, F.J. and Fanjul, E.A., 2016. How is the surface Atlantic water inflow through the Gibraltar Strait forecasted? A lagrangian validation of operational oceanographic services in the Alboran Sea and the Western Mediterranean. Deep Sea Research Part II: Topical Studies in Oceanography, 133, pp.100-117.

Stephenson Jr, G.R., Sprintall, J., Gille, S.T., Vernet, M., Helly, J.J. and Kaufmann, R.S., 2011. Subsurface melting of a free-floating Antarctic iceberg. Deep Sea Research Part II: Topical Studies in Oceanography, 58(11-12), pp.1336-1345.

Straneo, F., Sutherland, D.A., Stearns, L.A., Catania, G., Heimbach, P., Moon, T., Cape, M.R., Laidre, K.L., Barber, D., Rysgaard, S. and Mottram, R., 2019. The case for a sustained Greenland Ice sheet-Ocean Observing System. Frontiers in Marine Science, 6, p.138.

Sudom, D., Timco, G. and Tivy, A., 2014, September. Iceberg sightings, shapes and management techniques for offshore Newfoundland and Labrador: Historical data and future applications. In 2014 Oceans-St. John's (pp. 1-8). IEEE.

Tandon, N.F., Saenko, O.A., Cane, M.A. and Kushner, P.J., 2020. Interannual variability of the global meridional overturning circulation dominated by Pacific Variability. Journal of Physical Oceanography, 50(3), pp.559-574.

Trenberth, Kevin, Zhang, Rong & National Center for Atmospheric Research Staff (Eds). Last modified 05 Jun 2021. "The Climate Data Guide: Atlantic Multi-decadal Oscillation (AMO)." Retrieved from https://climatedataguide.ucar.edu/climate-data/atlantic-multi-decadal-oscillation-amo.

The IMBIE Team. Mass balance of the Greenland Ice Sheet from 1992 to 2018. Nature 579, 233–239 (2020). https://doi.org/10.1038/s41586-019-1855-2

Tseng, P.H. and Cullinane, K., 2018. Key criteria influencing the choice of Arctic shipping: a fuzzy analytic hierarchy process model. Maritime Policy & Management, 45(4), pp.422-438.

Van Sebille, E., Sprintall, J., Schwarzkopf, F.U., Sen Gupta, A., Santoso, A., England, M.H., Biastoch, A. and Böning, C.W., 2014. Pacific-to-Indian Ocean connectivity: Tasman leakage, Indonesian Throughflow, and the role of ENSO. Journal of Geophysical Research: Oceans, 119(2), pp.1365-1382.

Van Der Veen, C.J., Plummer, J.C. and Stearns, L.A., 2011. Controls on the recent speed-up of Jakobshavn Isbræ, West Greenland. Journal of Glaciology, 57(204), pp.770-782.

Wadley, M.R. and Bigg, G.R., 2002. Impact of flow through the Canadian Archipelago and Bering Strait on the North Atlantic and Arctic circulation: An ocean modelling study. Quarterly Journal of the Royal Meteorological Society: A journal of the atmospheric sciences, applied meteorology and physical oceanography, 128(585), pp.2187-2203.

Wadey, M.P., Haigh, I.D., Nicholls, R.J., Brown, J.M., Horsburgh, K., Carroll, B., Gallop, S.L., Mason, T. and Bradshaw, E., 2015. A comparison of the 31 January–1 February 1953 and 5–6 December 2013 coastal flood events around the UK. Frontiers in Marine Science, 2, p.84.

Wagner, T.J., Dell, R.W. and Eisenman, I., 2017. An analytical model of iceberg drift. Journal of Physical Oceanography, 47(7), pp.1605-1616.

Whitworth, T.I.I.I. and Peterson, R.G., 1985. Volume transport of the Antarctic Circumpolar Current from bottom pressure measurements. Journal of Physical Oceanography, 15(6), pp.810-816.

Wilton, D.J., Bigg, G.R. and Hanna, E., 2015. Modelling twentieth century global ocean circulation and iceberg flux at 48 N: implications for west Greenland iceberg discharge. Progress in Oceanography, 138, pp.194-210.

Wilton, D.J., Jowett, A., Hanna, E., Bigg, G.R., Van Den Broeke, M.R., Fettweis, X. and Huybrechts, P., 2017. High resolution (1km) positive degree-day modelling of Greenland ice sheet surface mass balance, 1870–2012 using reanalysis data. *Journal of Glaciology*, *63*(237), pp.176-193.

Widell, K., Fer, I. and Haugan, P.M., 2006. Salt release from warming sea ice. Geophysical research letters, 33(12).

Woodgate, R.A., Weingartner, T.J. and Lindsay, R., 2012. Observed increases in Bering Strait oceanic fluxes from the Pacific to the Arctic from 2001 to 2011 and their impacts on the Arctic Ocean water column. Geophysical Research Letters, 39(24).

Xu, X., Chassignet, E.P., Firing, Y.L. and Donohue, K., 2020. Antarctic circumpolar current transport through Drake Passage: What can we learn from comparing high-resolution model results to observations?. Journal of Geophysical Research: Oceans, 125(7), p.e2020JC016365.

Yang, Q., Dixon, T.H., Myers, P.G., Bonin, J., Chambers, D., Van Den Broeke, M.R., Ribergaard, M.H. and Mortensen, J., 2016. Recent increases in Arctic freshwater flux affects Labrador Sea convection and Atlantic overturning circulation. Nature communications, 7, p.10525.

Yao, P., Lu, H., Shi, J., Zhao, T., Yang, K., Cosh, M.H., Gianotti, D.J.S. and Entekhabi, D., 2021. A long term global daily soil moisture dataset derived from AMSR-E and AMSR2 (2002–2019). Scientific data, 8(1), pp.1-16.

Yool, A., Palmiéri, J., Jones, C.G., de Mora, L., Kuhlbrodt, T., Popova, E.E., Nurser, A.J., Hirschi, J., Blaker, A.T., Coward, A.C. and Blockley, E.W., 2021. Evaluating the physical and biogeochemical state of the global ocean component of UKESM1 in CMIP6 historical simulations. Geoscientific Model Development, 14(6), pp.3437-3472.

Yu, L., Gao, Y. and Otterå, O.H., 2016. The sensitivity of the Atlantic meridional overturning circulation to enhanced freshwater discharge along the entire, eastern and western coast of Greenland. Climate dynamics, 46(5-6), pp.1351-1369.

Zhang, W., Wang, Q., Wang, X. and Danilov, S., 2020. Mechanisms driving the interannual variability of the Bering Strait Throughflow. Journal of Geophysical Research: Oceans, 125(2), p.e2019JC015308.

Zhao, J., Yang, J., Semper, S., Pickart, R.S., Våge, K., Valdimarsson, H. and Jónsson, S., 2018. A numerical study of interannual variability in the North Icelandic Irminger Current. Journal of Geophysical Research: Oceans, 123(12), pp.8994-9009.

Zhao, Y., Bigg, G.R., Billings, S.A., Hanna, E., Sole, A.J., Wei, H.L., Kadirkamanathan, V. and Wilton, D.J., 2016. Inferring the variation of climatic and glaciological contributions to West Greenland iceberg discharge in the twentieth century. Cold Regions Science and Technology, 121, pp.167-178.

Zhao, Y., Hanna, E., Bigg, G.R. and Zhao, Y., 2017. Tracking nonlinear correlation for complex dynamic systems using a Windowed Error Reduction Ratio method. *Complexity*, *2017*.

Zheng, W., Pritchard, M.E., Willis, M.J., Tepes, P., Gourmelen, N., Benham, T.J. and Dowdeswell, J.A., 2018. Accelerating glacier mass loss on Franz Josef Land, Russian Arctic. Remote Sensing of Environment, 211, pp.357-375.

Zhu, C. and Liu, Z., 2020. Weakening Atlantic overturning circulation causes South Atlantic salinity pile-up. Nature Climate Change, 10(11), pp.998-1003.

Appendices

Table S1. The ensemble of WERR Models used for the 2021 forecast. All terms are listed, however only those in bold were used for prediction. Columns: Rank – order of selection of term in model; Term – linear or quadratic term in variables NAO, LSST or SMB (North Atlantic Oscillation, Labrador Sea Surface Temperature or the Surface Mass Balance of the Greenland Ice Sheet), with lags, in x months, given by '(t-x)'; ERR – error reduction per term; Coefficient – multiplying factor for term. For example of the model structure, the first term for the sliding window January 1979 to December 2008 is 22.54386.NAO(t-15)^2. Then add the second term etc. until the ERR is below 0.02. Note that only models with the 8 month prediction constraint were used here (see [7] for details on why this was done).

Rank	Term	ERR	Coefficient
1979-Jan to 2008-Dec			
1	**NAO(t-15)*NAO(t-15)**	**0.36292**	**22.54386**
2	**LSST(t-9)**	**0.06819**	**-70.76018**
3	**LSST(t-8)*LSST(t-9)**	**0.05564**	**80.73332**
4	**NAO(t-28)*NAO(t-29)**	**0.03827**	**14.7938**
5	**NAO(t-15)*NAO(t-39)**	**0.03215**	**13.46352**
6	**SMB(t-9)*SMB(t-21)**	**0.02603**	**0.01171**
7	**SMB(t-8)*SMB(t-46)**	**0.0353**	**-0.01422**
8	NAO(t-40)*LSST(t-38)	0.01844	44.47945
9	SMB(t-35)*NAO(t-38)	0.01536	0.54795
10	NAO(t-15)*LSST(t-15)	0.01609	28.32399
11	NAO(t-14)*NAO(t-47)	0.01414	14.75576
12	SMB(t-35)*NAO(t-14)	0.01377	-0.56135
13	NAO(t-14)*LSST(t-41)	0.01414	-37.87206
14	NAO(t-17)*NAO(t-29)	0.013	13.62479
15	SMB(t-9)*NAO(t-35)	0.01145	0.40612
1980-Jan to 2009-Dec			
1	**NAO(t-15)*NAO(t-15)**	**0.36127**	**20.05216**
2	**NAO(t-28)*NAO(t-28)**	**0.06116**	**9.24127**
3	**LSST(t-9)**	**0.05229**	**-72.82291**
4	**LSST(t-8)*LSST(t-9)**	**0.03991**	**89.56479**
5	**SMB(t-8)*SMB(t-46)**	**0.03371**	**-0.0175**
6	**SMB(t-9)*SMB(t-21)**	**0.0483**	**0.01255**

7	**NAO(t-15)*LSST(t-14)**	**0.02701**	**29.19803**
8	**NAO(t-40)*LSST(t-38)**	**0.02608**	**39.73453**
9	NAO(t-17)*NAO(t-29)	0.01626	16.87268
10	SMB(t-35)*NAO(t-38)	0.01357	0.43758
11	NAO(t-14)*LSST(t-41)	0.01363	-44.02547
12	**SMB(t-35)*NAO(t-14)**	**0.02171**	**-0.56654**
13	LSST(t-21)*LSST(t-28)	0.01304	-62.2622
14	SMB(t-20)*NAO(t-41)	0.01225	0.3938
15	SMB(t-33)*NAO(t-40)	0.01305	-0.3572
1981-Jan to 2010-Dec			
1	**NAO(t-15)*NAO(t-15)**	**0.35175**	**22.48843**
2	**NAO(t-28)*NAO(t-29)**	**0.06108**	**15.24083**
3	**NAO(t-39)*NAO(t-39)**	**0.05227**	**15.07007**
4	**NAO(t-15)*NAO(t-16)**	**0.03661**	**18.08788**
5	**NAO(t-15)*NAO(t-47)**	**0.03002**	**22.31135**
6	**SMB(t-40)*NAO(t-27)**	**0.02655**	**0.62498**
7	**NAO(t-25)*NAO(t-28)**	**0.02787**	**23.96898**
8	**SMB(t-9)*LSST(t-21)**	**0.02465**	**-1.02514**
9	**SMB(t-8)*NAO(t-13)**	**0.02535**	**-0.50573**
10	SMB(t-46)*SMB(t-46)	0.01922	0.00887
11	NAO(t-15)*LSST(t-13)	0.01604	39.84936
12	NAO(t-37)*LSST(t-9)	0.01423	-26.86158
13	NAO(t-26)*NAO(t-29)	0.01223	18.05206
14	SMB(t-44)*NAO(t-27)	0.01233	-0.3173
15	SMB(t-8)*SMB(t-31)	0.01185	-0.00703
1982-Jan to 2011-Dec			
1	**NAO(t-15)*NAO(t-15)**	**0.27508**	**13.92661**
2	**SMB(t-29)*NAO(t-15)**	**0.09331**	**0.44737**
3	**NAO(t-28)*NAO(t-28)**	**0.06794**	**15.03671**
4	**SMB(t-8)*SMB(t-46)**	**0.04255**	**-0.01963**
5	**SMB(t-9)*SMB(t-9)**	**0.03728**	**0.00635**
6	**NAO(t-17)*NAO(t-29)**	**0.03936**	**18.49671**
7	**NAO(t-15)*NAO(t-41)**	**0.0275**	**29.05513**
8	**SMB(t-31)*SMB(t-35)**	**0.02058**	**0.00956**
9	NAO(t-28)*NAO(t-34)	0.01747	27.8608
10	NAO(t-37)*LSST(t-43)	0.01744	-31.56919
11	SMB(t-9)*NAO(t-25)	0.01639	0.35875
12	NAO(t-39)*LSST(t-16)	0.01723	32.54011
13	NAO(t-39)*LSST(t-8)	0.01654	-43.98501
14	SMB(t-24)*NAO(t-27)	0.01647	0.39752
15	NAO(t-15)*NAO(t-16)	0.01474	12.61278

1983-Jan to 2012-Dec			
1	**NAO(t-15)*NAO(t-15)**	**0.25965**	**23.22433**
2	**NAO(t-15)*LSST(t-15)**	**0.10281**	**56.57531**
3	**NAO(t-28)*NAO(t-28)**	**0.06036**	**7.75748**
4	**SMB(t-8)*SMB(t-46)**	**0.04467**	**-0.01339**
5	**SMB(t-9)*SMB(t-9)**	**0.04717**	**0.00704**
6	**NAO(t-17)*NAO(t-29)**	**0.03505**	**18.43852**
7	**SMB(t-15)*NAO(t-27)**	**0.02649**	**0.45616**
8	**LSST(t-8)*LSST(t-13)**	**0.02242**	**-51.99037**
9	SMB(t-35)*LSST(t-19)	0.01928	1.3139
10	SMB(t-35)*LSST(t-31)	0.01995	-1.07768
11	NAO(t-39)*NAO(t-47)	0.01926	23.17552
12	SMB(t-31)*NAO(t-39)	0.01653	0.2898
13	SMB(t-23)*NAO(t-13)	0.01365	0.39849
14	NAO(t-40)*LSST(t-38)	0.01545	35.97512
15	NAO(t-15)*NAO(t-47)	0.01358	18.63497
1984-Jan to 2013-Dec			
1	**NAO(t-15)*NAO(t-15)**	**0.26073**	**18.8801**
2	**NAO(t-15)*LSST(t-15)**	**0.12472**	**51.77163**
3	**NAO(t-28)*NAO(t-28)**	**0.04867**	**5.97852**
4	**NAO(t-40)*LSST(t-38)**	**0.04186**	**42.85402**
5	**SMB(t-8)*SMB(t-46)**	**0.02943**	**-0.01435**
6	**SMB(t-9)*SMB(t-9)**	**0.03366**	**0.00722**
7	**NAO(t-39)*LSST(t-26)**	**0.02725**	**33.35643**
8	**NAO(t-16)*NAO(t-29)**	**0.02344**	**17.05896**
9	NAO(t-15)*NAO(t-41)	0.01945	20.78917
10	**SMB(t-11)*NAO(t-38)**	**0.02181**	**0.45834**
11	NAO(t-14)*NAO(t-47)	0.01994	19.0679
12	NAO(t-28)*NAO(t-34)	0.0173	24.64092
13	LSST(t-19)*LSST(t-39)	0.01327	-79.55168
14	NAO(t-29)*NAO(t-29)	0.01393	10.40664
15	NAO(t-16)*NAO(t-43)	0.01313	16.68583
1985-Jan to 2014-Dec			
1	**NAO(t-15)*NAO(t-15)**	**0.23536**	**26.22621**
2	**NAO(t-15)*LSST(t-15)**	**0.11772**	**57.48812**
3	**NAO(t-14)*LSST(t-44)**	**0.08303**	**-44.64461**
4	**NAO(t-28)*NAO(t-28)**	**0.05376**	**13.7081**
5	**SMB(t-21)*LSST(t-21)**	**0.03382**	**-0.91717**
6	**SMB(t-30)*NAO(t-27)**	**0.02698**	**0.45883**
7	**NAO(t-15)*NAO(t-41)**	**0.02258**	**21.51814**
8	**SMB(t-35)*LSST(t-21)**	**0.02225**	**1.00672**
9	**SMB(t-8)*SMB(t-46)**	**0.0244**	**-0.00938**

10	**SMB(t-24)*NAO(t-27)**	**0.02232**	**0.37697**
11	NAO(t-25)*NAO(t-28)	0.01732	20.61168
12	SMB(t-8)*NAO(t-13)	0.01594	-0.29197
13	SMB(t-42)*LSST(t-38)	0.0128	0.84207
14	NAO(t-15)*NAO(t-47)	0.01381	20.0413
15	LSST(t-29)*LSST(t-37)	0.01582	-64.35686
1986-Jan to 2015-Dec			
1	**NAO(t-15)*NAO(t-15)**	**0.23001**	**24.57823**
2	**NAO(t-15)*LSST(t-15)**	**0.11673**	**79.44829**
3	**NAO(t-14)*LSST(t-44)**	**0.07637**	**-39.44514**
4	**SMB(t-21)*SMB(t-21)**	**0.05615**	**0.00648**
5	**NAO(t-25)*NAO(t-28)**	**0.04729**	**22.98647**
6	**SMB(t-8)*SMB(t-46)**	**0.04408**	**-0.01472**
7	**NAO(t-16)*LSST(t-21)**	**0.02465**	**-36.97192**
8	**NAO(t-15)*LSST(t-29)**	**0.02255**	**-44.99723**
9	**NAO(t-28)*NAO(t-29)**	**0.02514**	**22.9113**
10	**SMB(t-9)*NAO(t-25)**	**0.02224**	**0.34153**
11	SMB(t-42)*NAO(t-27)	0.01827	0.32732
12	NAO(t-30)*NAO(t-39)	0.01294	-17.41382
13	NAO(t-14)*NAO(t-18)	0.01598	20.91167
14	NAO(t-15)*NAO(t-47)	0.00919	18.25769
15	SMB(t-44)*LSST(t-32)	0.01046	0.60053
1987-Jan to 2016-Dec			
1	**NAO(t-15)*NAO(t-15)**	**0.22126**	**28.83026**
2	**NAO(t-15)*LSST(t-15)**	**0.12799**	**76.26225**
3	**NAO(t-14)*NAO(t-41)**	**0.06971**	**19.85428**
4	**SMB(t-21)*SMB(t-21)**	**0.05596**	**0.00747**
5	**SMB(t-8)*SMB(t-46)**	**0.05079**	**-0.01328**
6	**NAO(t-25)*NAO(t-28)**	**0.03681**	**22.82284**
7	**NAO(t-27)**	**0.03061**	**19.06752**
8	**NAO(t-16)*LSST(t-21)**	**0.02426**	**-41.07141**
9	**SMB(t-33)*NAO(t-25)**	**0.02072**	**0.30667**
10	LSST(t-29)*LSST(t-37)	0.01789	-58.94801
11	NAO(t-28)*NAO(t-37)	0.01708	18.53296
12	NAO(t-28)*NAO(t-29)	0.01646	16.22431
13	NAO(t-15)*LSST(t-29)	0.016	-39.75001
14	SMB(t-23)*NAO(t-13)	0.01302	0.38256
15	NAO(t-39)*NAO(t-47)	0.01138	16.57262
1988-Jan to 2017-Dec			
1	**SMB(t-21)*SMB(t-21)**	**0.17465**	**0.00274**
2	**SMB(t-8)*SMB(t-34)**	**0.16158**	**-0.01125**

3	**NAO(t-39)*NAO(t-39)**	**0.06454**	**0.75169**
4	**LSST(t-8)**	**0.03628**	**-130.24051**
5	**Const.**	**0.0624**	**96.53238**
6	**SMB(t-34)*NAO(t-15)**	**0.02786**	**-0.35014**
7	**NAO(t-15)**	**0.02645**	**22.04743**
8	**NAO(t-15)*LSST(t-8)**	**0.02614**	**-17.86106**
9	**SMB(t-44)*NAO(t-9)**	**0.02109**	**-0.27316**
10	**SMB(t-22)*NAO(t-10)**	**0.02029**	**-0.29914**
11	**SMB(t-8)*NAO(t-10)**	**0.02725**	**0.32247**
12	**SMB(t-21)**	**0.02098**	**-0.76746**
13	NAO(t-11)*NAO(t-17)	0.01616	5.05314
14	SMB(t-9)*NAO(t-43)	0.01415	-0.18014
15	SMB(t-8)*LSST(t-8)	0.01391	0.8745
1989-Jan to 2018-Dec			
1	**SMB(t-9)*SMB(t-9)**	**0.15921**	**0.00835**
2	**SMB(t-8)*SMB(t-46)**	**0.16535**	**-0.01443**
3	**NAO(t-39)*NAO(t-39)**	**0.05918**	**1.90957**
4	**LSST(t-8)**	**0.04041**	**-146.26204**
5	**Const.**	**0.06605**	**81.05327**
6	**SMB(t-8)*LSST(t-12)**	**0.02859**	**0.86102**
7	**SMB(t-22)*SMB(t-35)**	**0.02387**	**-0.00704**
8	SMB(t-21)*LSST(t-21)	0.01987	-1.3694
9	**LSST(t-8)*LSST(t-20)**	**0.0259**	**144.90364**
10	**SMB(t-9)*NAO(t-43)**	**0.02134**	**-0.26567**
11	**NAO(t-15)*LSST(t-35)**	**0.02035**	**26.38009**
12	SMB(t-34)*NAO(t-15)	0.01721	-0.19223
13	SMB(t-32)*NAO(t-8)	0.01577	-0.19769
14	NAO(t-13)*NAO(t-32)	0.01426	4.91804
15	NAO(t-15)*NAO(t-47)	0.01491	4.67722

Table S2. Input data for FRUGAL Run 5, varying monthly and yearly over the input locations (in t/yr).

	Latitude, Longitude										
Time	(64.51,-51.31)	(60.94,-46.13)	(72.66,-20.57)	(75.03,-57.55)	(80.75,-12.43)	(71,-22.83)	(71.29,-51.68)	(65.95,-37.92)	(69.98,-27.18)	(68.49,-32.93)	(70.95,-22.3)
01/1977	1.06E-06	1.16E-06	3.64E-08	3.73E-08	3.49E-10	1.64E-10	2.10E-09	1.51E-08	0	1.03E-10	0
02/1977	5.55E-06	1.16E-06	1.59E-07	1.68E-07	7.81E-10	3.29E-10	1.19E-09	3.84E-08	0	2.88E-10	0
03/1977	2.24E-06	6.65E-06	5.06E-08	8.00E-07	1.30E-08	1.19E-08	1.98E-08	1.65E-08	2.05E-11	0	0
04/1977	6.89E+01	165.4123428	150.2081121	3.18E-05	4.10E-06	2.87E-06	2.79E-06	2.28E-05	7.92E-08	1.22E-06	0
05/1977	3769.458458	14808.61716	7727.490255	1175.301494	1.15E+01	2.71E-05	8.01E-05	1975.184206	2.72E-06	1.03E-04	3.59E-06
06/1977	27014.542	83374.59579	40786.72864	34498.05302	13972.90609	10447.74843	7787.853966	62270.39816	1939.226397	13328.57642	5.47E+01
07/1977	133761.0822	274915.224	208217.4276	246244.9778	67332.33335	53614.28168	70949.27431	280404.234	9221.919294	327491.2066	84089.5612
08/1977	160188.19	329415.6328	181664.9654	338392.1839	63645.29298	58167.77791	108818.2263	222685.7274	7035.128839	302647.7576	51446.07356
09/1977	95808.85114	73494.6824	48531.76308	25528.77741	1608.661249	1381.482878	10600.4368	34738.57921	105.0804032	6451.647445	1.05E+01
10/1977	976.1973369	3811.868625	4.25E+01	132.5721278	2.64E-06	2.34E-06	1.27E-05	1.06E-05	1.32E-07	1.38E-05	1.34E-09
11/1977	2.72E-06	5.41E-06	5.79E-08	1.13E-07	1.85E-09	1.50E-09	3.56E-08	8.26E-09	0	2.77E-09	0
12/1977	2.91E-05	3.25E-05	4.79E+01	9.87E-06	2.22E-07	1.53E-07	3.34E-07	1.23E-05	6.57E-10	2.10E-07	0
01/1978	1.52E-06	1.18E-06	2.44E-07	9.02E-08	8.42E-10	4.72E-10	4.91E-09	2.13E-07	0	1.94E-08	0
02/1978	7.72E-06	4.91E-06	2.55E-07	7.38E-07	5.30E-09	3.62E-09	2.02E-08	8.01E-08	1.03E-10	0	0

03/1978	2.71E-06	2.79E-06	1.55E-07	1.12E-06	1.84E-08	1.77E-08	2.74E-08	4.14E-08	1.23E-10	3.82E-09	0
04/1978	4.89E+00	5.60E+01	2.66E+01	1.09E-05	6.54E-07	3.31E-07	9.35E-07	1.42E-05	2.78E-08	1.20E-06	2.05E-10
05/1978	7925.953421	18213.91804	12074.13291	348.7652975	8.25E-06	6.68E-06	1.88E-05	2.48E+01	1.70E-07	3.59E-05	2.30E-07
06/1978	49709.10437	133044.3144	56939.02514	45928.31998	15173.83126	11037.18583	7428.524322	44393.24591	2170.773013	4246.87608	1100.232469
07/1978	132228.9086	260401.7921	169000.4882	246237.0596	64926.09107	52718.78822	78385.8904	206722.2171	9609.971656	252527.9275	81518.92018
08/1978	177442.4232	233000.3478	167097.5728	230974.5492	50361.55296	46685.86034	91841.66909	157064.4762	7421.086934	263378.9984	47884.50793
09/1978	49631.03261	22650.21909	19133.33287	11085.30563	1190.77114	1035.018292	6230.640176	12879.26027	9.78E+01	16475.32118	119.332931
10/1978	8437.033384	7431.338655	2337.521056	577.4665505	2.72E-06	2.67E-06	1.49E-05	474.9921833	5.27E-08	5.76E-06	9.22E-09
11/1978	5.18E-06	7.08E-06	1.20E-07	4.66E-07	1.26E-08	1.05E-08	1.48E-07	2.76E-08	3.49E-10	1.56E-08	0
12/1978	1.13E-06	8.03E-06	2.31E-07	1.69E-06	4.05E-08	2.15E-08	1.87E-07	5.53E-08	4.52E-10	3.57E-09	0
01/1979	7.51E-06	7.51E-06	3.64E-06	1.38E-06	8.89E-09	7.87E-09	2.95E-08	4.95E-06	6.16E-11	7.98E-07	0
02/1979	2.55E-06	5.40E-06	1.16E-07	8.11E-07	5.32E-09	3.06E-09	3.47E-08	8.24E-08	0	4.11E-10	0
03/1979	1.00E-05	1.07E-05	2.53E-07	3.24E-06	1.72E-07	4.63E-08	1.27E-07	1.78E-07	2.14E-09	6.94E-09	0
04/1979	5.02E-05	4.52E-05	4.45E-06	5.10E-06	2.89E-07	2.52E-07	4.43E-07	7.46E-07	5.59E-09	1.57E-07	2.67E-10
05/1979	2298.837155	31201.6773	15710.50602	5134.74812	639.7172746	369.3870635	1.07E-04	19669.07165	2.83E-06	1.91E-04	2.18E-06
06/1979	73741.51836	182249.7836	131771.97	85033.97814	34041.79276	24333.40532	18705.49298	180240.5895	5774.255429	78820.44561	1947.175174
07/1979	188334.1281	325877.859	252803.7023	301531.5151	79502.78768	67728.33855	119862.6736	259096.8276	9697.177793	407732.7829	64124.38855
08/1979	177476.7292	191753.7526	111710.3449	203331.5957	42923.49606	41841.29389	96866.45331	143383.7007	5572.786013	281784.4931	51197.84811

09/1979	95196.78789	84110.57073	35514.87771	41185.55698	4098.63695	3504.297655	21525.72273	33956.80852	499.0892553	36218.16076	124.8150076
10/1979	5170.098711	1619.440894	2382.857311	157.898416	2.36E-07	1.81E-07	3.13E-06	7.71E+01	1.77E-08	1067.799691	1.01E-08
11/1979	9.64E+00	4.34E-01	5.31E-01	1.18E-06	1.83E-08	1.62E-08	9.46E-08	7.03E-07	4.11E-10	5.02E-06	0
12/1979	1.88E-06	9.11E-07	1.23E-07	1.54E-07	1.52E-09	1.31E-09	6.39E-09	3.45E-08	0	2.71E-09	0
01/1980	9.26E-07	2.16E-07	1.01E-08	2.00E-08	0	0	3.08E-10	6.04E-09	0	0	0
02/1980	2.11E-07	1.25E-07	3.62E-09	2.08E-08	2.05E-10	1.64E-10	1.50E-09	1.50E-09	0	0	0
03/1980	2.81E-06	3.82E-07	8.49E-08	8.65E-08	5.34E-10	2.67E-10	3.82E-09	3.26E-08	0	0	0
04/1980	9.44E-05	3.78E+01	2.18E-05	2.61E-05	2.10E-06	1.11E-06	2.28E-06	8.86E-06	1.07E-08	1.77E-07	0
05/1980	1625.701161	24533.6945	8272.903853	2688.340215	8.41E+01	2.55E+01	6.85E-05	3202.84756	3.24E-06	1.34E-04	7.30E-07
06/1980	43974.32448	177720.7885	103499.9874	87792.94015	25947.22512	18780.48755	15692.444	151059.4376	3894.846628	103667.1939	4748.539321
07/1980	145513.2315	320295.9027	280075.227	291539.2726	64818.85082	55377.65014	98501.13787	280032.2116	8451.278184	414099.0603	92495.47825
08/1980	152334.7469	293340.7128	225979.7728	245689.1959	55195.52374	51583.23517	94436.67643	160487.7012	6598.222788	202101.9973	31124.89575
09/1980	93706.83861	95523.40082	68002.30286	48380.88403	5301.443732	4402.730971	21152.17221	23487.90675	556.9763699	16412.70956	2.00E-06
10/1980	1061.67643	2815.649664	4.95E+01	284.878576	2.82E-07	2.63E-07	1.56E+00	8.74E-06	3.18E-08	1.13E-05	1.60E-09
11/1980	6.53E-06	2.40E-06	1.89E-07	4.52E-07	1.42E-08	1.28E-08	1.01E-07	4.68E-08	4.11E-11	3.17E-07	0
12/1980	3.26E-06	5.51E-07	2.49E-07	1.00E-07	5.55E-10	5.14E-10	8.44E-09	7.26E-08	0	7.70E-08	0
01/1981	9.34E-07	1.47E-07	1.55E-07	2.72E-08	2.67E-10	2.05E-10	1.70E-09	1.06E-07	0	3.33E-09	0
02/1981	4.18E-07	4.74E-06	3.27E-08	8.14E-07	5.82E-08	3.69E-08	4.67E-08	4.43E-08	4.11E-11	0	0

03/1981	1.37E-06	1.54E-06	4.88E-08	9.21E-07	2.41E-08	2.20E-08	6.55E-08	2.07E-08	4.72E-10	0	0
04/1981	7.24E-05	4.33E-05	2.27E-05	1.90E-05	1.14E-06	7.22E-07	1.02E-06	4.25E-06	1.58E-08	9.91E-08	0
05/1981	1964.386506	6719.97878	6951.933336	2.92E+01	1.89E-05	1.46E-05	4.26E-05	8.37E+01	8.42E-07	2.30E-05	9.99E-07
06/1981	59047.23225	120492.1307	95328.76863	73757.49681	22570.96109	16034.85573	8503.986661	72224.20839	3893.780537	23061.42178	1797.459874
07/1981	171834.6778	309502.2892	287064.2149	308299.0431	75733.38889	64416.41559	96025.3803	239924.5831	9773.938067	317544.2516	92219.98712
08/1981	153454.1548	199563.9548	193546.4716	222376.3732	49741.00215	47621.1137	92185.06417	130574.7078	6745.190432	161544.0967	34754.41784
09/1981	11582.6142	12879.57805	4680.885703	4731.829216	6.84E+01	6.02E+01	1412.95505	3462.198683	3.37E-07	1346.119265	1.05E-07
10/1981	3926.984133	8556.317476	509.5421255	594.4534267	3.17E-06	2.34E-06	1.45E-05	8.92E-01	1.37E-07	1.23E-06	4.31E-10
11/1981	4.06E-06	2.51E-06	1.10E-07	2.63E-07	1.47E-08	9.68E-09	9.29E-08	1.01E-08	4.31E-10	4.68E-08	0
12/1981	3.44E-07	2.35E-06	1.90E-08	7.11E-08	1.03E-10	8.22E-11	7.52E-09	4.31E-09	0	0	0
01/1982	1.43E-08	5.46E-08	0	2.23E-08	5.55E-10	4.93E-10	4.21E-09	0	0	0	0
02/1982	1.07E-06	1.85E-06	7.30E-08	4.54E-07	5.53E-09	5.28E-09	1.70E-08	1.35E-08	0	0	0
03/1982	1.33E-06	2.32E-07	2.25E-08	2.36E-08	1.23E-10	8.22E-11	2.24E-09	4.72E-10	0	0	0
04/1982	7.87E-05	8.49E-05	2.05E-05	6.38E-06	1.79E-07	1.06E-07	3.37E-07	7.50E-07	3.29E-10	5.05E-09	0
05/1982	2925.741402	32970.24108	12910.29536	5053.875995	1038.260822	671.2291226	1.05E-04	1556.411016	3.48E-06	6.35E-05	5.12E-07
06/1982	52149.37103	169074.1812	86812.88819	57815.16389	20714.27088	14938.64854	15558.23233	79057.72094	2631.989904	38557.3265	1095.667921
07/1982	132896.1553	323861.3389	184447.0722	270075.5632	72489.3286	59396.48646	98463.70732	223945.8946	9680.675713	367384.8786	92530.19645
08/1982	105461.7167	188388.3782	79449.75391	170105.9722	38420.62035	34917.85875	72311.19942	84800.14621	4752.290982	124917.346	35294.63191

09/1982	49328.71139	59810.25506	24423.88252	33313.55476	3538.668696	3004.4711	17249.36697	21044.16349	273.0011394	17737.27937	9.18E-07
10/1982	662.7627259	1198.464003	9.03E+01	4.80E-06	1.53E-07	1.45E-07	6.24E+01	5.45E-06	9.97E-01	6.23E-06	0
11/1982	3.24E-05	191.346579	1.04E-05	2.61E-06	3.41E-08	2.47E-08	1.17E-07	4.60E-07	1.85E-10	2.30E-07	0
12/1982	1.65E-06	5.58E-07	6.70E-08	1.09E-07	5.75E-10	2.67E-10	1.16E-08	5.80E-08	0	1.86E-08	0
01/1983	6.80E-08	2.62E-07	6.57E-10	3.44E-08	8.63E-10	8.22E-10	2.10E-08	2.88E-10	0	0	0
02/1983	2.16E-08	1.59E-07	0	1.22E-07	8.42E-10	8.42E-10	1.64E-08	0	0	0	0
03/1983	4.02E-06	5.25E-06	8.92E-08	1.12E-06	2.01E-08	1.63E-08	3.85E-08	3.55E-08	5.14E-10	4.52E-10	0
04/1983	2.76E-05	4.10E-05	1.23E-06	9.47E-06	2.23E-06	1.70E-06	2.57E-06	4.76E-07	6.38E-08	6.40E-08	0
05/1983	3490.212494	17121.71617	7484.104638	137.1288383	3.86E-05	3.93E-05	6.73E-05	7.12E+01	4.09E-06	3.32E-05	2.77E-06
06/1983	53020.97017	140283.7718	89745.81392	50674.30766	19441.8921	13650.56524	6663.085345	99671.49964	3676.150591	88562.08849	5002.526118
07/1983	198327.1119	370475.3415	242899.8915	324664.9999	80739.27734	66129.06343	99227.5624	231235.369	11003.28672	457781.0293	132817.308
08/1983	143912.37	317377.0741	171536.8573	249126.5115	58969.15942	54435.73886	100687.2427	142117.0451	6892.936103	261373.9595	32527.73642
09/1983	49543.43322	108617.3434	20773.48617	34456.42548	1390.505701	1150.702627	9212.295727	18725.48268	6.04E+01	5681.282769	4.51E-07
10/1983	3379.754103	6801.156088	567.3605449	347.6618005	2.58E-06	2.38E-06	1.76E+01	7.96E+01	6.31E-08	107.4655755	0
11/1983	2.56E-05	195.8166103	5.09E+00	6.59E-06	1.41E-07	1.28E-07	4.06E-07	1.65E-07	3.94E-09	2.94E-08	0
12/1983	3.09E-07	3.35E-06	1.96E-08	3.08E-06	5.00E-08	4.02E-08	2.91E-07	1.37E-08	1.00E-08	1.01E-09	0
01/1984	8.29E-06	3.78E-06	1.75E-06	2.42E-07	1.45E-08	1.30E-08	4.53E-08	5.62E-07	1.03E-10	4.44E-09	0
02/1984	5.55E-07	1.42E-06	1.25E-08	1.45E-07	4.31E-10	2.05E-10	5.83E-09	5.14E-10	0	0	0

03/1984	1.26E-05	7.15E-06	4.09E-07	2.08E-07	6.88E-09	4.91E-09	3.12E-08	4.49E-08	0	6.16E-11	0
04/1984	9.01E-05	254.1958667	3.00E+01	1.52E-05	1.94E-06	1.67E-06	1.60E-06	8.14E-06	7.93E-09	1.71E-07	0
05/1984	6094.069714	47819.55382	34773.99806	3710.825577	439.5821802	242.4286401	1.32E-04	31484.58945	4.28E-07	153.3100572	8.16E-06
06/1984	79919.13235	192069.28	137152.7785	53833.52535	22549.11498	16208.48588	11153.15028	165179.0967	3496.433374	110666.6922	1228.699685
07/1984	181618.4941	289788.5873	251936.9566	212015.8351	72524.69405	58741.00762	95455.71124	230529.4133	10177.20452	390548.5035	85703.70821
08/1984	192184.2899	297070.4869	167790.2433	243069.9459	48674.58033	44369.10007	95582.32548	158204.4164	5865.349222	342686.575	37037.13394
09/1984	101979.0061	74839.43105	37821.62411	40030.88929	3874.124398	3608.859964	19300.73838	27687.61546	343.7963559	38080.18435	2.42E-06
10/1984	5795.254243	10061.10314	739.7493625	8.34E+01	1.23E-06	1.01E-06	9.70E-06	2.32E-06	1.06E-08	6.81E-06	0
11/1984	2.68E-05	5.20E+01	6.96E-06	2.50E-06	3.43E-08	1.70E-08	1.84E-07	1.61E-06	1.85E-10	1.67E-06	0
12/1984	4.59E-06	8.36E-07	4.45E-07	1.22E-07	8.22E-11	8.22E-11	1.62E-09	1.73E-07	0	2.27E-08	0
01/1985	1.87E-06	3.54E-06	1.51E-07	1.82E-07	3.64E-09	3.25E-09	1.80E-08	1.15E-07	0	1.62E-09	0
02/1985	1.04E-05	5.33E-06	1.63E-06	1.03E-06	2.73E-08	1.72E-08	7.27E-08	2.63E-06	8.22E-11	3.26E-07	0
03/1985	8.31E-07	1.85E-06	4.62E-08	6.94E-07	9.47E-09	7.54E-09	2.32E-08	7.50E-09	0	0	0
04/1985	1.43E-04	1676.159173	6.25E+00	1.70E-05	2.20E-06	1.74E-06	1.23E-06	2.43E-06	2.65E-08	5.08E-08	0
05/1985	2089.87051	26099.01236	10377.01086	541.3822103	3.71E-05	2.82E-05	5.38E-05	436.844122	4.72E-07	4.81E-05	5.14E-06
06/1985	35105.34012	108499.4701	60817.99684	30670.84535	12782.59535	9319.294907	4462.199589	62516.62013	2496.807739	1001.377044	1286.505723
07/1985	156842.07	295946.2274	207992.0847	172450.9637	49309.18065	38534.31462	54195.03263	185047.3602	7652.649607	90197.80826	47263.35106
08/1985	191740.6417	277707.5204	202940.3647	249970.9224	46263.1782	39447.02278	77004.21496	208699.0728	6627.729525	283658.1428	40486.04617

09/1985	135027.6018	117629.4088	91727.87655	42317.31832	2231.5173	1789.080837	9895.660456	34278.76131	190.0457871	18366.16206	9.62E-07
10/1985	393.3265261	2276.408154	1.33E+01	1.54E-05	1.12E-06	9.19E-07	1.07E-05	5.22E-02	6.91E-08	1.49E+01	1.23E-10
11/1985	4.20E+01	1.23E-06	3.13E-08	1.44E-07	1.15E-08	4.95E-09	1.27E-07	2.57E-09	6.78E-10	1.15E-09	0
12/1985	3.23E-07	5.97E-07	2.45E-08	5.63E-07	1.82E-08	1.44E-08	5.02E-08	2.08E-08	1.23E-10	1.22E-08	0
01/1986	7.23E-06	3.93E-05	2.16E-06	1.27E-05	3.02E-07	1.84E-07	3.09E-07	7.38E-07	2.71E-09	1.63E-08	0
02/1986	3.04E-06	8.75E-06	8.07E-08	1.07E-06	9.33E-09	5.24E-09	1.24E-08	2.05E-10	0	0	0
03/1986	2.66E-06	6.43E-06	1.90E-07	1.18E-06	1.63E-08	1.26E-08	4.20E-08	2.38E-08	2.47E-10	0	0
04/1986	4.34E-05	4.50E-05	2.63E-06	2.46E-05	4.30E-06	4.07E-06	6.72E-06	2.79E-07	2.52E-07	4.19E-09	7.46E-09
05/1986	2061.642503	14728.20117	7175.60004	538.867446	6.41E-05	5.88E-05	1.02E-04	6650.213604	6.19E-06	1.18E-04	3.61E-06
06/1986	83277.10635	168823.8698	141851.8403	56021.61442	21206.17227	14516.48678	5172.778649	210321.2754	3422.880055	122514.644	429.3860319
07/1986	185235.2973	320269.6626	225532.6689	223063.346	67639.98302	54449.4141	88116.31886	200679.6503	9486.773189	261646.0217	70627.93967
08/1986	201113.9639	232436.9785	211918.4886	213700.7907	41204.12301	37471.58919	97492.48274	215651.3665	4833.260617	362538.892	44653.99917
09/1986	74069.57992	85088.54503	40338.28768	31525.43373	2596.111489	2165.355516	10859.40086	35171.98843	122.0267059	27371.94214	3.32E-07
10/1986	883.3303029	323.5263947	1.69E+00	7.73E-06	1.03E-07	8.27E-08	3.15E-06	1.79E-06	1.12E-08	136.9799502	0
11/1986	2.57E-05	271.5826447	6.99E-06	6.16E-06	7.18E-08	6.04E-08	8.09E-07	9.43E-07	1.64E-10	1.12E-06	0
12/1986	1.91E-05	4.56E+01	1.38E+00	1.34E-06	9.88E-09	6.33E-09	3.65E-08	4.11E-08	0	0	0
01/1987	3.41E-07	2.53E-07	7.54E-09	2.06E-08	8.22E-11	8.22E-11	1.19E-09	6.45E-09	0	0	0
02/1987	2.54E-06	2.72E-06	7.93E-08	1.60E-07	4.13E-09	3.18E-09	1.85E-08	1.47E-07	1.23E-10	3.92E-09	0

03/1987	1.72E-05	6.43E-06	9.07E-07	2.34E-07	4.42E-09	2.77E-09	7.35E-09	6.54E-08	0	1.03E-10	0
04/1987	6.00E-05	2.23E-05	1.19E-05	4.37E-06	1.48E-07	5.64E-08	1.40E-07	3.83E-06	2.14E-09	2.08E-07	0
05/1987	2668.395949	15606.53699	8848.737582	1665.117499	2.13E+01	2.61E-05	6.79E-05	12150.77757	2.54E-06	404.8018833	4.91E-06
06/1987	33408.40064	100610.2969	47072.51187	53838.1726	25397.50384	18764.86871	18638.95213	88980.34506	4118.190505	56681.73908	2214.230903
07/1987	127984.1986	273059.2032	184157.1162	328854.1269	84875.54877	71979.35228	110491.7837	247315.6012	10993.42163	349526.3546	91513.39289
08/1987	173610.0612	304456.1507	189504.8385	284691.9661	59648.60166	54550.9975	94550.5428	173146.4659	7063.871685	249397.0053	21214.70979
09/1987	78749.23843	67495.77018	40204.99712	36053.22778	2654.319552	2172.396542	9622.120432	33740.64422	302.3384727	27437.6487	6.38E+00
10/1987	12691.98088	13144.2466	2315.921288	1767.299278	9.56E-07	8.99E-07	8.92E+00	2.09E+00	2.15E-08	554.0266942	8.63E-10
11/1987	171.3094766	817.7293089	156.6479827	7.09E-06	1.21E-07	1.08E-07	3.60E-07	1.16E-06	4.60E-09	5.17E-07	0
12/1987	6.07E-07	1.13E-06	2.69E-08	1.59E-07	3.62E-09	3.66E-09	1.70E-08	6.59E-09	0	0	0
01/1988	1.50E-07	3.48E-07	1.07E-09	5.89E-08	8.42E-10	7.40E-10	5.38E-09	4.11E-11	0	0	0
02/1988	1.94E-08	1.38E-07	0	4.60E-08	2.88E-10	1.23E-10	2.22E-09	1.23E-10	0	0	0
03/1988	3.76E-07	1.09E-06	5.63E-09	7.06E-08	6.78E-10	6.16E-10	3.82E-09	2.67E-10	0	0	0
04/1988	4.11E-05	4.59E-05	9.45E-06	1.25E-05	1.03E-06	5.70E-07	1.23E-06	5.69E-07	1.06E-08	1.92E-07	0
05/1988	1134.860999	9965.831263	3183.652128	5.42E-05	1.59E-05	1.36E-05	4.32E-05	5.61E+01	1.68E-06	3.48E-05	5.55E-07
06/1988	51841.61781	146711.5393	72554.53813	54605.57382	19358.25733	13886.13192	9453.073091	72124.69151	3537.370236	27468.16976	3907.360437
07/1988	152935.0226	296375.2576	171937.0535	262122.5992	67622.52543	55718.87431	85658.09394	204498.0825	8561.560244	223831.3653	87757.18233
08/1988	190976.5354	289280.9715	203664.2855	207907.0961	41459.5459	37469.10697	72100.41968	139308.7596	4793.696665	160603.5237	20029.31927

09/1988	18844.2671	21714.295	6367.257495	6273.632082	479.712476	420.5143811	3168.01072	1594.314779	2.99E+00	2685.378631	3.99E-07
10/1988	4391.353643	8202.52757	1246.866842	5.78E+01	3.95E-07	3.30E-07	3.10E-06	3.83E+00	5.98E-09	1.48E-01	0
11/1988	3.02E-05	9.56E+01	4.99E+00	7.40E-06	1.97E-07	1.59E-07	6.15E-07	1.15E-06	8.22E-09	2.75E-06	0
12/1988	4.54E-06	7.52E-06	1.53E-07	1.66E-06	1.21E-08	1.05E-08	4.26E-08	1.40E-07	4.11E-11	1.04E-08	0
01/1989	2.75E-07	1.70E-06	3.07E-08	2.63E-07	1.22E-08	9.12E-09	7.21E-08	4.27E-09	3.08E-10	0	0
02/1989	2.32E-07	5.71E-07	2.28E-09	6.13E-08	8.63E-10	4.31E-10	7.76E-09	7.19E-10	0	0	0
03/1989	3.71E-07	1.85E-07	9.28E-09	1.34E-08	2.67E-10	1.44E-10	1.64E-09	1.23E-10	0	0	0
04/1989	2.89E-05	6.20E-06	8.35E-07	1.16E-06	6.00E-08	5.53E-08	1.70E-07	3.55E-07	1.29E-09	1.88E-07	0
05/1989	2460.808831	25551.14299	20944.59743	7822.206225	1035.879667	650.7059795	2.11E+01	22675.83336	1.85E+00	5.02E+01	2.92E-06
06/1989	64484.54852	165820.5192	114499.9181	117916.5027	45033.05451	34164.9573	48296.71791	203067.0871	6232.582385	167084.1387	1238.05861
07/1989	195664.1689	307012.9906	264873.9665	331115.2288	84940.21374	77911.60385	145896.0155	252595.5493	10792.97727	406337.2994	89772.51053
08/1989	176858.7767	275317.6282	214911.7377	266402.2243	65675.76911	64347.91978	128407.9914	143253.7325	7074.645057	255016.0026	33420.861
09/1989	55954.16389	53397.65847	26101.12574	14302.67721	1831.192455	1600.790087	10106.93255	9693.515962	174.3800169	8961.8934	2.20E+01
10/1989	5368.319238	9607.199372	3280.892019	201.173527	8.89E-07	6.99E-07	5.15E+00	1.07E-05	6.32E-08	7.13E-07	0
11/1989	496.9891125	2129.063766	1626.618286	1.11E-05	2.98E-07	2.43E-07	1.41E-06	3.35E-06	1.11E-09	2.41E-08	0
12/1989	5.44E-07	3.11E-06	8.09E-08	2.17E-06	6.32E-08	6.24E-08	2.26E-07	1.36E-08	5.09E-09	2.79E-09	0
01/1990	4.07E-07	1.28E-06	1.03E-08	1.74E-07	2.09E-08	8.52E-09	8.55E-08	2.65E-09	2.88E-10	0	0
02/1990	2.28E-06	6.90E-06	3.45E-07	1.09E-06	1.10E-08	5.85E-09	5.18E-08	4.22E-07	2.05E-11	4.73E-08	0

03/1990	7.78E-06	6.90E-06	2.91E-07	5.16E-07	4.36E-08	3.28E-08	7.84E-08	8.10E-08	1.85E-10	1.05E-09	0
04/1990	3.30E-05	1.41E-05	3.56E-07	1.25E-06	4.84E-08	4.41E-08	1.80E-07	1.17E-07	6.57E-10	4.89E-09	0
05/1990	1024.589773	9143.482096	6246.387946	6.37E+01	3.30E-05	3.16E-05	8.89E-05	447.9614541	1.03E-06	1.72E-05	5.75E-07
06/1990	38987.88568	110792.4337	115044.4499	44603.4693	18017.07456	12758.15125	8703.294473	128503.7003	3139.140426	67046.87149	1389.976635
07/1990	162368.9008	272361.7121	248663.6325	210810.3122	66710.50752	54314.19557	94734.21255	235873.8545	8074.158507	260744.9133	51631.56662
08/1990	162900.9623	197589.0086	106935.3883	165436.3418	37233.262	34198.02405	87499.79506	80143.5515	4678.079741	71473.51066	35715.16901
09/1990	91372.9645	94816.3489	33723.70095	40350.59447	2702.135155	2283.402953	18280.77591	14846.31147	203.7222849	7744.897802	1.94E+01
10/1990	3902.92499	4254.064383	731.4203736	4.23E+01	9.92E-07	8.55E-07	5.50E-01	4.35E-06	1.45E-08	6.83E-06	2.88E-10
11/1990	5.68E-06	7.64E-07	6.27E-08	1.71E-07	1.21E-08	1.15E-08	7.18E-08	1.78E-08	1.64E-10	1.33E-07	0
12/1990	9.25E-07	1.84E-06	1.60E-07	2.14E-07	5.42E-09	3.35E-09	2.67E-08	4.68E-08	0	3.68E-09	0
01/1991	5.21E-07	4.26E-07	6.27E-08	2.14E-07	4.44E-09	4.13E-09	2.91E-08	3.60E-08	0	1.40E-09	0
02/1991	5.14E-08	2.65E-07	0	7.09E-08	6.57E-10	6.16E-10	2.67E-09	6.16E-11	0	0	0
03/1991	5.16E-06	6.33E-06	8.12E-08	3.43E-07	6.86E-09	3.43E-09	8.75E-09	1.62E-09	0	0	0
04/1991	4.10E-05	2.32E-05	3.03E-06	1.98E-06	2.28E-07	1.32E-07	4.94E-07	9.35E-07	1.27E-08	3.33E-08	1.70E-09
05/1991	1.40E-04	219.6631148	5.56E+00	6.83E-05	1.58E-05	1.27E-05	3.78E-05	3.47E-05	1.85E-06	5.80E-06	5.89E-07
06/1991	9252.365466	59692.15894	24584.90505	16833.20494	10872.8604	8119.035077	3136.229335	10512.20058	2134.22189	3218.182936	140.1912683
07/1991	77549.63951	171289.2375	98376.64013	116769.7415	49267.66234	38830.41934	63101.24231	121232.8748	7218.519756	164528.4396	28534.02963
08/1991	117471.4205	171477.8969	88258.7415	117342.5508	25813.9846	22260.69332	54770.64817	78630.40246	3714.617732	113781.5883	20256.00076

09/1991	36811.43333	53041.33389	12785.99506	30198.80464	6507.09022	5440.522732	18947.0954	20073.13486	704.6439831	19908.18754	160.7009344
10/1991	15703.545	53350.61425	15778.6219	6084.055552	164.2421902	120.1962427	597.6685976	2288.615969	7.16E-07	8100.406329	1.01E-08
11/1991	1.12E-05	2.24E-05	3.12E-07	2.69E-06	1.69E-07	1.74E-07	8.81E-07	4.54E-08	7.89E-09	2.75E-09	6.16E-11
12/1991	3.35E-07	3.99E-07	6.02E-09	8.81E-08	1.11E-09	7.40E-10	1.81E-08	2.07E-09	0	2.05E-11	0
01/1992	2.51E-08	2.16E-08	0.00E+00	6.16E-09	0.00E+00	0.00E+00	8.63E-10	3.49E-10	0	0.00E+00	0
02/1992	1.61E-07	1.48E-07	2.22E-09	8.19E-08	4.11E-10	3.08E-10	4.97E-09	2.90E-09	0	0	0
03/1992	6.02E-07	2.19E-06	2.51E-09	5.02E-07	1.47E-08	9.57E-09	2.87E-08	2.05E-11	4.11E-11	0	0
04/1992	7.51E-05	8.20E-05	1.21E-05	1.82E-05	2.16E-06	1.37E-06	2.14E-06	3.98E-06	3.94E-09	2.18E-07	2.05E-10
05/1992	3.15E+03	13226.5819	7.01E+03	4.09E+02	4.05E-05	4.14E-05	6.36E-05	4.07E+03	2.42E-06	9.70E-05	2.45E-06
06/1992	84598.63501	125074.0608	114065.1496	52617.71832	15045.86895	10488.65838	3454.816131	135179.046	2946.726914	75627.01226	2272.082536
07/1992	167607.8145	248048.1408	190761.041	247525.3248	72144.28434	57195.08231	60159.90697	202337.0276	10116.58153	284286.0036	82686.53203
08/1992	212685.8999	306027.1395	172217.756	242299.0974	49896.85232	42851.90517	76395.02474	165005.2488	6545.077982	233462.5561	62559.61721
09/1992	116047.3949	198598.6378	113828.696	97488.40954	10403.46941	8717.604512	29506.57147	99780.39787	940.6339866	148043.4517	3.88E+01
10/1992	16251.04494	30233.86465	10663.10203	3386.219327	5.06E-06	3.88E-06	4.13E+00	1265.102001	2.00E-07	1932.12207	3.96E+00
11/1992	2.81E-06	1.11E-05	4.90E-08	5.26E-06	2.11E-07	2.01E-07	2.15E-06	2.67E-08	1.78E-08	3.16E-08	0.00E+00
12/1992	3.66E-07	1.74E-06	2.55E-08	1.56E-07	5.07E-09	4.42E-09	3.18E-08	2.14E-09	0	8.42E-10	0
01/1993	2.61E-07	2.08E-07	5.18E-09	1.56E-08	5.55E-10	5.14E-10	3.59E-09	7.66E-09	0	0	0
02/1993	5.55E-07	3.06E-06	4.31E-08	8.79E-07	2.44E-08	1.01E-08	3.81E-08	1.97E-07	6.16E-11	5.38E-09	0

03/1993	7.33E-07	1.03E-06	4.23E-09	1.85E-07	8.79E-09	5.63E-09	3.08E-08	0	0	0	0
04/1993	7.08E-05	8.52E-05	8.30E+00	3.07E-05	3.67E-06	2.51E-06	3.13E-06	9.93E-06	4.22E-08	7.67E-07	2.67E-10
05/1993	15549.65322	26333.48353	28624.96148	2727.982401	1.39E+01	3.27E-05	8.97E-05	12627.8297	2.80E-06	1.27E-04	2.22E-06
06/1993	84806.1138	105885.7934	74326.77081	36322.28694	11440.37475	8315.526166	3541.539669	86953.40676	1716.083338	23639.15633	1266.909913
07/1993	194362.2284	266425.6391	212765.4277	180863.0087	62405.50001	48191.17847	54783.06231	236528.9246	9162.125733	333939.6167	60587.39569
08/1993	197373.2891	302074.6973	161698.4978	219084.4108	48155.95374	42010.61846	85333.90791	147764.7893	6206.041016	174889.2442	52453.90255
09/1993	102162.9345	103276.8878	34854.12341	37073.68359	3796.011219	3109.634458	13853.92043	14097.88434	488.8317089	2981.709835	190.0029393
10/1993	10485.2991	3611.840434	2429.129181	811.6606634	3.21E-08	2.63E-08	1.11E-06	4.31E-06	1.81E-09	6.56E-07	8.63E-10
11/1993	1.84E-05	1.41E-05	2.06E-06	5.55E-06	4.48E-08	4.26E-08	2.99E-07	2.62E-07	1.31E-09	1.73E-07	0
12/1993	1.12E-07	4.61E-07	3.94E-09	2.41E-07	3.27E-09	2.61E-09	2.84E-08	1.85E-10	2.05E-11	0	0
01/1994	3.18E-07	2.91E-07	2.32E-09	4.53E-08	3.35E-09	2.67E-09	1.97E-08	3.29E-10	2.05E-11	0	0
02/1994	3.03E-07	1.54E-06	5.32E-09	1.33E-08	8.22E-11	8.22E-11	1.60E-09	8.42E-10	0	0	0
03/1994	2.95E-07	3.43E-07	4.48E-09	4.84E-08	9.45E-10	7.40E-10	1.29E-08	5.96E-10	0	0	0
04/1994	4.28E+00	5.77E-05	338.4047121	2.18E-05	1.28E-06	7.79E-07	1.42E-06	1.68E-05	1.16E-07	4.58E-06	2.73E-09
05/1994	14585.64768	30556.8702	26743.34547	12672.89938	453.949014	249.5638934	7.03E-05	17464.97245	1.78E-06	5.89E+00	2.15E-06
06/1994	110102.4409	218833.277	160973.295	198945.0798	49044.40816	37864.41487	50525.74533	229369.6652	5542.672226	98301.90885	8822.102994
07/1994	189239.9668	304848.3902	257814.3082	314150.253	74551.15503	67114.97223	123331.2624	266009.9181	9610.381102	434785.3135	95466.91793
08/1994	193153.8052	322804.4048	237500.8635	267851.7194	52841.22331	48923.59095	101338.5445	183648.5829	6340.969439	248277.6358	38882.84122

09/1994	67427.20541	84212.57768	58218.79996	28862.0312	3487.508686	2933.186193	16040.83066	45257.95176	539.2860344	77855.59749	379.4720685
10/1994	689.9018991	651.5591359	6.57E+01	967.0486769	1.89E-07	1.78E-07	6.01E-01	2.80E-06	1.18E-08	1.07E-05	1.64E-10
11/1994	266.1837674	5787.79796	1849.712309	787.4453915	3.75E-07	2.78E-07	1.06E-06	2.73E-05	1.99E-08	3.50E-05	0
12/1994	3.46E-06	4.41E-06	3.98E-07	1.74E-06	2.67E-08	1.80E-08	7.25E-08	1.83E-07	2.26E-10	3.68E-09	0
01/1995	3.02E-06	2.92E-06	1.34E-07	1.54E-06	3.66E-08	3.67E-08	1.70E-07	3.45E-07	2.67E-10	1.73E-08	0
02/1995	4.00E-06	5.94E-06	1.09E-06	1.01E-06	8.44E-09	5.94E-09	1.77E-08	2.08E-07	2.05E-11	2.55E-09	0
03/1995	1.62E-05	4.65E-05	8.66E-06	1.44E-05	6.87E-07	4.40E-07	3.04E-07	4.70E-07	9.24E-09	3.50E-08	0
04/1995	1.69E+01	3232.89946	8.62E+01	3.49E-05	3.78E-06	2.89E-06	2.47E-06	2.94E-05	1.50E-07	5.78E-06	0
05/1995	10978.53584	42489.31118	20353.47628	3232.057886	1.82E+01	4.10E-05	7.90E-05	2892.696251	2.94E-06	1.23E-04	6.26E-07
06/1995	54699.77532	150755.71	83096.27481	45583.14561	18010.00858	13284.34415	17527.23409	81972.53246	2151.897876	3938.377973	4339.512178
07/1995	154312.7438	285756.0446	171690.1038	191929.9824	74996.90074	63686.59932	117414.8483	140195.7723	10029.77358	94826.11523	92180.01528
08/1995	148521.41	227605.6739	108255.2722	163552.338	38470.36068	36547.06443	79920.96201	93981.70199	4457.045641	92392.04055	12051.97574
09/1995	113203.5281	192637.7066	63904.35924	64129.22355	8217.561572	6727.309387	27287.94029	24258.6846	475.385722	9120.804377	7.78E-06
10/1995	5333.893468	6667.634086	336.4751427	4.48E+01	5.96E-07	6.04E-07	6.43E-06	1.12E-01	6.31E-08	3.42E+01	4.11E-11
11/1995	1.79E-05	9.53E-06	3.18E-06	5.76E-07	2.78E-08	1.94E-08	1.56E-07	3.75E-07	8.63E-10	3.77E-07	0
12/1995	3.36E-06	6.03E-06	7.21E-07	1.03E-06	8.13E-09	5.65E-09	7.94E-08	5.19E-07	2.05E-11	5.99E-07	0
01/1996	5.92E-06	1.28E-06	4.37E-07	2.52E-07	5.51E-09	4.93E-09	1.78E-08	2.09E-07	0	2.42E-09	0
02/1996	1.28E-07	2.52E-07	7.40E-10	1.07E-07	3.45E-09	2.51E-09	2.14E-08	2.51E-09	0	0	0

03/1996	1.05E-06	7.25E-07	1.18E-08	1.31E-07	5.11E-09	3.16E-09	6.51E-09	6.92E-09	0	1.44E-10	0
04/1996	1.03E-04	1.07E-04	1.31E-05	1.60E-05	1.25E-06	5.05E-07	9.24E-07	1.33E-06	2.37E-08	7.60E-08	0
05/1996	1462.216549	21521.11997	6719.309956	1073.836355	2.91E-05	2.60E-05	4.86E-05	1832.254396	3.55E-06	1.13E-04	6.69E-07
06/1996	60562.66122	164837.5447	147392.4089	74037.62777	24096.7467	17127.1472	9946.061491	179897.2243	3801.637617	82300.73104	1563.664941
07/1996	187112.7411	385237.8636	224042.5138	309806.5094	69903.06067	58011.39432	94768.97296	185435.9746	8728.456503	196149.8252	35326.42226
08/1996	170332.5673	267008.2723	101875.1669	242748.8702	51968.29616	48669.05442	93819.79474	112829.9985	6549.011088	161193.8841	20466.527
09/1996	117393.6962	128769.0079	51847.79592	35021.19063	3645.410174	3066.879912	17015.07716	17824.58044	289.6992504	3608.779828	1.08E-06
10/1996	16998.56282	24630.72052	9381.285298	1617.028189	6.44E-07	6.46E-07	2.60E+01	8.77E+01	1.18E-08	1.49E+01	2.67E-10
11/1996	1.40E+00	2.06E+00	4.85E-06	5.93E-06	1.76E-07	1.61E-07	6.30E-07	9.94E-07	8.09E-09	6.01E-07	0
12/1996	8.16E-06	1.78E-05	1.56E-06	2.15E-06	6.03E-08	5.62E-08	1.10E-07	7.69E-07	1.56E-09	7.73E-08	0
01/1997	2.50E-06	8.84E-07	1.45E-07	1.49E-07	1.09E-09	9.24E-10	7.25E-09	8.16E-08	0	8.63E-10	0
02/1997	3.09E-07	6.50E-07	2.20E-09	4.84E-08	4.52E-10	8.22E-11	3.33E-09	6.57E-10	0	0	0
03/1997	1.08E-06	9.30E-07	2.24E-08	1.65E-07	2.63E-09	2.28E-09	3.86E-09	3.33E-09	4.11E-11	0	0
04/1997	175.9941001	898.3403626	178.1130137	3.24E-05	3.42E-06	2.61E-06	2.42E-06	3.27E-05	1.19E-08	1.13E-06	4.11E-10
05/1997	14147.47218	58205.80518	16234.45045	11729.78027	1722.31893	1086.97659	1.86E+00	8784.813411	5.41E-06	1.84E-04	1.41E-06
06/1997	111283.9748	190317.324	116289.3422	116530.7367	39050.91486	28706.87214	27005.06619	125204.7175	6373.568255	69096.05112	2221.554235
07/1997	198598.8273	331835.8824	217237.9624	352978.1064	87578.97496	76801.78331	120079.6627	255267.2435	11418.5534	326538.2707	100673.8463
08/1997	187579.7472	315019.9766	155532.454	289290.6123	60981.9056	56165.25378	86229.62488	175203.5861	8234.823767	206787.2029	55675.80198

09/1997	87597.1699	60723.02071	54494.57455	23868.18718	2002.000523	1715.928463	11317.82001	39937.33202	8.69E+01	39846.53811	4.44E+00
10/1997	1853.333084	767.4906855	151.9924881	6.05E+01	4.18E-07	4.07E-07	6.01E-06	4.08E-06	3.17E-08	1.55E-05	0
11/1997	6.76E+00	295.1449897	4.13E-06	5.71E-06	1.70E-07	1.12E-07	6.06E-07	4.42E-07	4.60E-09	1.59E-07	0
12/1997	1.28E-05	1.64E-05	4.68E-06	9.93E-07	1.24E-08	1.20E-08	3.01E-08	5.51E-07	0	1.24E-08	0
01/1998	4.74E-07	1.80E-06	1.32E-08	1.07E-07	4.72E-10	3.49E-10	1.18E-08	4.58E-09	0	0	0
02/1998	2.68E-07	2.60E-07	1.21E-08	5.77E-08	1.23E-09	1.15E-09	3.27E-09	3.29E-10	0	0	0
03/1998	6.97E-06	7.34E-07	1.83E-07	8.67E-08	1.46E-09	6.57E-10	1.00E-08	1.03E-08	0	2.05E-11	0
04/1998	5.85E+01	407.3413248	5.98E+01	1.97E-05	2.10E-06	1.69E-06	1.46E-06	1.68E-05	2.40E-08	2.79E-07	0
05/1998	9947.625299	31298.57079	7328.61166	6331.965939	703.7408636	429.481865	1.15E-04	216.5578937	1.20E-05	4.55E-05	1.59E-05
06/1998	54389.13882	152863.9867	66484.75396	66334.4974	23937.94619	17194.15803	12450.19846	91859.584	3584.045766	38553.74316	952.7775611
07/1998	183206.6842	388972.3386	269359.2883	352442.469	90910.0675	77806.78254	129372.3905	271871.6669	11370.32158	406700.0422	98743.44875
08/1998	204731.3696	329832.5382	216424.5601	252792.7381	40699.70983	40129.96033	104251.2819	233657.655	4525.958566	327262.4017	17528.02411
09/1998	61670.23375	81639.91886	15280.88995	46640.3381	4318.376582	3551.233115	17313.74451	7459.123253	386.3357687	19424.25011	3.50E-06
10/1998	5707.16033	8589.22649	978.1777312	2.47E+01	9.73E-07	1.01E-06	9.36E-06	5.72E-06	2.44E-08	115.1834728	0
11/1998	1.46E-05	8.18E-06	3.86E-07	1.96E-06	4.43E-08	3.54E-08	2.96E-07	1.01E-07	6.92E-09	1.30E-07	0
12/1998	7.83E-07	8.31E-07	7.26E-08	1.12E-07	9.65E-10	6.78E-10	7.85E-09	7.49E-08	0	1.21E-09	0
01/1999	1.81E-06	2.22E-06	9.30E-08	3.84E-07	4.79E-09	3.10E-09	1.28E-08	3.80E-08	2.05E-11	7.81E-10	0
02/1999	1.40E-07	4.65E-07	1.68E-09	6.03E-08	6.98E-10	2.47E-10	3.62E-09	3.68E-09	0	0	0

03/1999	1.25E-06	2.75E-07	4.95E-09	1.23E-07	3.25E-09	1.89E-09	9.10E-09	5.55E-10	0	0	0
04/1999	1.33E-04	1.04E-04	4.28E+00	1.56E-05	7.25E-07	3.98E-07	1.22E-06	2.69E-05	8.55E-09	1.21E-06	0
05/1999	1502.753048	18766.45707	4008.070888	2164.179161	291.3856956	149.6258403	9.16E-05	5.32E-05	2.72E-06	1.31E-05	4.73E-07
06/1999	32001.45833	98876.18434	65257.59521	35706.07404	15289.58457	10908.43096	4888.224215	51310.42288	3022.511916	17073.80137	1136.780303
07/1999	131433.9594	240613.2644	187334.9822	159664.3328	51310.36681	40701.84458	66489.81859	216413.3104	7853.486711	273941.4628	66625.82671
08/1999	189606.1902	374257.871	235202.8711	277605.5039	51048.91241	44303.49181	91651.41175	193671.2749	6122.900029	261093.1624	21644.90133
09/1999	100431.6347	149442.3723	98337.1635	72541.22092	7974.874515	6579.50031	31087.3019	73778.22213	817.9054873	44971.03962	2.59E-06
10/1999	2572.363677	3241.449641	785.6817538	2.68E+01	9.11E-07	9.22E-07	1.52E-05	2.58E-06	5.28E-08	1.28E-06	0
11/1999	9.56E+00	1.08E+01	6.60E-01	1.28E+01	4.28E-08	4.08E-08	3.35E-07	1.10E-06	9.86E-10	1.89E-06	0
12/1999	8.00E-06	4.21E-06	8.35E+00	3.44E-07	4.72E-10	4.31E-10	1.95E-08	1.31E-07	0	1.36E-08	0
01/2000	4.43E-07	1.71E-06	2.97E-08	7.45E-07	6.06E-09	5.38E-09	2.63E-08	2.71E-09	0	0	0
02/2000	6.11E-07	1.89E-06	1.80E-08	1.32E-07	6.78E-10	6.57E-10	1.14E-08	9.55E-09	0	0	0
03/2000	1.31E-05	2.74E-06	7.11E-08	1.44E-07	5.69E-09	2.05E-09	6.12E-09	6.49E-09	0	0	0
04/2000	4.99E+01	5.53E-05	2.90E+00	1.28E-05	6.64E-07	5.98E-07	7.55E-07	2.00E-05	1.05E-08	7.32E-07	0
05/2000	10989.28967	30152.71288	11673.58403	3490.342812	112.3864871	3.45E+01	9.14E-05	135.043874	2.41E-06	1.21E-04	2.49E-06
06/2000	110084.4244	201777.0331	116424.4903	62203.13424	17122.28661	12166.88439	7475.081008	72628.79401	2661.352626	17203.06322	3383.126595
07/2000	209562.4003	327577.7329	275835.7222	249146.2892	66276.48183	53347.24588	70824.21597	256888.7646	9514.951171	301251.2632	99193.09896
08/2000	217780.3572	286995.4944	241844.8415	297162.9786	68947.59257	64662.22091	130276.8099	234491.4754	9192.024447	426553.5966	75989.44973

09/2000	142335.1017	194691.1121	119854.3506	61126.90321	5488.613162	4561.194586	29256.82787	73355.19691	506.218267	90585.07718	2.99E-06
10/2000	15943.99615	21681.71818	6223.463544	1837.372535	2.28E-06	1.70E-06	219.8132209	731.773547	2.19E-08	370.3037661	9.45E-10
11/2000	1.81E-05	7.94E-06	1.14E-06	2.05E-06	4.73E-08	4.24E-08	1.70E-07	1.96E-07	1.11E-09	1.64E-07	0
12/2000	1.54E-05	2.73E-05	4.68E-06	8.80E-06	2.30E-07	1.54E-07	4.41E-07	2.79E-07	1.51E-08	5.23E-08	0
01/2001	1.87E-06	2.09E-06	1.02E-07	1.09E-07	2.03E-09	1.15E-09	8.26E-09	2.34E-07	0	1.56E-09	0
02/2001	7.62E-08	4.08E-08	1.23E-10	4.25E-09	4.11E-11	4.11E-11	9.04E-10	0	0	0	0
03/2001	2.66E-06	2.01E-06	1.47E-08	2.29E-07	1.75E-09	1.19E-09	2.79E-09	3.53E-09	0	0	0
04/2001	5.51E-05	4.99E-05	3.50E-06	1.39E-05	1.23E-06	8.59E-07	1.08E-06	4.34E-07	6.57E-09	9.59E-09	0
05/2001	3112.095238	15860.29434	10927.21888	3374.940885	194.9710179	7.77E+01	9.19E-05	13474.28698	4.38E-06	1.73E-04	3.53E-06
06/2001	65002.45984	136726.1621	109656.4846	74621.95949	27993.98216	19795.21834	11196.34263	163910.1881	4808.870607	62313.65158	1305.144326
07/2001	162284.2438	314881.0889	232593.0118	268677.2914	72193.4433	60041.5486	105889.8702	249344.0761	10141.45989	336884.2161	96953.25481
08/2001	156708.0735	207279.7902	106904.891	153011.1485	35910.32642	32183.76058	67776.86935	90696.73431	4511.100951	92151.82252	30053.36251
09/2001	102551.0705	150103.9282	62910.09725	68849.63828	9790.971606	8488.806424	38371.71293	61424.81088	938.9151584	88133.69393	1.43E-01
10/2001	11147.97479	6487.108346	2507.761909	1024.847969	7.08E+00	2.24E+00	397.7370477	1038.864	1.03E+01	3153.310289	1.38E-07
11/2001	836.0023265	5453.28593	686.3999906	1.92E+01	1.48E-06	1.10E-06	5.54E-06	1.45E+01	1.46E-08	6.32E-07	0
12/2001	8.09E-06	1.67E-05	7.31E-07	8.38E-06	2.29E-07	2.27E-07	5.20E-07	3.65E-07	2.55E-09	1.21E-07	0
01/2002	1.16E-05	6.88E-06	1.38E-06	1.17E-07	6.98E-10	4.93E-10	1.03E-08	2.81E-07	0	5.46E-09	0
02/2002	1.63E-07	4.37E-06	8.03E-09	3.35E-07	1.57E-08	1.09E-08	4.39E-08	2.63E-09	0	0	0

03/2002	8.08E-06	1.77E-05	4.13E-07	3.73E-06	4.63E-08	3.59E-08	1.86E-07	9.45E-08	8.01E-10	1.05E-09	0
04/2002	9.35E-05	6.11E-05	8.79E-02	1.25E-05	3.86E-06	2.93E-06	3.69E-06	6.12E-06	4.30E-08	6.63E-08	0
05/2002	6754.655061	12490.75874	10459.17619	220.9814727	3.56E-05	2.63E-05	7.18E-05	2088.677864	2.70E-06	7.06E-05	1.10E-06
06/2002	94378.52939	138836.8987	133157.5387	38020.27067	18076.92523	12938.11757	6587.59151	178871.262	3677.348275	128943.3577	1437.535149
07/2002	205485.811	271408.0473	207920.3424	175703.6642	73368.14097	59711.95824	95070.18363	236344.0903	10180.33667	387228.9876	92987.14949
08/2002	257660.4878	379219.4202	313749.3612	343179.4094	69266.80256	66760.31758	169102.0839	247548.9405	8770.565103	344849.2443	56830.26972
09/2002	177877.8581	200596.3231	172390.5242	70632.95056	6118.400733	5110.247748	26791.60974	36673.9777	611.3093781	21936.77812	2.33E-06
10/2002	44782.90082	36233.3163	19258.89664	835.614782	2.76E-06	2.32E-06	8.02E+01	1797.123733	3.18E-08	3727.96227	4.95E-09
11/2002	7.88E+00	3.46E+01	3.33E-06	2.79E-06	2.31E-07	1.67E-07	2.11E-06	2.66E-07	2.23E-08	1.71E-07	0
12/2002	5.35E-06	3.90E-06	8.61E-07	1.04E-07	4.31E-10	8.22E-11	7.42E-09	1.26E-07	0	2.55E-08	0
01/2003	6.62E-06	3.76E-06	2.68E-07	3.97E-07	7.19E-09	6.94E-09	2.07E-08	1.34E-08	0	0	0
02/2003	2.95E-06	3.03E-06	1.27E-07	2.48E-07	3.06E-09	2.55E-09	1.86E-08	2.53E-08	0	0	0
03/2003	5.53E-06	2.97E-05	8.58E-08	9.28E-06	4.94E-07	2.72E-07	3.95E-07	3.12E-09	3.94E-09	0	0
04/2003	1.34E-04	486.6414643	2.74E-05	2.82E-05	5.35E-06	4.06E-06	5.42E-06	3.01E-06	3.05E-07	6.31E-07	1.30E-08
05/2003	6428.248742	27325.3199	15367.38834	1965.030736	153.5754917	5.83E+01	1.03E-04	14188.94587	7.14E-07	1004.70019	7.61E-06
06/2003	90902.84559	216021.9577	153177.285	99835.79657	36653.8934	26037.4756	14685.73462	228211.9364	5527.41908	198013.6541	3362.090916
07/2003	226097.2369	407698.5335	341712.2881	407373.965	101648.1788	88186.51397	144902.0592	326787.5627	12489.30179	505607.7721	120056.2573
08/2003	218375.4829	372073.6111	408312.0667	353254.4591	65829.67059	64106.8828	133904.8982	232720.9753	8241.79525	365815.6164	51354.29712

09/2003	103568.6448	161496.0187	48852.74439	69864.44404	7581.095419	6317.889768	32781.98551	23727.32846	631.5694627	29512.43487	144.0804961
10/2003	20207.11316	16131.13966	4124.578852	3101.421631	8.81E+00	4.39E+00	384.4192632	9.68E+01	1.18E+00	6789.590484	9.37E-09
11/2003	4.43E+01	1.69E-05	9.79E-01	1.12E-06	1.76E-08	1.78E-08	1.86E-07	1.68E-06	1.23E-10	8.92E-07	0
12/2003	1.80E-07	1.47E-07	1.81E-09	5.61E-08	8.22E-10	6.37E-10	7.21E-09	1.85E-10	0	0	0
01/2004	1.47E-07	1.18E-06	1.23E-08	4.32E-07	2.50E-08	2.19E-08	7.29E-08	1.98E-08	8.63E-10	2.67E-10	0
02/2004	1.28E-05	1.13E-05	1.84E-06	3.53E-06	4.55E-08	2.90E-08	4.44E-08	3.75E-07	2.47E-10	2.82E-08	0
03/2004	3.33E-05	5.50E-05	1.11E-05	7.52E-06	2.36E-07	1.54E-07	1.59E-07	1.20E-06	6.57E-09	1.28E-07	0
04/2004	6.49E-01	3084.649729	2.23E+01	3.14E-05	1.61E-06	1.04E-06	2.04E-06	6.45E-06	8.42E-08	8.51E-08	2.34E-09
05/2004	9274.236679	57011.54902	15828.34946	4583.894294	263.3465062	128.3888811	6.82E-05	321.9278244	2.71E-06	1.62E-04	2.58E-06
06/2004	76685.13443	207220.2447	101236.7864	99314.52727	38264.91928	28525.04235	25661.78552	89014.63338	5821.407682	28287.70426	2750.282421
07/2004	188342.77	398932.4017	244585.7278	390166.253	94927.2789	85637.06073	137622.2044	306356.0679	11699.92618	352128.0184	104862.1758
08/2004	174408.5823	266067.046	176031.8414	248938.4775	55020.33211	53237.49938	98018.59193	186161.2322	6945.115908	304905.875	45193.97795
09/2004	59840.0558	42389.33946	14786.39645	19311.77204	1736.885569	1570.697268	11796.21851	3047.162296	144.9715527	6007.890475	1.83E-06
10/2004	5520.102423	1965.999851	309.9134794	368.0945664	5.98E-02	1.89E-07	3.87E-06	6.92E-06	9.86E-09	1.54E-05	1.19E-09
11/2004	2.71E+01	337.7605813	4.72E+01	6.87E-06	6.57E-08	3.84E-08	2.63E-07	2.29E-06	1.31E-09	4.54E-07	0
12/2004	3.44E-06	5.69E-06	1.50E-07	1.06E-06	5.55E-08	3.98E-08	1.55E-07	9.72E-08	3.70E-10	2.01E-08	0
01/2005	2.03E-07	1.91E-07	5.55E-10	4.60E-07	4.89E-09	4.33E-09	3.06E-08	1.03E-10	1.85E-10	0	0
02/2005	2.75E-06	6.61E-06	1.34E-07	1.49E-06	1.72E-08	1.44E-08	5.86E-08	2.26E-08	8.22E-11	1.03E-10	0

03/2005	2.12E-05	1.62E-05	2.01E-06	1.31E-06	2.30E-08	1.21E-08	3.36E-08	2.52E-08	2.47E-10	1.64E-10	0
04/2005	7.51E-05	2.63E-05	9.44E-06	8.59E-06	1.71E-06	1.27E-06	2.10E-06	4.47E-07	2.66E-08	3.14E-08	7.40E-09
05/2005	4816.687102	20010.19695	18352.35154	1155.325168	2.50E+01	5.11E-05	1.05E-04	5821.445472	2.39E-06	1.80E-04	4.46E-06
06/2005	54556.91366	144553.7347	88431.86438	52707.61966	18616.38957	13127.6295	6046.417987	109028.2367	2733.24439	53778.88858	139.4418415
07/2005	170805.1468	313286.7153	222790.2058	258121.8945	67562.38843	54028.23741	72764.11008	255789.5447	9380.334113	372941.8533	50380.39766
08/2005	211742.7063	414926.6157	242686.0077	347802.0988	65540.2518	60545.3784	119503.1901	246675.0259	8002.624586	280078.9259	32889.55126
09/2005	123725.8457	155123.4331	84914.70233	72976.24309	6072.373427	5021.204075	27092.95859	82019.56006	620.9811595	110071.1553	9.19E+01
10/2005	12742.51632	16881.03448	4475.117962	1931.59129	2.41E-06	1.82E-06	2.76E+00	2510.522591	9.47E-08	1081.360025	1.70E-09
11/2005	5.77E-06	1.89E-06	1.40E-07	3.61E-07	8.59E-09	8.75E-09	7.64E-08	7.81E-09	1.64E-10	1.48E-08	0
12/2005	2.35E-06	1.67E-05	2.38E-07	2.73E-06	2.14E-08	1.83E-08	1.73E-07	8.08E-08	2.67E-10	5.55E-09	0
01/2006	9.97E-07	1.95E-06	1.30E-07	2.36E-07	1.34E-09	1.01E-09	6.10E-09	3.80E-08	0	7.40E-10	0
02/2006	6.99E-06	5.76E-06	5.66E-07	2.82E-07	5.09E-09	4.25E-09	2.03E-08	6.00E-07	0	6.78E-09	0
03/2006	3.09E-06	6.97E-06	1.04E-07	8.15E-07	1.27E-08	1.22E-08	4.35E-08	2.09E-08	6.16E-11	4.11E-11	0
04/2006	8.26E-05	5.54E-05	9.94E-06	1.06E-05	7.51E-07	5.58E-07	8.02E-07	1.69E-06	1.05E-08	3.68E-07	1.17E-09
05/2006	1532.905918	7754.228135	3888.707272	523.5806853	3.10E-05	2.76E-05	5.71E-05	1186.919524	1.71E-06	8.54E-05	2.15E-06
06/2006	77450.14943	220145.4844	144649.9556	137720.0402	37343.41413	27047.98298	21003.88159	195128.7003	6301.354058	89873.82497	4527.245104
07/2006	242273.2407	439260.4783	351714.9342	386601.061	86560.52132	79203.24417	155184.9074	266600.5522	10142.00301	410678.1787	100266.638
08/2006	252397.3222	362061.5352	438277.5857	253831.8127	56317.7128	56948.84727	121985.4869	226895.1563	7167.016356	304180.4101	68593.89995

09/2006	80298.50072	93451.17102	29141.14258	22671.99459	1608.849594	1363.102157	8796.044448	7053.430247	6.29E+01	5831.383015	2.36E-06
10/2006	8923.748532	4836.38795	891.5091721	165.3565879	8.13E-07	7.17E-07	5.69E-06	1.04E-06	3.94E-08	1.88E-06	6.78E-10
11/2006	2.81E-05	2.61E-05	5.26E-06	1.29E-06	1.34E-08	1.16E-08	1.06E-07	3.35E-07	3.08E-10	2.29E-07	0
12/2006	3.75E-07	3.80E-06	1.40E-08	7.19E-07	7.93E-09	5.55E-09	5.41E-08	1.26E-08	2.05E-11	1.99E-09	0
01/2007	1.51E-07	1.56E-07	1.38E-09	3.30E-08	2.16E-09	1.91E-09	2.35E-08	1.34E-09	0	0	0
02/2007	1.31E-07	7.61E-08	1.01E-09	1.56E-07	9.06E-09	8.46E-09	3.95E-08	3.12E-09	3.49E-10	1.03E-10	0
03/2007	7.67E-06	9.60E-06	2.23E-07	2.80E-07	4.44E-09	2.53E-09	1.21E-08	1.12E-07	0	1.13E-09	0
04/2007	2.47E+01	7.61E+01	3.76E+01	1.81E-05	7.46E-07	3.93E-07	1.21E-06	2.35E-05	7.62E-09	4.56E-07	0
05/2007	16248.02997	48158.48433	34737.59286	4241.878528	367.1144054	188.5834837	9.46E-05	11234.44055	7.06E-07	1.91E-04	1.25E-06
06/2007	121274.9508	230432.6661	162103.6786	92185.46477	35097.89955	24792.91571	13421.65281	166629.5904	5768.946606	174273.4801	5874.988254
07/2007	238141.604	356186.6143	309223.3826	327389.3198	88035.93069	73921.9574	125094.5535	273173.9302	11504.97299	460825.1897	113175.4928
08/2007	202673.0171	331411.887	266430.599	313732.5056	66079.12759	63771.02648	137401.1187	152786.2658	8710.837826	329789.8284	73858.33253
09/2007	103704.8519	148775.1431	54687.27898	66083.40539	12356.52407	10471.80022	41843.94735	22932.33503	2034.640494	33566.75462	352.1991527
10/2007	3241.001514	5279.260351	193.2698282	7.92E+00	4.23E-07	3.84E-07	5.11E-06	4.99E-06	1.18E-08	1.20E-05	2.67E-10
11/2007	3.74E-05	9.18E+00	1.39E-05	1.23E-06	1.50E-08	1.47E-08	7.69E-08	1.55E-07	1.03E-10	1.52E-08	0
12/2007	1.14E-06	5.01E-06	1.83E-07	1.66E-06	4.95E-08	2.46E-08	1.96E-07	3.87E-08	3.49E-10	8.63E-09	0
01/2008	12448.49517	9342.663611	10301.7864	7520.359688	5788.62815	5904.781339	8210.825994	5356.317718	4557.885755	1403.181597	4059.849339
02/2008	11412.15468	8697.788748	8948.649354	6065.042908	5088.438493	5040.409496	7169.716367	4530.082481	3955.608835	1691.978712	2304.279192

03/2008	10806.95239	8168.206323	8282.402416	5689.129956	5312.607881	4555.581755	6056.903649	4748.958965	3986.702895	1352.799193	2401.482392
04/2008	11142.26422	8322.48254	10288.58418	7973.405791	5409.971131	5376.666771	6002.959313	5486.52417	3989.710594	3274.999231	1712.614633
05/2008	21195.12017	16240.75778	18315.10496	11176.74159	10125.22743	7448.838607	6179.902095	5493.66654	5344.201201	2262.999611	1047.129266
06/2008	23142.34841	18928.84667	18407.79949	16598.51611	16338.78746	14732.68359	14921.6189	12794.94241	12284.65956	6625.507831	5777.900497
07/2008	18703.49913	16099.6961	17562.84653	17301.51845	16425.46522	16270.22305	20205.08942	19020.16597	18016.5451	8814.623776	6232.687175
08/2008	18326.36477	15795.78087	13898.12478	14577.59823	13448.64685	13883.18648	17712.7431	18789.22719	18027.00321	8216.144577	4737.263284
09/2008	15803.39877	13614.87454	14331.45962	18086.17194	9158.033788	20834.6171	21709.13132	18874.48218	18738.9881	5769.648905	3379.774531
10/2008	16451.18047	14698.38558	13344.3529	13150.26133	9021.68283	12953.40177	13154.34056	10749.29829	10633.57833	4085.805394	1127.985808
11/2008	15555.88726	11445.11892	14690.85286	10679.28662	7676.340363	9777.438767	9526.205381	7872.620131	7559.070888	3451.531524	1284.007742
12/2008	15905.69484	11045.57457	12830.0587	8889.110207	7292.090036	7362.041344	7371.957899	6360.289434	6153.799709	3310.300023	1384.716536
01/2009	14138.39935	10793.21259	11516.16785	7487.650977	6789.258311	6257.220737	6333.867091	5806.064954	5012.004219	3116.959223	2190.64924
02/2009	12996.94927	10088.58053	10569.51843	6885.701527	6252.635348	5703.872519	7083.768494	6091.587521	5524.796143	2747.427565	3567.087919
03/2009	11799.00531	9660.189858	9783.939975	5443.274097	6325.807588	4428.147655	5687.281755	4206.167427	3931.770023	2468.055829	1089.058324
04/2009	11065.24329	9361.670882	9025.501781	5079.183401	6122.053982	5275.48242	5481.75224	4141.637032	3848.796399	1631.343544	1047.129266
05/2009	14988.4631	15698.64484	11714.81654	8668.920157	10315.40448	9763.65765	8827.995356	8768.045273	8750.430571	4567.078541	1047.129266
06/2009	25629.40158	17035.05724	20749.96343	16074.83345	11732.48099	12984.75986	12971.12599	9285.866223	9153.610995	4346.125989	2953.419377
07/2009	21048.26389	17263.67914	17982.28721	17560.44221	15932.36005	16725.94253	19927.49272	20325.71185	18546.52371	11444.845	9562.572813
08/2009	15728.62727	14162.88779	16371.33787	13074.85935	10734.26878	12614.2194	19813.63027	19256.31091	18196.39305	8443.317311	3274.999231

09/2009	14010.34056	13094.00061	15698.01393	13564.62083	9065.407103	11944.28543	11781.19527	11230.38604	11193.08942	3177.333571	1047.129266
10/2009	12871.84505	12106.54927	13628.47492	12615.19645	7767.600213	12000.77207	10369.85421	8736.663646	8663.983776	3115.72771	1047.129266
11/2009	12809.24529	11298.06445	12001.76852	10179.5323	7377.016074	9173.551083	8967.130961	7149.183352	6581.349266	2510.51701	1047.129266
12/2009	11478.34825	10382.8507	10622.46064	9420.121814	6499.430323	6889.483218	7485.090221	5950.730819	5303.694093	1823.528436	1047.129266
01/2010	10057.81708	7721.939059	9326.32953	6209.820393	4961.505635	5037.112031	5142.822871	3699.354719	2267.660797	1594.568276	1246.660574
02/2010	10306.51742	7498.514701	10200.2653	7749.718933	4533.576569	5035.225826	5416.501469	3953.314398	2499.079416	4209.544791	3914.675155
03/2010	9878.600406	7286.012166	8357.388507	4938.56475	4209.544791	5683.951964	5333.291213	3619.879581	1312.392747	3499.062883	4498.390233
04/2010	10006.71967	7713.304681	9953.525921	4592.169749	4328.962522	3690.59467	5108.223741	2568.015484	2391.068201	4046.015455	3659.602129
05/2010	19130.86605	17585.88678	21648.76877	12565.47545	10953.64494	8488.207227	8174.833456	7363.585674	7293.888942	5222.524356	2234.620446
06/2010	21301.10813	18652.0059	21825.49566	20347.02513	15387.00649	14834.84858	14719.66807	13436.73361	13261.63281	7637.786664	4534.740068
07/2010	21734.6562	18507.39451	20787.42332	15634.71421	19106.68619	12203.6072	12976.81025	13502.84982	13413.3089	7302.421653	6823.593712
08/2010	24609.84843	17055.02252	21817.78497	16653.80986	20763.31587	14596.25945	12199.34945	10633.6841	10580.85442	4751.609055	1736.739134
09/2010	19288.60747	13470.03764	19679.96398	23310.41875	9104.675616	19479.30307	13150.88375	8757.141864	8316.261671	6030.381026	1450.184572
10/2010	16593.65275	12826.49756	20473.23532	20088.40476	8440.967937	15252.88502	11111.15769	7085.912924	6656.422976	4117.088226	1744.633511
11/2010	15217.53769	11234.08315	17095.46823	14169.32433	7253.65159	10848.37007	9012.121281	6668.816571	5690.976956	3398.516732	4117.088226
12/2010	15976.94834	12257.01815	16393.04061	10876.54858	6543.021765	8172.506228	6861.399742	5854.269251	4220.987486	2200.573041	1438.720182
01/2011	14807.78955	10823.61876	14036.18816	9418.773848	5842.730615	7496.59986	5482.548139	4000.201992	3823.602964	3041.274772	1057.925174
02/2011	12778.63024	9534.106359	11633.55488	7479.108299	6411.030769	5799.316188	5300.716162	3871.271632	3698.48058	3488.284407	2742.665983

03/2011	11718.04014	8956.707172	10130.94052	7743.54068	6852.751444	4958.588817	4308.442765	3733.986779	3004.629339	2578.851121	1510.221734
04/2011	10979.4017	8340.745747	9036.792835	6387.373613	5449.724913	4559.612227	5938.547067	3593.214527	2862.922255	523.564633	1488.948172
05/2011	13092.46579	12355.41839	10397.80633	7329.236992	6970.420322	5966.562681	6329.093567	5691.71542	4353.079802	2809.397102	1246.660574
06/2011	23721.4168	20287.9788	17508.58945	15716.14446	16290.12291	12889.21822	13471.28993	11301.4365	10846.94714	5838.172554	7320.543545
07/2011	24559.90449	21626.18645	18398.58261	16799.9165	21623.55218	12441.69976	12731.65604	14131.81483	13490.57217	8404.892102	7961.536381
08/2011	21456.72415	17834.01077	17961.73639	16565.89444	14274.16521	12121.95202	12707.48294	12251.76173	11350.01395	8329.038939	5806.774439
09/2011	16250.86314	13307.71534	14727.44706	15440.26692	9576.807906	14088.14204	12736.30272	11039.59158	8940.128107	8399.979436	2594.935847
10/2011	14898.64714	12232.68927	13492.28056	13975.89132	8523.418118	12624.35836	11589.37909	10299.98296	8860.258131	8981.238886	3417.054463
11/2011	13857.63637	11699.1088	11655.86965	11115.22494	7792.693492	9820.907353	9150.469644	6874.584534	6834.621036	1969.745754	2784.939739
12/2011	12577.05424	10559.98166	10196.93068	9200.474755	6826.931312	7913.892058	7388.645536	4870.448203	4817.437861	1626.837047	1889.453703
01/2012	11674.67812	10101.02109	8819.700528	7337.243447	6447.199736	6146.210616	7284.209367	4823.61407	4041.627149	2063.822454	2547.9092
02/2012	11233.32496	9639.511589	8811.544109	6987.853811	6235.149229	5369.209526	7445.819652	5847.981094	4199.396379	2403.554423	2635.160248
03/2012	10738.41905	9391.733122	9167.720465	6552.50644	5706.811903	4534.158393	5074.54318	4131.15183	4123.428721	1779.30414	2333.196909
04/2012	15897.70148	10622.77862	15188.19759	6766.086601	5377.494078	5176.069963	6362.94916	4154.149607	3283.895708	2185.653443	3102.116335
05/2012	21817.48346	18462.80268	19741.19413	8543.619369	11425.36321	6371.504297	7130.884515	7214.112027	7129.002395	3485.333235	2555.257212
06/2012	27451.25022	23387.11477	21034.13557	16797.37358	22880.32708	13036.19666	13889.14085	12514.44147	11822.92541	6906.575037	5355.066826
07/2012	30109.7889	25476.34667	25246.91556	13684.01218	26237.3655	10915.33328	13278.20512	14237.61986	13454.66163	8257.921405	8333.518955
08/2012	25005.89441	20873.3937	21935.76162	12778.19077	21717.62938	9478.122518	10490.99831	9814.20671	9540.549125	4689.892861	5344.201201

09/2012	19113.26891	14308.36323	15383.52016	9638.095547	9627.655493	7709.080857	12167.44231	11212.43472	11177.98608	3394.369667	3276.113935
10/2012	20012.57337	13035.91515	16878.70396	10298.40444	8703.160583	8359.27165	9936.233072	9234.680718	9125.835297	6462.127185	1575.526834
11/2012	19713.44297	12531.90518	16040.74201	10185.87634	8159.413265	7582.233404	7104.206896	5742.213509	5492.477435	2687.505697	1626.837047
12/2012	16610.92213	12092.66139	13860.43842	9175.824437	7666.585651	7095.903147	6422.069267	4894.529921	4592.169749	3583.927293	2547.9092
01/2013	14281.96787	11355.48889	12156.36467	7219.393728	7170.879489	7201.21979	6808.920932	5203.158674	4312.305109	2354.963063	1657.874095
02/2013	12754.70855	10820.14658	10955.73784	6842.548948	6488.08551	5844.481823	7698.198288	5468.586409	4681.17658	1421.173064	4652.069497
03/2013	11675.20459	10171.56221	9477.856245	5436.40331	6190.219146	3228.627324	4688.805097	3028.288812	2954.789873	0.262413601	3416.029859
04/2013	11330.11123	9921.675001	8982.721355	4742.054855	6225.28932	3415.00464	4754.256191	3001.977414	2723.45228	1899.450998	2322.159862
05/2013	12213.55715	10468.23765	11211.86389	6071.214166	6107.980981	5725.479691	7405.912364	5269.459193	5163.540307	1966.658373	1515.447457
06/2013	22036.70721	20880.638	20836.65578	17835.402	16836.02755	13769.38475	13944.59352	13035.2817	12630.65884	6131.61224	3312.48144
07/2013	21503.17578	20662.03632	20679.78228	17450.53851	18398.33529	12383.4027	15346.33545	17562.5751	16108.41218	10248.20345	6617.324142
08/2013	16848.08638	16746.01151	18003.93505	14508.83735	14416.20661	12665.87065	11440.00362	11281.36186	10916.03591	5036.169105	3042.567281
09/2013	16852.42503	15029.66185	17036.82925	13198.84011	10165.5475	13338.57432	12661.39595	13527.86122	12680.1685	10027.69693	1047.129266
10/2013	17296.84255	13578.71122	14711.71507	11754.94144	8592.494178	10399.02304	11229.43767	11261.30983	8927.990952	10001.34202	3266.054157
11/2013	15330.01668	12227.25191	13098.46351	9636.16391	7553.20562	8965.345747	9426.18289	7798.990779	7763.832132	2610.823605	3529.086755
12/2013	13740.49603	11070.41793	11800.46559	7801.742648	6666.12623	7506.376567	8106.070423	6142.72601	5999.970783	1858.808496	3855.244656
01/2014	12417.15909	10414.26313	10496.21171	6711.038926	6291.247854	6825.134548	6861.653774	5146.437896	5068.963688	1608.556432	3154.663126
02/2014	11467.08097	10237.83019	9534.501065	6332.674385	6293.966239	6621.964049	6068.617271	4735.663938	4735.663938	1455.849413	3389.171543

03/2014	10603.56018	9644.143001	8501.797132	5366.303885	5742.576205	5711.215309	5587.556873	3828.505024	3745.104992	630.9326251	2504.81127
04/2014	10059.47201	8816.624407	8278.739488	6852.24204	6177.709196	5103.6362	4817.437861	3321.17851	3242.337159	0.262413601	1047.129266
05/2014	16278.26105	11740.29552	16779.55155	8164.97842	6716.610898	6595.401423	7043.739577	5810.319262	5631.267856	1740.695273	1146.480666
06/2014	23442.02336	19113.03973	21631.22302	18175.09289	17644.85758	14629.47285	13829.61586	13056.36351	12472.06711	8016.999673	2854.14023
07/2014	19221.25154	16455.5984	17468.82132	13995.15249	21411.50544	12378.25309	21966.68808	21929.69518	20078.08568	11434.51785	7990.48836
08/2014	20571.5741	22308.94661	16117.07279	13766.92414	19911.87943	11914.36639	13838.98946	12693.24659	12372.86482	5010.575483	4263.519191
09/2014	15174.70559	14058.00837	16501.14138	18098.26605	10568.23358	14423.45397	14910.54534	13076.32836	12312.96606	6516.93691	2413.861386
10/2014	13492.74044	13109.05072	15473.25659	14437.58263	9429.815797	14064.17846	13628.47492	12136.50381	11044.5942	7824.469532	2657.362904
11/2014	12735.93406	11973.80507	13243.79172	10837.38345	8131.11116	10919.04615	10928.16707	8606.079938	8575.288691	3095.889669	3671.174774
12/2014	12091.10723	10824.12919	11540.73474	9091.527322	7570.565526	9311.455634	9762.904833	6895.27376	6882.67318	2038.23524	1756.342812
01/2015	10759.3291	10170.52171	8481.063386	4506.06064	6665.587901	6131.294111	6551.949277	4805.037708	4501.343484	2983.28134	1261.86525
02/2015	10727.30987	9788.310928	8439.289011	3850.410489	6213.230169	5579.116442	5837.119682	4827.209567	4412.8464	2315.486952	1748.554049
03/2015	9807.248216	9407.300531	7687.487245	2809.397102	5921.200697	4670.783656	4552.698475	3983.690652	3772.1953	775.5290836	1985.039423
04/2015	9561.395542	9138.455509	7450.131696	4533.576569	5651.560888	6242.83064	5369.209526	4694.781564	4149.292571	2123.834766	599.3318924
05/2015	11732.48099	12143.15835	10125.11077	5426.673708	7780.265876	5126.94706	5663.145051	5221.208527	4158.303759	3061.824549	1704.420179
06/2015	25034.78092	22216.13788	21885.78753	15213.92158	17089.49138	13524.52735	13966.82326	12075.4616	11821.98416	5462.180093	2784.939739
07/2015	21610.37121	19742.26819	18469.29131	14769.40003	18888.90719	14356.39699	17334.09954	17864.23058	16524.69492	10440.33272	7453.362456
08/2015	19307.39462	17406.28169	15237.65322	12030.92447	12108.18105	12478.36866	21602.81369	23032.96695	20654.63783	13392.66993	5346.712575

09/2015	18159.43857	14180.57422	18516.74759	18924.30595	9566.102885	16391.74986	15987.34305	14604.0022	14458.03736	5307.517954	0
10/2015	14499.79811	12301.27973	14756.06474	14272.52146	7975.662628	13544.57116	12370.44248	10401.56616	10185.41522	4080.065888	0
11/2015	13663.5429	11251.87105	13633.17395	10876.75077	7011.288416	10318.77531	9443.112568	7519.30218	7098.514991	3815.404819	0
12/2015	12656.0968	10427.36922	11220.13518	8114.61615	6242.523747	8225.347176	7815.668757	6314.729617	5864.024062	2648.86744	0

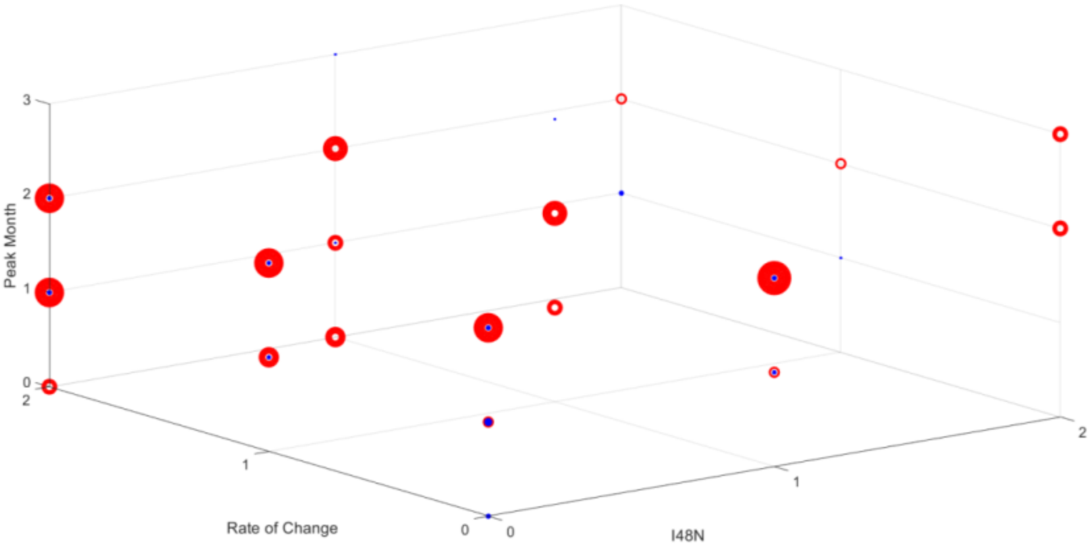

Figure S1. Plot of the linear SVM combinations from the testing period of 1931-2017, where I48N, the rate of change and the peak month are marked on the axis. A red circle corresponds to one peak, while blue represents multiple peaks. The larger the circle, the more times that combination has occurred.

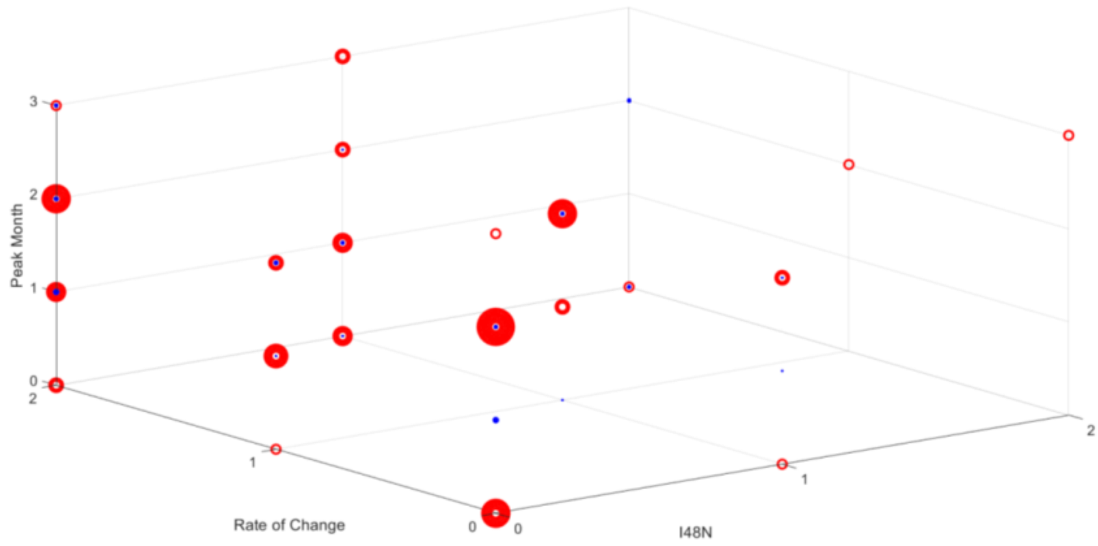

Figure S2. Plot of the quadratic SVM combinations from the testing period of 1931-2017, in the same format as Figure S1.

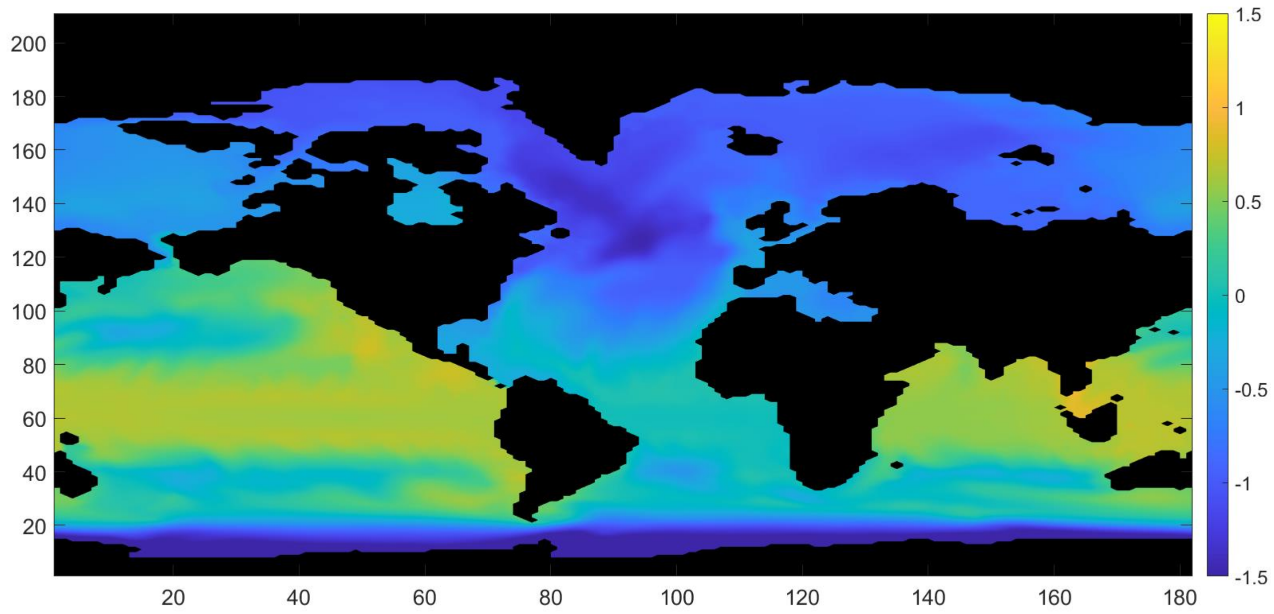

Figure S3. Plot of the FRUGAL Run 2 surface height for the decade 1995-2004, m.

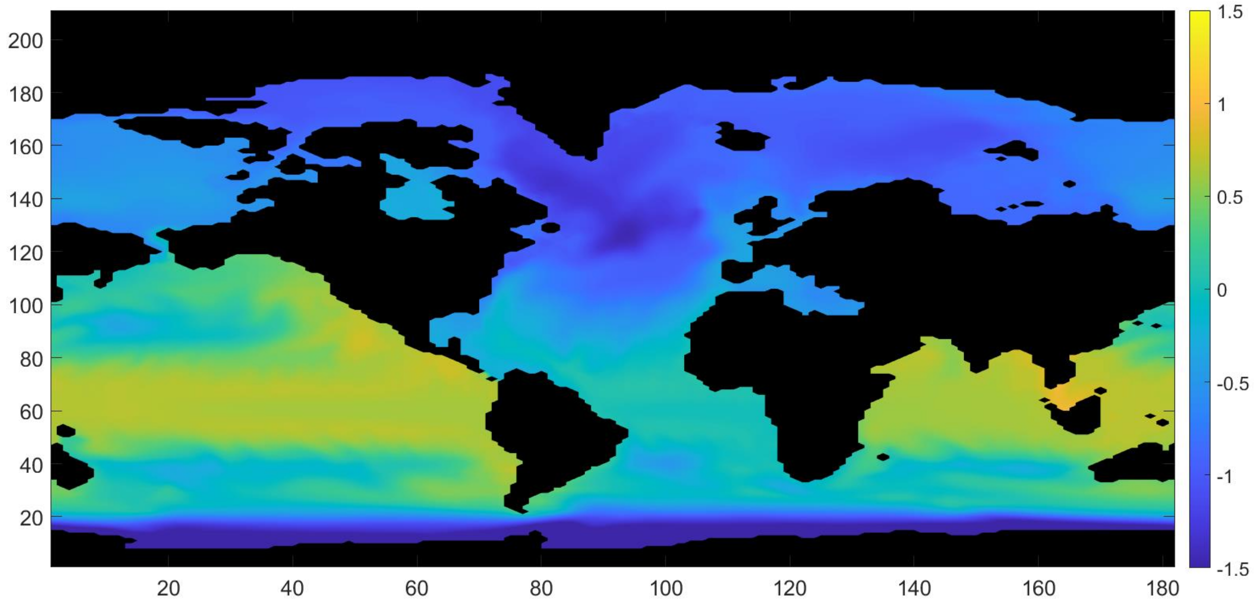

Figure S4. Plot of the FRUGAL Run 3 surface height for the decade 1995-2004, m.

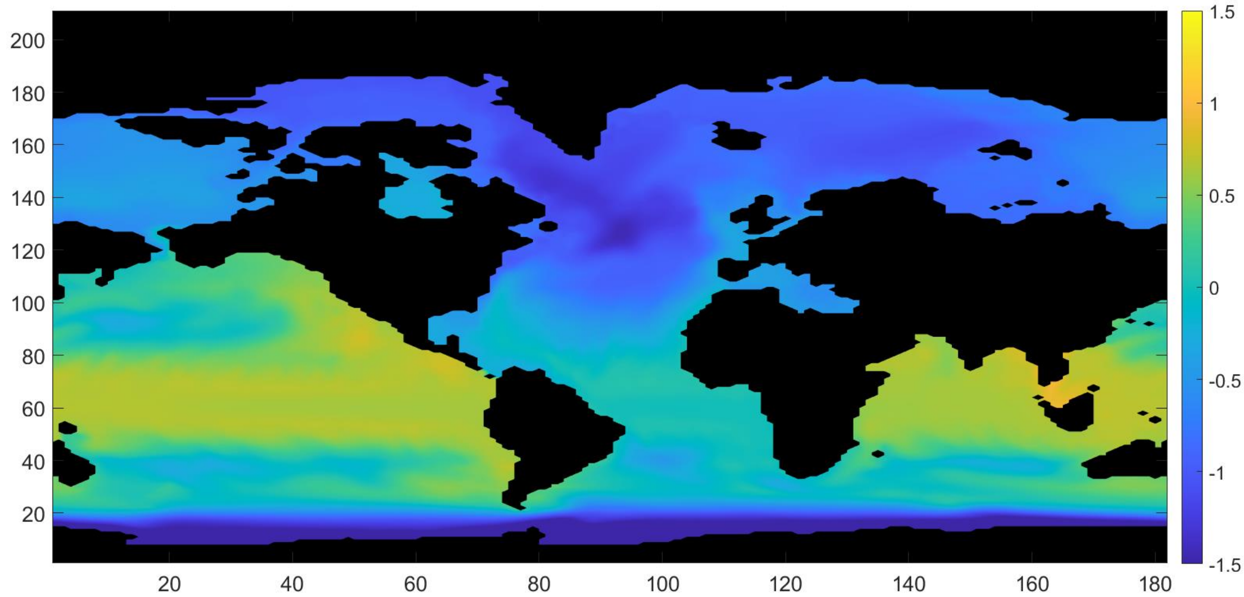

Figure S5. Plot of the FRUGAL Run 4 surface height for the decade 1995-2004, m.

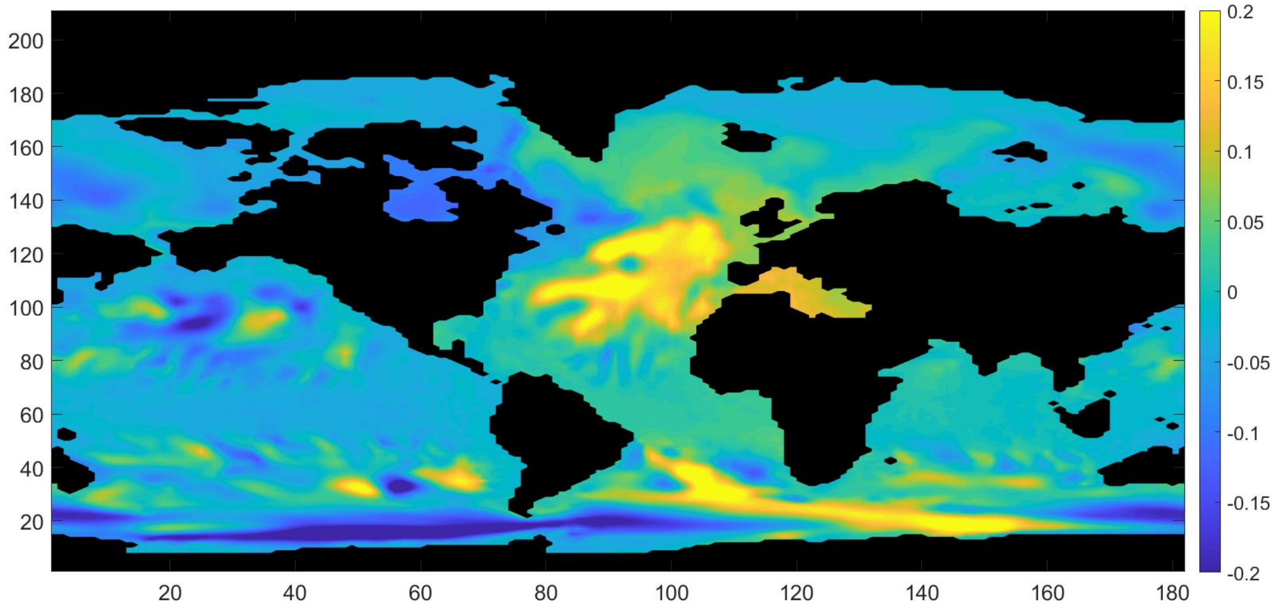

Figure S6. Plot of the FRUGAL Run 2 surface height for the decade 2005-14 minus the average for the decade 1995-2004, m.

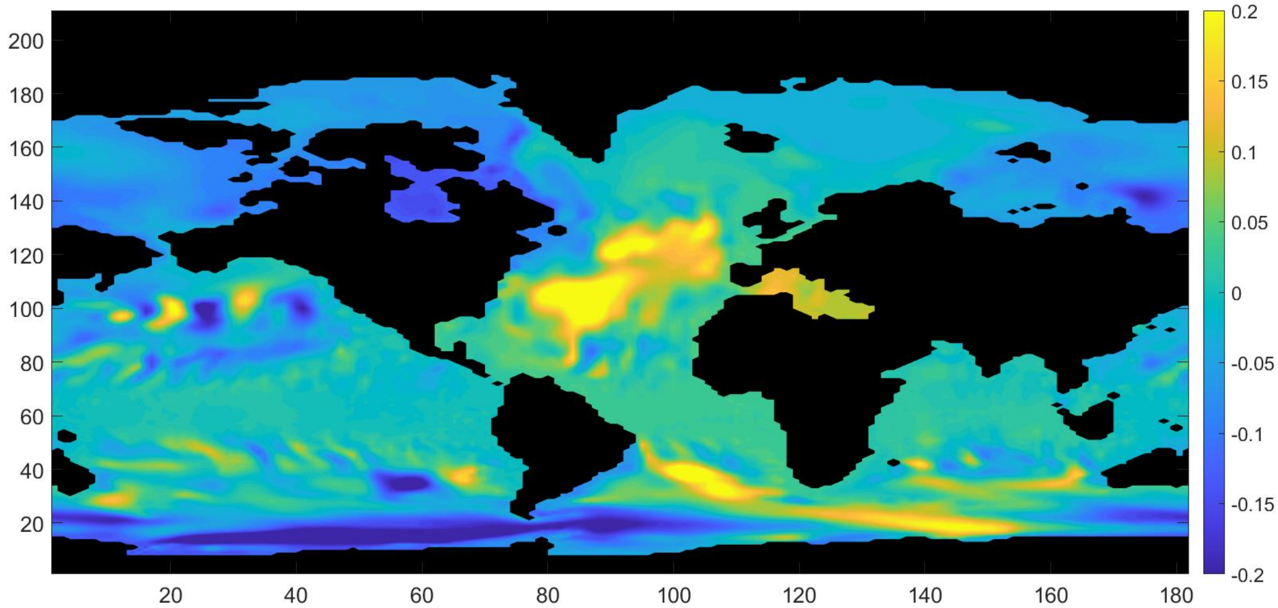

Figure S7. Plot of the FRUGAL Run 3 surface height for the decade 2005-14 minus the average for the decade 1995-2004, m.

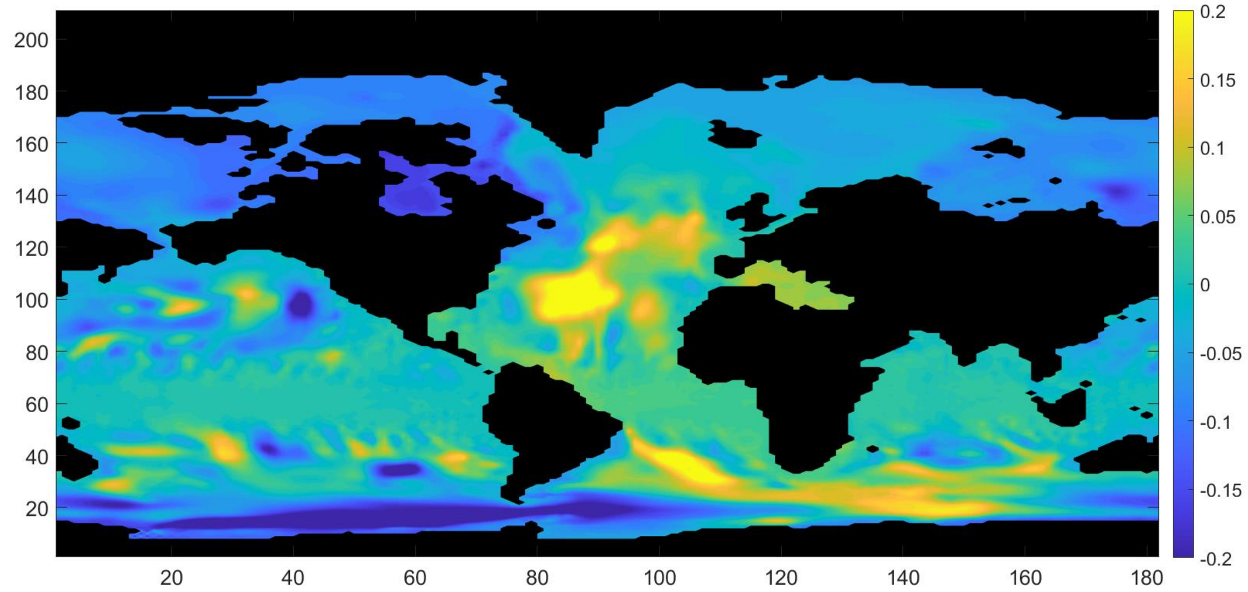

Figure S8. Plot of the FRUGAL Run 4 surface height for the decade 2005-14 minus the average for the decade 1995-2004, m.

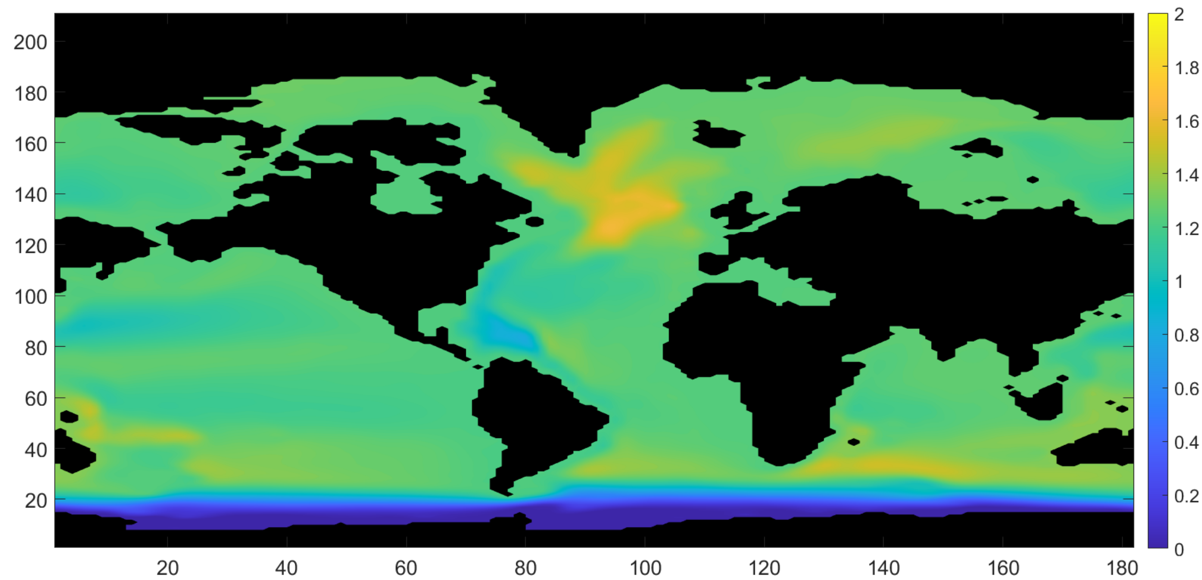

Figure S9. Plot of the FRUGAL Run 2 surface stream function for the decade 1995-2004, m.

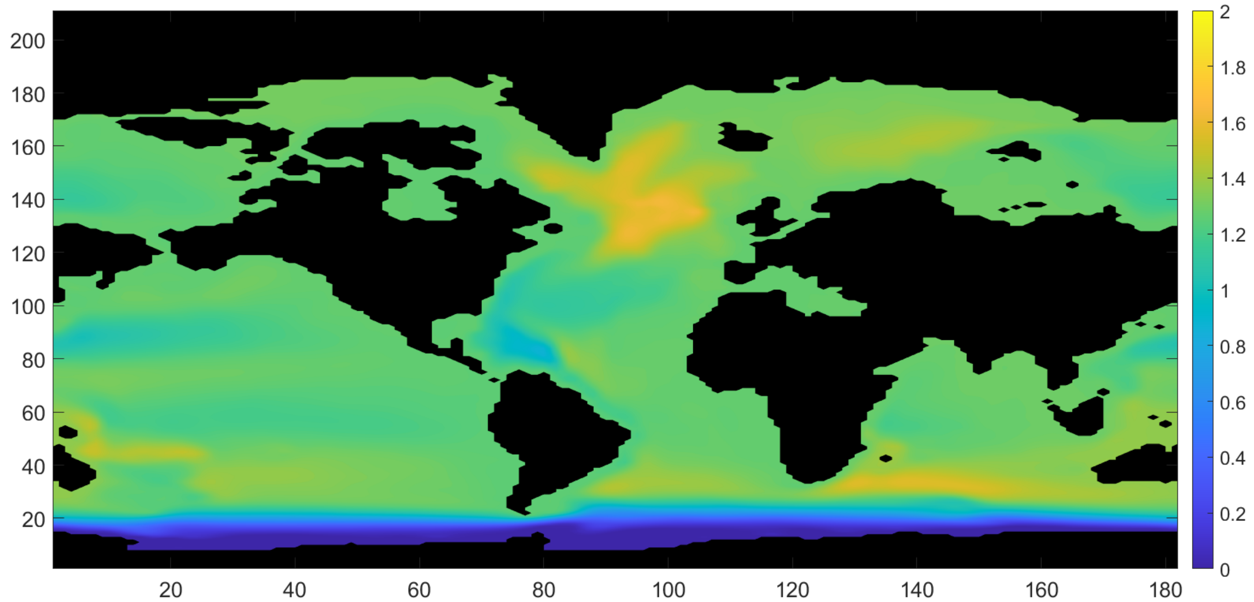

Figure S10. Plot of the FRUGAL Run 3 surface stream function for the decade 1995-2004, m.

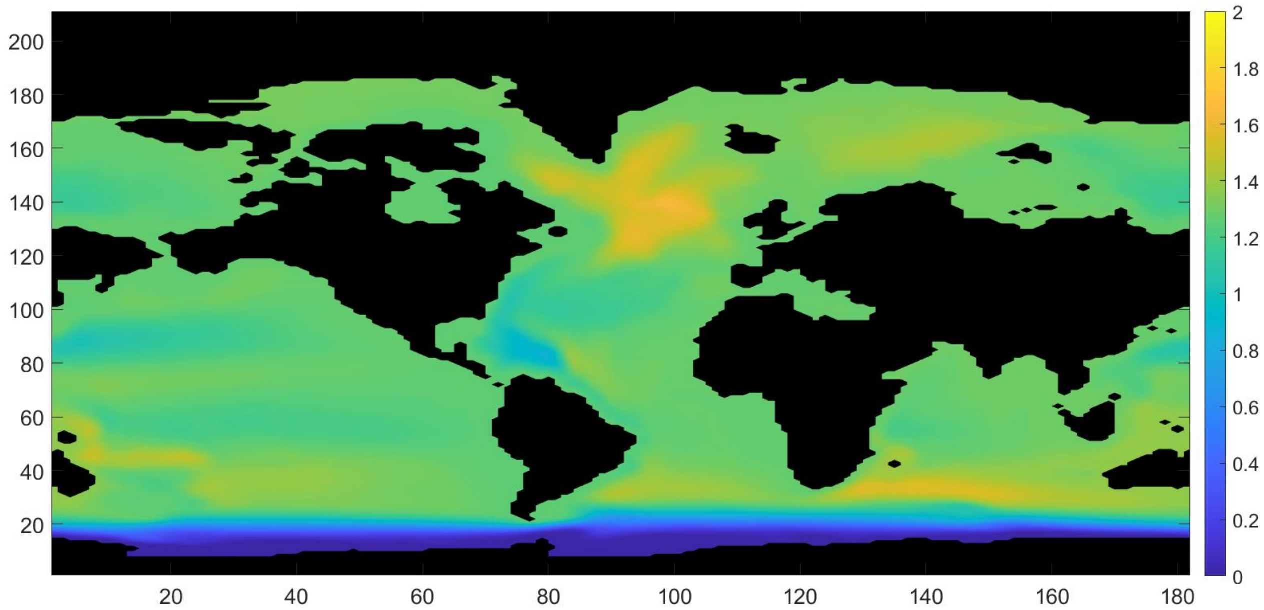

Figure S11. Plot of the FRUGAL Run 4 surface stream function for the decade 1995-2004, m.

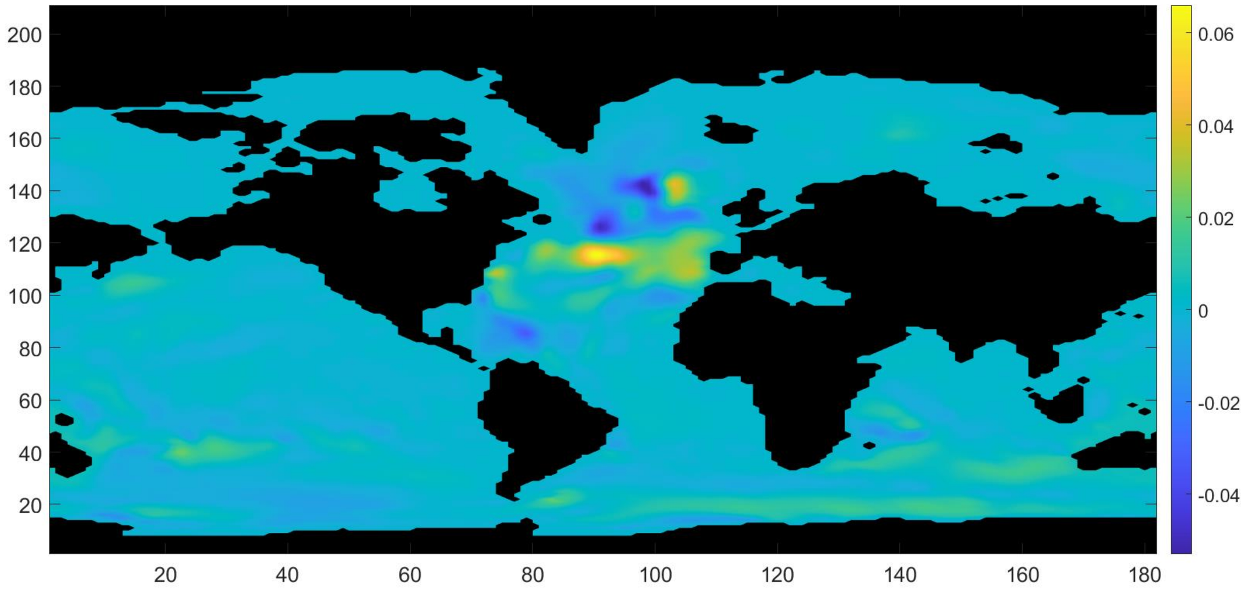

Figure S12. Plot of the FRUGAL Run 2 surface stream function for the decade 2005-14, m, minus the control run for the same decade.

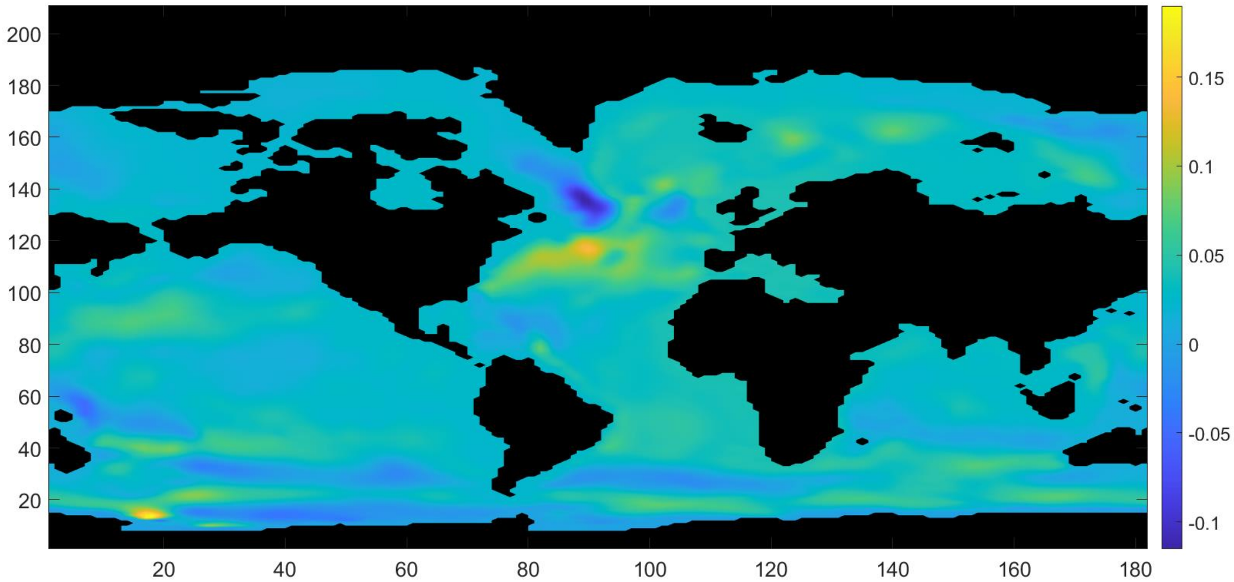

Figure S13. Plot of the FRUGAL Run 3 surface stream function for the decade 2005-14, m, minus the control run for the same decade.

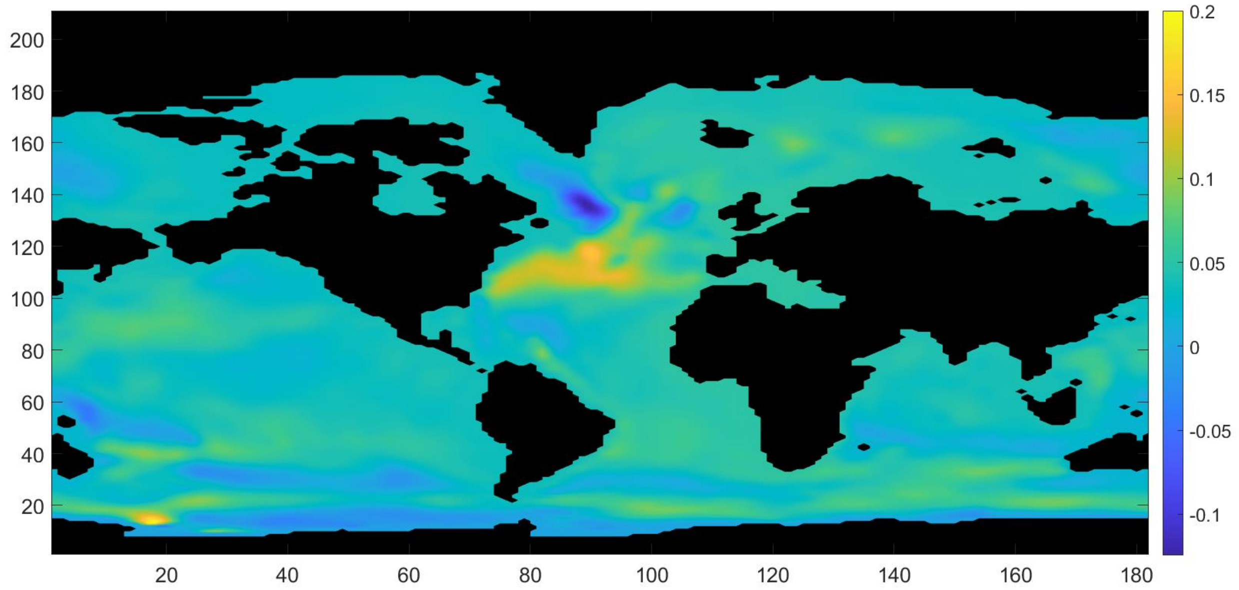

Figure S14. Plot of the FRUGAL Run 4 surface stream function for the decade 2005-14, m, minus the control run for the same decade.